Ph.D. Thesis

High energy resummations

&

QCD phenomenology

Clara Salas Hernández

Supervisor: Agustín Sabio Vera

Instituto de Física Teórica UAM/CSIC

Madrid, 2013

A mi familia

Contents

Acknowledgements

I can only start thanking my supervisor, Agustín Sabio Vera, because without him none of the work here presented would have been possible. This is probably the most common sentence in the world of PhD thesis. Maybe what it is not that common is that, not only I have learned so much physics during these years but I have specially enjoyed every discussion with him because of his constant positivism, energy and so much fun. Our offices were adjacent and whenever he had someone in for discussion the walls were vibrating because of the laughs of the visitor. He also gave me the opportunity of going all over the world giving seminars and attending conferences in a very hard economical period for our country. Thank you for all your constant support and care, it meant (and means) a lot to me. It has been a great pleasure to have you as advisor.

Secondly, I would like to give a special mention to Martin Hentschinski, without you my year in Cambridge would not have been the same, and I will always remember that, thank you a lot!

Martin and Grigorios Chachamis, thank you so much for all the patience you had during these years and all the hours you spent instructing me without any obligation. You are both great persons and I feel so lucky I got to work with the two of you.

I also have to thank the economical support of the LHC-Phenonet, which covered almost all the conferences and workshops I attended and Germán Rodrigo for his constant "sí a todo" whenever I was asking for money.

También tengo que agradecer mucho a las mejores secretarias del mundo, Isabel Chabe y Roxanna, una vez más, ¡¡qué habría hecho yo sin vosotras!! Como siempre digo, lo de los cimientos está sobrevaloradísimo, ¡el IFT lo levanta la quinta planta! Y, Andrés, lo dejo con la cita a la canción, “Sin ti no soy nada”. Un millón de gracias por haberme salvado la vida tantas veces con el ordenador.

During my studentship I had the privilege of paying a 6-month visit in 2012 to the Cavendish Laboratory of Cambridge, UK. I thank Prof. J.W. Stirling for hospitality during this period and for interesting discussions.

Francesco and Beatrice, thank you for the patience, specially during the last

month. It is a pleasure working with Cosenzians! Grazie per tutto. Y Jose y Edu, also thank you to you too. I had so much fun with you, it was great sharing supervisor with the two of you! Specially at the end, Jose, so convenient! Thank you so much for the last details! Edu, ¿viaje en furgo?

Regarding the IFT, I would like to thank my officemates, Alicia and Mikel. Alicia, thank you so much for the difficult times you helped me in passing and the confidence and support you gave me, I will not forget it. Mikel, thank you so much for all the printing!

Yianni, I enjoyed very much all the things we did together, thank you very much for your company, it meant a lot to me.

Jesús Moreno, it was nice knowing that there was always someone with me at the latest evening hours in the IFT building. Juan Bellido, thank you for all the music and inspiring conversations. And other PhD students, Germán Gómez, Fran, Rodrigo, Antonio, Luis Fer, Víctor, Zuma... Each of you helped me in different ways, thank you!

And now my friends from the university, the people I started my university studies with. Paloma y Emilio, gracias por ser dos constantes en mi vida, ¡os quiero! Vuestra amistad es un pilar básico para mí. Fito, especiales gracias por haber tenido siempre plena confianza en mí con respecto a la física. Miguel, muchas gracias por tantas conversaciones que me han sido tan necesarias durante este período. Me has ayudado mucho, tanto en el campo profesional como en el personal. Paula, gracias por esos momentos, experiencias y conversaciones que hemos pasado juntas estos años y nos han unido. Pablo, Edu, Yago, Manuela, Luis, Pep, Drino, Paco, Ernesto, me ENCAaaaNTA cerrar los ojos y veros a todos allí juntos en las mesas.

I also would like to thank Jo Gaunt, Eleni Vryonidou and Lucian Harland-Lang, my beloved office mates in Cambridge and also good friends. Thank you for the formals, beers, and salsa!

I should give a special mention to my friends Snezana, mi Guapa, and Ennio, who made possible my one month stay at CERN during the summer of 2012, from which a big part of this thesis was finally finished. I would also like to thank my officemates and friends Marc, Valerio and Andrew, that made working every day until night during August to be a great pleasure.

Stef, you became a very important person in my life, you mean a lot to me. Thank you so much for being there. You are wonderful, Troia.

Esta tesis se la dedico a mi familia. A mis padres y mi hermana (¡y Jonny!). Porque son los que más me quieren y apoyan en este mundo y porque siempre estarán ahí para mí, para lo bueno y para lo malo. Os quiero.

"QCD nowadays has a split in personality.
It embodies hard and soft physics, both being
hard subjects and the softer the harder"

Yuri Dokshitzer [1]

Resumen y conclusiones

En los últimos tres años el acelerador de partículas del CERN, Ginebra, con siglas LHC (Large Hadron Collider), ha generado una gran cantidad de nuevos datos experimentales en la física de partículas a unas energías jamás cubiertas hasta el momento. En 2012 el acelerador alcanzó una energía máxima de 4 TeV por haz de protones seguida un parón programado de 20 meses tras el cual se espera que el sistema se reinicie a una respetable energía de centro de masas de 14 TeV. Esto nos coloca en un período especialmente importante en el mundo de la física de las altas energías.

Dado que resulta poco probable que vaya a surgir nueva física en este primer período de toma de datos, parece que tras haber confirmado todo el Modelo Estándar (SM) de las interacciones fundamentales lo único que queda por hacer es análisis de background. Sin embargo, los rangos de energía y luminosidad provistos en este período por el LHC proporcionan una ocasión única para analizar en mayor detalle el límite de altas energías de la teoría de las interacciones fuertes, también conocido como *límite de Regge* [2, 3]. Dicho límite se alcanza cuando el cuadrado de la energía del centro de masas de un proceso de dispersión, s, es mucho mayor que cualquier otra escala involucrada en la interacción, en concreto el momento transferido entre las dos partículas dispersadas, t. En función de la variable x de Bjorken, definida en Deep Inelastic Scattering (DIS, que podría traducirse como dispersión altamente inelástica) como $x \simeq |t|/s$, este límite se conoce también como el límite de baja x. Un aspecto interesante de este límite es que vive en la frontera entre la física perturbativa y la no perturbativa, permitiéndonos de este modo que nos acerquemos al estudio del infrarrojo (IR) basándonos en propiedades de analiticidad y unitariedad de amplitudes de dispersión.

Hoy en día la física de las interacciones fuertes viene descrita por la Cromodinámica Cuántica (QCD). Sin embargo, en la década de los 60, antes incluso de la existencia de ninguna teoría de campos, la teoría de Regge fue capaz de hacer una predicción importante acerca del comportamiento de secciones eficaces hadrónicas en el límite de altas energías. Asumiendo la existencia de polos de Regge en la amplitud de dispersión y basándose en sus propiedades fundamentales (los

postulados de la matriz $\mathcal{S}$ de dispersión, esta teoría predijo un crecimiento de la sección eficaz total de dispersión como una potencia de la energía: $\sigma \sim s^{\lambda_p}$, donde λ_p es el denominado *pomeron intercept*.[1] Esta predicción fue corroborada experimentalmente unos años más tarde, proporcionándole a la teoría un importante apoyo. Mediante ajustes a los datos experimentales [4] se obtuvo valor para el pomeron intercept del orden de 0.1. En términos de Regge, este crecimiento de la sección eficaz con la energía viene dado por el intercambio de un objeto que acarrea los números cuánticos del vacío entre los hadrones sometidos al proceso de colisión (partícula reggeizada, por definición). A dicho objeto se lo conoce como el *pomerón no perturbativo*.

Tras la llegada de QCD de manera consecuente se trató de explicar este pomerón en función de teoría de perturbaciones, dando como fruto el intento la llamada ecuación BFKL (Balitski-Fadin-Kuraev-Lipatov) [5–9], tema base de esta tesis doctoral. En el proceso de cálculo de observables físicos en el límite de Regge, aparecen logaritmos de energía grandes junto con la constante de acoplo fuerte que hacen que los términos de la serie perturbativa sean de orden 1 y tengan, de ese modo, que ser resumados para asegurar la convergencia de la serie perturbativa. Esta resumación es se consigue resolviendo la ecuación BFKL y su solución nos proporciona lo que se conoce como pomerón perturbativo o pomerón de QCD, que es el estado ligado de dos gluones reggeizados intercambiados entre los dos hadrones en el canal t. El pomeron intercept para el caso perturbativo calculado a primer orden en teoría de perturbaciones, LO, es $4 \ln 2 \bar{\alpha}_s$, que, para un acoplo típico de $\bar{\alpha}_s \simeq 0.2$ da ~ 0.5, un valor muy diferente al encontrado para el pomeron no perturbativo. Sin embargo, si se calcula al siguiente orden en teoría de perturbaciones, NLO, el valor baja a 0.3. Si estos dos pomerones son o no de la misma naturaleza es algo que aun no se sabe a ciencia cierta y es un tema de discusión interesante hoy en día. Encontrar una transición continua entre el uno y el otro significaría ser capaces de dar con un puente entre la física perturbativa y la no perturbativa, como será analizado en el contenido de esta tesis.

Con el trabajo aquí presentado se pretende entender mejor el límite de altas energías de las interacciones fuertes a través de ciertos estudios fenomenológicos seleccionados involucrando datos experimentales de distintos colisionadores. Algunos observables físicos, como la sección eficaz total de dispersión de dos fotones virtuales creados en colisionadores leptónicos son puramente descritos en términos de teoría de perturbaciones, dado que, si las virtualidades de los fo-

[1] La elaboración de esta sección se ha intentado hacer siendo lo más fieles posible al castellano puro. Lamentablemente, hay ciertos términos técnicos para los que no ha sido posible encontrar traducción.

tones son suficientemente grandes, nos sirven como escalas duras para correr el acoplo. Sin embargo, cuando hay hadrones involucrados en el proceso de dispersión, la situación se vuelve más complicada porque la física no perturbativa entra en juego y necesita ser modelada de alguna manera. En general, una colisión hadrónica está sometida a procesos tanto de larga (no perturbativos) como de corta (perturbativos) distancia. Gracias a la libertad asintótica [10, 11] podemos utilizar teoremas de factorización que nos permiten escribir cualquier sección eficaz como una convolución de estos dos procesos, permitiéndonos separar nuestra ignorancia de nuestro conocimiento, modelar la primera y fijarla haciendo uso del experimento, y utilizar toda esta información para hacer predicciones.

El tipo de factorización a utilizar dependerá de la región cinemática que estemos considerando. En el límite de x grande, por ejemplo, habría que usar factorización colineal y escribir la sección eficaz total como una convolución del sub-proceso partónico (perturbativo) con las llamadas funciones de distribución partónicas (PDF) [12]. Estas últimas son objectos universales (que no dependen del proceso considerado) extraídos de los datos experimentales y que contienen toda la información de la estructura del protón. Por otro lado, en el límite de x baja, habría que usar la factorización de altas energías, en la que la información del protón viene dada en lo que se conoce como factor de impacto del protón [13].

Este trabajo se ha dividido en dos grandes bloques. En el primero nos centramos en la descripción a un nivel más fundamental del formalismo BFKL, mientras que en el segundo viramos al nivel fenomenológico, proponiendo análisis de diferentes obervables relevantes en el límite de altas energías.

Pasamos brevemente a explicar los resultados a los que ha dado fruto esta tesis doctoral. Como hemos explicado, está basada en el análisis del formalismo de la resumación BFKL a LO y a NLO, especialmente desde el punto de vista fenomenológico.

A NLO, la ecuación BFKL está gobernada por lo que se conoce como quasi-multi-Regge-kinematics (QMRK), y resuma términos de la forma $\bar{\alpha}_s(\bar{\alpha}_s \ln(s/s_0))^n$. Al contrario de lo que ocurre a LO, la escala de energía s_0 no es un parámetro libre a NLO. Se sabe que las correcciones NLO a la función de Green del gluón son grandes y negativas comparadas con las LO, de modo que es necesario estabilizarlas para conseguir descripciones significativas de los datos experimentales y poder hacer predicciones fiables. Este comportamiento viene dado por la libre elección de la escala s_0 a LO, que introduce logaritmos dobles en momento transverso que son incompatibles con evolución del grupo de renormalización (RG) y se hacen muy grandes numéricamente en las regiones colineales del espacio de fases. Cuando el kernel de la ecuación BFKL se exponencia siguiendo

argumentos de bootstrap y la serie perturbativa se trunca a NLO, queda una dependencia residual en estos logaritmos que se vería cancelada de forma exacta si se consideraran órdenes más altos de la serie perturbativa. Una forma de mejorar esta situación es introduciendo correcciones colineares a todos los órdenes en teoría de perturbaciones siguiendo los trabajos [14, 15]. Todos los estudios fenomenológicos propuestos en esta tesis evidencian la importancia de añadir correcciones colineares al resultado NLO para obtener una descripción adecuada de los observables.

El primer ejemplo lo encontramos en el capítulo 4, donde analizamos datos experimentales de DIS en la región de baja x de Bjorken usando resumación BFKL. Vimos cómo la solución puramente NLO no era suficiente para reproducir los datos y sólo cuando añadimos correcciones colineales pudimos obtener una buena descripción de la región perturbativa parametrizada por la virtualidad del fotón, Q^2. Además, para obtener una buena descripción de los datos combinados de HERA en la zona de bajo Q^2 (del infrarrojo o no perturbativa), nos hizo falta introducir un esquema físico con escala óptima de renormalización y utilizar un modelo para el acoplo con comportamiento analítico en el infrarrojo. De esta forma fuimos capaces de conseguir una transición continua y/o suave del pomerón perturbativo al no perturbativo en buena concordancia con los datos experimentales [16, 17]. La precisión de los resultados se podría mejorar incluyendo correcciones menores como la masa de los quarks o considerando efectos de umbral en la dependencia del acoplo en las masas de los quarks. Estamos considerando también la posibilidad de implementar el factor de impacto del fotón a NLO usando nuestro código para técnicas de Monte Carlo.

Otro punto importante a tener en cuenta a la hora de incluir correcciones a NLO es el tratamiento de la dependencia del acoplo con las escalas. Desde un punto de vista analítico, sabemos que el tratamiento de la escala genera una cierta incertidumbre teórica que entra como correcciones más altas del acoplo, $\mathcal{O}(\bar{\alpha}_s^3)$, pero que aun así dan lugar a efectos numéricamente importantes al calcular los observables. En este caso es mejor tratar el acoplo de forma numérica. En la sección 3.2.2 presentamos una solución iterativa a la ecuación BFKL a LO con momento transferido $t \neq 0$ incluyendo dependencia del acoplo en las escalas internas de momento transverso imponiendo compatibilidad con bootstrap y dimos resultados numéricos para la función de Green del gluón usando técnicas de Monte Carlo [18]. El siguiente paso en esta dirección será convolucionar esta función de Green con los factores de impacto adecuados para poder dar predicciones para observables exclusivos como puedan ser decorrelaciones de ángulos azimutales de jets (ver sección 5.1) o producción de múltiples jets. Estos procesos

son necesarios para discernir entre las predicciones dadas por distintas teorías de resumación.

En la sección 5.1 estudiamos la producción de jets de Mueller-Navelet con los vértices de los jets calculados a NLO usando la aproximación de "small-cone" (cono pequeño) y con la función de Green del glúon también a NLO. Para fijar las escalas de factorización, renormalización y energía, empleamos el llamado principio de sensibilidad mínima (PMS), considerando como escalas óptimas aquéllas para las cuales la cantidad física que estemos evaluando exhiba variaciones mínimas. Esta forma de fijar las escalas hace que nuestra teoría sea predictiva, dado que no necesitamos nada externo para fijarlas. Un resultado importante de este trabajo es que el hecho de añadir correcciones colineales al caso NLO reduce de forma natural el valor de las escalas haciéndolas más parecidas al cuadrado del momento transverso típico de los jets producidos. Además, también pudimos encontrar zonas de estabilidad para los parámetros usando resumación colineal en regiones lejanas a QMRK (donde los jets tienen momentos muy diferentes), no siendo así para el caso NLO puro. Por último, también mostramos en este estudio cómo los mejores observables son decorrelaciones de ángulos azimutales, por ser bastante poco susceptibles a las contributiones colineares y muy convergentes en el contexto de QCD. También queremos implementar este observable con el código de Monte Carlo para así poder acceder a toda la información del estado final y poder estudiar cómo afectaría el tratamiento del acoplo a las regiones de estabilidad de los parámetros de la teoría.

Los últimos dos pequeños estudios fenomenológicos (preliminares) realizados están relacionados con la producción de quarks pesados en el LHC. Del análisis que hicimos sobre DIS comparando con datos de HERA en la sección 4.2.2 extrajimos un modelo para el factor de impacto del protón que luego hemos podido usar en la construcción de estas dos secciones eficaces usando factorización de altas energías. En el primero de ellos una pareja de quarks pesados se produce en la región central de rapidez, dejando espacio de fases suficiente entre los hadrones y el vértice perturbativo para emitir radiación gluónica e incorporar resumación BFKL. En el segundo caso, sin embargo, la pareja de quarks pesados se produce colinealmente a uno de los hadrones de modo que se tienen que usar los dos tipos de factorización, colineal y de altas energías. Los resultados presentados son preliminares e inacabados. Es nuestra intención presentar un análisis comparativo de estos dos estudios junto con los resultados presentados en [19].

Con esto se cierra esta tesis doctoral, elaborada en un momento óptimo dentro de la fenomenología de partículas, que, con los datos ya medidos, nos va a seguir dando muchos resultados que analizar durante los años venideros.

Chapter 1

Overview

Over the last three years the Large Hadron Collider (LHC) at CERN, Geneva, has generated new, interesting particle physics results covering unprecedented energy ranges. By the end of 2010 it had already beaten Tevatron maximum beam energies reaching 1.78 TeV per beam. This lead to the 'rediscovery' of the Standard Model (SM) of fundamental interactions. On top of it, the 4th of July of 2012 with a beam energy of 7 TeV, both ATLAS and ZEUS collaborations announced the discovery of a sign compatible with a Higgs boson, whose confirmation would be a significant signal in the completion of the SM. In the very same year the accelerator finally reached 4 TeV per beam, followed by a 20 month stop to get ready for the exciting era of the 14 TeV center of mass energy. We are therefore living a specially important period in the world of high energy particle physics.

Since it is unlikely that new physics arise at the energy range of this first stage of the collider and after having confirmed all the SM properties it may seem that background analysis is the only activity left for this period. However, the actual energy range and luminosities achieved by the LHC experiments provide a unique occasion for analyzing the high energy limit of the theory of strong interactions –also known as the *Regge limit* [2, 3]– in deeper detail. Consider a $2 \to 2{+}n$ scattering process. The Regge limit is attained when the squared center of mass energy s of the process is much larger than any other scale involved in the interaction, in particular the momentum transferred between the two scattered particles, t. In terms of the x of Bjorken defined in Deep Inelastic Scattering (DIS) roughly as $x \simeq |t|/s$, this is also known as the low x limit. One of the interesting aspects of this limit comes from the fact that it lies at the interface between perturbative and non-perturbative physics, allowing to test important properties of the infrared (IR) region based on analyticity and unitarity properties of scattering amplitudes.

The dynamics of the strong interactions is described nowadays by the theory of quantum chromo-dynamics (QCD). Notwithstanding, back in the 60's, prior to the conception of QCD, Regge theory was able to make an important prediction about total hadronic cross sections in the high energy limit. Under the assumption of the existence of Regge poles in the scattering amplitude and based on very fundamental properties of it – the well known $\mathcal{S}$-matrix postulates–, Regge theory predicted a growth of the total cross section as a power of energy, $\sigma \sim s^{\lambda_P}$, where λ_P is known as the pomeron intercept. This prediction was experimentally corroborated a few years later, giving an important support to the theory. Accurate fits to the data using this power growth [4] gave values for the intercept of the order of 0.1 for different hadronic cross sections. In the Regge approach this growth with energy is explained by the exchange between the colliding hadrons of an object carrying the quantum numbers of the vacuum (reggeized particle, by definition), known as the *soft pomeron*.

After the advent of QCD a natural step to do was trying to explain this pomeron in terms of perturbation theory. This attempt resulted in the construction of the so-called Balitsky-Fadin-Kuraev-Lipatov (BFKL) equation [5–9], main topic of this thesis. In the computation of physical observables in the Regge limit large logarithms of energy accompanying the strong coupling constant arise spoiling the convergence of the perturbative series. A resummation is therefore needed to be able to apply perturbation theory. This resummation is driven by the BFKL evolution equation, whose solution leads to the QCD or *hard pomeron*, a bound state of two reggeized gluons exchanged in the t-channel between the hadrons. The hard pomeron intercept calculated at leading logarithmic accuracy (LLA) was found to be $4 \ln 2 \, \bar{\alpha}_s$, which for a typical coupling of $\bar{\alpha}_s \simeq 0.2$ gives ~ 0.5, very different to the soft one. However, its calculation at next-to-leading logarithmic accuracy (NLLA) lowered this value down to 0.3. The question of whether or not these two pomerons are of the same nature is still unknown and constitutes a very interesting topic under discussion nowadays. Finding smooth transition between the two would imply finding an interesting bridge between hard (perturbative) and soft (non-perturbatve) physics, as it will be discussed in what follows.

The work presented in this thesis aims to achieve a better understanding of the high energy limit of strong interactions through some selected phenomenological studies involving data from different colliders. Some physical observables such as the total cross section for the scattering of virtual photons at lepton colliders can be described within perturbation theory since, provided two large virtualities of the photons. The situation is more complicated when hadrons are involved in

the scattering process since non-perturbative physics enters the game and needs to be modeled somehow. In general, a hadronic collision will involve both long and short distance effects. The natural expansion parameter of the perturbative series is the running coupling constant. In the case of QCD, the strong coupling, $\alpha_s(Q)$ (where Q is a hard scale present in the physical process) is already large at relatively large distances distances. For $1/Q \sim 1$ fm, the running scale of the coupling is of the order of the QCD confinement scale, making $\alpha_s(\mu_R)$ too big to be a good expansion parameter. Conversely, it becomes small at short distances. Asymptotic freedom [10,11] allows for the construction of factorization theorems with which we can express any hadronic cross section as a convolution of the long-distance effects and the short-distance or partonic level ones.

Depending on the kinematic region under consideration different factorization theorems need to be used. In the large x limit collinear factorization holds, and we can write the total cross section as a convolution of the partonic (perturbative) process with the so-called parton distribution functions (PDF's) [12]. These are universal -process independent- objects extracted from the data that encode the information of the structure of the proton. Alternatively, low x limit a different factorization must be applied in which the information about the proton is enclosed into an object known as the proton impact factor [13]. This impact factor accounts for the coupling of the pomeron to the hadrons and regulates the IR divergences of the total (hadronic) amplitude due to the integration over the full transverse momentum space.

This thesis is divided in two main blocks: The first one describes the main theoretical aspects of the BFKL formalism, and the second one is focused on the construction and phenomenological analysis of different physical observables that are relevant in the high energy limit. The organization is as follows:

Chapter 2 contains a short review of the basic tools and properties of perturbative QCD needed for the computation of the physical observables that will be analyzed. In chapter 3 we compute the BFKL equation and analyze its LL and NLL solutions. For the former we include a numerical analysis of the solution to the equation which takes into account NLL effects related to the running of the coupling, being compatible with the high energy bootstrap condition to all orders in perturbation theory. For the latter the running coupling effects need to be taken into account formally, leading to some theoretical uncertainties that will be identified and discussed. We will show that, due to the truncation of the perturbative expansion, the pure NLL solution presents collinear instabilities that may generate negative cross sections in those regions. To solve this problem, this chapter concludes with section 3.4 where we present a formalism consisting

of an all-order resummation of the collinear poles which already appear at NLL accuracy through the inclusion of higher order corrections. We will show that these collinear improvements are needed to obtain stable predictions providing good agreement with the experimental data.

In the second building block two types of observables are analyzed. In chapter 4 we present a description of the structure functions of the proton F_2 and F_L in the low x limit and compare our formalism with the latest combined HERA data results. We address the problem of the transition from the hard to the soft pomeron and, from the comparison with the data, we extract a universal model for the proton impact factor that will be used in the study of other observables.

In chapter 5 we analyze more exclusive observables, which are useful in order to discriminate the predictions given by different evolution equations. We focus in particular on the central and forward production of heavy quarks at the LHC and on the exclusive production of Mueller-Navelet jets at NLO including collinear corrections.

We finish with a summary of our conclusions and a discussion of some open questions in chapter 6.

Chapter 2

Brief introduction to perturbative QCD

2.1 Asymptotic freedom & collinear factorization

2.1.1 Ultraviolet renormalization

Let us start by writing the Lagrangian of QCD:

$$\mathcal{L}_{QCD} = -\frac{1}{4}F^A_{\alpha\beta}F^{\alpha\beta}_A + \bar{\Psi}(i\not{D} - m)\Psi + \mathcal{L}_{gauge\ fixing}. \tag{2.1}$$

The field strength tensor $F^A_{\alpha\beta}$ for a spin-1 gluon field $\mathcal{A}^A_\alpha$ is given by

$$F^A_{\alpha\beta} = \partial_\alpha \mathcal{A}^A_\beta - \partial_\beta \mathcal{A}^B_\alpha - g f^{ABC}\mathcal{A}^B_\alpha \mathcal{A}^C_\beta \ , \tag{2.2}$$

where the capital indices run over the 8 color degrees of freedom of the gluon field and f^{ABC} are the SU(3) group structure constants. Since the third term in eq. (2.2) is non-abelian, it does not appear in the QED Lagrangian. It is responsible for the triplet and quartic gluon self interactions and leads to the essential property of *asymptotic freedom*, as we shall see.

The QCD Lagrangian of eq. (2.1) is known to generate ultraviolet (UV) divergent scattering amplitudes. However, they can be eliminated by a process known as renormalization. The idea of renormalization is to introduce a mass regulator acting as a momentum cutoff to separate the divergent terms from the physical, finite ones and absorb the divergent pieces into a redefinition of the fields and parameters, being the final result independent of the regulator.

An alternative to the introduction of a cutoff is to work in $D = 4 - 2\epsilon$ dimensions. In this way the UV divergences translate into poles in ϵ. They can

be removed by introducing a subtraction scale μ_R^2 called renormalization scale. Once the divergences have been regularized they are eliminated by the addition of counter terms in the Lagrangian, which introduce the following renormalization constants: Z_g, μ_R^2, Z_1 and Z_3. They relate the bare (non renormalized) quantities to the physical, finite ones. In particular, the relation for the coupling g would be given by

$$g = \mu_R^{\epsilon}\, Z_g\, g_R \ , \tag{2.3}$$

where the parameter μ_R has been introduced by dimensional analysis.

It is a very remarkable property of QCD that it is a renormalizable theory. This allows to define the renormalization constants in a way that makes any physical observable free of ϵ-divergences. There is not a unique way to define these constants. Depending on the renormalization scheme these parameters will have more or less information about the finite pieces. Possibly the most standard renormalization scheme is the so-called $\overline{\text{MS}}$ or modified minimal subtraction scheme, in which in addition to the pure divergent part one also absorbs into the counter terms a certain 'universal' constant which is always present together with the divergences. If the physical observables could be calculated exactly (taking into account all orders in the perturbative series) the model would be independent of the choice of renormalization scheme. For a fixed order calculation this is not possible, so a good choice for an observable would be the one that minimizes the dependence on the renormalization scales. We will discuss this in Chapter 4.

2.1.2 Running of the coupling

After the subtraction of the UV divergences all the renormalized fields and parameters depend on the renormalization scale μ_R^2. However, this is not the case for the bare quantities. Therefore, we can study the scale evolution of the coupling g by imposing $g(\mu_R) = g(\mu'_R)$. By means of eq. (2.3), this leads to the relation

$$g_R(\mu'_R) = Z_g(\mu'_R, \mu_R)\, g_R(\mu_R) \ , \quad \text{with} \quad Z_g(\mu'_R, \mu_R) = \frac{\mu_R^{\epsilon}\, Z_g(\mu_R)}{(\mu'_R)^{\epsilon}\, Z_g(\mu'_R)} \ . \tag{2.4}$$

We can now study differential renormalization group (RG) transformations by considering the shift $\mu'_R = \mu_R + \delta\, \mu_R$, with $\delta \to 0$. The strong coupling constant α_s is related to g_R by $\alpha_s(\mu_R) = g_R^2(\mu_R)/(4\pi)$. Inserting this into eq. (2.4) and applying a differential transformation of scale, we find the following equation for it:

$$\mu_R^2 \frac{\partial^2 \alpha_s(\mu_R)}{\partial \mu_R^2} = \beta\left(\alpha_s(\mu_R)\right) \ , \tag{2.5}$$

driven by the so-called β-function, which can be written as a perturbative expansion in α_s:

$$\beta(\alpha_s) = -\frac{\alpha_s^2}{4\pi}\left(\beta_0 + \alpha_s\,\beta_1 + \alpha_s^2\,\beta_2 + \cdots\right) \ . \tag{2.6}$$

The first two coefficients of the expansion are known to be independent of the renormalization scheme. In particular, the first coefficient is

$$\beta_0 = \frac{1}{3}\left(11 C_A - 4 T_R\, n_f\right) \ , \tag{2.7}$$

In QCD $C_A = 3$ and $T_R = 1/2$, leading to $\beta_0 = (11 - 2/3 n_f)$, n_f being the number of active flavors. For small values of α_s the dominant behavior is given by the solution of eq. (2.5) at 1-loop, *i.e.*, with $\beta = -\alpha_s^2 \beta_0$, which leads to

$$\alpha_s(\mu_R) = \frac{1}{\frac{\beta_0}{4\pi}\ln(\mu_R^2/\Lambda^2_{\rm QCD})} = \frac{\alpha_s(\mu_0)}{1 + \alpha_s(\mu_0)\,\frac{\beta_0}{4\pi}\,\ln(\mu_R^2/\mu_0^2)} \ . \tag{2.8}$$

The parameter $\Lambda^2_{\rm QCD}$ is known as the *confinement scale of QCD* and it is defined as the scale at which the strong coupling goes to infinity, *i.e.*, the position of the Landau pole. Eq. (2.8) is the running of the coupling, meaning that the strong coupling is not a constant but varies with μ_R^2. The fact that β_0 is positive (in contrast with QED) makes the coupling constantly decrease while decreasing the distance $1/\mu_R$. This behavior suggests that the QCD constituents, quarks and gluons, behave as free particles at asymptotically small distances, since the interaction among them tends to zero. This concept is known as asymptotic freedom and will be an important element in the calculation of physical observables involving hadrons in quantum field theory. It will lead to the motivation of *factorization theorems* that will allow to decouple the long distance (non perturbative) behavior from the short distance one, computable by means of perturbation theory.

2.1.3 Factorization of perturbative and non perturbative dynamics

Consider a general hadronic scattering process of the type

$$A + B \to A + B + X \ ,$$

where A and B label the two hadrons and X stands for any other possible final state particles. This process is characterized by two physically different regions. When the distance $1/\mu_R$ between the scattered particles is small enough so that a hard scale μ_R^2 is present, meaning that $\mu_R^2 >> \Lambda^2_{\rm QCD}$, it is possible to define an

infrared (IR) save quantity and use perturbation theory to calculate it, taking the strong coupling $\alpha_s(\mu_R) << 1$ as the expansion parameter. In a total hadronic cross section this would correspond to the partonic level process. On the other hand, when large distances are considered a hadronization scale of the order of the QCD confinement scale is present and perturbation theory is no longer applicable. The main non-perturbative information in the cross section is then encoded in the parton distribution functions, which are universal for different processes and encode the hadronization of the final state particles.

Factorization allows to separate these two pieces in the calculation of a hadronic cross section. Mathematically speaking, the observable can be written as a convolution of an IR safe quantity computable by means of perturbation theory and a non perturbative object that needs to be modeled and extracted from the experimental data. The partonic (IR safe) cross section $\hat{\sigma}_a$ for a parton a will depend on a hard scale Q^2 and on the fraction of longitudinal momentum, x, that it gets from its parent hadron. It can be written as

$$\hat{\sigma}_a(Q^2, x) = \sum_{k=0}^{\infty} c_{a,k}(Q^2, \mu_R^2, x)\, \alpha_s^k(\mu_R) \;, \tag{2.9}$$

where the coefficients $c_{a,k}$ are finite functions that can be computed analytically.

The way of defining the above mentioned factorization depends on the kinematic region under consideration, as we shall see later on in this section. Consider the case of Deep Inelastic Scattering (DIS) as an illustrative example, in which a lepton l^- scatters off a proton A very energetically via the exchange of a virtual photon γ^*, making the proton to shatter into its constituents and leading to a final state consisting of the remnants of the proton, X, and the lepton: $l^- A \to l^- X$. The scales involved in the process are the virtuality of the exchanged photon, Q^2, the renormalization scale μ_R^2 and the Bjorken x. The cross section for this process would be given by

$$\sigma_{lA}(Q^2, s) = \sum_{partons\, a} \int_x^1 \mathrm{d}\xi\, f_{a/A}(\xi, \mu_F^2)\, \hat{\sigma}_{lA}(\xi, \alpha_s(\mu_R), Q^2) \;, \tag{2.10}$$

where $f_{a/A}(\xi, \mu_F^2)$ are the parton distribution functions (PDF's). It gives the probability of finding the parton a inside the hadron A, carrying a fraction ξ of the longitudinal momentum of the parent hadron. This specific factorization is only valid when $\xi \to 1$ and $Q^2 >> \Lambda^2_{\mathrm{QCD}}$. As a prize to pay when making such separation, a factorization scale μ_F needs to be introduced in the calculation. Although the physical cross section should be independent of both the renormalization and factorization scales, due to the unavoidable truncation of the

perturbative series a remaining dependence on them will always be present in the calculations. It is therefore needed to always choose natural values for these scales to make the predictions to observables more trustful. There are different ways to do this. A good hint of how to choose μ_R, for example, comes from the fact that higher order corrections to eq. (2.10) are power suppressed by at least $1/\mu_R^2$, making it a very good approximation. Therefore, in the region of large momentum transfer Q a natural choice would be $\mu_R^2 = Q^2$. Another possible way to fix the scales is through the so-called *Principle of Minimum Sensitivity* (PMS) [20], based on the existence of a region of stability in the parameter space for which the observable is minimally affected by changes of the scales (see section 5.1 for an example of its practical application).

2.2 DIS, structure functions & evolution equations

The process of DIS, depicted in fig 2.1, allows for the extraction of the proton structure functions, usual objects for the understanding of the internal structure of the hadron at short distances, needed to make predictions for any physical process involving hadrons.

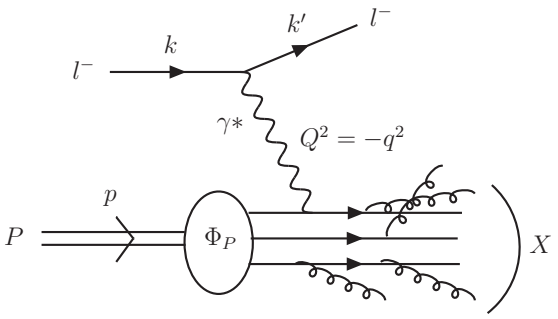

Figure 2.1: Deep Inelastic Process.

Consider the scattering process shown in fig. 2.1, with center of mass energy $s = (p + k)^2$:

$$P(p) + l^-(k) \to l^-(k') + X \ .$$

The relevant kinematic invariants are

$$\begin{aligned} Q^2 &= -q^2 > 0 \,, \\ \nu &= (Q^2 + W^2)/2 \\ W^2 &= (p+q)^2 \,, \\ x &= \frac{Q^2}{2p\cdot q} \simeq \frac{Q^2}{Q^2+W^2} \,, \\ y &= \frac{p\cdot q}{p\cdot k} \simeq \frac{Q^2}{xs} \,, \end{aligned}$$

where the approximations become exact in the limit of a massless lepton and proton, q^2 is the momentum transfer squared, x is the Bjorken x and y is also known as the inelasticity.

The cross section for this process is constructed as the contraction of a lepton tensor, calculated using QED, $L_{\mu\nu}$, and a hadronic one [21], $W_{\mu\nu}$: $\mathrm{d}^2\sigma/(\mathrm{d}x\mathrm{d}Q^2) \propto L_{\mu\nu}W^{\mu\nu}$. Considering unpolarized beams and taking into account Lorentz and time reversal invariance, the hadronic tensor can be written in terms of two dimensionless, independent structure functions, one for each polarization of the virtual photon, longitudinal (F_L) and transverse (F_T). For convenience, one can define a linear combination of the other two, as $F_2 = F_L + F_T$, in terms of which the differential cross section can be written as

$$\frac{\mathrm{d}^2\sigma}{\mathrm{d}x\mathrm{d}Q^2} = \frac{2\pi\alpha_{em}^2}{xQ^4}\left\{\left[1+(1-y)^2\right]F_2(x,Q^2) - y^2F_L(x,Q^2)\right\} \,. \tag{2.11}$$

From this equation the dependence of the structure functions on the two polarization modes of the cross section can be extracted:

$$\begin{aligned} F_2(x,Q^2) &= \frac{Q^2}{4\pi^2\alpha_{em}}\left[\sigma_T(x,Q^2) + \sigma_L(x,Q^2)\right] \,, \\ F_L(x,Q^2) &= \frac{Q^2}{4\pi^2\alpha_{em}}\sigma_L(x,Q^2) \,. \end{aligned} \tag{2.12}$$

These two observables have been analyzed in great detail, both theoretically and experimentally. They are of special interest in the study of the high energy or low Bjorken x limit, since ZEUS [22,23] and H1 [24–26] detectors cover a broad range of Q^2 and x [1], this one going down to 10^{-6}. Moreover, there are proposed experiments at the LHC site, such as the (Large Hadron Electron Collider) LHeC [31] which would be able to reach lower values of x for $Q^2 >> \Lambda^2_{\mathrm{QCD}}$, as illustrated in fig. 2.2.

[1] Recently, HERA published the combined ZEUS and H1 results for the determination of the proton structure function F_2 and F_L [27–30].

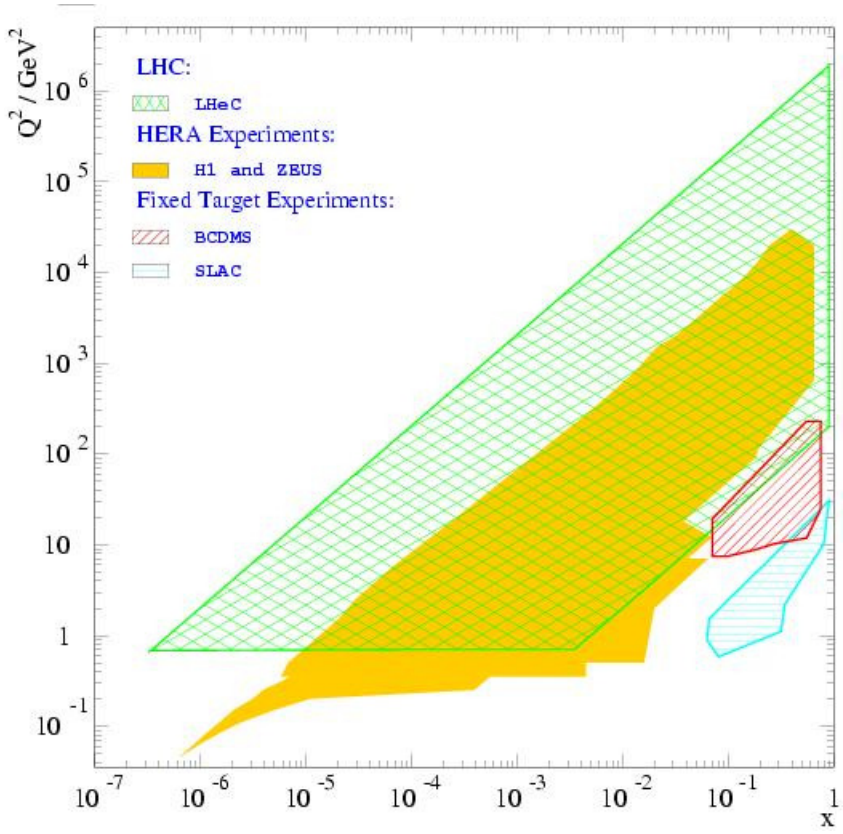

Figure 2.2: Kinematic regions covered by different experiments [31].

An interesting asymptotic region is the so-called *Bjorken limit*, given by $Q^2, \nu \to \infty$ for x fixed. In this limit a very impressive experimental work including results of many different detectors showed how the structure functions obeyed the scaling law $F_i(x, Q^2) \to F_i(x)$ or *Bjorken scaling*, valid for a quite large range of Q^2. This scaling implies that the virtual photon scatters off point-like particles in the proton. Otherwise the cross section would be forced to depend on both the virtuality of the photon and the typical length of the constituents of the scattered hadron, $1/Q_0^2$. However, when the Bjorken x is small enough the scaling is broken, as it can be seen in fig. 2.5. This fact naturally emerges as a result of a perturbative QCD calculation.

The naïve parton model explains the proton composition based on the Bjorken scaling. In this model the DIS cross section is calculated at Born level, meaning that no gluon emissions or virtual, self energy, contributions are taken into account to calculate the hadronic tensor $W_{\mu\nu}$. In this way the proton structure function's dependence on the soft physics enters through some scaled parton distribution functions (pdf's) $f_i(x)$ which give the probability of finding a quark,

antiquark or a gluon i in the proton with a fraction x of its longitudinal momentum. By means of eqs. (2.12), the structure function F_2 is given in the parton model by

$$F_2(x) \;= \sum_{flavors\ q} e_q^2\, x\,(f_q(x) + f_{\bar{q}}(x)) \;. \tag{2.13}$$

Note that this result has no contribution of perturbative QCD. In order to introduce it one needs to go to the first radiative correction, $\mathcal{O}(\alpha_s)$, that is, consider the possibility of emitting one gluon. The first diagram of fig. 2.3 leads to eq. (2.13) while the second and third ones give the first QCD correction.

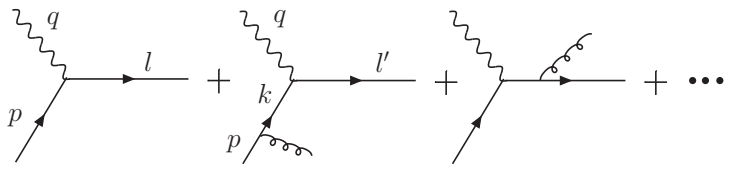

Figure 2.3: Born approximation and one gluon emission contributions to the construction of the hadronic tensor.

We will give a qualitative explanation for the breakdown of the Bjorken scaling by logarithms of Q^2. A detailed calculation of it can be extensively found in the literature, for example in [32, 33]. The idea is that the contribution of the second diagram of fig. 2.3 introduces a term in the phase space integration for the scattered parton of the form $\alpha_s\, \mathrm{d}k_T^2/k_T^2$, where k_T is the transverse momentum acquired by the parton because of the gluon emission. The upper integration bound is essentially given by the photon virtuality, therefore leading to contributions proportional to $\alpha_s \ln(Q^2/Q_0^2)$ that cannot be dismissed and break the scaling. The scale Q_0 is a lower momentum cutoff that has been introduced in the calculation *ad hoc*. When the gluon is emitted in the same direction as the quark, $Q_0^2 = 0$, a collinear singularity appears which needs to be cancelled by the soft contribution coming from the PDF's. Making use of eq. (2.10), it can be shown that the corrections to the naïve parton model cross section

$$\sigma_{\mathrm{DIS}}^{(0)} = \sum_{partons\ j} e_j^2 \int_0^1 \mathrm{d}x\; f_j(x)\hat{\sigma}^{(0)}(x) \;, \tag{2.14}$$

where the hat stands for the partonic cross section, are proportional to

$$\sum_{partons\ j} e_j^2\, x \int_{Q_0^2}^{Q^2} \frac{\mathrm{d}k_T^2}{k_T^2} \int_x^1 \frac{\mathrm{d}\zeta}{\zeta}\; P_{qq}(z)\, f_j\left(\frac{x}{\zeta}\right) \;,$$

where x is the momentum fraction of the parton before emitting the gluon and $z = x\,\zeta$ after it has been emitted. $P_{qq}(\zeta)$ is known as the Altarelli-Parisi splitting function [34] for the quark to quark transition, a known function that appears in the perturbative calculation of the amplitude of the process. This translates into the following modification for the parton density:

$$f_j(x) \to f_j(x) + \ln\left(\frac{Q^2}{Q_0^2}\right)\frac{\alpha_s}{2\pi}\int_x^1 \frac{\mathrm{d}\zeta}{\zeta}\, P_{qq}(z)\, f_j\left(\frac{x}{\zeta}\right) \ . \tag{2.15}$$

As we saw in section 2.1.1, another way to regularize this collinear divergence is through dimensional regularization, which introduces a renormalization scale μ_R. If we had applied it, we would need to do the replacement $Q^2 \to \mu_R^2$ in eq. (2.15). By splitting the logarithm as

$$\ln\left(\frac{\mu_R^2}{Q_0^2}\right) = \ln\left(\frac{\mu_R^2}{Q^2}\right) + \ln\left(\frac{Q^2}{Q_0^2}\right)$$

and rearranging terms, eq. (2.15) can be rewritten as

$$f(x,Q^2) = f(x,\mu_R^2) + \ln\left(\frac{Q^2}{\mu_R^2}\right)\frac{\alpha_s}{2\pi}\int_x^1 \frac{\mathrm{d}\zeta}{\zeta}\, P_{qq}(z)\, f\left(\frac{x}{\zeta}\right) \ , \tag{2.16}$$

where we have dropped the parton index j. Using the fact that $F_2(x,Q^2)$ is a physical observable that cannot depend on any unphysical scale, we can use the differential renormalization group equation as given in eq. (2.5) on eq. (2.16) and obtain

$$\mu_R^2\,\frac{\mathrm{d}f(x,\mu_R^2)}{\mathrm{d}\ln(\mu_R^2)} = \frac{\alpha_s}{2\pi}\int_x^1 \frac{\mathrm{d}\zeta}{\zeta}\, P_{qq}(z)\, f\left(\frac{x}{\zeta},\mu_R^2\right) \ . \tag{2.17}$$

This equation, emerging as a direct result of renormalization group invariance, is known as the Dokshitzer-Gribov-Lipatov-Altarelli-Parisi (DGLAP) evolution equation [34–36], which effectively resums logarithms of Q^2, driving the partonic evolution in momentum scale. This can be easily seen if we rewrite eq. (2.17) in terms of the variable $L = \ln(Q^2/\mu_R^2)$ as

$$\frac{\mathrm{d}f(x,L)}{\mathrm{d}L} = \frac{\alpha_s}{2\pi}\int_x^1 \frac{\mathrm{d}\zeta}{\zeta}\, P_{qq}(z)\, f\left(\frac{x}{\zeta},L\right) \ . \tag{2.18}$$

We can now take a Taylor expansion of $f(x,L)$ around $L = 0$:

$$f(x,L) = f(x,0) + L\frac{\mathrm{d}f(x,0)}{\mathrm{d}L} + \frac{1}{2!}L^2\frac{\mathrm{d}^2 f(x,0)}{\mathrm{d}L^2} + \cdots \tag{2.19}$$

and use the iterative equation 2.18 to find the second and higher order derivatives.

It can be seen that the n-th derivative is given by

$$f^{(n)}(x,t) = \frac{\alpha_s}{2\pi}\int_x^1 \frac{\mathrm{d}\zeta_1}{\zeta_1} P_{qq}(\zeta_1)\frac{\alpha_s}{2\pi}\int_{x_1}^1 \frac{\mathrm{d}\zeta_2}{\zeta_2} P_{qq}(\zeta_2)\cdots\frac{\alpha_s}{2\pi}\int_{x_{n-1}}^1 \frac{\mathrm{d}\zeta_n}{\zeta_n} P_{qq}(\zeta_n) f\left(x_n,t\right) \ , \tag{2.20}$$

where we have introduced the notation $x_j \equiv \frac{x}{\zeta_1\zeta_1\cdots\zeta_j}$. This makes the $n-th$ term of the Taylor expansion to be proportional to

$$\frac{1}{n!}\left(\alpha_s L\right)^n = \frac{1}{n!}\left(\alpha_s \ln\frac{Q^2}{\mu_R^2}\right)^n \ . \tag{2.21}$$

In order to construct the equation, strong ordering in transverse momentum has to be imposed between consecutive soft gluon emissions. In the collinear regime one starts from an initial hard scale Q^2 and, due to this ordering, it goes down to small scales, always with big values of the Bjorken x.

Note that the calculation we have indicated here is for the specific case of quark-photon fusion to give a quark in the final state, as shown in fig. 2.3. Similar calculations would lead to the contributions of a gluon coming from the proton splitting into a $q\bar{q}$ pair and any other possible $\mathcal{O}(\alpha_s)$ contribution, the difference coming through the specific splitting functions, all of them calculated perturbatively. We refer the reader to the literature [32,33,37,38] for more the details of the computation.

Kinematic regions & other resummations

The collinear resummation is not unique and its range of applicability lies within certain kinematic boundaries. In principle, any physical observable can be written in perturbative QCD (p-QCD) as a series of the form

$$\sum_{n=0}^{\infty} C_n\,\alpha_s^n(L^n + a_{n-1}L^{n-1} + ... + a_0) \ , \tag{2.22}$$

L being a function of energy and momentum that depends on the process and kinematic region under analysis. In the DIS process the dominant terms of the perturbative expansion will depend on either the photon virtuality or on the Bjorken x. There are three kinematic cases of interest, shown in fig. 2.4:

1. When the photon virtuality is much bigger than the renormalization scale and almost all the longitudinal momentum of the proton is acquired by the scattered parton, that is, $Q^2 >> \mu^2$ and $x \to 1$, the perturbative series is dominated by logarithms of momentum of the form $L = \ln(Q^2/\mu^2) >> \ln(1/x)$. This corresponds to the already described DGLAP region, which

resums the collinear singularities explained above by imposing strong ordering in the transverse momentum of subsequent soft gluon emissions in the parton evolution: $Q^2 >> k^2_{nT} >> k^2_{(n-1)T} >> ... >> k^2_{1T}$.

2. On the other hand, when $Q^2 \simeq \mu^2$ and $x \to 0$ or $s >> Q^2 >> \Lambda^2_{\rm QCD}$, the leading logarithms are of energy and can be expressed in terms of the Bjorken x as $L = \ln(1/x) >> \ln(Q^2/\mu^2)$, this limit corresponding to the BFKL region.

3. Finally, we have regions where both logarithms are important, having the limits $Q^2 >> \mu^2$ and $x \to 0$. In this case the leading coefficients would be given by: $L = \ln(Q^2/\mu^2) \cdot \ln(1/x)$. This is known as the double asymptotic limit or double leading logarithmic approximation, DLLA, which was first examined in [**?**] and is accounted for in the Catani-Ciafaloni-Fiorani-Marchesini (CCFM) equation [39–41]. In this case one has to impose strong ordering in rapidity and in transverse momentum between consecutive gluon emissions, then finding a resummation of terms of the form $[\alpha_s \ln(1/x) \ln(Q^2/\mu^2)]^n$.

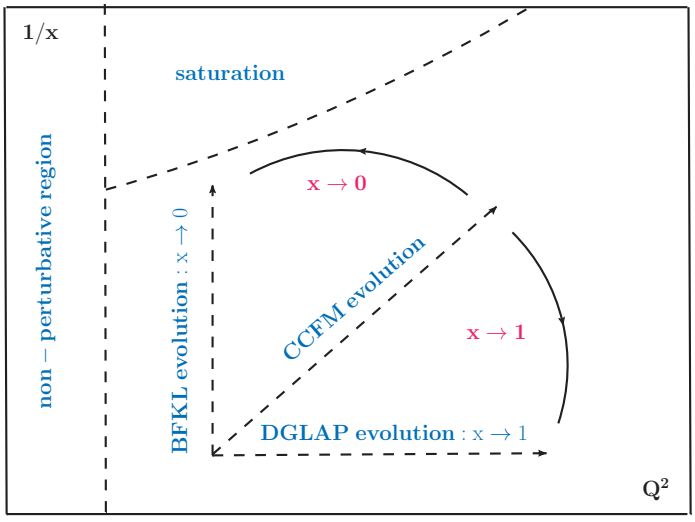

Figure 2.4: Different kinematic regions of p-QCD, depending on the hard scale involved Q^2 and Bjorken x variable.

Small x region: Regge limit

In this region a very similar argument to the one given for DGLAP holds in order to find the resummation of the large logarithms of energy, which are the leading ones in this kinematic regime.

The Regge limit corresponds to having $s >> Q^2 >> \Lambda^2_{\rm QCD}$. This is governed by Multi-Regge kinematics, which impose strong ordering in the rapidity between consecutive gluon emissions, while their transverse momenta are of the same order. In this case, the BFKL evolution equation at leading order resums terms of the form $[\alpha_s \ln(s/s_0)]^n$, with $s/s_0 = 1/x$. This type of resummation is needed to calculate the amplitude for the production of n soft gluons when $s >> |t|$. Imposing strong ordering in rapidity, which is equivalent to having a regge limit in each sub-channel, the phase space will introduce the following contribution:

$$\sum_{n=0}^{\infty}(\chi\alpha_s)^n \int_0^Y \mathrm{d}y_1 \int_0^{y_1} \mathrm{d}y_2 \cdots \int_0^{y_{n-1}} \mathrm{d}y_n = \sum_{n=0}^{\infty} \frac{(\chi\alpha_s)^n Y^n}{n!} = \mathrm{e}^{\alpha_s \chi \mathrm{Y}} \,, \qquad (2.23)$$

with $Y = \ln(1/x) = \ln(s/s_0)$ being the rapidity, χ a function coming from the solution of the BFKL equation as we will see later and s_0 a typical energy scale. A detailed derivation of this resummation and the BFKL equation will be given in chapter 3.

The type of factorization that holds in this limit is the so-called k_T-factorization [42], as we shall describe in section 3.2.1.

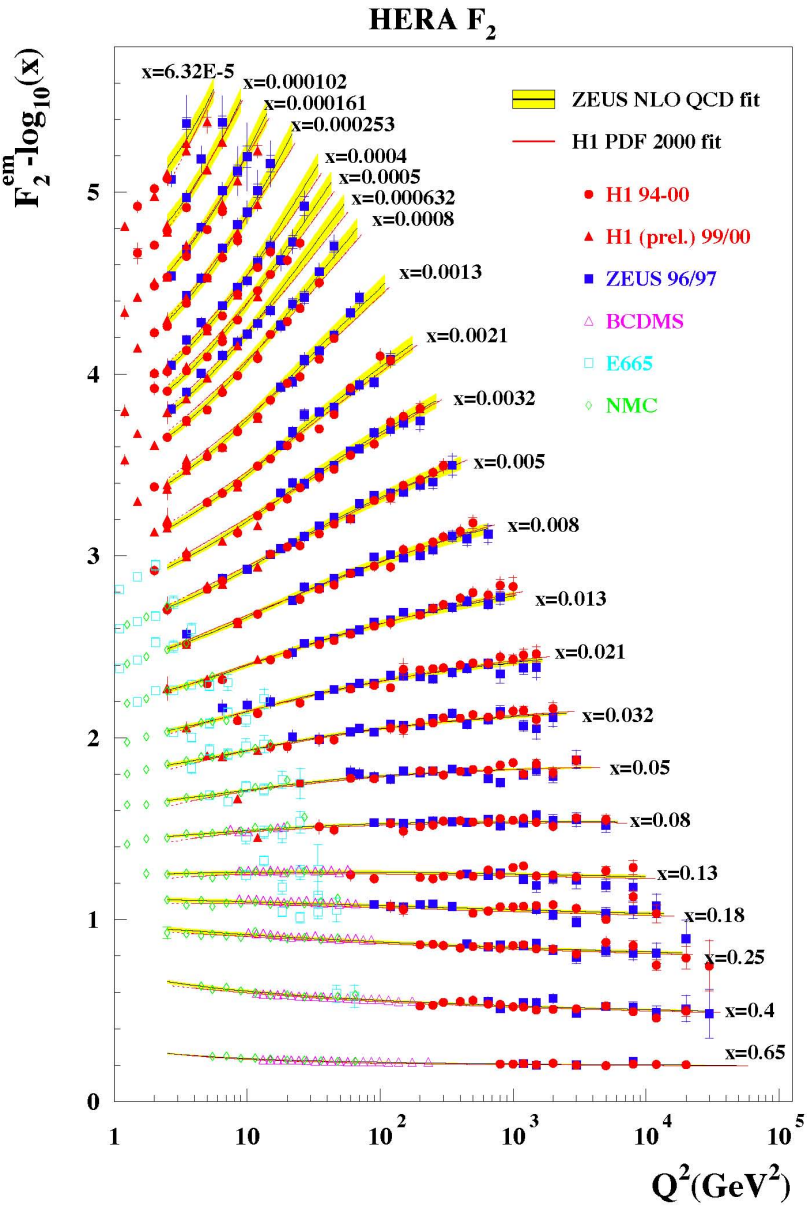

Figure 2.5: Experimental evidence of the breakdown of Bjorken scaling for small values of the Bjorken x.

Chapter 3

BFKL dynamics

3.1 BFKL equation & the pomeron

The aim of this chapter is to introduce the theory of BFKL resummation following the historical line presented in chapter 1.

3.1.1 Regge Theory & the soft pomeron

As we stated in the introductory chapter, back in the sixties, before the arrival of QCD, a consistent framework for the description of high energy scattering was developed, based on the work of Pomeranchuk, Gribov, Froissart, Martin and Regge, among others. Sustained on basic properties of the elastic scattering amplitude of quantum mechanics, Regge theory was able to make reliable qualitative predictions for the theory of strong interactions. Using the postulates of the $\mathcal{S}$-matrix as a starting point essential tools as the optical theorem were derived and are still used nowadays. A remarkable landmark was the contribution of Tullio Regge with the introduction of the complex angular momenta [43] (1959-1960). This lead to the definition of the Regge poles and Regge trajectories, basic blocks of all the theory presented in this section.

We will briefly discuss in this section the main aspects of Regge theory that led to the idea of the soft pomeron and the construction of the hard or QCD one and the BFKL equation.

S-matrix postulates and consequences

The matrix of elastic scattering amplitudes is a linear operator which goes from the initial ($t = -\infty$) state $|\, i \,\rangle$ of a scattering process to its final ($t = \infty$) state $|\, f \,\rangle$. It can therefore be defined as $\mathcal{S} = \langle\, i \,|\, f \,\rangle = U(-\infty, \infty)$, U being the time evolution operator. We can express it in terms of the transition matrix T as

$\mathcal{S} = \mathbb{1} + i\,T$. By means of this relation a matrix element would be given by $\mathcal{S}_{\rm if} = \langle\, f \,|\, \mathcal{S} \,|\, i \rangle = \delta_{\rm if} + i\,T_{\rm if}$, with

$$T_{\rm if} = (2\pi)^4 \delta^4(p_f - p_i)\, A(i \to f) \tag{3.1}$$

and $A(i \to f)$ being the relativistic scattering amplitude. p_i and p_f are the momentum eigenstates of the initial and final states and they obey the normalization relation $\langle\, p_i \,|\, p_f \,\rangle = (2\pi)^3\, 2E\, \delta^3(\bar{p}_i - \bar{p}_f)$.

The linearity of this operator is needed in order to accomplish the superposition principle of Quantum Mechanics, relativistic invariance and the very well known postulates of analyticity, unitarity and crossing.

Analyticity allows us to express the scattering amplitude as a function of pure Lorentz invariant quantities, the Mandelstam variables: $A = f(s,t,u)$. Due to the relation $s+t+u=0$ (given in the relativistic limit, where the quark masses can be neglected), we can express the amplitude just in terms of two of the invariants. The $\mathcal{S}$-matrix is analytic for any set of its arguments with the exception of some unavoidable singularities that will come from unitarity.

Unitarity simply states the conservation of probability: *all that comes in goes out*. Mathematically this is given by $\mathcal{S}\mathcal{S}^\dagger = \mathcal{S}^\dagger\mathcal{S} = 1$. We can write this in terms of the transition matrix: $i\,(T^\dagger - T) = T^\dagger T$. From this expression and using the closure relation we find

$$\begin{aligned} i\,\langle\, f \,|\, (T^\dagger - T) \,|\, i \,\rangle &= \sum_n \int \prod_{j=1}^{n} \frac{{\rm d}^3 q_j}{(2\pi)^3 2E_j} \langle\, f \,|\, T^\dagger \,|\, n \,\rangle\, \langle\, n \,|\, T\, i \,\rangle \\ \Rightarrow\ 2{\rm Im}(T) &= \sum_n \int \prod_{j=1}^{n} \frac{{\rm d}^3 q_j}{(2\pi)^3 2E_j} T^*_{\rm fn}\, T_{\rm in}\ . \end{aligned} \tag{3.2}$$

This set of equations is a unitary relation, very useful for calculating total cross sections using perturbation theory. The real part of the scattering amplitude can be extracted out from the imaginary part using the so-called dispersion relations, which come as a consequence of analyticity. The reader might be familiar with this concept in optics, where the dispersion relation allows one to go from the refractive (real) part of the complex refractive index to the absorptive (imaginary) one through an integral expression (see [44] for detailed information about this).

The so-called **Cutkosky rules** are found by imposing unitarity to eq. (3.1):

$$2\,\mathcal{I}m A_{ab} = (2\pi)^4 \delta^4 \left(\sum_a p_a - \sum_b p_b \right) \sum_c A_{ac} A_{cb}\ . \tag{3.3}$$

They allow for the determination of the imaginary part of an amplitude by considering the scattering amplitudes of the incoming and outgoing states into all possible intermediate states.

A special case of these Cutkosky rules is the **optical theorem**. It states that the total cross section for a scattering process $1+2 \to X$ is given by the imaginary part of the amplitude for the elastic scattering $1+2 \to 1+2$ process in the forward direction ($t=0$), as depicted in figure 3.1. Mathematically,

$$F\,\sigma_{\rm tot} = 2\,\mathcal{I}m\,A(s,0) = (2\pi)^4\delta^{(4)}(p_{in}-p_{out})\sum_n |A_{in\to n}|^2\ , \tag{3.4}$$

F being the flux factor.

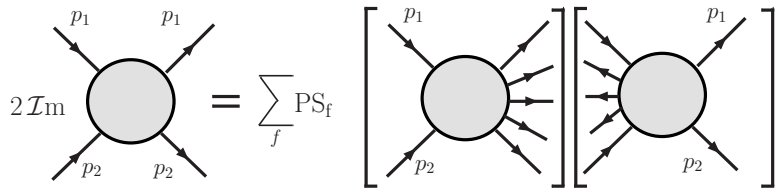

Figure 3.1: Optical theorem.

The symmetry of **crossing** comes as a consequence of analyticity. It allows us to relate the amplitude of the scattering process under consideration in different channels. For example, the s-channel process $a+b \to c+d$, where $s>0$ and $t,u<0$ would be equivalent to the t-channel one: $a+\bar{c} \to \bar{b}+d$, with $t>0$ and $s,u<0$. The relation between the s and u channels would be given by a simple change of signs: $s \leftrightarrow -u$.

The property of analyticity together with unitarity allows for the understanding of the singularity structure of the scattering amplitude $\mathcal{A}(s,t)$ in the s plane, with its poles, cuts and branch points. As a consequence of its particular structure we can apply the Schwarz reflection principle, with which the property $\mathcal{A}(s,t)^* = \mathcal{A}(s^*,t)$ holds -given that the amplitude $\mathcal{A}$ is real in some region of the real s-axis-, and use it to write the following property for the imaginary part of the amplitude:

$$\mathcal{I}m\mathcal{A}(s,t) = \frac{1}{2i}\lim_{\epsilon\to 0}\left[\mathcal{A}(s+i\epsilon,t)-\mathcal{A}(s-i\epsilon,t)\right] \equiv \Delta_s\mathcal{A}(s,t)\ , \tag{3.5}$$

from which the following useful relation holds: $\ln(-s) = \ln(s) - i\pi$.

The dispersion relations [44] come directly from the Cauchy integral formula,

from which the amplitude can be written as

$$\mathcal{A}(s,t) = \frac{1}{2\pi i}\oint_C \mathrm{d}s' \, \frac{\mathcal{A}(s',t)}{s'-s} \, , \tag{3.6}$$

where the contour C does not contain any singularities of $\mathcal{A}$. A particularly interesting application for our purposes is the reconstruction of an amplitude with its imaginary part being $C(\ln(s/s_0))^n$. By means of the dispersion relations its real part would be

$$-\frac{C}{\pi(n+1)}\left(\ln\left(\frac{s}{s_0}\right)\right)^{n+1} \, ,$$

coinciding with the total amplitude at leading order in $\ln s$.

Let us now study the effect of the Regge limit on the scattering amplitudes in order to arrive to the Regge prediction about the strong interactions [43, 45].

Regge poles and trajectories in relativistic quantum mechanics

Before going to relativistic quantum mechanics let us introduce the concepts of Regge poles and trajectories in the non-relativistic case. Consider a spherically symmetric potential $V(r)$. A nice property of central potentials is that its scattering amplitude does not depend on the azimuthal angle, we can integrate over it obtaining the following expression for its associated elastic differential cross section: $\mathrm{d}\,\sigma_{\text{elast}}/\mathrm{d}\cos\theta = 2\pi\,|\mathcal{A}(s,\theta)|^2$, where θ is the scattering angle in the center of mass frame and has a direct relation to the Mandelstam invariants, given by $\cos(\theta) = 1 + 2t/s$. The amplitude $\mathcal{A}$ can be generally expanded in a partial wave series

$$\mathcal{A}(s,t)_{t\ channel} = \sum_{l=0}^{\infty}(2l+1)a_l(s)P_l\left(1+\frac{2t}{s}\right) \, , \tag{3.7}$$

where l is the angular momentum and P_l are the Lagrange Polynomials. Making use of the property of crossing, the s-channel amplitude is then

$$\mathcal{A}(s,t)_{s\ channel} = \sum_{l=0}^{\infty}(2l+1)a_l(t)P_l\left(1+\frac{2s}{t}\right) \, . \tag{3.8}$$

The partial wave amplitudes are of the form

$$a_l(s) = \frac{\mathrm{e}^{2\mathrm{i}\delta_\mathrm{l}(\mathrm{s})}-1}{2is} \, , \tag{3.9}$$

with δ_l being the so-called phase shift which accounts for the difference between the wave functions with and without potential. The exponential is the element of the scattering matrix $\mathcal{S}$ in a state of angular momentum l. The bound states happen to be poles of the partial wave amplitude and therefore also of the $\mathcal{S}$-matrix, for a given $l \in \mathbb{Z}$. If we do an analytical continuation of the angular momentum to the complex plane [43], the partial wave amplitude $a_l(t)$ transforms into an interpolating function $a(l,t)$. The poles are no-longer unique but they are functions of k: $l = \alpha(t) \in \mathbb{C}$. This analytic continuation transforms eq. 3.8 into

$$\mathcal{A}(s,t) = \frac{1}{2i} \oint_C \mathrm{d}l(2l+1)\, \frac{a(l,t)}{\sin(\pi l)}\, P\left(l, 1+\frac{2s}{t}\right) , \tag{3.10}$$

where the contour C surrounds the positive real t-axis.

The entire set of families or group of bound states which make the amplitude to be singular at a certain momentum transfer $t = -k^2$ is called a Regge trajectory (see [32] for a detailed explanation).

We are interested in what happens in the asymptotic, Regge limit, $s >> |t|$. The Legendre polynomial P_l is in that limit dominated by

$$P_l(1+2s/t) \to \frac{\Gamma(2l+1)}{\Gamma^2(l+1)} \left(\frac{s}{2t}\right)^l . \tag{3.11}$$

Unfortunately, a price must be paid to extend the idea of Regge poles and trajectories to the high energy limit or relativistic quantum mechanics. The fact that there is nothing such as the Schrödinger equation in the $\mathcal{S}$-matrix theory makes it impossible to determine the scattering amplitudes analytically. This makes the prevalence of Regge poles over brunch cuts in the field of strong interactions to be a conjecture which cannot be mathematically proven. For what follows this conjecture will be assumed to hold.

Suppose that the scattering amplitude $\mathcal{A}(l,t)$ presents simple Regge poles at $l = \alpha(t)$. Then it can be shown that each pole would contribute asymptotically as

$$\mathcal{A}(s \to \infty, t) \sim \frac{\Sigma + \mathrm{e}^{-\mathrm{i}\pi\alpha(\mathrm{t})}}{2} \beta(t)\, s^{\alpha(t)} , \tag{3.12}$$

where only the leading Regge pole, *i.e.*, the pole with the largest real part, contributes. The parameter Σ is a signature that takes the values ± 1 and comes from some contributions to the partial wave amplitudes that alternate sign via a coefficient $(-1)^l$. The function $\beta(t)$ does not depend on s. Therefore, all the s dependence enters in the term $s^{\alpha(t)}$, where $\alpha(t)$ is the so-called Regge trajectory.

This object can be approximated by a linear function[1]: $\alpha(t) \simeq \alpha(0) + \alpha'(0)t$, where α_0 is the Regge intercept and α' is the slope.

The amplitude 3.12 can be physically interpreted as the t-channel exchange of an object with its angular momentum being $\alpha(t)$. It cannot be a particle in the high energy limit because the trajectory is a continuous function of t instead of an integer or half integer and that could imply a violation of unitarity. Whatever is exchanged is known as a **reggeon**, which can be seen as the superposition of the amplitudes of all possible particles exchanged in the t-channel or, in Regge terms, the t-channel exchange of one or more Regge trajectories. The propagator of these reggeons is of the form

$$D_{\mu\nu}(\mathbf{k}) \propto \frac{1}{\mathbf{k}^2}\left(\frac{s}{s_0}\right)^{\alpha(t)} , \tag{3.13}$$

with[2] $t = -\mathbf{k}^2$, and therefore any object that has such a propagator is called a reggeized particle.

If the scattering process under consideration is elastic (t=0), the total cross section can be deduced from eq. (3.12) via the optical theorem, giving

$$\sigma_{\text{tot}} \sim s^{\alpha(0)-1} . \tag{3.14}$$

We can define $\lambda_p \equiv \alpha(0) - 1$ as the **pomeron intercept**[3]. Most of the Regge trajectories have $\alpha(0) < 1$ and therefore make the cross section decrease with increasing energy. However, it is also possible to have a positive pomeron intercept, which corresponds to the exchange of the vacuum quantum numbers and would lead to a growth of the total hadronic cross section with the center of mass energy. The importance of this result is that at some point it was verified experimentally.

A phenomenological evidence and the Soft Pomeron

Figure 3.2 shows how the total hadronic cross section grows with energy.

Although we cannot determine whether Regge theory in high energy particle physics is applicable or not, its prediction about the growth of the cross section based on the exchange of a single Regge pole was surprisingly accurate, for a

[1] Chew and Frautschi verified this linear behavior by plotting the spins of different mesons versus their mass squared $t = M^2$ and realizing that they where all lying on the same straight line [46, 47].

[2] We have introduced the bold notation so that the transverse momentum squared is given by $k_\perp^2 = -\mathbf{k}^2$. Such notation will be used throughout the rest of the manuscript.

[3] Name given for Pomeranchuk [48].

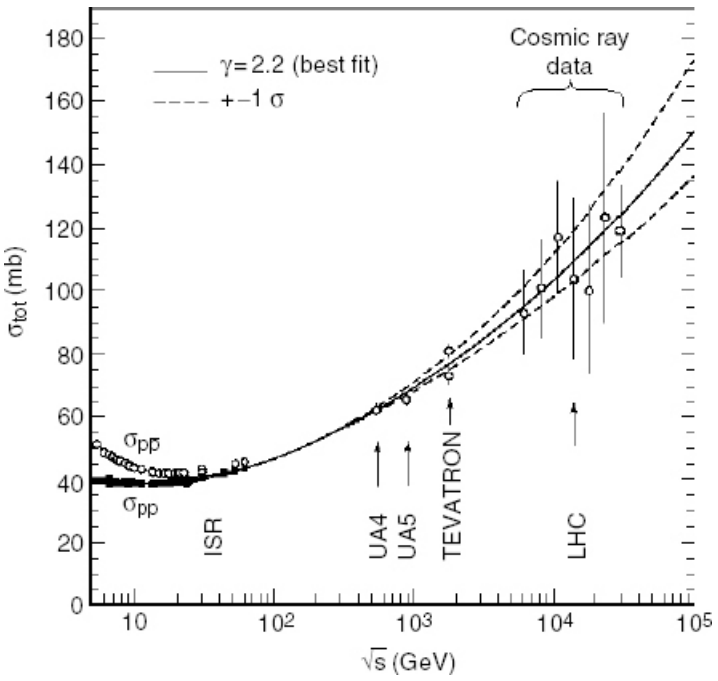

Figure 3.2: Experimental growth of the total hadronic cross sections pp and $p\bar{p}$ with energy for all available data. The lines are fits based on Regge theory.

pomeron of intercept

$$\lambda_P \simeq 0.08 \, . \tag{3.15}$$

A fit to the data is shown in fig. 3.2, being the first one done by Donnachie and Landshoff in 1992 [4].

Foldy and Peierls showed that if a cross section grows with energy then the process must be dominated by the exchange of the quantum numbers of the vacuum [49], that is, a process having zero isospin and being even under charge conjugation. This means that, in terms of Regge theory, if we assume that a single Regge pole has been exchanged in the t-channel, then the reggeon must carry vacuum quantum numbers, being this trajectory called the soft or non-perturbative pomeron.

Time after all this approach to the strong interactions was developed, QCD appeared becoming the best way to explain the high energy limit in particle physics we have so far. A clear step at this point was to check if the predictions of Regge theory could be explained within QCD. With this idea in mind the BFKL formalism was developed. Our task for the next section will be to reproduce the main points of the construction of this equation, referring the reader to [13, 32] for a detailed and careful mathematical derivation.

3.1.2 QCD & the hard pomeron

In order to derive the BFKL equation, we will consider quark-quark scattering [4] in the leading logarithmic approximation, LLA, basically following the procedure given in [13].

As we saw in the previous section, the way to find the pomeron in QCD is to consider all t-channel contributions leading in $\alpha_s \ln(s/s_0)$. We will perform the calculations for a general color octet representation for convenience and then project into the color singlet, since the pomeron, if there is a QCD-like one, must carry the quantum numbers of the vacuum. This procedure will lead to the reggeization of the gluon and the construction of the so-called gluon ladder, main ingredients of the BFKL equation. Its asymptotic solution at leading logarithmic accuracy will give us the hard pomeron intercept.

Kinematics of the high energy limit

We will be working in the high energy limit all the time, given by

$$s >> |t|,\ u \simeq -s\ .$$

As we mentioned already, with this choice only terms leading in $[\alpha_s \ln(1/x)]$ will be retained. This can be achieved by introducing the constraint of strong ordering in rapidity between consecutive gluon emissions of the gluon chain driving the partonic evolution, leading to the kinematic region of multi-Regge kinematics (MRK).

Concerning the mathematical treatment of the momenta of the particles involved, the Sudakov parametrization will be used. It allows us to write any four-momentum as

$$q^\mu = \alpha p_1^\mu + \beta p_2^\mu + q_\perp^\mu\ , \tag{3.16}$$

where $q_\perp^\mu = (0, \mathbf{q}, 0)$ lives in the plane transverse to the beam axis and p_1 and p_2 are two light-like momenta, *i.e.*, they lie on the plane given by the longitudinal axis and the energy. They have the same energy and opposite directions and in the $s \to \infty$ limit coincide with the momenta of the incoming protons p_A and p_B:

$$p_1 \ = \ p_A - \frac{m_P^2}{s} p_B, \qquad p_2 \ = \ p_B - \frac{m_P^2}{s} p_A, \tag{3.17}$$

with $s = (p_A + p_B)^2$ being the squared center of mass energy of the hadronic

[4] In order to compute the hadronic cross section k_T-factorization will be used, introducing two proton impact factors to account for the information of the two parent hadrons.

process. In the limit $s \to \infty$ we have

$$s \simeq 2p_1p_2 \qquad \text{and} \qquad |t| \simeq q^2 = \alpha\beta s - \mathbf{q}^2 \ . \tag{3.18}$$

The t-channel gluons will be governed by the metric tensor $g_{\mu\nu} = \frac{2}{s} p_{1\mu} p_{2\mu}$.

Derivation of the BFKL equation

We have to take into account all possible virtual and real corrections in the t-channel which are leading in $\alpha_s \ln(s/s_0)$. The virtual ones will be responsible for the reggeization of the gluon while the real emissions will introduce the so-called Lipatov effective vertex, a very useful tool that will make our life much easier in the construction of the gluon ladder.

1. Virtual corrections

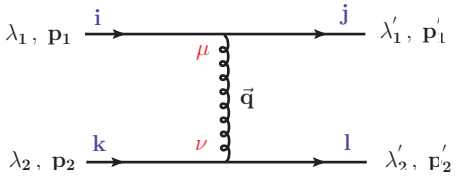

Figure 3.3: Two-quark scattering at LLA. First diagram for the color octet.

Let us begin by calculating the tree level amplitude for the $qq \to qq$ process (fig. 3.3). The upper and lower vertices are, respectively:

$$\begin{aligned} -ig_s\bar{u}(p_1+q)\gamma_\mu u(p_1) &\simeq -ig_s\bar{u}(p_1)\gamma_\mu u(p_1) = -2ig_s p_1^\mu \qquad \text{and} \\ -ig_s\bar{u}(p_2-q)\gamma_\nu u(p_2) &\simeq -ig_s\bar{u}(p_2)\gamma_\nu u(p_2) = -2ig_s p_2^\nu \ , \end{aligned} \tag{3.19}$$

where the *eikonal approximation*, $p_1, p_2 >> q$, has been used. This approximation is valid whenever the exchanged gauge particle is soft, that is, when all its components are small compared to the momentum of the incoming quark. Using eq. (3.19) and adding the color factor the amplitude can be easily calculated, giving

$$\mathcal{A}_8^{(0)}(s,t) = 8\pi\,\alpha_s\, t^\alpha_{ij} t^\alpha_{kl}\, \frac{s}{t} \ . \tag{3.20}$$

The first correction to this diagram corresponds to the emission of an additional gluon. Luckily, we will not need to consider all diagrams, since we are only interested in the leading $\alpha_s \ln(s/s_0)$ terms. Specifically, we will neglect the diagrams containing self energy and vertex corrections. One can check that the only di-

agrams contributing to our process at this level are the ones given in fig. 3.4.

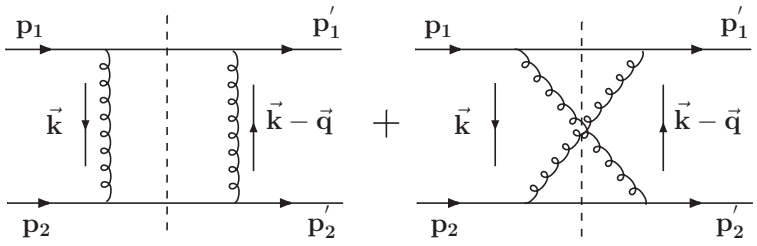

Figure 3.4: Two-quark scattering at next to leading order. The two virtual contributions leading in $\alpha_s \ln(s/s_0)$.

By means of the Cutkosky rules and the optical theorem introduced earlier in this chapter in eqs. (3.3,3.4), to calculate the amplitude for the diagrams given in fig. 3.4 we only need to obtain the imaginary part and then apply the dispersion relation $\ln(-s) = \ln s - i\pi$ to extract the total amplitude. This relation allows us to write a generic amplitude $\mathcal{A}$ in terms of its real and imaginary parts as

$$\mathcal{A} = \mathcal{R}e\mathcal{A} + i\,\mathcal{I}m\mathcal{A} = \left(-\frac{1}{\pi}\ln\frac{s}{|t|} + i\right)\mathcal{I}m\mathcal{A}\,. \tag{3.21}$$

This procedure will be used throughout all this chapter. Let us define the amplitude of the process as $\mathcal{A}^{(1)}(s,t)$. Its imaginary part is given by

$$\mathcal{I}m\mathcal{A}_8^{(1)}(s,t) = \frac{1}{2}\int \mathrm{dPS}^{(2)}\mathcal{A}_8^{(0)}(s,k^2)\mathcal{A}_8^{(0)\dagger}(s,(k-q)^2)\,, \tag{3.22}$$

with $\mathcal{A}^{(0)}$ being the tree level amplitude for the cut processes. The quark lines are on shell at the cut points (see fig. 3.4). The two-body phase is

$$\int \mathrm{dPS}^{(2)} = \int \frac{\mathrm{d}^4k}{(2\pi)^2}\,\delta((p_1-k)^2)\,\delta((p_2+k)^2) = \frac{1}{8\pi^2 s}\int \mathrm{d}^2\mathbf{k}\,, \tag{3.23}$$

where we have used the relation $\mathrm{d}^4k = \frac{s}{2}\,\mathrm{d}\alpha\,\mathrm{d}\beta\,\mathrm{d}^2\mathbf{k}$.

By inserting the value of the two tree level amplitudes, which have an expression similar to eq. (3.20), the imaginary part of $\mathcal{A}^{(1)}$ is given by

$$\mathcal{I}m\mathcal{A}_8^{(1)}(s,t) = 4s\,\alpha_s^2\,(t^\alpha t^\beta)_{ij}\,(t^\alpha t^\beta)_{kl}\int \frac{\mathrm{d}^2\mathbf{k}}{\mathbf{k}^2(\mathbf{k}-\mathbf{q})^2}\,. \tag{3.24}$$

By means of the dispersion relations, the left hand side diagram of fig. 3.4 reads

$$\begin{aligned}\mathcal{A}_8^{(1)}(s,t) &= -4\frac{\alpha_s^2}{\pi}(t^\alpha t^\beta)_{ij}(t^\alpha t^\beta)_{kl}\ln\left(\frac{s}{t}\right)\, s\int\frac{\mathrm{d}^2\mathbf{k}}{\mathbf{k}^2(\mathbf{k}-\mathbf{q})^2} \\ &= -\frac{16\pi\alpha_s}{N_c}(t^\alpha t^\beta)_{ij}(t^\alpha t^\beta)_{kl}\,\frac{s}{t}\ln\left(\frac{s}{t}\right)\,\epsilon(t)\,, \end{aligned} \tag{3.25}$$

with

$$\epsilon(t=-\mathbf{q}^2) \equiv \frac{\bar{\alpha}_s}{4\pi}\int\frac{-\mathbf{q}^2\mathrm{d}^2\mathbf{k}}{\mathbf{k}^2(\mathbf{k}-\mathbf{q})^2}\,, \tag{3.26}$$

with $\bar{\alpha}_s \equiv \alpha_s N_c/\pi$. Note that this function is infrared divergent, the reason for it being that the external quarks have been treated as on mass-shell particles. However, one has to take into account that these quarks are actually bound inside the hadrons and therefore they are off shell particles with off-shellness of the order of their transverse momentum. The way to account for this is by inserting an infrared cutoff in the integrals for the expression of the hadronic observable. We will see how the expression of the integral equation for the hard pomeron is in fact infrared safe, being the divergence introduced by eq. (3.26) regularized and therefore not present in the final result.

The amplitude for the crossed channel, right hand diagram given in fig.3.4, is

$$\mathcal{A}_{8,cross}^{(1)}(s,t) = -\frac{16\pi\alpha_s}{N_c}(t^\alpha t^\beta)_{ij}(t^\alpha t^\beta)_{kl}\,\frac{u}{t}\ln\left(\frac{u}{t}\right)\,\epsilon(t)\,. \tag{3.27}$$

Using the approximation $s \simeq -u$ and summing both contributions, one finally obtains the one loop expression for the amplitude, that can be written in terms of the tree level one:

$$\mathcal{A}_{8,tot}^{(1)}(s,t) = 8\pi\alpha_s\, t_{ij}^\alpha\, t_{kl}^\alpha\frac{s}{t}\ln\left(\frac{s}{|t|}\right)\epsilon(t) = \mathcal{A}_8^{(0)}\ln\left(\frac{s}{|t|}\right)\epsilon(t)+\cdots\,. \tag{3.28}$$

The dots contain an extra term that will eventually be canceled with the real contributions[5]. The derivation of the color factor can be found in Appendix I at the end of this chapter.

In general, calculating the full two loop amplitude would be quite hard, since several diagrams would need to be taken into account. However, only the virtual-gluon contributions are leading in $\alpha_s\ln(s/s_0)$, so the amplitude must be calculated just for the diagrams appearing in fig. 3.5. These virtual corrections are once again computed by means of the Cutkosky rules and the on-shell conditions

[5]Note that this cancellation only holds for the projection in the color octet.

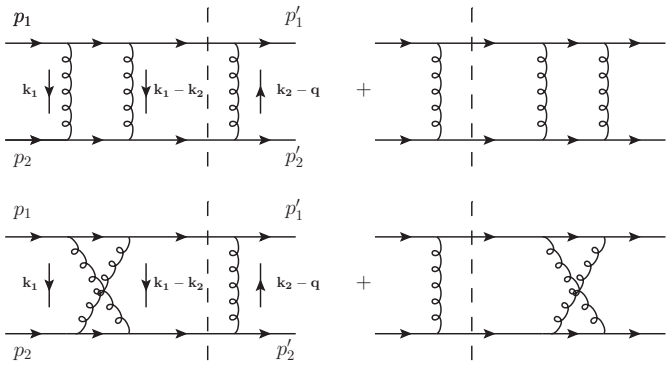

Figure 3.5: One loop virtual corrections for the qq scattering

at the cut lines, finding

$$\mathcal{I}m\mathcal{A}_8^{(2)} = \sum_{pol} \int \mathrm{dPS}^{(3)} \mathcal{A}_{8,\mu}^{(2\to 3)}(s, k_1^2, k_2^2) \mathcal{A}_{8,\nu}^{\dagger(2\to 3)}(s, (k_1-q)^2, (k_2-q)^2) + \cdots \,. \tag{3.29}$$

The contribution of the sum over the polarizations of the intermediate gluon is $g_{\mu\nu}/2$. The dots refer to an extra term that, together with the 1-loop correction one, will be canceled with the real contributions.

Taking into account the sum over polarizations, the helicities, the color factor $F_{c,8}^{(2)}$ derived in Appendix II and eq. (3.36) for the calculation of the amplitude for 1-gluon real emission $\mathcal{A}_{8,\mu}^{(2\to 3)}$, the integrand of eq. (3.29) without the phase space contribution turns out to be [13]

$$-\frac{1}{2}\mathcal{A}_{8,\mu}^{(2\to 3)}(s, k_1^2, k_2^2)\mathcal{A}_{8,\nu}^{\dagger(2\to 3)}(s, (k_1-q)^2, (k_2-q)^2) = -(4\pi)^2 \frac{\alpha_s^2 N_c^2 s}{4} \mathcal{A}_8^{(0)} \mathbf{q}^2 \times \left[\frac{\mathbf{q}^2}{\mathbf{k}_1^2 \mathbf{k}_2^2 (\mathbf{k}_1 - \mathbf{q})^2 (\mathbf{k}_2 - \mathbf{q})} - \left\{ \frac{1}{\mathbf{k}_1^2 (\mathbf{k}_1 - \mathbf{k}_2)^2 (\mathbf{k}_2 - \mathbf{q})^2} + \mathbf{k}_1 \leftrightarrow \mathbf{k}_2 \right\} \right], \tag{3.30}$$

where we have used the on-shell condition for the emitted gluon: $(\mathbf{k}_1 - \mathbf{k}_2)^2 = -\alpha_1 \beta_2 s$.

The phase-space for a $2 \to 2+n$ process in the Regge limit, using the on-mass shell condition to integrate over the α_i's, is given by

$$\int \mathrm{dPS}^{(n+2)} = \frac{2^{-(n+1)}}{(2\pi)^{3n+2}} \prod_{i=1}^{n} \prod_{j=1}^{n+1} \int_{\beta_{i+1}}^{1} \frac{\mathrm{d}\beta_i}{\beta_i} \mathrm{d}^2\mathbf{k}_j \mathrm{d}\beta_{j+1}\, \delta(s\beta_{n+1} - \mathbf{q}^2) \,, \tag{3.31}$$

where the constraints imposed by multi-Regge kinematics (eqs. (3.38)) have been used. These are all the ingredients needed to compute the integral in eq. (3.29),

which after some algebra reads

$$\mathcal{I}m\mathcal{A}_8^{(2)}(s,t) = -\frac{\alpha_s^2 N_c^2 s}{32\pi^3}\mathcal{A}_8^{(0)}\mathbf{q}^2\int_{t/s}^1\frac{\mathrm{d}\beta_1}{\beta_1}\mathrm{d}\mathbf{k}_1^2\mathbf{k}_2^2\left[\frac{\mathbf{q}^2}{\mathbf{k}_1^2\mathbf{k}_2^2(\mathbf{k}_1-\mathbf{q})^2(\mathbf{k}_2-\mathbf{q})}\right.$$
$$\left. - \left\{\frac{1}{\mathbf{k}_1^2(\mathbf{k}_1-\mathbf{k}_2)^2(\mathbf{k}_2-\mathbf{q})^2} + \mathbf{k}_1 \leftrightarrow \mathbf{k}_2\right\} + \text{extra term}\right]. \quad (3.32)$$

The structure of the first term of this expression allows us to write it in terms of the function $\epsilon(-\mathbf{q}^2)$ defined in eq. (3.26) as

$$-\pi\frac{1}{2}\mathcal{A}_8^{(0)}\ln(s/t)\epsilon^2(t)\ .$$

The whole second line cancels exactly with some contributions coming from the real emissions. Following the same procedure than for the $\mathcal{O}(\alpha_s)$ correction, the real part can be calculated from the imaginary one, giving

$$\mathcal{R}e\mathcal{A}_8^{(2)} = \frac{1}{4}\mathcal{A}_8^{(0)}\ln^2(s/t)\epsilon^2(t)\ .$$

Taking into account the crossed (u) channels given in the second line of fig. 3.5 the result for the total 2-loop amplitude in terms of the Born amplitude is

$$\mathcal{A}_{8,tot}^{(2)}(s,t) = A^{(0)}(s,t)\frac{1}{2}\ln^2\left(\frac{s}{|t|}\right)\epsilon^2(t)\ . \quad (3.33)$$

Looking at equations (3.28) and (3.33), one is tempted to write the all-orders amplitude as an expansion in $\ln\left(\frac{s}{|t|}\right)\epsilon(t)$ in the following way:

$$\mathcal{A}_8(s,t) = A^{(0)}(s,t)\left(1+\ln\left(\frac{s}{|t|}\right)\epsilon(t)+\frac{1}{2}\ln^2\left(\frac{s}{|t|}\right)\epsilon^2(t)+\ldots\right)\ , \quad (3.34)$$

which naturally leads to the ansatz

$$\mathcal{A}_8(s,t) = \mathcal{A}^{(0)}(s,t)\left(\frac{s}{|t|}\right)^{\epsilon(t)}\ . \quad (3.35)$$

This result exhibits the reggeization of the gluon, since such amplitude must stem from an object with the propagator given in eq. (3.13). If one calculates the amplitude for one gluon exchange using that propagator instead of the usual one and takes into account eq. (3.19), eq. (3.35) is obtained. This reggeization of the gluon is shown pictorically in fig. 3.6, where it can be seen how the sum of all virtual contributions in the t-channel lead to a reggeized gluon with its

propagator being

$$\frac{1}{\mathbf{k}^2}\left(\frac{s}{s_0}\right)^{\epsilon(-\mathbf{k}^2)} .$$

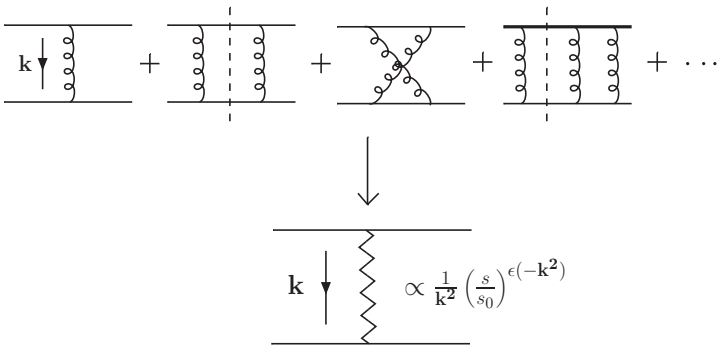

Figure 3.6: Gluon reggeization.

The **bootstrap equation** proves this ansatz to all orders using inductive arguments: first consider eq. (3.35) to actually hold. As we will show from here to the end of this section, this will allow us to compute an integral equation for the Mellin transform of the imaginary part of the total amplitude[6] for the color octet exchange, the BFKL equation. This equation will present a pole-like solution in the Mellin space at $\omega = \epsilon(t)$, which means that the amplitude in momentum space will behave as $s^{\alpha(t)}$, as found in eq. (3.12), therefore justifying the ansatz used to construct the equation. For a rigorous proof see [13,32].

2. Real emissions

All one-gluon real emissions on top of fig. 3.3 can be taken into account by calculating the amplitude for the most-right hand side diagram shown in fig. 3.7, where the blob is the gauge invariant *Lipatov effective vertex*:

$$\Gamma^{\sigma}_{\mu\nu}(k_1,k_2) = \frac{2p_{2\mu}p_{1\nu}}{s}\left[\left(\alpha_1 + \frac{2\mathbf{k}_1^2}{\beta_2}\right)p_1^{\sigma} + \left(\beta_2 + \frac{2\mathbf{k}_2^2}{\alpha_1}\right)p_2^{\sigma} - (k_1+k_2)_{\perp}^{\sigma}\right] , \tag{3.36}$$

The kinematic region we are interested in is given by

$$1 >> \alpha_1 >> \alpha_2 \quad \text{and} \quad 1 >> |\beta_2| >> |\beta_1| . \tag{3.37}$$

This means that the gluon with momentum k_1 essentially goes in the forward

[6] With total we mean the amplitude for all possible real and virtual contributions leading in $\alpha_s \ln(1/x)$.

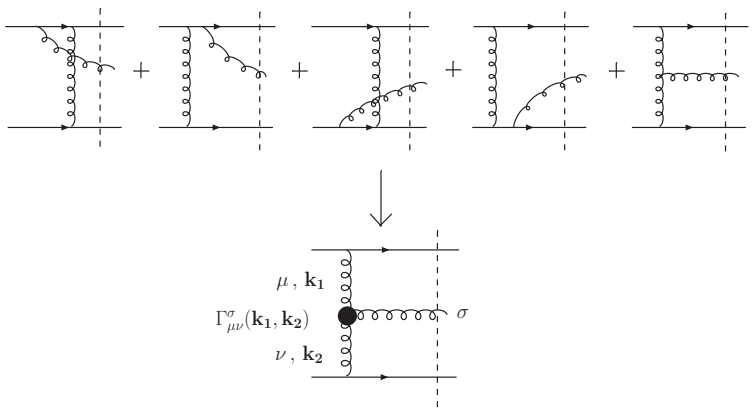

Figure 3.7: Absortion of all 1-loop real emissions into the Lipatov effective non-local vertex.

direction forward while the one with momentum k_2 goes in the backward one with respect to the beam axis.

The gluon ladder

We are now ready to calculate the BFKL gluon ladder with the color octet exchange in the t-channel and then project the solution for the color singlet to find the QCD pomeron. In order to do that we need to compute the $2 \to 2+n$ amplitude considering corrections to all orders leading in $\ln(s)$. This might seem to be very hard to do, but using the structure of the amplitude $\mathcal{A}_8^{(2)}$ and the reggeization of the gluon it will turn out to be a rather simple task. It will be sufficient to calculate the $2 \to 2+n$ amplitude at tree level and then, by means of bootstrap (its proof will be derived in this section), replace the usual gluon propagators by reggeized ones. In other words, we need to construct the amplitude for the diagram shown in fig. 3.8, in which there are $n+1$ reggeized gluon propagators in the t channel, attached to n real gluons by Lipatov effective vertices. This diagram is called the gluon ladder. We will see how the computation of this amplitude will give rise to an integral equation whose solution will lead to the construction of the perturbative pomeron.

The imaginary part of the amplitude of the gluon ladder is given by contracting the two tree level amplitudes to the left and right hand side of the cut, after integrating over the $(n+2)$-body phase space. The kinematic region that retains the leading logarithms is in this case given by the so-called *multi-Regge*

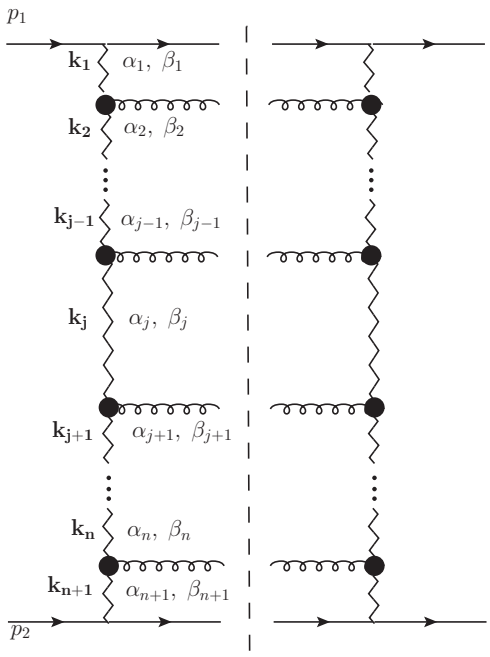

Figure 3.8: The gluon ladder.

kinematics (MRK):

$$\begin{aligned}
&\mathbf{k}_1^2 \simeq \mathbf{k}_2^2 \simeq \cdots \simeq \mathbf{k}_i^2 \simeq \cdots \simeq \mathbf{k}_{i+1}^2 \simeq \cdots \simeq \mathbf{k}_n^2 \simeq \mathbf{k}_{n+1}^2 >> \mathbf{q}^2 \simeq s_0 \ , \\
&1 >> \alpha_1 >> \alpha_2 >> \cdots >> \alpha_i >> \alpha_{i+1} >> \cdots >> \alpha_{n+1} >> \frac{s_0}{s} \ , \\
&1 >> |\beta_{n+1}| >> |\beta_n| >> \cdots >> |\beta_2| >> |\beta_1| >> \frac{s_0}{s} \ . \qquad (3.38)
\end{aligned}$$

Let us start the calculation. The scattering amplitude for the left-hand side of fig. 3.8 is equivalent to the Born level one, but replacing the exchange of the gluon propagators $i/\mathbf{k}^2$ by reggeized ones, which can be written as:

$$\frac{i}{\mathbf{k}_i^2}\left(\frac{s}{s_0}\right)^{\epsilon(-\mathbf{k}_i^2)} \simeq \frac{i}{\mathbf{k}_i^2}\left(\frac{\alpha_{i-1}}{\alpha_i}\right)^{\epsilon(-\mathbf{k}_i^2)} \ ,$$

where we have used the fact that in MRK all transverse momenta are of the same order. The expression for the born level amplitude has been derived in [50] and

can be also found in [13].

$$\begin{aligned}\mathcal{A}_{8,\sigma_1\cdots\sigma_n}^{(2\to 2+n)} &= 2\,i\,s\,(4\pi\alpha_s)^n\delta_{\lambda_1,\lambda_1'}\delta_{\lambda_2,\lambda_2'}F_{c,8}^{(n)}\,\frac{i}{\mathbf{k}_1^2}\left(\frac{1}{\alpha_1}\right)^{\epsilon(-\mathbf{k}_1^2)} \\ &\prod_{i=1}^{n}\frac{2p_1^{\mu_i}p_2^{\nu_{i+1}}}{s}\Gamma^{\sigma_i}_{\mu_i,\nu_{i+1}}\frac{i}{\mathbf{k}_{i+1}^2}\left(\frac{\alpha_i}{\alpha_{i+1}}\right)^{\epsilon(-\mathbf{k}_{i+1}^2)}\,, \end{aligned} \tag{3.39}$$

where σ_i labels the i-th real emitted gluon while μ_i,ν_i label the gluons propagating in the t-channel. λ_i,λ_i' stand for the helicities of the incoming and outgoing quarks, as pictured in fig. 3.3. The expression for the color factor $F_{c,8}^{(n)}$ is given in eq. (3.52).

Following now the same procedure as for the $\mathcal{O}(\alpha_s^2)$ amplitude, the corresponding equation for the imaginary part of the amplitude for the whole gluon ladder is equivalent to eq. (3.29), replacing the $2\to 3$ amplitudes by the new ones, eq. (3.39). The color factor is the one given in eq. (3.53), and reads:

$$\begin{aligned}\mathcal{I}m\mathcal{A}_8^n(s,t) = N_c(\pi\alpha_s)^2 s\sum_{n=0}^{\infty}(-N_c)^n\int \mathrm{dPS}^{(n+2)}\mathcal{A}_8^{(0)}(s,t)\frac{\mathbf{q}^2}{\mathbf{k}_1^2(\mathbf{k}_1-\mathbf{q})^2} \\ \times\prod_{i=1}^{n}\left[\frac{1}{\mathbf{k}_{i+1}^2(\mathbf{k}_{i+1}-\mathbf{q})^2}\left(\mathbf{q}^2-\frac{\mathbf{k}_i^2(\mathbf{k}_{i+1}-\mathbf{q})^2+(\mathbf{k}_i-\mathbf{q})^2\mathbf{k}_{i+1}^2}{(\mathbf{k}_i-\mathbf{k}_{i+1})^2}\right)\right] \\ \times\left(\frac{1}{\alpha_1}\right)^{\epsilon\left(-\mathbf{k}_1^2\right)+\epsilon\left(-(\mathbf{k}_1-\mathbf{q})^2\right)}\left(\frac{\alpha_i}{\alpha_{i+1}}\right)^{\epsilon\left(-\mathbf{k}_{i+1}^2\right)+\epsilon\left(-(\mathbf{k}_{i+1}-\mathbf{q})^2\right)}\end{aligned} \tag{3.40}$$

the last line of this expression are the propagators of the reggeized gluons. Notice how the dependence on the transverse momentum is similar to the one in eq. (3.32).

It is convenient at this point to introduce the *Mellin transform*, which will allow us to work more easily, since the integration over the phase space will be nested. In the Mellin space a multi-nested integral becomes a product of integrals, as we show in Appendix II, given at the end of this section. The Mellin transform of the imaginary part of the amplitude would be given by

$$\mathcal{F}(\omega,t)\equiv\int\frac{\mathrm{d}^2\mathbf{k}_1\mathrm{d}\mathbf{k}_2^2}{\mathbf{k}_2^2(\mathbf{k}_1-\mathbf{q})^2}f_\omega(\mathbf{k}_1,\mathbf{k}_2,\mathbf{q})=\int_1^\infty\mathrm{d}\left(\frac{s}{s_0}\right)\left(\frac{s}{s_0}\right)^{-\omega-1}\frac{\mathcal{I}m\,\mathcal{A}_0(s,t)}{s}\,, \tag{3.41}$$

where $f_\omega(\mathbf{k}_1,\mathbf{k}_2,\mathbf{q})$ is the BFKL gluon Green's function for $\mathbf{q}$ momentum transfer.

Justification of the gluon reggeization

Before defining the BFKL Green's function (projected in the color singlet) that leads to the BFKL equation let us introduce a very similar one with which we will justify the ansatz introduced to state eq. (3.35) and therefore the gluon reggeization. Let us define $\tilde{f}^8_\omega(\mathbf{k},\mathbf{q})$ as a specific Mellin transform of the amplitude projected on the color octet, reading

$$\int \mathrm{d}\left(\frac{s}{s_0}\right)\left(\frac{s}{s_0}\right)^{-\omega-1}\left(\frac{\mathcal{I}m\mathcal{A}^{(n)}_8(s,t)}{\mathcal{A}^{(0)}_8(s,t)}\right) = \int \frac{\mathrm{d}^2\mathbf{k}}{\mathbf{k}^2(\mathbf{k}-\mathbf{q})^2}\tilde{f}^8_\omega(\mathbf{k},\mathbf{q})\ . \tag{3.42}$$

After some algebra (the reader can check the details in, *e.g.*, [13,32]) the following expression for it is found:

$$\begin{aligned}\left(\omega-\epsilon\left(-\mathbf{k}^2\right)-\epsilon\left(-(\mathbf{k}-\mathbf{q})^2\right)\right)\tilde{f}^8_\omega(\mathbf{k},\mathbf{q}) &= \frac{\alpha_s N_c\mathbf{q}^2}{8\pi} - \frac{\alpha_s N_c}{4\pi^2}\int \mathrm{d}^2\mathbf{l}\tilde{f}^8_\omega(\mathbf{l},\mathbf{q}) \\ &\times\left(\frac{\mathbf{q}^2}{\mathbf{l}^2(\mathbf{l}-\mathbf{q})^2}-\frac{\mathbf{k}^2}{\mathbf{l}^2(\mathbf{k}-\mathbf{l})^2}-\frac{(\mathbf{k}-\mathbf{q})^2}{(\mathbf{k}-\mathbf{l})^2(\mathbf{l}-\mathbf{q})^2}\right)\ .\end{aligned} \tag{3.43}$$

Taking into account how $\epsilon(-\mathbf{q}^2)$ is defined in eq. (3.26) it can be easily checked how if the function $\tilde{f}_\omega(\mathbf{k},\mathbf{q})$ does not depend on $\mathbf{k}$, eq. (3.43) presents a pole-like solution of the form[7]

$$\tilde{f}_\omega(\text{whatever},\mathbf{q}) = \frac{\alpha_s N_c\mathbf{q}^2}{8\pi}\frac{1}{\omega-\epsilon(-\mathbf{q}^2)}\ . \tag{3.44}$$

Going now back to momentum space using eq. (3.42) we find the usual expression for the imaginary part of the amplitude:

$$-\frac{\pi}{2}\mathcal{A}^{(0)}_8\epsilon(t)\left(-s/s_0\right)^{\epsilon(t)}\ .$$

Adding the contribution from the crossed channel and using dispersion relations this leads to a Regge trajectory of the form of eq. (3.12) with signature $\Sigma=-1$, justifying the ansatz of gluon reggeization.

BFKL equation

We are now ready to define the BFKL gluon Green's function in the color octet, $f_\omega(\mathbf{k}_1,\mathbf{k}_2,\mathbf{q})$, which is the Mellin transform of the imaginary part of the amplitude (projected on the color singlet) over the center of mass energy with the integration over the transverse momenta $\mathbf{k}_1$ and $\mathbf{k}_2$ still to be performed (see

[7] Note once again that the cancellation of $\epsilon(-\mathbf{q}^2)$ function needed to get eq. (3.44) holds just because we are working in the color octet representation.

eq. (3.41). An iteration pattern is found for the expression of this Green's function. The procedure is equivalent to the one done to find eq. (3.43): first consider the gluon ladder with a single soft gluon emission in the s-channel ($n = 1$) and calculate the corresponding $f_\omega^{(1)}$ and start adding one emission at a time. This leads to the following integral equation for the gluon Green's function f_ω:

$$\omega f_\omega(\mathbf{k}_1,\mathbf{k}_2,\mathbf{q}) = \delta^2(\mathbf{k}_1-\mathbf{k}_2) + \frac{\bar{\alpha}_s}{2\pi}\int \mathrm{d}^2\mathbf{l}\left[\frac{-\mathbf{q}^2}{(\mathbf{l}-\mathbf{q})^2\mathbf{k}_1^2} f_\omega(\mathbf{l},\mathbf{k}_2,\mathbf{q}) + \frac{1}{(\mathbf{l}-\mathbf{k}_1)^2}\left(f_\omega(\mathbf{l},\mathbf{k}_2,\mathbf{q}) - \frac{\mathbf{k}_1^2 f_\omega(\mathbf{k}_1,\mathbf{k}_2,\mathbf{q})}{\mathbf{l}^2+(\mathbf{k}_1-\mathbf{l})^2}\right) + \frac{1}{(\mathbf{l}-\mathbf{k}_1)^2}\left(\frac{(\mathbf{k}_1-\mathbf{q})^2\,\mathbf{l}^2\, f_\omega(\mathbf{l},\mathbf{k}_2,\mathbf{q})}{(\mathbf{l}-\mathbf{q})^2\,\mathbf{k}_1^2} - \frac{(\mathbf{k}_1-\mathbf{q})^2\, f_\omega(\mathbf{k}_1,\mathbf{k}_2,\mathbf{q})}{(\mathbf{l}-\mathbf{q})^2+(\mathbf{k}_1-\mathbf{l})^2}\right)\right]. \quad (3.45)$$

Eq. (3.45) is one of the most common ways to present the BFKL equation. It is infrared finite, since the terms in parenthesis multiplying the factor $1/(\mathbf{l}-\mathbf{q})^2$ vanish at $\mathbf{l}=\mathbf{k}$. This cancellation of the IR divergences [51] can be used to justify the use of the strong ordering in longitudinal momenta (the multi-Regge regime). We established that the leading logarithm contribution to the integration over the longitudinal momenta requires the MRK and the fact that there are no further logarithms generated by the integration over the transverse momenta. The IR finiteness of the BFKL equation means that there are no such extra logarithms. Fig. 3.9 shows this iterative equation diagramatically (see also eq. (3.61)).

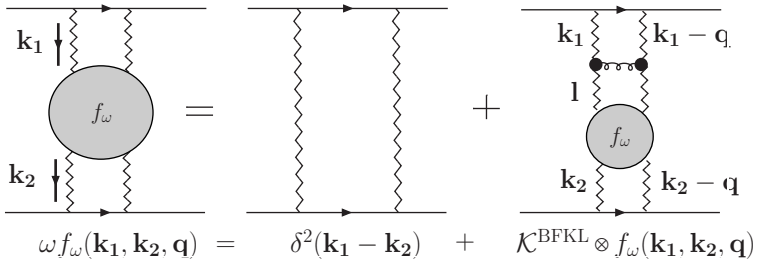

Figure 3.9: BFKL interative equation for the gluon Green's function.

The Green's function needed to reconstruct the imaginary part of the amplitude under consideration is obtained by solving the BFKL equation. Two steps are needed to find this amplitude: the first one is to take the inverse of the Mellin transform in order to go back to the energy space:

$$f(s,\mathbf{k}_1,\mathbf{k}_2,\mathbf{q}) = \frac{1}{2\pi i}\int_{\mathcal{C}-i\infty}^{\mathcal{C}+i\infty}\mathrm{d}\omega\left(\frac{s}{s_0}\right)^\omega f_\omega(\mathbf{k}_1,\mathbf{k}_2,\mathbf{q})\,, \quad (3.46)$$

where the integration contour$\mathcal{C}$ lies to the right of all the singularities of f_ω.

The second step is to perform the integrations over the momenta of the reggeized gluons:

$$\mathcal{A}_0(s,t) = i\,(8\pi\alpha_s)^2 s\,\frac{N_c^2-1}{4N_c^2}\int \frac{\mathrm{d}^2\mathbf{k}_1}{(2\pi)^2}\frac{\mathrm{d}^2\mathbf{k}_2}{(2\pi)^2}\frac{f(s,\mathbf{k}_1,\mathbf{k}_2,\mathbf{q})}{\mathbf{k}_2^2(\mathbf{k}_1-\mathbf{q})^2}\ . \tag{3.47}$$

Appendix I: Color factors in the color octet

Let us introduce the notation $t^a_{ij}t^b_{kl} = t^a \otimes t^b$, where t^a_{ij} is the generator of the color group $SU(N)$ in the fundamental representation.

The color factor for the virtual contributions to the octet exchange amplitude to order α_s (see fig. 3.3) is

$$F^{(0)}_{c,8} = t^a \otimes t^b\ .$$

From this result we can construct the corresponding one for the amplitude to order α_s^2 (see fig. 3.4):

$$\begin{aligned} F^{(1)}_{c,8} &= (t^a t^b)\otimes(t^a t^b) - (t^a t^b)\otimes(t^b t^a) \\ &= (t^a t^b)\otimes[t^a,t^b] \\ &= \frac{1}{2}(t^a t^b + t^b t^a + i f_{abd}\,t^d)\otimes(i f_{abc} t^c) \\ &= \frac{i f_{abc}\,i f_{abd}}{2}t^d\,t^c + \frac{1}{2}\{t^a,t^b\}\otimes[t^a,t^b] \\ &= \frac{i f_{abc}\,i f_{abd}}{2}t^d\,t^c = -\frac{N}{2}F^{(0)}_{c,8}\ . \end{aligned} \tag{3.48}$$

In the first line of the equation the first term at the right hand side corresponds to the color factor for the box diagram and the second one to the crossed box diagram (left and right graphs of fig. 3.4, respectively). At the end of the third line we have used $[t^a,t^b] = i f_{abc}\,t^c$ and

$$t^a t^b = \frac{1}{2}(t^a t^b + t^a t^b) = \frac{1}{2}(t^a t^b + t^b t^a + i f_{abc}\,t^c)\ ,$$

where f^{abc} are the generators of the group. For the last term of eq. (3.48) we made use of the property

$$(t^a t^b)\otimes(t^a t^b - t^b t^a) = (t^b t^a)\otimes(t^b t^a - t^a t^b) = -(t^b t^a)\otimes(t^a t^b - t^b t^a)\ .$$

Let us now go to the color octet exchange amplitude to order α_s^3:

$$F^{(2)}_{c,8} = -f_{abc}f_{dec}(t^a t^d)\otimes(t^b t^e) + f_{aec}f_{dbc}(t^a t^d)\otimes(t^e t^b)\ , \tag{3.49}$$

where the first contribution accounts for the s-channel and the second one for the u-channel (first row and second row of fig. 3.5, respectively). Let us consider the s contribution only. Noticing the symmetry of the two contributions it is worth to antisymmetrize in the labels e and b, that is, to use the relation

$$f_{abc}f_{dec} = \frac{1}{2}(f_{abc}f_{dec} - f_{aec}f_{cdb}) \ .$$

Making also use of the Jacobi relations

$$f_{abc}f_{dec} + f_{aec}f_{bdc} + f_{adc}f_{ebc} = 0 \ , \tag{3.50}$$

the first term of eq. (3.49) can be rewritten as $-\frac{1}{2}f_{adc}f_{cbe}(t^a t^d) \otimes (t^b t^e)$, leading to the color factor

$$F_{c,8}^{(2)} = \frac{1}{8}f_{adc}f_{adf}f_{cbe}f_{gbe}\, t^f t^g = \frac{N^2}{8}F_{c,8}^{(0)} \ , \tag{3.51}$$

where we have made use of commutators.

The same procedure can be done with higher order terms, by using eq. (3.50) as many times as needed. The color factor of the amplitude for the left hand side of the n-gluon ladder shown in fig. 3.8 would be given by

$$F_{c,8}^{(n)}(c_1, \cdots, c_n) = \prod_{i=1}^{n} f_{a_i a_{i+1} c_i}\, t^{a_1} \otimes t^{a_{n+1}} \ , \tag{3.52}$$

where c_i is the color of the i-th emitted gluon. Consequently, the color factor for the squared amplitude, still projected in the color octet, would be

$$F_{c,8}^{(n)}(c_1, \cdots, c_n) \times F_{c,8}^{(n)}(c_1, \cdots, c_n) = \left(\frac{N}{2}\right)^n \frac{N}{4}T_{c,8}^{(0)} \ . \tag{3.53}$$

Appendix II: Mellin transform

The Mellin transform of a function $f(s)$ is defined as

$$\mathcal{F}(\omega) = \int_1^\infty \mathrm{d}\left(\frac{s}{\mathbf{k}^2}\right)\left(\frac{s}{\mathbf{k}^2}\right)^{-\omega-1} f(s) \ , \tag{3.54}$$

with its inverse given by

$$f(s) = \frac{1}{2\pi i}\int_C \mathrm{d}\omega \left(\frac{s}{\mathbf{k}^2}\right)^{\omega} \mathcal{F}(\omega) \ , \tag{3.55}$$

where the contour C is located to the right of all ω-plane singularities of $\mathcal{F}(\omega)$.

Convolutions

Let $f(s)$ be given in terms of a convolution of a set of n functions, $f_i(s/\mathbf{k}^2)$, $i = 1, \ldots, n$ by

$$f(s) = \mathbf{k}^2 \prod_{i=1}^{n} \int_{\rho_{i+1}}^{1} \frac{\mathrm{d}\rho_i}{\rho_i} f_i\left(\frac{\rho_i - 1}{\rho_i}\right) \delta(\rho_n s - \mathbf{k}^2) \,, \tag{3.56}$$

with $\rho_0 = 1$ and $\rho_{n+1} = 0$. The Mellin transform is given by

$$\mathcal{F}(\omega) = \mathbf{k}^2 \int_1^\infty \mathrm{d}\left(\frac{s}{\mathbf{k}^2}\right) \left(\frac{s}{\mathbf{k}^2}\right)^{-\omega-1} \prod_{i=1}^{n} \int_{\rho_{i+1}}^{1} \frac{\mathrm{d}\rho_i}{\rho_i} f_i\left(\frac{\rho_i - 1}{\rho_i}\right) \delta(\rho_n s - \mathbf{k}^2) \,. \tag{3.57}$$

After performing the integration over $s/\mathbf{k}^2$ one obtains

$$\mathcal{F}(\omega) = \prod_{i=1}^{n} \int_{\rho_{i+1}}^{1} \frac{\mathrm{d}\rho_i}{\rho_i} f_i\left(\frac{\rho_i - 1}{\rho_i}\right) \rho_n^\omega = \prod_{i=1}^{n} \int_0^1 \mathrm{d}\tau_i \tau_i^{\omega-1} f_i\left(\frac{1}{\tau_i}\right) = \prod_{i=1}^{n} \mathcal{F}_i(\omega) \,, \tag{3.58}$$

$\mathcal{F}_i(\omega)$ are the Mellin transforms of the functions $f_i\left(\frac{s}{\mathbf{k}^2}\right)$. The change of variables $\tau_i \equiv \frac{\rho_i}{\rho_i - 1} \;\rightarrow\; \rho_n = \tau_1 \tau_2 \ldots \tau_n$, has been used.

3.2 LL solution & applications

3.2.1 LL solution in the forward case & hadronic cross section

In the case of zero momentum transfer, eq. (3.45) gives

$$\omega f_\omega(\mathbf{k}_1, \mathbf{k}_2) = \delta^2(\mathbf{k}_1 - \mathbf{k}_2) + \int \mathrm{d}^2\mathbf{l} \mathcal{K}(\mathbf{k}_1, \mathbf{l}) \, f_\omega(\mathbf{l}, \mathbf{k}_2) \,, \tag{3.59}$$

where $\mathcal{K}(\mathbf{k}_1, \mathbf{l})$ is defined as

$$\mathcal{K}(\mathbf{k}_1, \mathbf{l}) = 2\epsilon(-\mathbf{k}_1^2)\delta^2(\mathbf{k}_1 - \mathbf{l}) + \frac{N_c \alpha_s}{2\pi^2} \frac{1}{(\mathbf{k}_1 - \mathbf{l})^2} \,. \tag{3.60}$$

The first term of $\mathcal{K}(\mathbf{k}_1, \mathbf{l})$ corresponds to the virtual corrections to the BFKL kernel (with $\mathbf{q}^2 = 0$), while the second one corresponds to the real ones.

Eq. (3.59) can be written in the symbolic form

$$\omega f_\omega = \mathbb{1} + \mathcal{K} \otimes f_\omega \,. \tag{3.61}$$

In order to solve this equation we can expand the function f_ω in terms of a

complete set of eigenfunctions of the kernel $\mathcal{K}$, $\phi_a(\mathbf{k})$, such that

$$\mathcal{K} \otimes \phi_a = \lambda_a \phi_a \ . \tag{3.62}$$

The eigenfunctions must obey the completeness relation given in the first equation of eqs. (3.67). They can be expanded in a Fourier series as

$$\phi_a(\mathbf{k}) = \sum_{n=0}^{\infty} \phi_{n,a}(\mathbf{k}) \frac{\mathrm{e}^{\mathrm{i}n\theta}}{\sqrt{2\pi}} \ , \tag{3.63}$$

where θ is the azimuthal polar coordinate of the transverse momentum $\mathbf{k}$. By introducing this expression in eq. (3.59), a set of equations for the Fourier components are found. Because of the completeness relation, they have to be of the form

$$\phi_{n\nu}(|\mathbf{k}|, \theta) = \frac{1}{\pi\sqrt{2}} \, (\mathbf{k}^2)^{-\frac{1}{2}+i\nu} \, \mathrm{e}^{\mathrm{i}n\theta} \ , \tag{3.64}$$

normalized such that $\langle \nu', n' \,|\, \nu, n \rangle = \delta(\nu - \nu') \, \delta_{n,n'}$ (see eqs. (3.67) for notation). Inserting this expression in the BFKL equation we find the solution for the eigenvalues:

$$\omega_n(\nu) = \bar{\alpha}_s \chi_n(\nu) \ , \tag{3.65}$$

with

$$\chi_0(\gamma) = 2\psi(1) - \psi(\gamma) - \psi(1-\gamma) \, , \quad \psi(\gamma) \equiv \frac{\Gamma'(\gamma)}{\Gamma(\gamma)} \ . \tag{3.66}$$

Two different representations have been used here, one for the momentum space and another one in the (ν, n)-space. The interplay between these two can be given by

$$\begin{aligned} \langle \mathbf{k}_1 | \mathbf{k}_2 \rangle &= \delta^2(\mathbf{k}_1 - \mathbf{k}_2) \ , \\ \langle \mathbf{k}_1 \,|\, \nu, n \rangle &= \frac{1}{\pi\sqrt{2}} \, (\mathbf{k}_1^2)^{i\nu - 1/2} \, \mathrm{e}^{\mathrm{i}n\theta_1} \ , \\ \mathcal{K} \,|\, \nu, n \rangle &= \omega(n, \nu) \,|\, \nu, n \rangle \ . \end{aligned} \tag{3.67}$$

The gluon Green's function in the LL approximation is then given in the new basis by

$$f_\omega(\mathbf{k}_1, \mathbf{k}_2) = \sum_{n=0}^{\infty} \int_{-\infty}^{\infty} \mathrm{d}\nu \, \left(\frac{k_1^2}{k_2^2} \right)^{i\nu} \frac{\mathrm{e}^{\mathrm{i}n(\theta_1 - \theta_2)}}{2\pi^2 k_1 k_2} \frac{1}{\omega - \bar{\alpha}_s \chi_n(\nu)} \ . \tag{3.68}$$

The hard or QCD pomeron intercept is given by the singularity (eigenvalue) which gives a leading behavior in $\ln(s/s_0)$. This corresponds to the one with largest real part. At LLA, since $\chi_n(\nu)$ is negative or zero for n different from

zero, the corresponding Fourier component will decrease with energy. Thus, we can take just the $n = 0$ component of the sum (see fig. 3.10). Moreover, we can see how χ_0 decreases with increasing ν, so we can expand the kernel in powers of ν, $\chi_0(\nu) = 4\ln 2 - 14\zeta(3)\nu^2 + \cdots$ and take $\nu = 0$ (saddle point approximation), getting

$$\lambda_P^{\rm LL} = \omega_0 = 4\bar{\alpha}_s \ln 2 \simeq 0.5 \; . \tag{3.69}$$

In this way we have found the perturbative pomeron in QCD. However, its value is much larger than the pomeron intercept given in Regge theory: $\lambda_P^{\rm QCD} \simeq 0.5 >> \lambda_P^{\rm Regge} = 0.08$. This hard pomeron has been calculated also at NLLA, finding a lower value than the LL solution: $\lambda_P^{\rm NLL} \simeq 0.3$, still very different than the Regge one. The reason for this difference is due to the fact that the soft pomeron deals with the scattering between two hadrons with a large transverse size while the hard one is exchanged between two systems characterized by a large scale. They correspond to different limits of the strong interaction. An ideal setup to study the transition or interplay between both regions takes place at the low x behavior of the proton structure function $F_2(x, Q^2)$. We refer the reader to chapter 4 for details on this. Another common approach to try to connect the hard and soft pomerons is to go to $N = 4$ super Yang-Mills theory (for studies in this direction see, *e.g.*, [52,53] and references therein.).

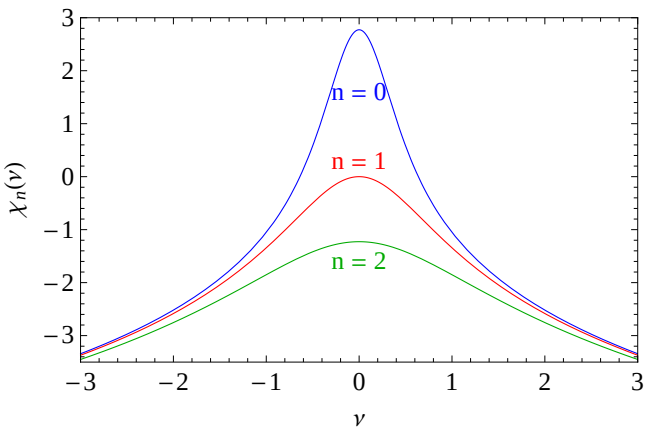

Figure 3.10: Behavior of the LL kernel $\chi_n(\nu)$ with n. The upper curve corresponds to $n = 0$, the next one to $n = 1$ and the lower one to $n = 2$.

Hadronic cross section at low x: k_T-factorization

The expression for the total cross section of a hadronic scattering process $A+B \to A+B$ with a momentum transferred t using k_t-factorization [8] is given by

$$\sigma_{AB}^{\rm had}(s, t \equiv -\mathbf{q}^2) = \frac{1}{(2\pi)^4} \int \frac{\mathrm{d}^2\mathbf{k}_1}{\mathbf{k}_1^2} \int \frac{\mathrm{d}^2\mathbf{k}_2}{\mathbf{k}_2^2} \Phi_A(\mathbf{k}_1) f(s, \mathbf{k}_1, \mathbf{k}_2, \mathbf{q}) \Phi_B(\mathbf{k}_2) \ . \quad (3.70)$$

This equation is the convolution of the hadron impact factors Φ_i with the gluon Green's function which accounts for soft gluon radiation in the scattering process. As we already said in the introduction, the impact factors are non-perturbative objects which can only be modeled and adjusted with fitted experimental data. They are universal, process independent, so, in principle, once we extract a model for them we can use them to make predictions for any hadronic-initiated process. Eq. (3.70) will be extensively used throughout the rest of this thesis.

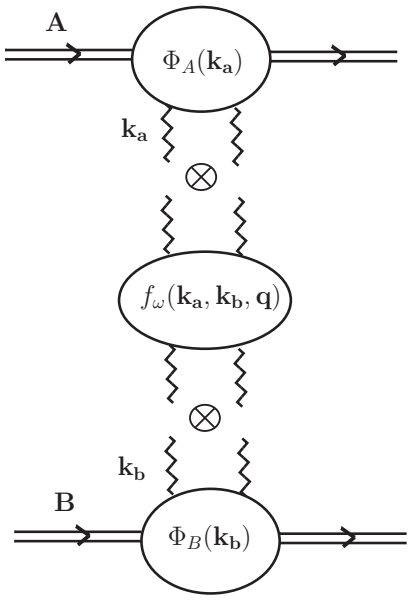

Figure 3.11: High energy factorization of a hadronic cross section in the Regge limit.

3.2.2 Monte Carlo solution in the non-forward case & consistency with bootstrap

In this section we present a study of this long-standing problem in high energy QCD: how to treat the running of the strong coupling in evolution equations

[8] In the high energy limit it can be also called high energy factorization.

driven by the BFKL equation. This subject has been extensively discussed in the literature (see, *e.g.* Refs. [54–59]). We put the emphasis on a particular form of writing the equation with running coupling which is consistent, in principle to all orders in a coupling expansion, with the bootstrap property of QCD scattering amplitudes at high energies [60–62]. Bootstrap in high energy QCD has been discussed in many papers [63] and we refer the reader to the original work by Braun [60] for a detailed discussion directly related to our present study. Our new contribution is to be able to study the problem using Monte Carlo integration techniques which solve the BFKL equation with a running coupling exactly and allow us to access exclusive information of the final states in the cut amplitude case, and of the diffusion pattern in the virtual diagrams for the non-forward elastic amplitude. We are particularly interested in the dependence of our solution on the total momentum transfer. For a connection of this representation of the BFKL equation with renormalon contributions we refer the reader to [61] and for a more recent related analysis in coordinate space to [62].

In the following the parametrization (3.123) for the running of the coupling, which we will explain later on, will be used.

Running coupling compatible with bootstrap

From a theoretical point of view there is little restriction on how to introduce the running and many different possibilities have been suggested in the literature. Our aim is to introduce it in the calculation of the gluon Green's function in a way consistent with gluon reggeization. In other words, whatever we do to the strong coupling constant to make it momentum-dependent must guarantee the bootstrap condition. As we saw in the introduction, bootstrap states that the integral equation for the t-channel exchange of two reggeized gluons in the color octet representation has a solution with a Regge pole in Mellin space of the form $\omega = \epsilon(\mathbf{q})$, ensuring a power-like growth of the total hadronic cross section with energy [4] and justifying gluon reggeization. As we showed in section 3.1.2, in order to find the trajectory $\epsilon(\mathbf{q})$ at first order in perturbation theory for fixed coupling constant it is sufficient to calculate the amplitude for the one-loop virtual corrections to the t-channel gluon exchange. This leads to the propagator of the reggeized gluon which goes like $\frac{1}{k^2}(s/s_0)^{\epsilon(q)}$, $\epsilon(q)$ being the gluon trajectory defined in eq. (3.26).

Let us start with the fixed coupling analysis. If we insert the pole like solution given in eq. (3.44) into eq. (3.43) we find the following bootstrap equation:

$$\omega - \epsilon(\mathbf{k}^2) - \epsilon(-(\mathbf{k}-\mathbf{q})^2) = \frac{\bar{\alpha}_s}{4\pi} \int \mathrm{d}^2\mathbf{l}\, \tilde{\mathcal{K}}(\mathbf{k},\mathbf{l},\mathbf{q})\, \tilde{f}^8_\omega(\mathbf{l},\mathbf{q})\,, \tag{3.71}$$

with

$$\tilde{\mathcal{K}}(\mathbf{k},\mathbf{l},\mathbf{q}) \equiv \frac{\mathbf{k}^2}{\mathbf{l}^2(\mathbf{k}-\mathbf{l})^2} + \frac{(\mathbf{k}-\mathbf{q})^2}{(\mathbf{k}-\mathbf{l})^2(\mathbf{l}-\mathbf{q})^2} - \frac{\mathbf{q}^2}{\mathbf{l}^2(\mathbf{l}-\mathbf{q})^2} \ . \tag{3.72}$$

It can be checked that in fact the leading order gluon trajectory satisfies the above equation.

The next step now is to introduce the running of the coupling constant in eq. (3.43)[9]. To do so we will first find the gluon trajectory for the reggeized gluon with running of the coupling and then insert it into the bootstrap eq. (3.71), assuming this one holds for the running case, to reconstruct the BFKL kernel. It can be checked that this formalism is consistent with the bootstrap condition by taking the fixed coupling limit and seeing how the leading order BFKL results are restored.

The gluon trajectory at first order in perturbation theory with running coupling is found by inserting fermion loops in the gluon propagator creating in this way gluon chains that effectively resum corrections of the type $(\alpha_s n_f)^n$, n_f being the number of flavors[10]. The amplitude for the sum of all diagrams that contribute to the first order correction to the gluon reggeization due to the running can be calculated by means of unitarity and the dispersion relation [13]

$$\mathcal{A}(2\to 2;\alpha_s^2) = \frac{1}{\pi}\left(\int \mathrm{d}s' \frac{\mathrm{Im}(\mathcal{A})_\mathrm{s}}{s'-s} + \int \mathrm{d}s' \frac{\mathrm{Im}(\mathcal{A})_\mathrm{u}}{u'-u}\right) \ . \tag{3.73}$$

As we already know, unitarity allows us to write the imaginary part of the $2\to 2$ amplitude shown in fig. 3.3 as

$$\mathcal{I}m\mathcal{A}\left(s, t=-\mathbf{q}^2\right) = \int \frac{\mathrm{d}^2k}{(2\pi)^2}\mathcal{A}(\mathbf{k}^2)\mathcal{A}^\dagger(-(\mathbf{q}-\mathbf{k})^2) \ . \tag{3.74}$$

Since the amplitude for each gluon chain with momentum transfer $\mathbf{k}$ is $\alpha_s(\mathbf{k})/\mathbf{k}^2$, the imaginary part of the first diagram in fig. 3.3 inserting gluon chains in the two gluon propagators is of the form

$$\mathcal{I}m\mathcal{A}\left(t=-\mathbf{q}^2\right) \propto \int \mathrm{d}^2\mathbf{k}\frac{\bar{\alpha}_s(\mathbf{k})\bar{\alpha}_s(\mathbf{k}-\mathbf{q})}{\mathbf{k}^2(\mathbf{k}-\mathbf{q})^2} \ . \tag{3.75}$$

We can then reconstruct the real part using eq. (3.73) to find the total amplitude. Calculating the simpler diagrams with an arbitrary number of fermion bubbles and then using naïve non-Abelianization it is possible to make an ansatz fot the

[9] This calculation could have been equivalently done using the BFKL equation for the color singlet, given by eq. (3.45). The results obtained do not depend on the particular choice of equation between those two.

[10] Each fermion bubble gives a contribution $\alpha_s n_f$

structure of the gluon Regge trajectory with running coupling effects. The final prescription reads

$$\tilde{\epsilon}(-\mathbf{q}^2) = -\frac{1}{4\pi}\int \mathrm{d}^2\mathbf{k}\frac{\mathbf{q}^2\,\bar{\alpha}_s(\mathbf{k})\bar{\alpha}_s(\mathbf{k}-\mathbf{q})}{\mathbf{k}^2(\mathbf{k}-\mathbf{q})^2\bar{\alpha}_s(\mathbf{q})}\,, \tag{3.76}$$

such that the corrected gluon propagator is of the form $\frac{1}{\mathbf{k}^2}(s/s_0)^{\tilde{\epsilon}(-\mathbf{q}^2)}$. This was first calculated by Levin in [61] and then by Kovchegov [62] and originally analyzed by Braun [60], who extended his work with Vacca [64].

Inserting the new trajectory into eq. (3.71) it is straightforward to find the modified kernel needed to satisfy the bootstrap condition. Let us introduce a function $\eta(\mathbf{q})$ given by

$$\eta(\mathbf{q}) \equiv \frac{\mathbf{q}^2}{\bar{\alpha}_s(\mathbf{q})}\,. \tag{3.77}$$

The expressions for both the corrected trajectory and kernel in terms of this new variable are

$$\tilde{\epsilon}(\mathbf{q}) = -\frac{1}{4\pi}\int\frac{\mathrm{d}^2\mathbf{k}}{\eta(\mathbf{k})}\frac{\eta(\mathbf{q})}{\eta(\mathbf{k}-\mathbf{q})}\,, \tag{3.78}$$

$$\tilde{\mathcal{K}}(\mathbf{k},\mathbf{l},\mathbf{q}) = \frac{\eta(\mathbf{k})}{\eta(\mathbf{l})\eta(\mathbf{k}-\mathbf{l})} + \frac{\eta(\mathbf{q}-\mathbf{k})}{\eta(\mathbf{q}-\mathbf{l})\eta(\mathbf{k}-\mathbf{l})} - \frac{\eta(\mathbf{q})}{\eta(\mathbf{l})\eta(\mathbf{q}-\mathbf{l})}\,. \tag{3.79}$$

It is now clear from the equations the consistency of this way of introducing the running with bootstrap.

In the following we will study the relevance of including the running coupling effects in the BFKL equation in this way.

LL BFKL equation with running coupling & Monte Carlo

Eq. (3.45) can be re-written in the equivalent form[11]:

$$\begin{aligned}\left(\omega - \epsilon\left(-\mathbf{k}_1^2\right) - \epsilon\left(-(\mathbf{k}_1-\mathbf{q})^2\right)\right) f_\omega(\mathbf{k}_1,\mathbf{k}_2,\mathbf{q}) = \delta^2(\mathbf{k}_1-\mathbf{k}_2) \\ -\frac{\bar{\alpha}_s}{2\pi}\int \mathrm{d}^2\mathbf{l}\left[\frac{\mathbf{q}^2}{(\mathbf{l}-\mathbf{q})^2\mathbf{k}_1^2} - \frac{1}{(\mathbf{l}-\mathbf{k}_1)^2}\left(1+\frac{(\mathbf{k}_1-\mathbf{q})^2\mathbf{l}^2}{(\mathbf{l}-\mathbf{q})^2\mathbf{k}_1^2}\right)\right] f_\omega(\mathbf{l},\mathbf{k}_2,\mathbf{q})\,.\end{aligned} \tag{3.80}$$

Note that the solution to this equation corresponds to a four point Green's function for four off-shell reggeized gluons carrying two-dimensional transverse momenta $-\mathbf{k}_1, \mathbf{k}_1-\mathbf{q}, \mathbf{k}_2, \mathbf{q}-\mathbf{k}_2$, all of them outgoing. $\mathbf{q}$ corresponds to the total momentum transfer in the t-channel. In order to match the normalization used

[11] For a Monte Carlo study of the total momentum transfer dependence of the BFKL gluon Green function in the LO and NLO adjoint representations in QCD and $N = 4$ SUSY see Refs. [65, 66]

by Braun in [60] we can introduce the rescaling

$$\mathcal{G}_\omega(\mathbf{l},\mathbf{k}_2;q) \equiv f_\omega(\mathbf{l},\mathbf{k}_2,\mathbf{q})\frac{\mathbf{l}^2}{\mathbf{k}_1^2}. \tag{3.81}$$

The set up under study can be simply implemented by replacing each of the squared transverse momenta $\mathbf{p}^2$ of eq. (3.80) with a general function $\eta(\mathbf{p})$. The new trajectory will then be given by eq. (3.78) and eq. (3.80) now reads

$$\begin{aligned}\left(\omega-\tilde{\epsilon}(-\mathbf{k}_1^2)-\tilde{\epsilon}(-(\mathbf{k}_1-\mathbf{q})^2)\right)\mathcal{G}_\omega(\mathbf{k}_1,\mathbf{k}_2,\mathbf{q}) &= \delta^{(2)}(\mathbf{k}_1-\mathbf{k}_2)\\ &+\int\frac{\mathrm{d}^2\mathbf{l}}{2\pi}\frac{\eta(\mathbf{k}_1)}{\eta(\mathbf{l})\eta(\mathbf{k}_1-\mathbf{l})}\left[1+\frac{\eta(\mathbf{k}_1-\mathbf{q})\eta(\mathbf{l})-\eta(\mathbf{q})\eta(\mathbf{k}_1-\mathbf{l})}{\eta(\mathbf{l}-\mathbf{q})\eta(\mathbf{k}_1)}\right]\mathcal{G}_\omega(\mathbf{l},\mathbf{k}_2,\mathbf{q}).\end{aligned} \tag{3.82}$$

As it has been shown in [60] (see the previous section), this equation is compatible with the bootstrap condition for the all-orders expansion of the function η.

Let us first study the simplest case, with $\mathbf{q}=\mathbf{0}$, corresponding to forward scattering, or, by the optical theorem, to a contribution to the total cross section. From now on we also fix $\eta(\mathbf{k})=\mathbf{k}^2/\bar{\alpha}_s(\mathbf{k})$ with α_s as in Eq. (3.123). We, therefore, can write

$$\left(\omega-2\,\tilde{\epsilon}(-\mathbf{k}_1^2)\right)\mathcal{G}_\omega(\mathbf{k}_1,\mathbf{k}_2)=\delta^{(2)}(\mathbf{k}_1-\mathbf{k}_2)+\int\frac{\mathrm{d}^2\mathbf{l}}{\pi}\frac{\eta(\mathbf{k}_1)}{\eta(\mathbf{l})\eta(\mathbf{k}_1-\mathbf{l})}\mathcal{G}_\omega(\mathbf{l},\mathbf{k}_2) \tag{3.83}$$

since $\eta(\mathbf{0})=\mathbf{0}$.

For our Monte Carlo implementation of the solution to this equation (see Refs. [67, 68] for similar studies in the fixed coupling case) it is convenient to introduce a shift in the integration momentum of the form $\mathbf{l}=\mathbf{k}+\mathbf{k}_1$ and a mass parameter λ to separate the resolved real emissions (with $\mathbf{k}^2>\lambda^2$) from the unresolved ones (with $\mathbf{k}^2<\lambda^2$). The latter, after integration over the phase space of the emitted gluons, generate infrared divergences which should cancel against those of the gluon Regge trajectories. The final results we show here are independent of λ in the limit $\lambda\to 0$. Taking the approximation $\mathcal{G}_\omega(\mathbf{k}+\mathbf{k}_1,\mathbf{k}_2)\simeq\mathcal{G}_\omega(\mathbf{k}_1,\mathbf{k}_2)$ for unresolved emissions we can then write

$$\begin{aligned}\left(\omega-2\,\tilde{\epsilon}_\lambda(-\mathbf{k}_1^2)\right)\mathcal{G}_\omega(\mathbf{k}_1,\mathbf{k}_2) &= \delta^{(2)}(\mathbf{k}_1-\mathbf{k}_2)\\ &+\int\frac{\mathrm{d}^2\mathbf{k}}{\pi}\frac{\eta(\mathbf{k}_1)\theta\left(\mathbf{k}^2-\lambda^2\right)}{\eta(\mathbf{k})\eta(\mathbf{k}+\mathbf{k}_1)}\mathcal{G}_\omega(\mathbf{k}+\mathbf{k}_1,\mathbf{k}_2),\end{aligned} \tag{3.84}$$

where

$$\tilde{\epsilon}_\lambda(-\mathbf{q}^2) = -\int\frac{\mathrm{d}^2\mathbf{k}}{2\pi}\frac{\eta(\mathbf{q})\theta\left(\mathbf{k}^2-\lambda^2\right)}{\eta(\mathbf{k})\left(\eta(\mathbf{k})+\eta(\mathbf{k}-\mathbf{q})\right)}. \tag{3.85}$$

We can rewrite eq. (3.84) as

$$\mathcal{G}_\omega(\mathbf{k}_1,\mathbf{k}_2) = \frac{\delta^{(2)}(\mathbf{k}_1-\mathbf{k}_2) + \int \frac{\mathrm{d}^2\mathbf{k}}{\pi}\theta\left(\mathbf{k}^2-\lambda^2\right)\xi\left(\mathbf{k}_1,\mathbf{k}\right)\mathcal{G}_\omega(\mathbf{k}+\mathbf{k}_1,\mathbf{k}_2)}{\omega - 2\,\tilde{\epsilon}_\lambda(-\mathbf{k}_1^2)}, \quad (3.86)$$

with

$$\xi(\mathbf{k}_1,\mathbf{k}) \equiv \frac{\eta(\mathbf{k}_1)}{\eta(\mathbf{k})\eta(\mathbf{k}+\mathbf{k}_1)}$$

and iterate the equation obtaining

$$\begin{aligned}
\mathcal{G}_\omega\left(\mathbf{k}_1,\mathbf{k}_2\right) &= \frac{\delta^{(2)}\left(\mathbf{k}_1-\mathbf{k}_2\right)}{\omega - 2\,\tilde{\epsilon}_\lambda(-\mathbf{k}_1^2)} \\
&+ \int \frac{\mathrm{d}^2\mathbf{p}_1}{\pi\mathbf{p}_1^2}\frac{\theta\left(\mathbf{p}_1^2-\lambda^2\right)\,\xi\left(\mathbf{k}_1,\mathbf{p}_1\right)}{\omega - 2\,\tilde{\epsilon}_\lambda(-\mathbf{k}_1^2)}\frac{\delta^{(2)}\left(\mathbf{k}_1+\mathbf{p}_1-\mathbf{k}_2\right)}{\omega - 2\,\tilde{\epsilon}_\lambda\left(-(\mathbf{k}_1+\mathbf{p}_1)^2\right)} \\
&+ \int \frac{\mathrm{d}^2\mathbf{p}_1}{\pi\mathbf{p}_1^2}\int \frac{\mathrm{d}^2\mathbf{p}_2}{\pi\mathbf{p}_2^2}\frac{\theta\left(\mathbf{p}_1^2-\lambda^2\right)\,\xi\left(\mathbf{k}_1,\mathbf{p}_1\right)}{\omega - 2\,\tilde{\epsilon}_\lambda\left(-\mathbf{k}_1^2\right)}\frac{\theta\left(\mathbf{p}_2^2-\lambda^2\right)\,\xi\left(\mathbf{k}_1+\mathbf{p}_1,\mathbf{p}_2\right)}{\omega - 2\,\tilde{\epsilon}_\lambda\left(-(\mathbf{k}_1+\mathbf{p}_1)^2\right)} \\
&\qquad \times\frac{\delta^{(2)}\left(\mathbf{k}_1+\mathbf{p}_1+\mathbf{p}_2-\mathbf{k}_2\right)}{\omega - 2\,\tilde{\epsilon}_\lambda\left(-(\mathbf{k}_1+\mathbf{p}_1+\mathbf{p}_2)^2\right)} \\
&+ \cdots
\end{aligned} \quad (3.87)$$

In order to go back to x space we use

$$\mathcal{F}(\mathbf{k}_1,\mathbf{k}_2,x) = \int \frac{\mathrm{d}\omega}{2\pi i}x^{-\omega}\mathcal{G}_\omega(\mathbf{k}_1,\mathbf{k}_2). \quad (3.88)$$

The final expression to be evaluated using Monte Carlo integration techniques is

$$\begin{aligned}
\mathcal{F}(\mathbf{k}_1,\mathbf{k}_2,x) = x^{-2\tilde{\epsilon}_\lambda(-\mathbf{k}_1^2)}\Bigg\{&\delta^{(2)}\left(\mathbf{k}_1-\mathbf{k}_2\right) + \\
&\sum_{n=1}^{\infty}\prod_{i=1}^{n}\int\frac{\mathrm{d}^2p_i}{\pi}\frac{\eta\left(\mathbf{k}_1+\sum_{l=1}^{i-1}\mathbf{p}_l\right)}{\eta(\mathbf{p}_i)\eta\left(\mathbf{k}_1+\sum_{l=1}^{i}\mathbf{p}_l\right)}\theta(\mathbf{p}_i^2-\lambda^2)\delta^{(2)}\left(\mathbf{k}_1+\sum_{l=1}^{n}\mathbf{p}_l-\mathbf{k}_2\right) \\
&\times\int_{x_{i-1}}^{1}\frac{\mathrm{d}x_i}{x_i}\,x_i^{2\left(\tilde{\epsilon}_\lambda\left(-\left(\mathbf{k}_1+\sum_{l=1}^{i-1}\mathbf{p}_l\right)^2\right)-\tilde{\epsilon}_\lambda\left(-\left(\mathbf{k}_1+\sum_{l=1}^{i}\mathbf{p}_l\right)^2\right)\right)}\Bigg\},
\end{aligned} \quad (3.89)$$

where $x_0 \equiv x$. Note that n corresponds to the number of on-shell gluons emitted with a longitudinal momentum fraction x_i and a transverse momentum k_i.

For completeness, we compare the gluon trajectory in the form

$$\tilde{\epsilon}_\lambda(-\mathbf{q}^2) = -\frac{\mathbf{q}^2}{\bar{\alpha}_s(\mathbf{q})}\int\frac{\mathrm{d}^2\mathbf{k}}{2\pi\mathbf{k}^2}\frac{\bar{\alpha}_s(\mathbf{k})\bar{\alpha}_s(\mathbf{k}-\mathbf{q})}{\mathbf{k}^2+(\mathbf{k}-\mathbf{q})^2}\theta(\mathbf{k}^2-\lambda^2), \quad (3.90)$$

with the usual one at leading order in our λ-regularization of infrared divergences

$$\epsilon_\lambda^{\rm LO}(-\mathbf{q}^2) \;=\; -\bar{\alpha}_s(\mathbf{q})\mathbf{q}^2\int\frac{\mathrm{d}^2\mathbf{k}}{2\pi\mathbf{k}^2}\frac{\theta(\mathbf{k}^2-\lambda^2)}{\mathbf{k}^2+(\mathbf{k}-\mathbf{q})^2} \;\simeq\; -\frac{\bar{\alpha}_s(\mathbf{q})}{2}\ln\frac{\mathbf{q}^2}{\lambda^2} \quad (3.91)$$

in fig. 3.12 (both lines are calculated with $\lambda = 0.01$ GeV). Note that the behaviour of both representations is quite different at large values of the modulus of the transverse momentum in the reggeized gluon propagators (which correspond to the power-like terms in Eq. (3.89)).

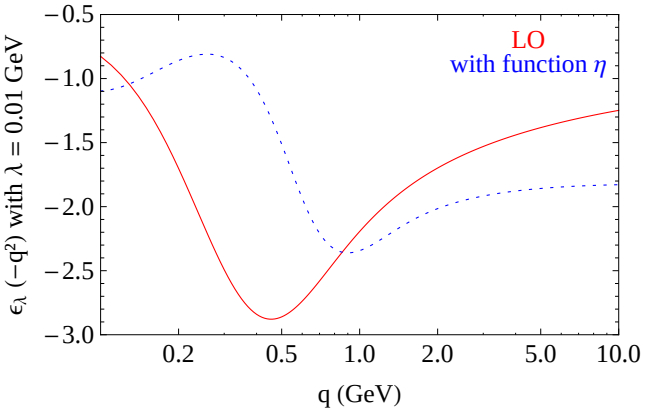

Figure 3.12: Gluon Regge trajectory in different schemes: the solid line is LO and the dotted LO plus running.

A similar iteration of the BFKL kernel applies for the more complicated non-forward equation. In this case eq. (3.89) would be

$$\begin{aligned}\mathcal{F}(\mathbf{k}_1,\mathbf{k}_2,\mathbf{q},x) =& \left\{\delta^{(2)}(\mathbf{k}_1-\mathbf{k}_2)+\sum_{n=1}^{\infty}\prod_{i=1}^{n}\int\mathrm{d}^2\mathbf{q}_i\,\mathcal{K}\left(\mathbf{k}_1+\sum_{l=0}^{i-1}\mathbf{q}_l,\mathbf{k}_1+\sum_{l=1}^{i}\mathbf{q}_l,\mathbf{q}\right)\right.\\ &\times\theta(\mathbf{q}_i^2-\lambda^2)\delta^{(2)}\left(\mathbf{k}_1+\sum_{l=1}^{n}\mathbf{q}_l-\mathbf{k}_2\right)\int_{x_{i-1}}^{1}\frac{\mathrm{d}x_i}{x_i}\,x_i^{\tilde{\epsilon}_\lambda\left(-\left(\mathbf{k}_1+\sum_{l=1}^{i-1}\mathbf{q}_l\right)^2\right)-\tilde{\epsilon}_\lambda\left(-\left(\mathbf{k}_1+\sum_{l=1}^{i}\mathbf{q}_l\right)^2\right)}\\ &\left.\times\,x_i^{\tilde{\epsilon}_\lambda\left(-\left(\mathbf{k}_1-\mathbf{q}+\sum_{l=1}^{i-1}\mathbf{q}_l\right)^2\right)-\tilde{\epsilon}_\lambda\left(-\left(\mathbf{k}_1-\mathbf{q}+\sum_{l=1}^{i}\mathbf{q}_l\right)^2\right)}\right\}x^{-\tilde{\epsilon}_\lambda(-\mathbf{k}_1^2)-\tilde{\epsilon}_\lambda\left(-(\mathbf{k}_1-\mathbf{q})^2\right)}, \quad (3.92)\end{aligned}$$

where $\mathbf{q}_0 = 0$ and

$$\mathcal{K}(\mathbf{k}_1,\mathbf{k}_2,\mathbf{q}) = \frac{1}{2\pi}\frac{\eta(\mathbf{k}_1)}{\eta(\mathbf{k}_2)\eta(\mathbf{k}_2-\mathbf{k}_1)}\left[1+\frac{\eta(\mathbf{k}_1-\mathbf{q})\eta(\mathbf{k}_2)-\eta(\mathbf{q})\eta(\mathbf{k}_2-\mathbf{k}_1)}{\eta(\mathbf{k}_2-\mathbf{q})\eta(\mathbf{k}_1)}\right] \quad (3.93)$$

The regularization of infrared divergences is identical to the forward scattering case, with a unique infrared regulator λ. Clearly the $|q| \to 0$ limit of Eq. (3.92) corresponds to Eq. (3.89). We are now ready to present the numerical results for

the evaluation of both functions in Eqs. (3.89) and (3.92). But before this let us explain in more detail the effective reggeon diagrams used to write our Monte Carlo solution.

Monte Carlo structure & effective Feynman rules

Eq. (3.92) has an iterative structure that arises directly from eq. (3.87), as shown diagrammatically in fig. 3.13. Once we have this expression it will be very easy to find a direct connection to the ladder diagram given in fig. 3.14 and construct some simple effective Feynman rules that could be used to build a Monte Carlo code to generate a gluon ladder at any order of accuracy given the expression for the gluon trajectory and the real contribution to the BFKL kernel. In order to have a more clear understanding of the kinematics involved we find it useful to rewrite eq. (3.92) in terms of its rapidity Y instead of the x variable, by making the change of variables $y = \ln(1/x)$, finding

$$\begin{aligned}\mathcal{F}(\mathbf{k}_1,\mathbf{k}_2,\mathbf{q},Y) =& \Bigg\{\delta^{(2)}(\mathbf{k}_1-\mathbf{k}_2) + \sum_{n=1}^{\infty}\prod_{i=1}^{n}\int \mathrm{d}^2\mathbf{q}_i\,\mathcal{K}\left(\mathbf{k}_1+\sum_{l=0}^{i-1}\mathbf{q}_l,\mathbf{k}_1+\sum_{l=1}^{i}\mathbf{q}_l,\mathbf{q}\right)\\ &\times\theta(\mathbf{q}_i^2-\lambda^2)\delta^{(2)}\left(\mathbf{k}_1+\sum_{l=1}^{n}\mathbf{q}_l-\mathbf{k}_2\right)\\ &\times\int_0^{y_{i-1}}\mathrm{d}y_i\,\mathrm{e}^{-\left(\tilde{\epsilon}_\lambda\left(-\left(\mathbf{k}_1+\sum_{\mathrm{l}=1}^{\mathrm{i}-1}\mathbf{q}_\mathrm{l}\right)^2\right)-\tilde{\epsilon}_\lambda\left(-\left(\mathbf{k}_1+\sum_{\mathrm{l}=1}^{\mathrm{i}}\mathbf{q}_\mathrm{l}\right)^2\right)\right)\mathrm{y_i}}\\ &\times\mathrm{e}^{-\left(\tilde{\epsilon}_\lambda\left(-\left(\mathbf{k}_1-\mathbf{q}+\sum_{\mathrm{l}=1}^{\mathrm{i}-1}\mathbf{q}_\mathrm{l}\right)^2\right)-\tilde{\epsilon}_\lambda\left(-\left(\mathbf{k}_1-\mathbf{q}+\sum_{\mathrm{l}=1}^{\mathrm{i}}\mathbf{q}_\mathrm{l}\right)^2\right)\right)\mathrm{y_i}}\Bigg\}\mathrm{e}^{\left(\tilde{\epsilon}_\lambda(-\mathbf{k}_1^2)+\tilde{\epsilon}_\lambda\left(-(\mathbf{k}_1-\mathbf{q})^2\right)\right)\mathrm{Y}}.\end{aligned} \tag{3.94}$$

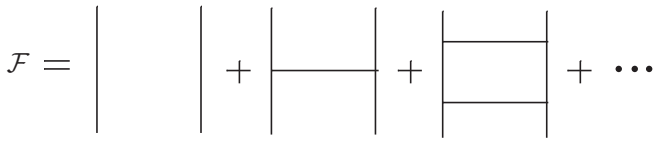

Figure 3.13: Diagrammatic iterative structure of the gluon Green's function.

Let us now take a careful look to fig. 3.14 and compare it to eq. (3.94). It is possible to check how the following structure can be assigned to each of the components of the ladder in order to be able to compute the whole iterative equation for the gluon Green's function:

1. t-channel reggeized gluon located between the i-th and the $i+1$ real emissions: its effective Feynman rule is given by

$$\mathrm{e}^{-\tilde{\epsilon}_\lambda\left(-\left(\mathbf{k}_1+\sum_{\mathrm{l}=1}^{\mathrm{i}}\mathbf{q}_\mathrm{l}\right)^2\right)(\mathrm{y_{i+1}}-\mathrm{y_i})}\times\mathrm{e}^{-\tilde{\epsilon}_\lambda\left(-\left(\mathbf{k}_1-\mathbf{q}+\sum_{\mathrm{l}=1}^{\mathrm{i}}\mathbf{q}_\mathrm{l}\right)^2\right)(\mathrm{y_{i+1}}-\mathrm{y_i})}$$

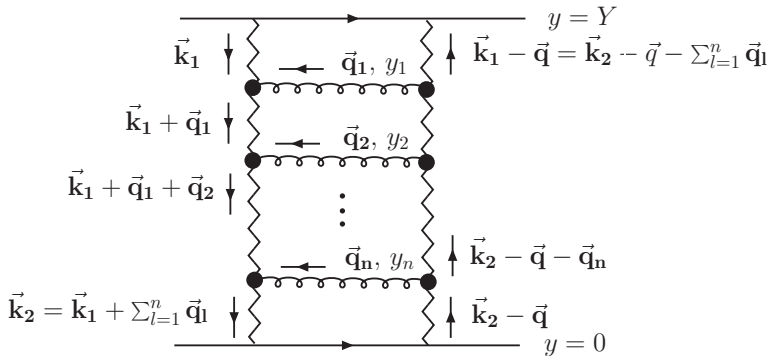

Figure 3.14: Gluon ladder used for the iterative equation (3.92).

The gluon trajectory or reggeized gluon propagator can be understood from this analysis as a form factor that controls the probability of no emission of a gluon in the rapidity range (y_i, y_{i+1}).

2. s-channel propagator for the i-th emitted gluon: its weight is simply given by the real emission part of the kernel. In our case,

$$\mathcal{K}\left(\mathbf{k}_1 + \sum_{l=0}^{i-1} \mathbf{q}_l, \mathbf{k}_1 + \sum_{l=1}^{i} \mathbf{q}_l, \mathbf{q}\right)$$

This rule goes together with an overall integration over the s-channel 2-dimensional phase-space: $\int \mathrm{d}^2\mathbf{q}_i\, \theta(\mathbf{q}_i^2 - \lambda^2)$, where lambda can be understood as a resolution scale or gluon mass.

3. Finally, we need to take into account the (ordered) integration over rapidity, $\int_0^{y_{i-1}} \mathrm{d}y_i$, and the conservation of transverse momentum, given by the delta function (see fig. 3.14)

$$\delta^2\left(\mathbf{k}_1 + \sum_{l=1}^{n} \mathbf{q}_l - \mathbf{k}_2\right) .$$

As we mentioned before, the interesting point of these rules is that they are generic. We will see in section 3.3.1 how the very same method can be used to build a Monte Carlo code for the non-forward NLL BFKL equation by simply modifying the trajectory and kernel.

Let us now proceed with a numerical analysis of the gluon Green's function in the forward case.

Numerical analysis of the gluon Green's function [18]

Let us present our numerical analysis for the dependence of the gluon Green's function on the x variable and its collinear behavior in the transverse momentum scales given for different values of the momentum transfer, comparing the results obtained with and without running effects.

Fig. 3.15 shows the evolution of the gluon Green's function with x for $\bar{\alpha}_s = 0.2$, $|\mathbf{k}_1| = 10\,\mathrm{GeV}$, $|\mathbf{k}_2| = 15\,\mathrm{GeV}$ and $x > 0.0003$. We present results for different values of the momentum transfer. It can be seen in both the case with fixed coupling (left figure) and with running (right figure) that the growth of the function as x decreases is more pronounced for small $\mathbf{q}$. However, with running coupling we have to go to smaller values of x to make it manifest, since it seems that the Green's function for this case is less affected by changes of $\mathbf{q}$ than in the fixed coupling configuration. Another effect observed is the reduction of the growth of the Green's function as x goes to zero when the running of the coupling is introduced. In fact, by looking not only at fig. 3.15 but also at figs. 3.16 and 3.17 we conclude that the reduction of the growth of the solution with the introduction of the running of the coupling in a way compatible with bootstrap to all orders is a general feature.

We can delve into the effect of the momentum transfer on the Green's function by looking into the collinear regions where $|\mathbf{k}_1|/|\mathbf{k}_2|$ is very different from unity. Let us for this purpose fix $|\mathbf{k}_2| = 20\,\mathrm{GeV}$, and study the solution to our equation as a function of $|\mathbf{k}_1|$ for fixed and running couplings, with different values of x. Fig. 3.16 compares the results obtained for fixed coupling at a relatively large x value, $x = 0.135$ (left figure) and at a low one of 0.018 (right). When the rapidity is small enough (corresponding to large values of x) to produce soft gluon emission the gluon Green's function has a Dirac delta behavior picked at $|\mathbf{k}_1| = |\mathbf{k}_2|$ due to momentum conservation. However, as the rapidity increases (or the x decreases) more soft gluon emissions are emitted, decorrelating the external systems connected by the gluon ladder and therefore smoothing the curve, as it can be seen in the comparative figures. Following the same reasoning, it is not surprising that the case for $x = 0.018$ (bigger rapidity and energy) is more sensitive to changes in transverse momentum than the case with $x = 0.135$. It is a general feature of these plots that the dependence on $\mathbf{q}$ is strongest in the region $|\mathbf{k}_1| \ll |\mathbf{k}_2|$.

Figure 3.17 shows the same analysis as fig. 3.16 but including the running of the coupling. It can be seen how the running completely eliminates any effect of introducing the momentum transfer for $x = 0.135$ and $\mathbf{q}$ from zero up to 6 GeV. We needed to reduce the value of x by one order of magnitude in order to start

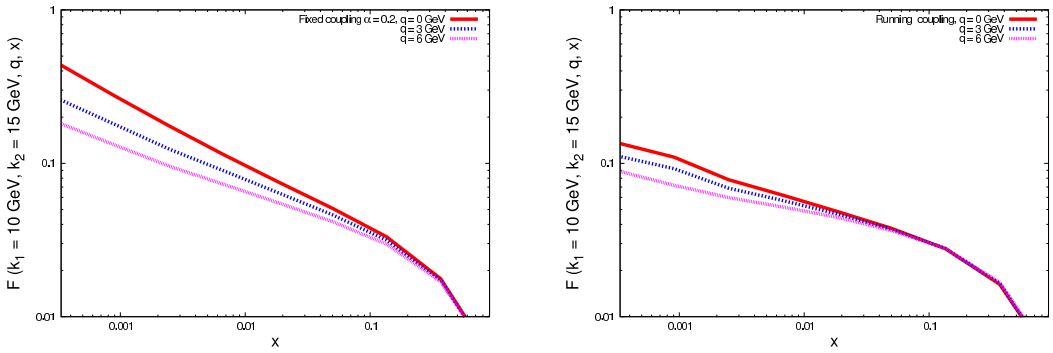

Figure 3.15: Evolution of the gluon Green's function with x, for fixed values of the transverse momenta with fixed (left) and running (right) coupling.

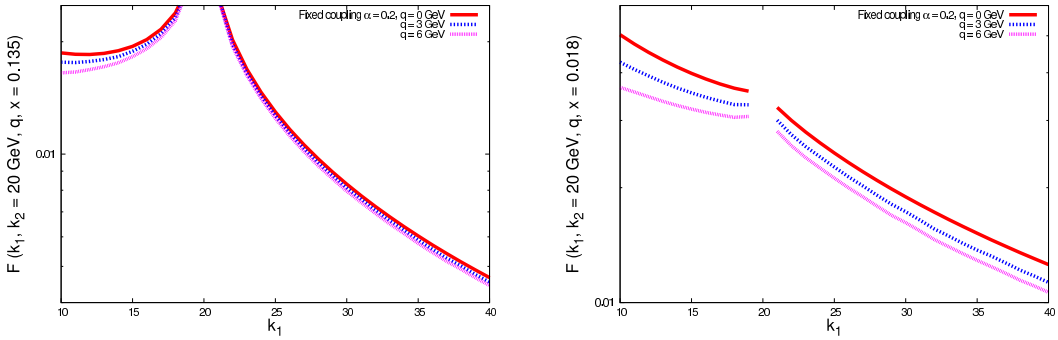

Figure 3.16: Collinear behavior of the gluon Green's function for fixed values of one transverse momentum, fixed coupling and $x = 0.135$ (left) and $x = 0.018$ (right).

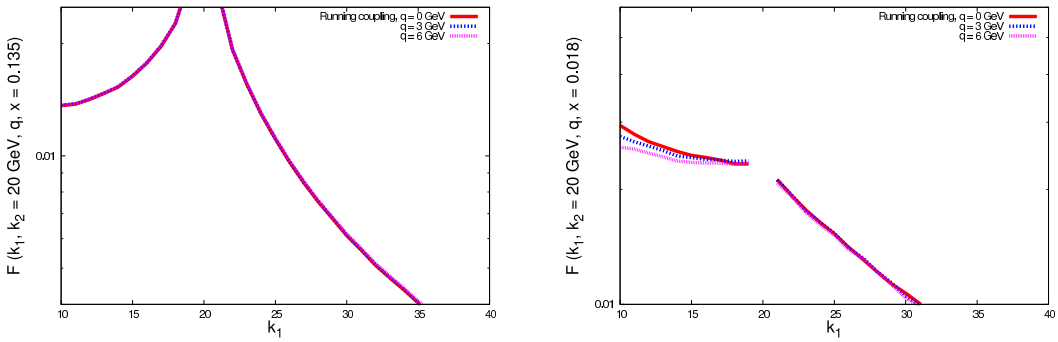

Figure 3.17: Collinear behaviour of the gluon Green's function for fixed values of one transverse momentum, running coupling and $x = 0.135$ (left), $x = 0.018$ (right).

finding a decrease of the Green function as $\mathbf{q}$ increases, for $|\mathbf{k}_1| < |\mathbf{k}_2|$, as in the fixed coupling case, as it is shown in the right figure.

Diffusion

A way to understand the importance of accounting for running coupling effects in the gluon ladder is given by the so-called diffusion pattern [69]. Consider any rung of the ladder. If it is close to one the (hadronic) edges, the integral over transverse momentum will be dominated by the contribution of the integrand around the typical hadronic momentum, of the size of the hadron and therefore close to the confinement scale. However, while increasing the number of soft gluon emissions between the hadron and the selected rung the integral will have more and more contributions from the intermediate transverse momenta. This is a diffusion effect that can be formally described as follows: consider the gluon Green's function $\mathcal{F}(\mathbf{k}_1, \mathbf{k}_2, \mathbf{q}, s)$ and a rung of the ladder with transverse momentum $\mathbf{k}$. It can be checked that when $s \to \infty$ the function $\Phi(y, \tau) = \sqrt{\mathbf{k}_1^2 \mathbf{k}_2^2}\, \mathcal{F}(\mathbf{k}_1, \mathbf{k}_2, \mathbf{q}, \hat{s})$ satisfies the diffusion equation

$$\frac{\partial \Phi(y,\tau)}{\partial y} = a\, \Phi(y,\tau) + b\, \frac{\partial^2 \Phi(y,\tau)}{\partial \tau^2} \,, \tag{3.95}$$

where the quantities $y = \ln(s/\mathbf{k}^2)$ and $\tau = \ln(\mathbf{k}_1/\mathbf{k}_2)$ have been introduced.

Since we have full access to the exclusive information of all momenta configurations in the gluon ladder we can proceed to investigate the diffusion cigar, also known as "Bartels cigar" –named after one of its two inventors [69]–. By looking at eq. (3.95), it is natural to present diffusion in terms of the mean value of variable $\tau = \ln < \mathbf{k}^2 > /(\mathrm{GeV}^2)$ as a function of the rapidity $\ln(1/x)$ along the ladder[12]. The way to do it is to numerically solve the BFKL iterative equation as given in eqs. (3.89,3.92) for the forward/non-forward cases with each rung labeled by $\{\mathbf{k}_i, y_i\}$ and study the evolution of τ and the weight of each configuration. A usual way of defining the standard deviation to the IR (σ_2) and to the UV (σ_1) is

$$\begin{aligned}
\sigma_1(\ln(1/x)) &= \frac{2\int_{\langle\tau\rangle(\ln(1/x))}^{\infty} \mathrm{d}\tau\, (\tau - \langle\tau\rangle(\ln(1/x)))^2\, \mathcal{F}(\mathbf{k}_1, \mathbf{k}_2, \mathbf{q}, \hat{s})}{\int_0^{\infty} \mathrm{d}\tau \mathcal{F}(\mathbf{k}_1, \mathbf{k}_2, \mathbf{q}, \hat{s})} \,, \\
\sigma_2(\ln(1/x)) &= \frac{2\int_0^{\langle\tau\rangle(\ln(1/x))} \mathrm{d}\tau\, (\tau - \langle\tau\rangle(\ln(1/x)))^2\, \mathcal{F}(\mathbf{k}_1, \mathbf{k}_2, \mathbf{q}, \hat{s})}{\int_0^{\infty} \mathrm{d}\tau \mathcal{F}(\mathbf{k}_1, \mathbf{k}_2, \mathbf{q}, \hat{s})} \,.
\end{aligned}$$

[12] Another usual way to present diffusion is in terms of the mean value of the transverse momentum along the ladder, $\langle \mathbf{k}^2 \rangle$, plus/minus the standard deviation [13, 67, 68, 70].

Let us present our numerical results. Fig. 3.18 shows the effect of introducing a non-zero momentum transfer for fixed coupling (left) and running coupling (right) cases and for $x = 0.37$ and $\bar{\alpha}_s = 0.2$. It can be seen how the momentum transfer acts as an effective IR cutoff, reducing the diffusion to the IR as $\mathbf{q}$ increases and leaving the UV one stable. The figures show a smaller suppression of the IR diffusion in the setup with a running coupling as $\mathbf{q}$ increases whereas the diffusion to the UV is suppressed with respect to the fixed coupling case, independently of de value of $\mathbf{q}$.

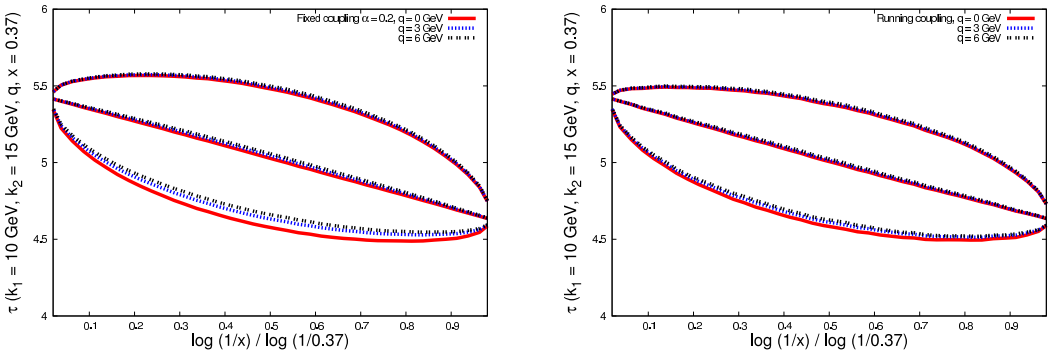

Figure 3.18: Distribution of the transverse momenta in the internal propagator of the gluon ladder for a fixed (left) and running (right) coupling and a large value of x.

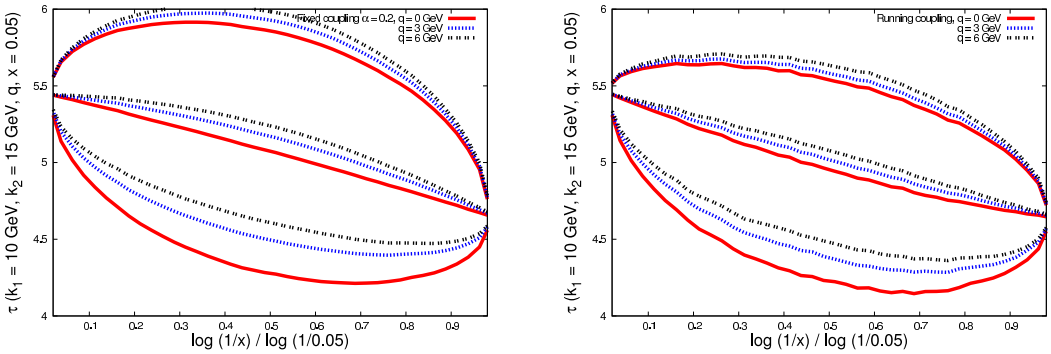

Figure 3.19: Distribution of the transverse momenta in the internal propagator of the gluon ladder for a fixed (left) and running (right) coupling and a small value of x.

The same analysis is done in fig. 3.19 for a smaller value of x. In this case the spread in transverse momentum in the internal gluon propagators is much

bigger, specially for the fixed coupling case (left figure). The effect of increasing the momentum transfer on the diffusion picture is double, it strongly suppresses the evolution into the IR but at the same time the UV one gets enhanced. In some sense, in the UV region a large momentum transfer is "pushing" the gluon momenta to live in more perturbative regions of phase space. The figures show how the diffusion to the UV is reduced in the case with a running coupling, being in this case the IR region a bit less sensitive to running coupling effects than for bigger values of Bjorken x.

Also, from the comparison of figs. 3.18 and 3.19 we observe how as the value of x gets smaller the influence of introducing a non-zero momentum transfer is larger, always "pulling" the Bartels cigar towards more perturbative regions in both, the fixed and running coupling scenarios.

Final remarks & future work

In this last subsection we have studied the LO BFKL equation incorporating the running of the coupling in a way compatible with bootstrap to all orders in perturbation theory. In order to find a solution we have written the equation in an iterative form in transverse momentum space which could be finally expressed in terms of integrals over transverse momenta and rapidity of the internal gluon propagators and then evaluated using Monte Carlo integration techniques. The advantage of this method of calculation to previous analysis in the literature is that we can solve the new BFKL equation exactly, with no asymptotic approximations. Our next goal will be to integrate these results with suitable impact factors in order to gauge the phenomenological relevance of the results here presented. Good candidates to be first tested using these Monte Carlo techniques are the observables presented in chapters 4 and 5.

3.3 NLL corrections to the BFKL equation

The final computation of the next-to-leading logarithmic (NLL) corrections to the BFKL equation was given by Fadin and Lipatov in 1998 in [71]. Needed ingredients were the two-loop gluon Regge trajectory [72, 73], the one-loop correction to the Lipatov effective vertex introduced in eq. (3.36) [74] and the -tree level- vertices for two gluon emission and for the production of a quark-antiquark pair within the gluon ladder [75–78].

One of the most relevant features of the NLL contributions to the BFKL equation is the inclusion of the running of the coupling. Unfortunately, the terms that account for the running, that is, the terms proportional to β_0, introduce a logarithmic dependence in momentum space representation that makes the numerical study of the equation much harder than in the leading-logarithmic approach [79]. An additional problem is that the NLL corrections to the gluon Green's function are known to be very large and negative [80], spoiling the convergence of the perturbative series and leading to non-physical (negative) cross sections. A way to improve the convergence of the series consists on a resummation of the problematic logarithms [14,15,81–83], as we will explain in sec. 3.4. Other approaches can be found in the literature [55, 56, 84–90].

3.3.1 Monte Carlo calculation of NLL BFKL evolution

In this subsection an iterative equation similar to eq. (3.92) will be given at NLLA. We will extract from its intrinsic structure some effective Feynman rules for the gluon ladder specially suited for the construction of a Monte Carlo code [67, 91, 92].

Forward case at NLL accuracy

Our starting point is the original NLL BFKL equation developed by Lipatov and Fadin in [71]. Other similar approaches and further analysis to the equation at this order of accuracy can be found in [67, 92–94]. Directly following the results of given in [67, 92], once we have introduced the cutoff λ we already used for the LL case and needed now to cancel the ϵ poles that appear in dimensional regularization, the NLL BFKL equation reads

$$\begin{aligned}\left(\omega-\epsilon_\lambda\left(-\mathbf{k}_a^2\right)\right) f_\omega\left(\mathbf{k}_a,\mathbf{k}_b\right) &= \delta^{(2)}\left(\mathbf{k}_a-\mathbf{k}_b\right) \\ &+\int d^2\mathbf{k}\left(\frac{1}{\pi\mathbf{k}^2}\xi\left(\mathbf{k}^2\right)\theta\left(\mathbf{k}^2-\lambda^2\right)+\widetilde{\mathcal{K}}_r\left(\mathbf{k}_a,\mathbf{k}_a+\mathbf{k}\right)\right) f_\omega\left(\mathbf{k}_a+\mathbf{k},\mathbf{k}_b\right),\end{aligned} \tag{3.96}$$

with

$$\xi\left(\mathbf{k}^2\right) = \bar{\alpha}_s(\mu_R) + \frac{\bar{\alpha}_s^2(\mu_R)}{4}\left[\frac{4}{3} - \frac{\pi^2}{3} + \frac{5}{3}\frac{\beta_0}{N_c} - \frac{\beta_0}{N_c}\ln\left(\frac{\mathbf{k}^2}{\mu_R^2}\right)\right] \tag{3.97}$$

and

$$\begin{aligned}
\widetilde{\mathcal{K}}_r\left(\mathbf{k}_1,\mathbf{k}_2\right) = \frac{\bar{\alpha}_s^2(\mu_R)}{4\pi}\Bigg\{&\left(1+\frac{n_f}{N_c^3}\right)\frac{\left(3(\mathbf{k}_1\cdot\mathbf{k}_2)^2-2\mathbf{k}_1^2\mathbf{k}_2^2\right)}{16\mathbf{k}_1^2\mathbf{k}_2^2}\left(\frac{2}{\mathbf{k}_1^2}+\frac{2}{\mathbf{k}_2^2}\right.\\
&+\left(\frac{1}{\mathbf{k}_2^2}-\frac{1}{\mathbf{k}_1^2}\right)\ln\frac{\mathbf{k}_1^2}{\mathbf{k}_2^2}\Bigg)+\frac{2(\mathbf{k}_1^2-\mathbf{k}_2^2)}{(\mathbf{k}_1-\mathbf{k}_2)^2(\mathbf{k}_1+\mathbf{k}_2)^2}\left(\frac{1}{2}\ln\frac{\mathbf{k}_1^2}{\mathbf{k}_2^2}\ln\frac{\mathbf{k}_1^2\mathbf{k}_2^2(\mathbf{k}_1-\mathbf{k}_2)^4}{(\mathbf{k}_1^2+\mathbf{k}_2^2)^4}\right.\\
&\left.+\left(\int_0^{-\mathbf{k}_1^2/\mathbf{k}_2^2}-\int_0^{-\mathbf{k}_2^2/\mathbf{k}_1^2}\right)du\frac{\ln(1-u)}{u}\right)-\frac{1}{(\mathbf{k}_1-\mathbf{k}_2)^2}\ln^2\frac{\mathbf{k}_1^2}{\mathbf{k}_2^2}\\
&-\left(3+\left(1+\frac{n_f}{N_c^3}\right)\left(1-\frac{(\mathbf{k}_1^2+\mathbf{k}_2^2)^2}{8\mathbf{k}_1^2\mathbf{k}_2^2}-\frac{(2\mathbf{k}_1^2\mathbf{k}_2^2-3\mathbf{k}_1^4-3\mathbf{k}_2^4)}{16\mathbf{k}_1^4\mathbf{k}_2^4}(\mathbf{k}_1\cdot\mathbf{k}_2)^2\right)\right)\\
&\times\int_0^\infty dx\frac{1}{\mathbf{k}_1^2+x^2\mathbf{k}_2^2}\ln\left|\frac{1+x}{1-x}\right|\\
&-\left(1-\frac{(\mathbf{k}_1^2-\mathbf{k}_2^2)^2}{(\mathbf{k}_1-\mathbf{k}_2)^2(\mathbf{k}_1+\mathbf{k}_2)^2}\right)\left(\left(\int_0^1-\int_1^\infty\right)dz\frac{1}{(\mathbf{k}_2-z\mathbf{k}_1)^2}\ln\frac{(z\mathbf{k}_1)^2}{\mathbf{k}_2^2}\right)\Bigg\}.
\end{aligned} \tag{3.98}$$

In eq. (3.96) the NLL kernel has been split into its virtual and real emission parts. The real contribution has to be integrated over the full phase space whereas the virtual piece is given by the Regge trajectory, which in $\overline{\text{MS}}$ is given by

$$\epsilon_\lambda\left(-\mathbf{k}_a^2\right) = -\xi\left(|\mathbf{q}|\,\lambda\right)\ln\frac{\mathbf{q}^2}{\lambda^2} + \bar{\alpha}_s^2(\mu_R)\frac{3}{2}\zeta(3), \tag{3.99}$$

where $\xi(\mathbf{k}^2)$ has been defined in eq. (3.97). Equivalently to what we did for the LL case in section 3.2.2, we can write the following iterative representation of the gluon Green's function:

$$\begin{aligned}
f(\mathbf{k}_a,\mathbf{k}_b,Y) = \exp\left(\epsilon_\lambda\left(-\mathbf{k}_a^2\right)Y\right)\Bigg\{&\delta^{(2)}(\mathbf{k}_a-\mathbf{k}_b)\\
&+\sum_{n=1}^{\infty}\prod_{i=1}^{n}\int \mathrm{d}^2\mathbf{k}_i\left[\frac{\theta\left(\mathbf{k}_i^2-\lambda^2\right)}{\pi\mathbf{k}_i^2}\xi\left(\mathbf{k}_i^2\right)+\widetilde{\mathcal{K}}_r\left(\mathbf{k}_a+\sum_{l=0}^{i-1}\mathbf{k}_l,\mathbf{k}_a+\sum_{l=1}^{i}\mathbf{k}_l\right)\right]\\
&\times\int_0^{y_{i-1}}\mathrm{d}y_i\,\exp\left[\left(\epsilon_\lambda\left(-\left(\mathbf{k}_a+\sum_{l=1}^{i}\mathbf{k}_l\right)^2\right)\right.\right.\\
&\left.\left.-\epsilon_\lambda\left(-\left(\mathbf{k}_a+\sum_{l=1}^{i-1}\mathbf{k}_l\right)^2\right)\right)y_i\right]\delta^{(2)}\left(\sum_{l=1}^{n}\mathbf{k}_l+\mathbf{k}_a-\mathbf{k}_b\right)\Bigg\}.
\end{aligned} \tag{3.100}$$

Also in section 3.2.2 we learned how to construct eq. (3.100) directly from eq. 3.96,

using the effective Feynman rules extracted from both eq. (3.94) and fig. 3.14 and taking the limit $\mathbf{q} \to 0$. Just to show the simplicity of the method, let us explicitly write down the needed replacements to get the correct result in this case compared to the LL one with running coupling:

$$\begin{aligned}
&\mathbf{q} \to 0 \\
&\tilde{\epsilon}_\lambda(-\mathbf{k}_a^2) \to \epsilon_\lambda(-\mathbf{k}_a^2) \\
&\theta(\mathbf{k}_i^2 - \lambda^2)\mathcal{K}(\mathbf{k}_a + \sum_{l=0}^{i-1}\mathbf{k}_l,\, \mathbf{k}_a + \sum_{l=1}^{i}\mathbf{k}_l,\, \mathbf{q}) \\
&\qquad\qquad \to \frac{\theta\left(\mathbf{k}_i^2 - \lambda^2\right)}{\pi \mathbf{k}_i^2}\xi\left(\mathbf{k}_i^2\right) + \widetilde{\mathcal{K}}_r\left(\mathbf{k}_a + \sum_{l=0}^{i-1}\mathbf{k}_l, \mathbf{k}_a + \sum_{l=1}^{i}\mathbf{k}_l\right) \quad ,
\end{aligned}$$

where $\tilde{\epsilon}_\lambda$ and $\mathcal{K}$ were defined in eqs. (3.85,3.93), respectively.

Non-forward NLL BFKL kernel

The complete non-forward NLL BFKL kernel was first given in [95, 96], with the addition of the contribution of the two-gluon production. A numerical solution for it can be found in [66] for the simpler case of $\mathcal{N} = 4$ supersymmetry in the adjoint representation. The great advantage of this theoretical corner is that very important cancellations between gluon, scalar and gluino contributions take place [97], leading to a much simpler final expression, compared to the non-supersymmetric counterpart. Another advantage of it is the lack of running coupling effects, appearing in QMRK as logs of transverse momentum accompanying the terms proportional to β_0.

The equation solved numerically in [66] was

$$\begin{aligned}
&\left\{\omega - \left(\frac{\bar{\alpha}}{2}\left(1 - \frac{\zeta_2}{2}\bar{\alpha}\right)\ln\left(\frac{\mathbf{k}_a^2 \mathbf{k}_a'^2}{\mathbf{q}^2\lambda^2}\right) + \frac{3}{4}\zeta_3\bar{\alpha}^2\right)\right\} f_\omega\left(\mathbf{k}_a, \mathbf{k}_b, \mathbf{q}\right) \;=\; \delta^{(2)}\left(\mathbf{q}_1 - \mathbf{q}_2\right) \\
&+ \int d^2\mathbf{k}\left\{\frac{\bar{\alpha}}{4}\left(1 - \frac{\zeta_2}{2}\bar{\alpha}\right)\frac{\theta\left(\mathbf{k}^2 - \lambda^2\right)}{\pi\mathbf{k}^2}\left(1 + \frac{\mathbf{k}_a'^2(\mathbf{k}_a + \mathbf{k})^2 - \mathbf{q}^2\mathbf{k}^2}{(\mathbf{k}_a' + \mathbf{k})^2\mathbf{k}_a^2}\right) + \Phi\left(\mathbf{k}_a, \mathbf{k}_a + \mathbf{k}\right)\right\} \\
&\qquad\qquad \times \frac{\mathbf{k}_a^2}{\left(\mathbf{k}_a + \mathbf{k}\right)^2} f_\omega\left(\mathbf{k}_a + \mathbf{k}, \mathbf{k}_b, \mathbf{q}\right) \quad , \qquad (3.101)
\end{aligned}$$

where $\mathbf{k}_a' \equiv \mathbf{k}_a - \mathbf{q}$. The function $\Phi(\mathbf{k}, \mathbf{q})$ can be found in [66]. What is interesting to see is that directly from this expression the iterative equation for the Monte

Carlo code could be given and used, since the equation is already of the form

$$(\omega-\omega_0(\mathbf{k}_a,\mathbf{q}))f_\omega(\mathbf{k}_a,\mathbf{k}_b,\mathbf{q}) = \delta^{(2)}\left(\mathbf{q}_1-\mathbf{q}_2\right)+\int \mathrm{d}^2\mathbf{k}\, \mathcal{K}_r(\mathbf{k}_a,\mathbf{k},\mathbf{q})f_\omega(\mathbf{k}_a+\mathbf{k},\mathbf{k}_b,\mathbf{q})\ , \tag{3.102}$$

where ω_0 is the Regge trajectory and $\mathcal{K}^r$ the contribution to the kernel accounting for real emissions.

The complete set of equations for the QCD sector of the theory can be found in [95, 96].

3.3.2 Analytic solution and the treatment of the running of the coupling

The action of the NLL BFKL kernel on the LL eigenfunctions including azimuthal angle dependence was first calculated by Kotikov and Lipatov [94]:

$$\begin{aligned}\mathcal{K}(n,\nu;n',\nu') \equiv \langle n,\nu\,|\,\hat{\mathcal{K}}|\,\nu',n'\rangle &= \int \mathrm{d}^2\mathbf{k}_1\,\mathrm{d}^2\mathbf{k}_2\,\langle n,\nu\,|\,\mathbf{k}_1\rangle\langle\mathbf{k}_1\,|\,\hat{\mathcal{K}}|\,\mathbf{k}_2\rangle\langle\mathbf{k}_2\,|\,n',\nu'\rangle \\ &= \frac{1}{2\pi^2}\int \mathrm{d}^2\mathbf{k}_1\bar{\alpha}_s(\mathbf{k}_1^2)\,(\mathbf{k}_1^2)^{i(\nu'-\nu)-1}\mathrm{e}^{\mathrm{i}(\mathrm{n}'-\mathrm{n})\theta_1}\Bigg\{\chi_0(\mathrm{n}',\nu')+\bar{\alpha}_\mathrm{s}\chi_1(\mathrm{n}',\nu') \\ &\quad+\bar{\alpha}_s^2\frac{\beta_0}{8N_c}\left[\psi'\left(\frac{1+n'}{2}+i\nu\right)-\psi'\left(\frac{1+n'}{2}-i\nu\right)\right]\Bigg\}\ ,\end{aligned} \tag{3.103}$$

with

$$\chi_0(n,\gamma) = 2\Psi(1)-\Psi\left(1+\gamma+n/2\right)--\Psi\left(1-\gamma+n/2\right)\ , \tag{3.104}$$

$$\begin{aligned}\chi_1(n,\gamma) =&(4-\pi^2+5\beta_0/N_c)/12\chi_0(n,\gamma)+\frac{3}{2}\zeta(3)-\frac{\beta_0}{8N_3}\chi_0^2(n,\gamma) \\ &+\frac{1}{4}\left[\Psi''\left(\gamma+n/2\right)+\Psi''\left(1-\gamma+n/2\right)-2\phi(n,\gamma)-2\phi(n,1-\gamma)\right] \\ &-\frac{\pi^2\cos(\pi\gamma)}{4\sin^2(\pi\gamma)(1-2\gamma)}\Bigg\{\left[3+\left(1+\frac{n_f}{N_c^3}\right)\frac{2+3\gamma(1-\gamma)}{(3-2\gamma)(1+2\gamma)}\right]\delta_{n,0} \\ &-\left(1+\frac{n_f}{N_c^3}\right)\frac{\gamma(1-\gamma)}{2(3-2\gamma)(1+2\gamma)}\delta_{n,2}\Bigg\}\end{aligned} \tag{3.105}$$

and

$$\begin{aligned}\phi(n,\gamma) = \sum_{k=0}^{\infty}\frac{(-1)^{k+1}}{k+\gamma+n/2}\Bigg(&\psi'(k+n+1)-\psi'(k+1) \\ &+(-1)^{k+1}\left[\beta'(k+n+1)+\beta'(k+1)\right]+\frac{\psi(k+1)-\psi(k+n+1)}{k+\gamma+n/2}\Bigg)\ ,\end{aligned} \tag{3.106}$$

$$\beta'(\gamma) = \frac{1}{4}\left[\psi'(1/2+\gamma/2) - \psi'(\gamma/2)\right]. \tag{3.107}$$

If we include the NLL contribution of the running of the coupling in eq. (3.103,

$$\bar{\alpha}_s(\mathbf{k}_1^2) \simeq \bar{\alpha}_s(\mu_R^2) - \bar{\alpha}_s^2(\mu_R^2)\frac{\beta_0}{4N_c}\log\left(\frac{\mathbf{k}_1^2}{\mu_R^2}\right), \tag{3.108}$$

we can rewrite the logarithmic term, together with the k-dependent part of the LL eigenfunction in such a way that the following replacement can be done,

$$\int \mathrm{d}^2\mathbf{k}_1 g(\mathbf{k}_1)\log(\mathbf{k}_1^2)(\mathbf{k}_1^2)^{i(\nu'-\nu)} = \int \mathrm{d}^2\mathbf{k}_1 g(\mathbf{k}_1)\,\frac{i}{2}\mathcal{D}(\nu,\nu')\,(\mathbf{k}_1^2)^{i(\nu'-\nu)}, \tag{3.109}$$

where $g(\mathbf{k}_1)$ is a function directly related to the kernel. The function $\mathcal{D}(\nu,\nu')$ has to be understood as a differential operator acting on ν-space (with $\gamma = 1/2 + i\nu$) which gives rise to the logarithm of transverse momentum that appears in the left hand side of eq. (3.109). There are different -mathematically equivalent- choices for this operator. One could think of a symmetric one, acting on both ν and ν',

$$\mathcal{D}(\nu,\nu') = \partial_\nu - \partial_{\nu'},$$

but it could also act only on one of the sides of the gluon ladder asymmetrically. Although the different choices are equivalent up to NLL accuracy, the higher order terms in the perturbative expansion lead to different numerical results. With the symmetric choice, the matrix element of the NLL kernel in the (n,ν)-space is given by

$$\begin{aligned}\mathcal{K}(n,\nu;n',\nu') = \Big\{&\bar{\alpha}_s\chi_0(n',\nu') + \bar{\alpha}_s^2\chi_1(n',\nu') \\ &+ \bar{\alpha}_s^2\frac{\beta_0}{8N_c}\left[\chi_0(i\partial_{\nu'} - i\partial_\nu + 2\log\mu_R^2) + i\partial_{\nu'}(\chi_0)\right]\Big\}\delta(\nu-\nu')\delta_{n,n'}.\end{aligned} \tag{3.110}$$

The first line of this equation is scale invariant, that is, it remains unchanged under the transformation $\gamma \to 1-\gamma$, whereas the second line, proportional to β_0, breaks it.

Action of the differential operator

Using the operator representation introduced in section 3.2.1 the gluon Green's function can be directly extracted from the BFKL equation in the following way:

$$\hat{f}_\omega = \left(\omega - \hat{\mathcal{K}}\right)^{-1} = \frac{1}{\omega}\sum_{j=0}^{\infty}\left(\frac{\hat{\mathcal{K}}}{\omega}\right)^j \;\Rightarrow\; \langle\hat{f}_\omega\rangle = \frac{1}{\omega}\sum_{j=0}^{\infty}\left(\frac{\langle\hat{\mathcal{K}}\rangle}{\omega}\right)^j, \tag{3.111}$$

with $\langle\hat{\mathcal{O}}\rangle \equiv \langle n,\nu|\,\hat{\mathcal{O}}\,|\nu',n'\rangle$. Following this notation, the proton structure function F_2 (see section 2.2) would be of the form

$$F_2 \propto \int \frac{\mathrm{d}\omega}{2\pi i}\int \mathrm{d}\nu\,\phi_{\gamma*}(\nu)\left[\frac{1}{\omega}\sum_{j=0}^{\infty}\left(\frac{\langle\hat{\mathcal{K}}\rangle}{\omega}\right)^j\right]\phi_P(\nu)\,\mathrm{e}^{\omega \mathrm{Y}}, \tag{3.112}$$

where we have made use of the k_T-factorization introduced in eq. (3.70). The objects $\phi_{\gamma*}$ and ϕ_P stand for the photon and proton impact factors, respectively. They were already introduced in the introductory chapter and will be analyzed in more detail in chapter 4.

At NLL accuracy the kernel can be written as $\hat{\mathcal{K}} = \bar{\alpha}_s\,\hat{\mathcal{K}}_0 + \bar{\alpha}_s^2\,\hat{\mathcal{K}}_1$, with

$$\begin{aligned}
\mathcal{K}_0 &\equiv \langle\hat{\mathcal{K}}_0\rangle = \tilde{\chi}_0\,\delta(\nu-\nu')\,\delta_{n,n'} \ \text{ and} \\
\mathcal{K}_1 &\equiv \langle\hat{\mathcal{K}}_1\rangle = \left\{\tilde{\chi}_1 + \frac{\beta_0}{8N_c}\tilde{\chi}_0\left[i\mathcal{D}(\nu,\nu') + \ln(\mu_R^2) + i\,\frac{\tilde{\chi}_0'}{\tilde{\chi}_0}\right]\right\}\delta(\nu-\nu')\,\delta_{n,n'}\,.
\end{aligned} \tag{3.113}$$

We have introduced the notation $\tilde{\chi} \equiv \chi(|n'|,\nu')$. The differential operator $\mathcal{D}(\nu,\nu')$ accounts for running coupling effects and breaks the scale invariance of the kernel. In other words, it introduces non-diagonal terms in the structure of the NLL kernel.

It is our aim in this section to develop a theoretical analysis of the action of the differential operator in its different representations to better gauge our uncertainties. It is important to have in mind that this theoretical uncertainty appeared as a consequence of trying to give an analytical expression to the NLL BFKL kernel in the Mellin space. If a Monte Carlo iterative code was used to numerically solve the equation directly in transverse momentum space, the running of the coupling would be treated exactly and no uncertainties of this type would appear. We will consider the three following options:

1. Symmetric choice: $\mathcal{D}(\nu,\nu') = \partial_\nu - \partial_{\nu'} \ \Leftrightarrow \ \mathcal{D}(\nu) = \overleftarrow{\partial}_\nu - \overrightarrow{\partial}_\nu$.
2. Operator acting on the proton side: $\mathcal{D}(\nu,\nu') = -2\partial_{\nu'} \Leftrightarrow \mathcal{D}(\nu) = -2\overrightarrow{\partial}_\nu$.
3. Operator acting on the photon side only: $\mathcal{D}(\nu,\nu') = 2\partial_\nu \ \Leftrightarrow \ \mathcal{D}(\nu) = 2\overleftarrow{\partial}_\nu$.

Symmetric choice

With the symmetric operator the $j-th$ term of the integrand of eq. (3.112) is of the form

$$\frac{1}{\omega^{j+1}}\Phi_{\gamma*}(\nu)(\mathcal{K}\cdot\mathcal{K}\cdot\mathcal{K}\cdots\mathcal{K})\Phi_P(\nu)\,\mathrm{e}^{\omega \mathrm{Y}}. \tag{3.114}$$

Each $\mathcal{K}$ will act not only on the impact factors but also on the other $\mathcal{K}$'s. However, the symmetric differential operator will cancel all contributions coming from $\mathcal{K}\cdot\mathcal{K}$ [98]:

$$\mathcal{K}(\overleftarrow{\partial}_\nu - \overrightarrow{\partial}_\nu)\,\mathcal{K} = 0\,. \tag{3.115}$$

The only remaining terms are $\partial_\nu\Phi_{\gamma*}(\nu)$ and $\partial_\nu\Phi_P(\nu)$. Precisely, we get

$$\Phi_{\gamma*}(\nu)(\overleftarrow{\partial}_\nu - \overrightarrow{\partial}_\nu)\Phi_P(\nu) = \Phi_{\gamma*}(\nu)\Phi_P(\nu)\,\partial_\nu \ln\left(\frac{\Phi_{\gamma*}(\nu)}{\Phi_P(\nu)}\right)\,, \tag{3.116}$$

yielding a set of diagonal terms that allow for the exponentiation of the whole kernel. We will come back to this result in chapter 4, with an extensive phenomenological study of the proton structure functions and comparison to the latest available experimental data.

Non-symmetric choices

Let us consider the first one, $\mathcal{D}(\nu) = -2\overleftarrow{\partial}_\nu$, being the reasoning for the second one equivalent. In this case the action of $\mathcal{K}$ on $\mathcal{K}$ does not cancel, so we need to truncate the perturbative series. At order $\mathcal{O}(\bar{\alpha}_s^2)$ we have

$$\langle\hat{f}_\omega^{\rm NLL}\rangle = \frac{1}{\omega-\bar{\alpha}_s\mathcal{K}_0} + \bar{\alpha}_s^2\frac{1}{\omega-\bar{\alpha}_s\mathcal{K}_0}\mathcal{K}_1\frac{1}{\omega-\bar{\alpha}_s\mathcal{K}_0} + \mathcal{O}(\bar{\alpha}_s^3)\,. \tag{3.117}$$

We can define A and B as

$$\begin{aligned} A &\equiv \chi_1 + \frac{\beta_0}{8N_c}\left(2\chi_0\ln(\mu_R^2) + i\chi_0'\right)\,, \\ B &\equiv i\frac{\beta_0}{4N_c}\chi_0\,, \end{aligned} \tag{3.118}$$

so that $\mathcal{K}_1 = A + B\overrightarrow{\partial}_\nu$. Eq.(3.117) then reads

$$\begin{aligned} \langle\hat{f}_\omega^{\rm NLL}\rangle &= \frac{1}{\omega-\bar{\alpha}_s\tilde{\chi}_0} + \bar{\alpha}_s^2\frac{1}{\omega-\bar{\alpha}_s\tilde{\chi}_0}(A+B\overrightarrow{\partial}_\nu)\frac{1}{\omega-\bar{\alpha}_s\tilde{\chi}_0} \qquad (3.119)\\ &= \frac{1}{\omega-\bar{\alpha}_s\tilde{\chi}_0} + \bar{\alpha}_s^2\left(\frac{1}{\omega-\bar{\alpha}_s\tilde{\chi}_0}\right)^2(A+B\overrightarrow{\partial}_\nu) + \bar{\alpha}_s^3\left(\frac{1}{\omega-\bar{\alpha}_s\tilde{\chi}_0}\right)^3 B\chi_0'\,, \end{aligned}$$

expression from which the action of $\langle\hat{f}_\omega^{\rm NLL}\rangle$ on the proton impact factor is

$$\begin{aligned} f_\omega^{\rm NLL}\Phi_P(\nu) = \Bigg\{ &\frac{1}{\omega-(\bar{\alpha}_s\tilde{\chi}_0 + \bar{\alpha}_s^2\left(A+B\partial_\nu\ln\phi_P(\nu)\right))} \\ &+ \bar{\alpha}_s^3\left(\frac{1}{\omega-\bar{\alpha}_s\tilde{\chi}_0}\right)^3 B\chi_0' + \text{h.o.}\Bigg\}\Phi_P(\nu)\,. \end{aligned} \tag{3.120}$$

Making use of the definition

$$\tilde{\mathcal{K}}(\nu) \equiv \bar{\alpha}_s^2 \left(A + B\partial_\nu \ln \phi_P(\nu)\right) \ , \tag{3.121}$$

the structure function would be given by

$$\begin{aligned} F_2 \ &\sim \ \int \frac{\mathrm{d}\omega}{2\pi i} \int \mathrm{d}\nu \left(\frac{Q/Q_0}{x}\right)^{\omega} \left(\frac{Q^2}{Q_0^2}\right)^{i\nu} \\ &\quad \Phi_{\gamma *}(\nu) \left[\frac{1}{\omega - \bar{\alpha}_s\tilde{\chi}_0 - \tilde{\mathcal{K}}(\nu)} + \bar{\alpha}_s^3 \left(\frac{1}{\omega - \bar{\alpha}_s\tilde{\chi}_0}\right)^3 B\tilde{\chi}_0'\right] \Phi_P(\nu) \\ &= \ \int \mathrm{d}\nu \left(\frac{Q/Q_0}{x}\right)^{\bar{\alpha}_s\tilde{\chi}_0} \left(\frac{Q^2}{Q_0^2}\right)^{i\nu} \\ &\quad \Phi_{\gamma *}(\nu)\, \Phi_P(\nu) \left[\left(\frac{Q/Q_0}{x}\right)^{\tilde{\mathcal{K}}(\nu)} + \bar{\alpha}_s^3\, B\, \tilde{\chi}_0' \frac{1}{2} \ln^2\left(\frac{Q/Q_0}{x}\right)\right] \ , \end{aligned} \tag{3.122}$$

where Q_0^2 is a non-perturbative scale of the typical size of the hadron coming from the specific model for the proton impact factor. The last term in the square brackets,

$$i\, \bar{\alpha}_s^3 \frac{\beta_0}{8N_c} \ln^2\left(\frac{Q/Q_0}{x}\right) \tilde{\chi}_0\, \tilde{\chi}_0' \ ,$$

is real, since $\tilde{\chi}_0'$ is purely imaginary and $\tilde{\chi}_0$ is real. This contributes with a triple pole in γ. However, one could write the leading order eigenfunction as

$$\chi_0(\gamma) = \chi_0(\gamma) - \frac{1}{\gamma} + \frac{1}{\gamma + \bar{\alpha}_s} + \mathcal{O}(\bar{\alpha}_s) \ ,$$

expression with which the product $\chi_0(\gamma)\chi_0'(\gamma)$ in the limit $\gamma \to 0$ would give

$$\chi_0(\gamma)\chi_0'(\gamma) \to -\frac{1}{\gamma^3} \ ,$$

leading to a large contribution of the form

$$-\frac{\beta_0}{8N_c} \ln^2\left(\frac{Q/Q_0}{x}\right) \ .$$

In the phenomenological analysis given in chapter 4 we will include just the symmetric choice. Nonetheless, the other two possibilities were also numerically investigated before getting any final results. It is noteworthy to say that acting only on the proton side was offering non-sense results whereas the other two cases were both equally reasonable, as one could expect.

Model for the running of the coupling

To model the running of the coupling in the infrared we can use a simple parametrization introduced by Webber in Ref. [99] which at low momentum scales is consistent with global data of infrared power corrections to perturbative observables (mainly related to jet event shapes). The relevant formula reads

$$\alpha_s(k) = \frac{4\pi}{\beta_0}\left(\frac{1}{\ln\frac{k^2}{\Lambda^2}} + \frac{125\left(\Lambda^2+4k^2\right)}{\left(\Lambda^2-k^2\right)\left(4+\frac{k^2}{\Lambda^2}\right)^4}\right), \tag{3.123}$$

which, for $\beta_0 = (11N_c - 2n_f)/3$, $n_f = 3$ and $\Lambda = 0.25\,\mathrm{GeV}$, gives $\alpha_s(91\mathrm{GeV}) = 0.118$. Its dependence on k is shown in fig. 3.20.

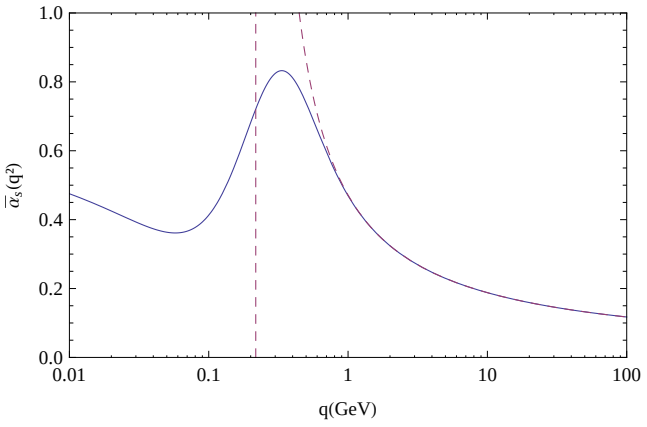

Figure 3.20: Model for the running of the coupling based on a fixed point in in the infrared (solid line) compared with the running coupling with Landau pole (dashed line).

Note that this is just a model to parametrize the infrared and therefore it is not unique. However, it is consistent with data and, as it can be seen in fig. 3.20, is different from the usual running coupling with Landau pole introduced in eq. (2.8) strictly in the IR, being the perturbative region safe from any changes.

Details about the parametrization can be found in [99].

3.4 Improving the collinear regions

The NLL gluon Green's function presents instabilities in the collinear region, where the two transverse momentum scales present at the edges of the gluon ladder are very different. The reason for this is the following: in the presence of two asymmetric external hard scales, the symmetric, Regge-like, energy scale

$s_0 = \sqrt{\mathbf{k}^2\mathbf{q}^2}$ present in the construction of the gluon ladder is not a natural scale anymore and it needs to be shifted to a DIS (asymmetric)-like one, $s_0 = \mathbf{q}^2$. This change of scale translates into an ω-shift of the BFKL kernel that gives rise to poles in $\gamma = 0, 1$ (if $\mathbf{q}^2 \gg \mathbf{k}^2$)[13] [80]. Indeed, we have

$$f(s,\mathbf{k},\mathbf{q}) = \frac{1}{2\pi\sqrt{\mathbf{q}^2\mathbf{k}^2}} \sum_{n=-\infty}^{\infty} \int \frac{\mathrm{d}\omega}{2\pi i} \int \frac{\mathrm{d}\gamma}{2\pi i} \left(\frac{\mathbf{q}^2}{\mathbf{k}^2}\right)^{\gamma-\frac{1}{2}} \left(\frac{s}{\sqrt{\mathbf{q}^2\mathbf{k}^2}}\right)^{\omega} \frac{\mathrm{e}^{\mathrm{in}\,\theta_{\mathrm{kq}}}}{\omega - \mathcal{K}\left(n,\,\gamma\right)}$$
$$= \frac{1}{2\pi\mathbf{q}^2} \sum_{n=-\infty}^{\infty} \int \frac{\mathrm{d}\omega}{2\pi i} \int \frac{\mathrm{d}\gamma}{2\pi i} \left(\frac{\mathbf{q}^2}{\mathbf{k}^2}\right)^{\gamma} \left(\frac{s}{\mathbf{q}^2}\right)^{\omega} \frac{\mathrm{e}^{\mathrm{in}\,\theta_{\mathrm{kq}}}}{\omega - \mathcal{K}\left(n,\,\gamma-\frac{\omega}{2}\right)}\,, \quad (3.124)$$

where θ_{kq} is the azimuthal angle between the transverse momenta $\mathbf{k}$ and $\mathbf{q}$. The pole structure of the conformal invariant part of the NLL BFKL kernel in γ-space, the first line of eq. (3.110) is given by

$$\chi_0\left(\gamma\right) \simeq \frac{1}{\gamma} + \left\{\gamma \to 1-\gamma\right\}, \quad (3.125)$$

$$\chi_1\left(\gamma\right) \simeq \frac{\mathrm{a}}{\gamma} + \frac{\mathrm{b}}{\gamma^2} - \frac{1}{2\gamma^3} + \left\{\gamma \to 1-\gamma\right\}. \quad (3.126)$$

and

$$\mathrm{a} = \frac{5}{12}\frac{\beta_0}{N_c} - \frac{13}{36}\frac{n_f}{N_c^3} - \frac{55}{36}, \quad \mathrm{b} = -\frac{1}{8}\frac{\beta_0}{N_c} - \frac{n_f}{6N_c^3} - \frac{11}{12}. \quad (3.127)$$

The cubic poles compensate for the ones that appear due to the shift in scales. Unfortunately, this is not the case with the double and single poles. Terms beyond NLLA that are not compatible with RG evolution (see the end of this section for explanation) are generated by this change of energy scale. Therefore, the truncation of the perturbative series at NLL accuracy generates a highly oscillatory behavior of the gluon Green's function in the region where $\mathbf{q}^2/\mathbf{k}^2$ is very far from unity, even leading to negative values of total cross sections.

A way to make the kernel more stable is to introduce a certain shift in ω that removes the γ-poles (effectively resums the double logs to all orders), *e.g.*,

$$\mathcal{K}(n,\,\gamma) \to \mathcal{K}(n,\,\gamma+\omega/2)\,. \quad (3.128)$$

The new gluon Green's function with Regge-like energy scale for this shift would

[13] This would correspond to big double logarithms of transverse momentum in momentum space representation.

be

$$f(s,\mathbf{k},\mathbf{q}) = \frac{1}{2\pi\sqrt{\mathbf{q}^2\mathbf{k}^2}}\sum_n \int \frac{\mathrm{d}\omega}{2\pi i}\int \frac{\mathrm{d}\gamma}{2\pi i}\,\left(\frac{\mathbf{q}^2}{\mathbf{k}^2}\right)^{\gamma-\frac{1}{2}}\left(\frac{s}{\sqrt{\mathbf{q}^2\mathbf{k}^2}}\right)^{\omega}\frac{\mathrm{e}^{\mathrm{in}\,\theta_{\mathrm{kq}}}}{\omega-\mathcal{K}\left(n,\,\gamma+\frac{\omega}{2}\right)}\,.$$

At LL accuracy, in order to solve one of the two Mellin integrations of the expression given above one has to find the solution to

$$\omega = \bar{\alpha}_s\left(2\Psi(1)-\Psi(\gamma+\omega/2)-\Psi(1-\gamma+\omega/2)\right)\,. \tag{3.129}$$

Following Ref. [15], a very good approximation to the numerical solution to this equation is given by the analytical expression

$$\omega = \int_0^1 \frac{dx}{1-x}\left\{\left(x^{\gamma-1}+x^{-\gamma}\right)\sqrt{\frac{2\bar{\alpha}_s}{\ln^2 x}}J_1\left(\sqrt{2\bar{\alpha}_s\ln^2 x}\right)-2\bar{\alpha}_s\right\}\equiv\mathcal{B}(\bar{\alpha}_s,\gamma), \tag{3.130}$$

with J_1 being the Bessel function of the first kind. This function can be usefully rewritten in the form

$$\begin{aligned}
&\mathcal{B}(\bar{\alpha}_s,\gamma)\\
&\quad=\sum_{m=0}^{\infty}\left\{\left((\gamma+m)^2+2\bar{\alpha}_s\right)^{\frac{1}{2}}+\left((1-\gamma+m)^2+2\bar{\alpha}_s\right)^{\frac{1}{2}}-1-2m-\frac{2\bar{\alpha}_s}{m+1}\right\}\\
&\quad=\bar{\alpha}_s\left(2\Psi(1)-\Psi(\gamma)-\Psi(1-\gamma)\right)+\mathcal{O}\left(\bar{\alpha}_s^2\right).
\end{aligned} \tag{3.131}$$

Eq. (3.128) accounts for the resummation of the leading unwanted γ-poles. To resum the secondary ones, we can use the more general shift

$$\begin{aligned}
\omega &= \bar{\alpha}_s\left(1+\mathrm{A}\,\bar{\alpha}_s\right)\left(2\psi(1)-\psi\left(\gamma+\frac{\omega}{2}+\mathrm{B}\,\bar{\alpha}_s\right)-\psi\left(1-\gamma+\frac{\omega}{2}+\mathrm{B}\,\bar{\alpha}_s\right)\right)\\
&\quad\bar{\alpha}_s\left(1+\mathrm{A}\bar{\alpha}_s\right)\sum_{m=0}^{\infty}\left(\frac{1}{\gamma+m+\frac{\omega}{2}+\mathrm{B}\,\bar{\alpha}_s}+\frac{1}{1-\gamma+m+\frac{\omega}{2}+\mathrm{B}\,\bar{\alpha}_s}-\frac{2}{m+1}\right).
\end{aligned} \tag{3.132}$$

The representation given by the second line is very useful since it allows for the decoupling between γ and ω spaces. It accounts for the solution of the ω shift at the γ poles plus a term related to the virtual contribution to the original BFKL equation. The value of the coefficients A and B is extracted from the matching with the conformal invariant NLL BFKL kernel[14]. Once this is done, the values $A=a$ and $B=-b$ are found. Finally, the NLL solution must be added to the full result, extracting the single and double γ poles to avoid double counting.

[14]Note that this collinear terms must be in agreement with the NLL result, entering only as higher order corrections.

The final analytic result was given in [15] and reads

$$\begin{aligned}\mathcal{B}(\bar{\alpha}_s,\gamma) &= \bar{\alpha}_s\chi_0(\gamma)+\bar{\alpha}_s^2\chi_1(\gamma)+\sum_{m=0}^{\infty}\left\{\left((\gamma+m-b\bar{\alpha}_s)^2+2\bar{\alpha}_s\left(1+a\bar{\alpha}_s\right)\right)^{\frac{1}{2}}\right.\\ &+\left.\left((1-\gamma+m-b\bar{\alpha}_s)^2+2\bar{\alpha}_s\left(1+a\bar{\alpha}_s\right)\right)^{\frac{1}{2}}-1-2m+2b\bar{\alpha}_s-\frac{2\bar{\alpha}_s\left(1+a\bar{\alpha}_s\right)}{m+1}\right\}\\ &-\sum_{m=0}^{\infty}\left\{\frac{\bar{\alpha}_s}{\gamma+m}+\bar{\alpha}_s^2\left(\frac{a}{\gamma+m}+\frac{b}{(\gamma+m)^2}-\frac{1}{2(\gamma+m)^3}\right)+\{\gamma\leftrightarrow 1-\gamma\}\right\}\\ &= \bar{\alpha}_s\chi_0(\gamma)+\bar{\alpha}_s^2\chi_1(\gamma)+\mathcal{O}\left(\bar{\alpha}_s^3\right). \end{aligned} \tag{3.133}$$

It is clear from eq. (3.133) how the NLL kernel is unperturbed, with the RG improvements starting from NNLA and beyond. Fig. 3.21 compares the BFKL kernels at LL, NLL accuracy and collinear improved one. It can be seen that the last one lowers the value of the Pomeron intercept from ~ 0.55 to ~ 0.3.

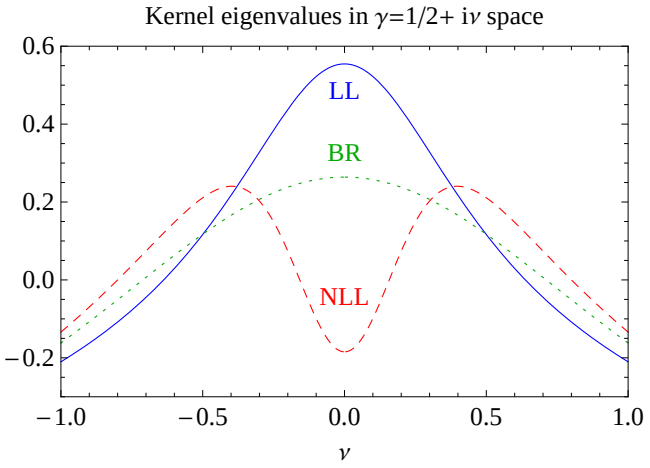

Figure 3.21: BFKL kernel in ν-space: comparison of LL, NLL and collinear improved cases.

Note that the complete NLL kernel given in eq. (3.113) breaks scale invariance so the pole structure in γ will differ from the one in $1-\gamma$. The exact coefficients accompanying the γ-poles will depend on the impact factors on which the differential operator will be acting, as well as on the choice of the later. A particular case will be shown in chapter 4.

For completeness, let us show the n-dependent conformal invariant piece of

the collinear contribution [15, 100, 101]:

$$\chi_{RG}(n,\nu) = \sum_{m=0}^{\infty}\left(\sqrt{2\left(\bar{\alpha}_s + a_n\bar{\alpha}_s^2\right) + \left(m - b_n\bar{\alpha}_s + \frac{1}{2} + i\nu + \frac{|n|}{2}\right)^2} - m - i\nu\right.$$
$$\left. + b_n\bar{\alpha}_s - \frac{1+|n|}{2} - \frac{\bar{\alpha}_s + a_n\bar{\alpha}_s^2}{m + \frac{1+|n|}{2} + i\nu} - \frac{\bar{\alpha}_s^2 b_n}{\left(m + \frac{1+|n|}{2} + i\nu\right)^2} + \frac{\bar{\alpha}_s^2}{\left(m + \frac{1+|n|}{2} + i\nu\right)^3}\right)$$
$$+ \{\nu \to -\nu\}, \tag{3.134}$$

with

$$a_n = \frac{4 - \pi^2 + 5\beta_0/N_c}{12} - \frac{\pi^2}{24} + \frac{\beta_0}{4N_c}\left(\psi(n+1) - \psi(1)\right) + \frac{1}{2}\psi'(n+1) \tag{3.135}$$
$$+\frac{1}{8}\left(\psi'\left(\frac{n+1}{2}\right) - \psi'\left(\frac{n+2}{2}\right)\right) - \frac{\delta_n^0}{36}\left(67 + 13\frac{n_f}{N_c^3}\right) - \frac{47\delta_n^2}{1800}\left(1 + \frac{n_f}{N_c^3}\right)$$

and

$$-b_n = \frac{\beta_0}{8N_c} + \frac{1}{2}\left(\psi(n+1) - \psi(1)\right) + \frac{\delta_n^0}{12}\left(11 + 2\frac{n_f}{N_c^3}\right) + \frac{\delta_n^2}{60}\left(1 + \frac{n_f}{N_c^3}\right). \tag{3.136}$$

Matching with the DGLAP anomalous dimension

Consider the gluon Green's function for the DIS region and conformal spin zero, *i.e.*, the second line of eq. (3.124) but with the substitution of the kernel by the Bessel function defined in eq. (3.130):

$$f(s,\mathbf{k},\mathbf{q}) = \frac{1}{2\pi\mathbf{q}^2}\int\frac{\mathrm{d}\omega}{2\pi i}\int\frac{\mathrm{d}\gamma}{2\pi i}\left(\frac{\mathbf{q}^2}{\mathbf{k}^2}\right)^{\gamma}\left(\frac{s}{\mathbf{q}^2}\right)^{\omega}\frac{1}{\omega - \mathcal{B}\left(\bar{\alpha}_s,\,\gamma - \frac{\omega}{2}\right)}$$
$$= \frac{1}{2\pi\mathbf{q}^2}\int\frac{\mathrm{d}\omega}{2\pi i}\left(\frac{\mathbf{q}^2}{\mathbf{k}^2}\right)^{\gamma_\omega}\left(\frac{s}{\mathbf{q}^2}\right)^{\omega}, \tag{3.137}$$

where γ_ω is the solution to the equation

$$\omega - \mathcal{B}\left(\bar{\alpha}_s,\,\gamma - \omega/2\right) = 0.$$

We mentioned before that the collinear poles appearing due to the change of energy scale from the symmetric to the asymmetric one were not compatible with RG or DGLAP analysis. However, a very nice property of this Bessel or collinear improved resummation is that it recaptures the needed terms to be compatible with a DGLAP anomalous dimensional analysis. In order to show this we need to find the expansion of the anomalous dimension for the relevant

twist two operators in the DIS region, that is, for the region dominated by

$$\begin{aligned}\omega &= \mathcal{B}\left(\bar{\alpha}_s, \gamma_\omega - \frac{\omega}{2}\right) = \mathcal{B}\left(\bar{\alpha}_s, \gamma_\omega\right) - \frac{\bar{\alpha}_s^2}{2}\chi_0(\gamma_\omega)\chi_0'(\gamma_\omega) + \mathcal{O}\left(\bar{\alpha}_s^3\right). \\ &= \frac{\bar{\alpha}_s}{\gamma_\omega} + \bar{\alpha}_s^2\left(\frac{a}{\gamma_\omega} + \frac{b}{\gamma_\omega^2} + c\right) + \mathcal{O}\left(\bar{\alpha}_s^3\right), \end{aligned} \tag{3.138}$$

as it can be directly seen from eq. (3.137). The anomalous dimension is given by [71]

$$\gamma_\omega = \bar{\alpha}_s\left(\frac{1}{\omega} + b\right) + \bar{\alpha}_s^2\frac{a}{\omega} + \bar{\alpha}_s^3\frac{c}{\omega^2} + \mathcal{O}\left(\bar{\alpha}_s^4\right). \tag{3.139}$$

Since

$$\begin{aligned} a &= \frac{5}{12}\frac{\beta_0}{N_c} - \frac{13}{36}\frac{n_f}{N_c^3} - \frac{55}{36}, \\ b &= \left(-\frac{1}{8}\frac{\beta_0}{N_c} - \frac{n_f}{6N_c^3} - \frac{11}{12}\right) + \frac{\beta_0}{8N_c}, \end{aligned}$$

this limit is in agreement with the exact calculation of the three loop anomalous dimension performed in [102] and [103]. The constant c was calculated in [71] and reads

$$c = -\frac{1}{4}\left(\frac{395}{27} - 2\zeta(3) - \frac{11}{3}\frac{\pi^2}{6} + \frac{n_f}{N_c^3}\left(\frac{71}{27} - \frac{\pi^2}{9}\right)\right).$$

The corrections of $\mathcal{O}\left(\bar{\alpha}_s^4\right)$ contain all-order terms of the form $\bar{\alpha}_s^n/\omega^n$ which are obtained by using the representation

$$\chi_0(\gamma_\omega) = \frac{1}{\gamma_\omega} + 2\sum_{L=1}^{\infty}\zeta(2L+1)\gamma_\omega^{2L}. \tag{3.140}$$

More explicitly, to eq. (3.139) we should add

$$2\zeta(3)\left(\frac{\bar{\alpha}_s}{\omega}\right)^4 + 2\zeta(5)\left(\frac{\bar{\alpha}_s}{\omega}\right)^6 + 12\zeta(3)^2\left(\frac{\bar{\alpha}_s}{\omega}\right)^7 + \ldots \tag{3.141}$$

Chapter 4

Description of structure functions at small x

We explained in section 2.2 how the use of renormalization group equations in DIS in the collinear limit naturally gives rise to DGLAP evolution, which resums logarithms of the type $\ln Q^2/\mu_R^2$. In this section we are interested in the description of DIS in the limit where $s >> Q^2 >> \Lambda^2_{\rm QCD}$. The fact that the photon virtuality is still a hard scale allows to probe the Regge limit of DIS by means of p-QCD. This makes the computation of DIS-like cross sections in the Regge limit very interesting from the theoretical point of view. Moreover, HERA data [27] was able to reach a very low region of Bjorken x for large values of Q^2, making it possible to develop meaningful phenomenological studies in this context, as it will be shown in this chapter.

In particular, we will show that it is possible to describe the effective Pomeron intercept at small values of Bjorken x using NLL BFKL evolution together with collinear improvements. To obtain a good description over the whole range of Q^2 we will use a non-Abelian physical renormalization scheme with the Brodsky-Lepage-Mackenzie (BLM) optimal scale setting, combined with a parametrization of the running coupling in the infrared region.

The work presented in this chapter is collected in [16, 17].

4.1 Theoretical setup

As we saw in the introduction, the proton structure functions F_2 and F_L can be written in terms of the cross section for the scattering of transverse and

longitudinal photons as

$$F_2(x,Q^2) = \frac{Q^2}{4\pi^2\alpha}\left(\sigma_T(x,Q^2)+\sigma_L(x,Q^2)\right) \quad \text{and} \quad F_L(x,Q^2) = \frac{Q^2}{4\pi^2\alpha}\sigma_L(x,Q^2)\ . \tag{4.1}$$

In the high energy limit the total cross section can be factorized as we already pointed out in eq. (3.70). Thus, we can write the structure functions in the form

$$F_\lambda(s,Q^2) = \int \frac{\mathrm{d}^2\mathbf{q}}{\pi\mathbf{q}^2}\int \frac{\mathrm{d}^2\mathbf{p}}{\pi\mathbf{p}^2}\Phi_\lambda(\mathbf{q})\Phi_p(\mathbf{p})f(s,\mathbf{q},\mathbf{p})\ , \tag{4.2}$$

where Φ_λ are the different components of the photon impact factor, with $\lambda = 2, L$. The gluon Green's function with DIS-like energy scale can be written in the form

$$f\left(s,\mathbf{q},\mathbf{p}\right) = \frac{1}{\pi}\int\frac{\mathrm{d}\omega}{2\pi i}\int\frac{\mathrm{d}\gamma}{2\pi i}\,\frac{1}{\mathbf{q}^2}\left(\frac{\mathbf{q}^2}{\mathbf{p}^2}\right)^\gamma\left(\frac{s}{\mathbf{q}^2}\right)^\omega\frac{1}{\omega-\bar{\alpha}_s\hat{\mathcal{K}}\left(\gamma-\omega/2\right)}. \tag{4.3}$$

For the sake of discussion let us assume that we know the solution to the equation

$$\omega - \bar{\alpha}_s\hat{\mathcal{K}}\left(\gamma-\omega/2\right) = 0 \tag{4.4}$$

to any desired order of accuracy and that it can be written as a sum of poles in γ of the form

$$\omega = \omega_0(\bar{\alpha}_s,\gamma)\ . \tag{4.5}$$

Under these assumptions the gluon Green's function can be rewritten in terms of this solution as

$$f\left(s,\mathbf{q},\mathbf{p}\right) = \frac{1}{\pi}\int\frac{\mathrm{d}\gamma}{2\pi i}\,\frac{1}{\mathbf{q}^2}\left(\frac{\mathbf{q}^2}{\mathbf{p}^2}\right)^\gamma\left(\frac{s}{\mathbf{q}^2}\right)^{\omega_0(\bar{\alpha}_s,\gamma)}. \tag{4.6}$$

Hence, it is very useful to express eq. (4.2) in γ-space. Making use of the definitions given in eqs. (4.9, 4.13) and inserting eq. (4.3) into eq. (4.2), we have:

$$\begin{aligned} F_\lambda &= \frac{1}{\pi}\int\frac{\mathrm{d}\gamma}{2\pi i}\,s^{\omega_0(\bar{\alpha}_s,\gamma)}\int\frac{\mathrm{d}^2\mathbf{q}}{\pi\mathbf{q}^2}\Phi_\lambda(\mathbf{q},Q^2)(\mathbf{q}^2)^{(\gamma-\omega_0(\bar{\alpha}_s,\gamma)-1}\int\frac{\mathrm{d}^2\mathbf{p}}{\pi\mathbf{p}^2}\Phi_p(\mathbf{p},Q_0^2)(\mathbf{p}^2)^{-\gamma} \\ &= \frac{1}{\pi}\int\frac{\mathrm{d}\gamma}{2\pi i}\,s^{\omega_0(\bar{\alpha}_s,\gamma)}\Phi_\lambda\left(\gamma-\omega_0(\bar{\alpha}_s,\gamma)\right)\,\Phi_p(\gamma). \end{aligned} \tag{4.7}$$

This is what one should do from a strict point of view. However, we will consider the photon impact factor at LO accuracy for the present analysis, so we can neglect the higher order corrections introduced by the ω-shift of eq. (4.7),

$$\Phi_\lambda\left(\gamma-\omega_0(\bar{\alpha}_s,\gamma)\right) = \Phi_\lambda\left(\gamma\right) - \bar{\alpha}_s\chi_0(\gamma)\Phi'_\lambda\left(\gamma\right) + \mathcal{O}(\bar{\alpha}_s^2)\ ,$$

where we have used the fact that the fist correction to ω_0 is the LL BFKL kernel, and take just the first term of the expansion being aware of the approximation underneath.

We can also express F_λ in terms of the Bjorken x by simply using the DIS relation $x \simeq Q^2/s$ to rewrite eq. (4.7) as

$$F_\lambda(x,Q^2) \;\simeq\; \frac{1}{\pi}\int \frac{\mathrm{d}\gamma}{2\pi i}\left(\frac{x}{Q^2}\right)^{-\omega_0(\bar{\alpha}_s,\gamma)} \Phi_\lambda(\gamma)\,\Phi_p(\gamma)\,. \tag{4.8}$$

Let us remark at this point that the main theoretical aspects needed for the calculation given in this section were already developed in sections 3.3.2 and 3.4. Therefore, we will just present here some very basic steps to follow the argument and leave the tedious analysis aside. More details will be given when needed, specially for the points not presented in the previous sections.

The ingredients needed for our determination of the structure functions are:

1. Proton impact factor
2. Photon impact factor
3. Collinear improved NLL BFKL kernel for DIS energy scale
4. Including running coupling effects
5. Choice of renormalization scale and scheme

Let us analyze each of these points in detail.

Proton impact factor

The choice of proton impact factor is subject to several constraints. It must rapidly fall to zero when the transverse momentum goes to both zero and infinity and it must have a clear maximum around the confinement scale. Having these bounds in mind one can think of a variety of models equally valid for it. In the case of DIS the proton impact factor is the only non-perturbative object entering the calculation, so all the freedom in making a fit of the structure functions will be coming from it when using k_t-factorization. Therefore, a too simple model for the impact factor could be problematic for the analyzer.

Let us discuss three different possibilities. The first proton impact factor under consideration is given in k-space by

$$\Phi_{1p}(\mathbf{k},Q_0^2) = A_p\left(\frac{\mathbf{k}^2}{\mathbf{k}^2+Q_0^2}\right)^{\delta} \mathrm{e}^{-\mathbf{k}^2/\mathrm{Q}_0^2}\,.$$

It is useful to go to γ-space, where the computations for the total cross section become much simpler. The transformation is given by

$$\tilde{\Phi}_p(\gamma) \equiv \int \frac{\mathrm{d}^2\mathbf{k}}{\pi\mathbf{k}^2}(\mathbf{k}^2)^{-\gamma}\Phi_p(\mathbf{k}^2)\ , \tag{4.9}$$

which in this case yields

$$\tilde{\Phi}_{1p}(\gamma) = A_p(Q_0^2)^{-\gamma}\left(\mathcal{B}(\delta-\gamma,\gamma)\ {}_1F_1(\delta-\gamma,|1-\gamma|,1) + \Gamma(-\gamma)\ {}_1F_1(\delta,|1+\gamma|,1)\right),$$

$\mathcal{B}$ being the β-function, defined as

$$\mathcal{B}(a,b) = \int_0^\infty \mathrm{d}x \frac{x^{a-1}}{(1+x)^{a+b}}\ , \qquad \mathcal{R}e(a) > 0,\ \mathcal{R}e(b) > 0\ , \tag{4.10}$$

iff $\mathrm{Re}(a)$, $\mathrm{Re}(b) > 0$. The second choice is

$$\Phi_{2p}(\mathbf{k},Q_0^2) = A_p\left(\frac{\mathbf{k}^2}{\mathbf{k}^2+Q_0^2}\right)^\delta, \qquad \tilde{\Phi}_{2p}(\gamma) = A_p(Q_0^2)^{-\gamma}\frac{\Gamma(\delta-\gamma)\Gamma(\gamma)}{\Gamma(\delta)}\ ,$$

provided that $\mathrm{Re}(\delta-\gamma) > 0$ and $\mathrm{Re}(\gamma) > 0$. The third and last choice is

$$\Phi_{3p}(\mathbf{k},Q_0^2) = A_p\left(\frac{\mathbf{k}^2}{Q_0^2}\right)^\delta \mathrm{e}^{-\mathbf{k}^2/\mathrm{Q}_0^2}, \qquad \tilde{\Phi}_{3p}(\gamma) = A_p(Q_0^2)^{-\gamma}\Gamma(\delta-\gamma)\ .$$

Fig. 4.1 compares the three choices in k-space using the same values for the

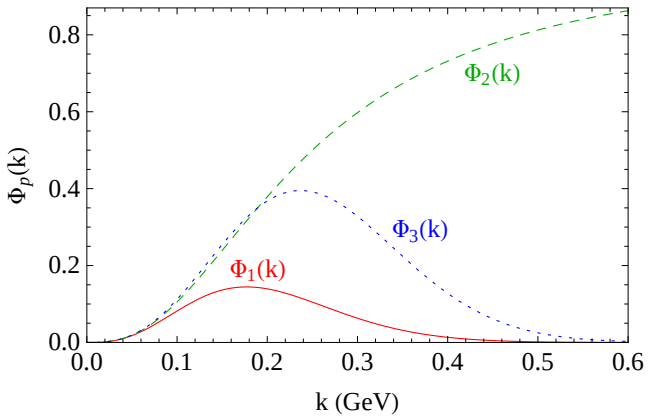

Figure 4.1: Comparison of the three proton impact factors under consideration. The values taken for the parameters are $A_p = \pi$, $\delta = 1.4$ and $Q_0^2 = 0.04 \simeq \Lambda^2_{\mathrm{QCD}}$

parameters in the three cases. It shows the importance of including the exponential term in making the impact factors to decay rapidly with increasing the

momentum. Choosing between Φ_{1p} and Φ_{3p} is a a matter of taste. The first one might give a bit more of intuition about the nature of the present parameters.[1] On the other hand, the expression for Φ_{3p} in γ-space is much simpler.

We choose the last one for the present study with the notation:

$$\Phi_P\left(p,Q_0^2\right) \;=\; \frac{\mathcal{C}}{\Gamma(\delta)}\left(\frac{p^2}{Q_0^2}\right)^{\delta} e^{-\frac{p^2}{Q_0^2}}, \tag{4.11}$$

where we have introduced two free parameters and a normalization.

Photon impact factor

We want to keep the impact factors as simple as possible in order to focus on the gluon Green's function. Having this philosophy in mind, we will work with the LO photon one and with a kinematically improved one proposed in [104,105]. Its LO expressions for the longitudinal and transverse photons in transverse momentum space are [13]

$$\begin{aligned}
\Phi_T(\mathbf{k}) &= 4\pi\alpha\alpha_s\sum_q e_q^2\int_0^1 \mathrm{d}\rho\int_0^1 \mathrm{d}\tau\,\frac{\mathbf{k}^2[\tau^2+(1-\tau)^2][\rho^2+(1-\rho)^2]}{\rho(1-\rho)Q^2+\tau(1-\tau)\mathbf{k}^2}\,, \qquad \text{and}\\
\Phi_L(\mathbf{k}) &= 4\pi\alpha\alpha_s\sum_q e_q^2\int_0^1 \mathrm{d}\rho\int_0^1 \mathrm{d}\tau\,\frac{\mathbf{k}^2\cdot 8[\rho(1-\rho)\,\tau(1-\tau)]}{\rho(1-\rho)Q^2+\tau(1-\tau)\mathbf{k}^2}\,.
\end{aligned} \tag{4.12}$$

In $\nu = i(1/2-\gamma)$-space they turn out to be really handy:

$$\tilde{\Phi}_\lambda(\gamma)\equiv\int\frac{\mathrm{d}^2\mathbf{q}}{\pi\mathbf{q}^2}\Phi_\lambda\left(\mathbf{q},Q^2\right)\left(\frac{\mathbf{q}^2}{Q^2}\right)^{\gamma-1} \;=\; \frac{\alpha_s(\mu_R^2)}{2\pi}\sum_{q=1}^{n_f}e_q^2\,c_\lambda(\nu)\,, \tag{4.13}$$

with

$$\begin{aligned}
c_\lambda(\nu) &\equiv \frac{\pi^2}{4}\frac{\Omega_\lambda(\nu)}{(\nu+\nu^3)}\,\mathrm{sech}(\pi\nu)\,\tanh\left(\pi\nu\right)\,, \\
\Omega_2 &= (11+12\nu^2)/8\,, \\
\Omega_L &= \nu^2+1/4\,.
\end{aligned} \tag{4.14}$$

The improved impact factors include part of the higher order corrections by broadening the phase-space given by QMRK to the one given by exact gluon kinematics. This translates into an extension from $\{\gamma,\,\omega=0\}$ to all $\{\gamma,\,\omega\}$

[1] In impact parameter representation Q_0^2 would be associated to the full size of the proton, being forced to be of the order of the QCD confinement scale.

space for the photon impact factor:

$$\tilde{\Phi}_\lambda(\gamma) \to \tilde{\Phi}_\lambda(\gamma,\omega)\ ,$$

where γ and ω are the two standard Mellin variables, conjugated to squared transverse momentum and energy respectively, used in the definition of our gluon Green's function given in eq. (4.3). In the strict limit $s \to \infty$ one has $\omega = 0$ and this is where k_t-factorization is proven to hold. However, if one assumes this factorization theorem can still be used in the case of exact gluon kinematics in the photon impact factor, an analytic expression for its longitudinal and transverse components in the whole $\{\gamma, \omega\}$-space can be found [105].

In this case eq. (4.2) would need to be replaced by

$$F_\lambda(s,Q^2) \propto \int \frac{\mathrm{d}^2\mathbf{q}}{\pi\mathbf{q}^2} \int \frac{\mathrm{d}^2\mathbf{p}}{\pi\mathbf{p}^2} \int \frac{\mathrm{d}\omega}{2\pi i} \int \frac{\mathrm{d}\gamma}{2\pi i}\, s^\omega\, \Phi_\lambda(\mathbf{q},\omega)\, \Phi_p(\mathbf{p})\, f_\omega(s,\mathbf{q},\mathbf{p})\ . \quad (4.15)$$

The implementation of the components of the kinematically improved impact factor require to replace the functions $c_\lambda(\nu)$ by $\tilde{c}_\lambda(\gamma,\omega)$ where

$$\tilde{c}_L(\gamma,\omega) = \frac{4\Gamma(\gamma{+}\xi{+}1)\Gamma(1{+}\gamma)\left((\psi(\gamma{+}\xi)-\psi(\gamma))\left(3\omega^2-\xi^2+1\right)-6\omega\xi\right)}{\xi\,\Gamma(1+\omega)\left(\xi^4-5\xi^2+4\right)} \quad (4.16)$$

and $\tilde{c}_2 = \tilde{c}_L + \tilde{c}_T$, with

$$\begin{aligned}\tilde{c}_T(\gamma,\omega) = \frac{\Gamma(\gamma{+}\xi)\Gamma(\gamma)}{\xi\Gamma(1{+}\omega)(\xi^4-5\xi^2+4)}\Big\{ &-2\xi\omega\left(\xi^2+3^2+6\omega+11\right)\\ &+\left[\psi(\gamma+\xi)-\psi(\gamma)\right]\left[\xi^4-10\xi^2+3\omega^2\left(\omega^2+2\omega+4\right)-2\omega\left(\xi^2{-}1\right)+9\right]\Big\}.\end{aligned} \quad (4.17)$$

$\psi(\gamma)$ is the logarithmic derivative of the Euler Gamma function and $\xi = 1{-}2\gamma{+}\omega$, ω being the Mellin variable conjugate to x in the definition of the gluon Green's function. The main difference between these impact factors is that the LO ones roughly double the value of their kinematically improved counterparts in the region with small $|\nu|$, while being very similar for $|\nu| \geq 1$, as it can be seen in fig. 4.2.

Collinear improved NLL BFKL kernel for DIS energy scale

Let us now build up the collinearly resummed terms specific for the DIS limit following the same arguments as given in section 3.4 and [15] to construct an expression for the function $\omega_0(\bar{\alpha}_s,\gamma)$ introduced in eq. (4.5).

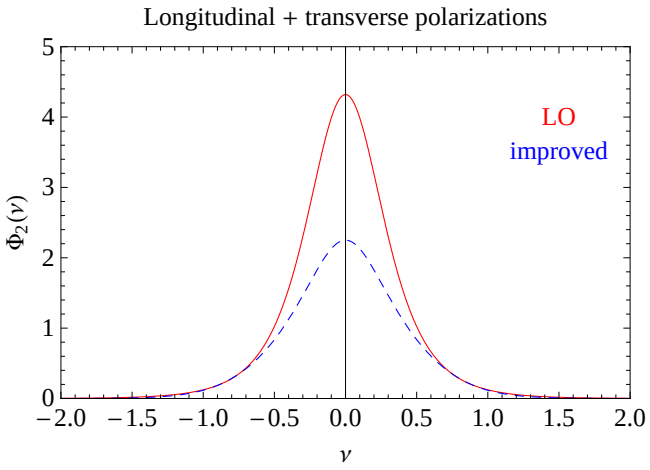

Figure 4.2: Comparison of the LO photon impact factor with the unpolarized kinematically improved one in ν-space.

The expansion of the scale invariant NLL BFKL kernel in terms of poles at $\gamma = 0, 1$ is given by

$$\begin{aligned}
\omega &= \bar{\alpha}_s \chi_0(\gamma - \frac{\omega}{2}) + \bar{\alpha}_s^2 \chi_1(\gamma) \\
&= \bar{\alpha}_s \chi_0(\gamma) + \bar{\alpha}_s^2 \chi_1(\gamma) - \frac{1}{2}\bar{\alpha}_s^2 \chi_0{}'(\gamma)\chi_0(\gamma) + \mathcal{O}(\bar{\alpha}_s^3) \\
&\simeq \frac{\bar{\alpha}_s}{\gamma} + \bar{\alpha}_s^2 \left(\frac{a}{\gamma} + \frac{b}{\gamma^2} - \frac{1}{2\gamma^3} \right) + \frac{\bar{\alpha}_s}{1-\gamma} + \frac{\bar{\alpha}_s^2}{2\gamma^3} - \frac{\bar{\alpha}_s^2}{2(1-\gamma)^3} \\
&+ \bar{\alpha}_s^2 \left[\frac{a}{1-\gamma} + \frac{b}{(1-\gamma)^2} - \frac{1}{2(1-\gamma)^3} \right] + \mathcal{O}(\bar{\alpha}_s^3), \qquad (4.18)
\end{aligned}$$

where $\chi_0{}'(\gamma) = \psi'(1-\gamma) - \psi'(\gamma)$. Now, as we have explained before, we resum in the Regge region, $Q^2 \simeq Q_0^2$, collinear logarithms by introducing a shift of the general form given by eq. (3.132) [14,15],

$$\omega = \bar{\alpha}_s(1 + A\bar{\alpha}_s) \left(2\psi(1) - \psi\left(\gamma + \frac{\omega}{2} + B\bar{\alpha}_s\right) - \psi\left(1 - \gamma + \frac{\omega}{2} + B\bar{\alpha}_s\right) \right), \qquad (4.19)$$

for which we derived a very good analytic approximation (eq. (3.133)) to its numerical solution (always within the uncertainty of the possible resummation schemes) by breaking its transcendentality, solving it pole by pole and summing up the different solutions [15]. In the DIS limit, $Q^2 \gg Q_0^2$, this shift should be

replaced by

$$\begin{aligned}\omega &= \bar{\alpha}_s(1+A\bar{\alpha}_s)\left(2\psi(1)-\psi\left(\gamma+B\bar{\alpha}_s\right)-\psi\left(1-\gamma+\omega+B\bar{\alpha}_s\right)\right) \\ &= \bar{\alpha}_s(1+A\bar{\alpha}_s)\sum_{m=0}^{\infty}\left(\frac{1}{\gamma+m+B\bar{\alpha}_s}+\frac{1}{1-\gamma+m+\omega+B\bar{\alpha}_s}-\frac{2}{m+1}\right).\end{aligned} \tag{4.20}$$

Following the same procedure as for the Regge case, the solution in terms of (anti-)collinear poles was found to be

$$\begin{aligned}\omega &= \sum_{m=0}^{\infty}\left\{\bar{\alpha}_s(1+A\bar{\alpha}_s)\left(\frac{1}{\gamma+m+B\bar{\alpha}_s}-\frac{2}{m+1}\right)\right. \\ &+ \left.\frac{1}{2}\left(\gamma-1-m-B\bar{\alpha}_s+\sqrt{(\gamma-1-m-B\bar{\alpha}_s)^2+4\bar{\alpha}_s(1+A\bar{\alpha}_s)}\right)\right\} \\ &= \sum_{m=0}^{\infty}\left\{\bar{\alpha}_s\left(\frac{1}{\gamma+m}+\frac{1}{1-\gamma+m}-\frac{2}{m+1}\right)\right. \\ &+ \bar{\alpha}_s^2\left(\frac{A}{\gamma+m}+\frac{A}{1-\gamma+m}-\frac{B}{(\gamma+m)^2}-\frac{B}{(1-\gamma+m)^2}\right. \\ &- \left.\left.\frac{1}{(1+m-\gamma)^3}-\frac{2A}{m+1}\right)\right\}+\mathcal{O}(\bar{\alpha}_s^3).\end{aligned} \tag{4.21}$$

In order to match the poles at NLLA in eq. (4.18) we need to fix $A = a$ and $B = -b$. Keeping the LL and NLL kernels unmodified and introducing only higher order corrections, our collinearly improved BFKL kernel then simply reads

$$\chi(\gamma) = \bar{\alpha}_s\chi_0(\gamma)+\bar{\alpha}_s^2\chi_1(\gamma)-\frac{1}{2}\bar{\alpha}_s^2\chi_0{}'(\gamma)\chi_0(\gamma)+\chi_{\mathrm{RG}}(\bar{\alpha}_s,\gamma,a,b), \tag{4.22}$$

with

$$\begin{aligned}\chi_{\mathrm{RG}}(\bar{\alpha}_s,\gamma,a,b) &= \bar{\alpha}_s(1+a\bar{\alpha}_s)\left(\psi(\gamma)-\psi(\gamma-b\bar{\alpha}_s)\right) \\ &-\frac{\bar{\alpha}_s^2}{2}\psi''(1-\gamma)-b\bar{\alpha}_s^2\frac{\pi^2}{\sin^2(\pi\gamma)}+\frac{1}{2}\sum_{m=0}^{\infty}\left(\gamma-1-m+b\bar{\alpha}_s\right. \\ &-\left.\frac{2\bar{\alpha}_s(1+a\bar{\alpha}_s)}{1-\gamma+m}+\sqrt{(\gamma-1-m+b\bar{\alpha}_s)^2+4\bar{\alpha}_s(1+a\bar{\alpha}_s)}\right).\end{aligned} \tag{4.23}$$

The first two terms of eq. (4.22) are the scale invariant part of the NLL kernel, the third one appears due to the shift from Regge to DIS energy scale and the last one has been already discussed. The next step will be to introduce the terms that account for the running of the coupling.

Including running coupling effects

The treatment of the insertion of the running into the BFKL equation was already analyzed in section 3.3.2. For the present study we will use the symmetric choice of the differential operator. Therefore, as we already discussed in eq. (3.110), the running coupling correction of the NLL kernel with symmetric choice of the differential operator [106] is given by

$$\hat{\chi}_{\rm RC}(\gamma) \;=\; \bar{\alpha}_s^2 \frac{\beta_0}{8N_c}\left(\chi_0(\gamma)\overrightarrow{\partial}_\gamma - \overleftarrow{\partial}_\gamma\chi_0(\gamma) + 2\log(\mu_R^2) + \chi_0'(\gamma)\right). \quad (4.24)$$

The ω_0 defined in eq. (4.5) would be given by

$$\omega_0(\bar{\alpha}_s,\gamma) = \chi(\gamma) + \chi_{\rm RC}(\gamma)\,, \quad (4.25)$$

with $\chi(\gamma)$ given by eq. (4.22).

Now, if we exponentiate only the scale invariant LL and NLL terms of the kernel, that is, eq. (4.22) and leave $\chi_{\rm RC}$ downstairs acting on the impact factors, the structure functions would look like

$$F_\lambda(x,Q^2) \;\propto\; \int_{-\infty}^{\infty} {\rm d}\nu\, x^{-\chi\left(\frac{1}{2}+i\nu\right)}\left(\frac{Q^2}{Q_0^2}\right)^{\frac{1}{2}+i\nu} c_\lambda(\nu)c_p(\nu)\Bigg\{1 \quad (4.26)$$
$$+\bar{\alpha}_s^2\ln\left(\frac{1}{x}\right)\frac{\beta_0}{8N_c}\chi_0\left(\frac{1}{2}+i\nu\right)\left(\log\left(\mu_R^4\right) + i\frac{\rm d}{{\rm d}\nu}\ln\left(\frac{\tilde{\Phi}_\lambda(1/2+i\nu)}{\tilde{\Phi}_p(1/2+i\nu)}\right)\right)\Bigg\},$$

where we have used $x \simeq Q^2/s$ and introduced $c_p \equiv \Gamma\left(\delta - \frac{1}{2} - i\nu\right)$. The last term of eq. (4.24), proportional to $\chi_0'(\gamma)$ is not present in this expression because it gives a zero contribution to the integral, being the only piece antisymmetric in ν. When convoluted with the ν-symmetric impact factors the term vanishes.

After acting with the derivative on the impact factors we find

$$F_\lambda(x,Q^2) \;\propto\; \int_{-\infty}^{\infty} d\nu\, x^{-\chi\left(\frac{1}{2}+i\nu\right)}\left(\frac{Q^2}{Q_0^2}\right)^{\frac{1}{2}+i\nu} c_I(\nu)c_P(\nu)\Bigg\{1$$
$$+\bar{\alpha}_s^2\log\left(\frac{1}{x}\right)\frac{\beta_0}{8N_c}\chi_0\left(\frac{1}{2}+i\nu\right)\left(-\log\left(\frac{Q^2Q_0^2}{\mu_R^4}\right) - \psi\left(\delta-\frac{1}{2}-i\nu\right)\right.$$
$$\left.+i\left(\pi{\rm coth}(\pi\nu) - 2\pi\tanh\left(\pi\nu\right) - M_\lambda(\nu)\right)\right)\Bigg\}, \quad (4.27)$$

where

$$M_2(\nu) \;=\; \frac{11+21\nu^2+12\nu^4}{\nu(1+\nu^2)(11+12\nu^2)}, \qquad M_L(\nu) \;=\; \frac{1-\nu^2+4\nu^4}{\nu(1+5\nu^2+4\nu^4)}. \quad (4.28)$$

For the kinematical improved version of F_I we replace $c_I(\nu)$ by $\tilde{c}_I(1/2+i\nu, \chi(1/2+i\nu))$.

In this study we prefer to take a conservative approach and among all the possible ways to treat the running of the coupling we consider the simplest: to only exponentiate the logarithmic term in eq. (4.27) carrying the dependence on the external scales, as we will proceed to explain now. The scale dependence appears as a consequence of the symmetric action of the differential operator $\partial/\partial\gamma$ present in the BFKL kernel on both impact factors.

Although there is some freedom in the treatment of the running of the coupling, it is natural to remove the μ_R dependent logarithm in the second line of Eq. (4.27) making the replacement

$$\bar{\alpha}_s - \bar{\alpha}_s^2 \frac{\beta_0}{8N_c} \log\left(\frac{Q^2 Q_0^2}{\mu_R^4}\right) \longrightarrow \bar{\alpha}_s\left(QQ_0\right), \tag{4.29}$$

and use this resummed coupling throughout our calculations.

Choice of renormalization scale and scheme

We pointed out back in the introduction that a crucial point for a proper understanding of BFKL dynamics is to be able to explain the transition in transverse momentum scale between the hard and the soft pomeron exchange, $\lambda_p(Q^2)$. In the region $x < 10^{-2}$ this can be obtained from experimental DIS data through a parametrization of the structure function of the form

$$F_2(x, Q^2) = c(Q^2) x^{-\lambda_p(Q^2)} . \tag{4.30}$$

The intercept $\lambda(Q^2)$ is $\mathcal{O}(0.3)$ at large values of Q^2 and $\mathcal{O}(0.1)$ at low values, closer to the confinement region. When trying to describe these data with our approach we found that it is rather difficult to get good agreement over the full range of $1\,\mathrm{GeV}^2 < Q^2 < 300\,\mathrm{GeV}^2$. There was something about the IR region that was still not correctly explained and new ideas needed to be considered.

A recent very interesting possibility is that proposed by Kowalski, Lipatov, Ross and Watt in [107], in which they determine the IR behavior of the BFKL forward amplitude through the discrete pomeron solution, allowing the IR phase to vary with the eigenvalues. Alternatively, we have found that moving from the $\overline{\mathrm{MS}}$ scheme to renormalization schemes inspired by the existence of a possible IR fixed point significantly helps in generating a natural fit for $\lambda(Q^2)$, in the sense of having sensible values for the two free parameters in our calculation which affect this observable: δ and Q_0 in the proton impact factor.

The first evaluation of the BFKL Pomeron intercept in non-Abelian physical renormalization schemes using the Brodsky-Lepage-Mackenzie (BLM) optimal scale setting [108] was performed in [87] in the context of virtual photon-photon scattering. A remarkable feature of the pomeron intercept with BLM scale is its tiny dependence on the virtuality of the reggeized gluon. Consequently the renormalization scale becomes physical even in the IR region through the isolation of the pieces of the NLL BFKL kernel proportional to β_0. The absorption of these terms in a new definition of the running of the coupling in a way that all vacuum polarization effects from the β_0 function are resummed, *i.e.*,

$$\tilde{\alpha}_s\left(QQ_0,\gamma\right) = \frac{4N_c}{\beta_0\left[\log\left(\frac{QQ_0}{\Lambda^2}\right)+\frac{1}{2}\chi_0(\gamma)-\frac{5}{3}+2\left(1+\frac{2}{3}Y\right)\right]}, \qquad (4.31)$$

where we are using the momentum space (MOM) physical renormalization scheme based on a symmetric triple gluon vertex [109] with $Y \simeq 2.343907$ and gauge parameter $\xi = 3$ (our results are very weakly dependent on this choice). This scheme is more suited to the BFKL context since there are large non-Abelian contributions to the kernel. Let us clarify that the BLM procedure is scheme-independent and the dependence of our results on different schemes is very small.

The relation between the running coupling in MOM and $\overline{\rm MS}$ schemes is given by [108]

$$\begin{aligned}\bar{\alpha}_{\rm MOM}(Q^2) &= \bar{\alpha}_{\overline{\rm MS}}(Q^2)\left[1+(A\beta_0-B)\frac{\bar{\alpha}_{\overline{\rm MS}}(Q^2)}{N_c}+\mathcal{O}(\bar{\alpha}^2)\right]\\ &\to \bar{\alpha}_{\overline{\rm MS}}(Q^2)\left[1-B\frac{\bar{\alpha}_{\overline{\rm MS}}(Q^{*2})}{N_c}B+\mathcal{O}(\bar{\alpha}^2)\right],\end{aligned}$$

where for the last line the β_0 dependence has been reabsorbed into the running, having $Q^{*2} = 0.077Q^2$. More details about the MOM scheme and BLM scale can be found in [87, 108].

The main reason to introduce the BLM procedure in our context is to eliminate the divergent renormalon series of the form $\alpha_s^n\beta_0^n n!$, which has a big effect in the small Q^2 region (see Ref. [110] for a modern review on the subject). The replacements we need in our kernel in order to introduce this new scheme are $\bar{\alpha}_s\left(QQ_0\right) \to \tilde{\alpha}_s\left(QQ_0\right)$ in eq.(4.29) and $\chi_1(\gamma) \to \tilde{\chi}_1(\gamma)$, where χ_1 was introduced in eq. (3.105), together with the corresponding adjustments for the coefficients

$a, b \to \tilde{a}, \tilde{b}$ which enter eq. (4.23). They read

$$\begin{aligned}
\tilde{\chi}_1(\gamma) &= \tilde{\mathcal{S}}\chi_0(\gamma) + \frac{3}{2}\zeta(3) + \frac{\Psi''(\gamma) + \Psi''(1-\gamma) - \phi(\gamma) - \phi(1-\gamma)}{4} \\
&- \frac{\pi^2 \cos(\pi\gamma)}{4\sin^2(\pi\gamma)(1-2\gamma)}\left[3 + \left(1 + \frac{n_f}{N_c^3}\right)\frac{2+3\gamma(1-\gamma)}{(3-2\gamma)(1+2\gamma)}\right] \\
&+ \frac{1}{8}\left[\frac{3}{2}(Y-1)\xi + \left(1 - \frac{Y}{3}\right)\xi^2 + \frac{17Y}{2} - \frac{\xi^3}{6}\right]\chi_0(\gamma), \qquad (4.32) \\
\tilde{a} &= -\frac{13}{36}\frac{n_f}{N_c^3} - \frac{55}{36} + \frac{3Y-3}{16}\xi + \frac{3-Y}{24}\xi^2 - \frac{1}{48}\xi^3 + \frac{17}{16}Y \qquad (4.33) \\
\tilde{b} &= -\frac{n_f}{6N_c^3} - \frac{11}{12}, \qquad (4.34)
\end{aligned}$$

where $\tilde{\mathcal{S}} = (4-\pi^2)/12$.

In order to access regions with $Q^2 \simeq 1\,\mathrm{GeV}^2$, we use the parametrization for the running coupling introduced in eq. (3.123) [99] that freezes in the IR, which can be rewritten in the form:

$$\bar{\alpha}_s\left(\mu_R^2\right) = \frac{4N_c}{\beta_0 \ln\frac{\mu_R^2}{\Lambda^2}} + f\left(\frac{\mu_R^2}{\Lambda^2}\right), \quad f\left(\frac{\mu^2}{\Lambda^2}\right) = \frac{4N_c}{\beta_0}\,\frac{125\left(1 + 4\frac{\mu_R^2}{\Lambda^2}\right)}{\left(1 - \frac{\mu_R^2}{\Lambda^2}\right)\left(4 + \frac{\mu_R^2}{\Lambda^2}\right)^4}. \qquad (4.35)$$

The final expression used in the numerical analysis is then given by

$$\hat{\alpha}_s(QQ_0, \gamma) = \tilde{\alpha}_s(QQ_0, \gamma) + f\left(\frac{QQ_0}{\Lambda^2}\right), \qquad (4.36)$$

which replaces eq. (4.31) in all expressions.

Another approach to optimize the pertubative series would consist on applying the principle of minimal sensitivity (PMS), mentioned in the introductory section. This tool will not be used in the present analysis but will be a key element in our next phenomenological study, presented in section 5.1.

4.2 Comparison to HERA data

4.2.1 Transition from soft to hard Pomeron

We can easily obtain λ_p from F_2 in the high energy limit, using eq. (4.30):

$$\lambda_p = \frac{1}{F_2}\frac{\mathrm{d}\ln F_2(x, Q^2)}{\mathrm{d}\ln(1/x)}\,.$$

To obtain our theoretical results we used eq. (4.27) with the modifications described in that section. For the comparison with DIS data we chose the values

$Q_0 = 0.28\,\mathrm{GeV}$ and $\delta = 8.4$ for the case with LO photon impact factor and $\delta = 6.5$, $Q_0 = 0.28$ GeV for the kinematically improved case (see fig. 4.5 for the comparison of the two). Note that the dependence on the overall normalization factor $\mathcal{C}$ cancels for this observable. We evaluate the QCD running coupling constant for $n_f = 4$ and $\Lambda = 0.21\,\mathrm{GeV}$, corresponding to a $\overline{\mathrm{MS}}$ coupling of $\alpha_s^{\overline{\mathrm{MS}}}(M_Z^2) = 0.12$. The result is shown in fig. 4.4.

The numerical input shown in the second column of table 4.1 and used as experimental data in fig. 4.4 has been derived from the combined analysis performed by H1 and ZEUS in Ref. [28] with $x < 10^{-2}$. To obtain the points we fit F_2 for each bin in Q_i^2 to the curve $F_2(Q_i^2, x_{\{j\}}) = c \cdot x_{\{j\}}^{-\lambda_p}$, $x_{\{j\}}$ being the set of x experimental values encountered between the x_{min} and x_{max} given in the third and fourth columns of the table. The error bars are taking into account both statistical and systematic uncertainties added in quadrature.

Regarding the theoretical results, it is of crucial importance to take into account the experimental cuts in x to get a meaningful result. In order to do so we have calculated the theoretical effective pomeron intercept at each Q^2 averaging its values in a sample of x space consistent with the actual experimental cuts in x, given in the last two columns of table 4.1. This is what is shown in fig. 4.4 as "Real cuts". To generate the continuous line with label "Smooth cuts" we have used as boundaries in x space those shown in fig. 4.3, which correspond to an interpolation of the real experimental boundaries. Note that the difference between both approaches is very small.

In fig. 4.4 we only show the results for the LO photon impact factor, the reason being purely historical, since this result was first presented in [16] only with the LO case. A comparison with the case for kinematically improved photon impact factor is given in fig. 4.5. It can be seen how the LO impact factor generates lower values than the kinematically improved one in the high Q^2 region and slightly higher ones when $Q^2 \lesssim 2\,\mathrm{GeV}^2$. It is interesting to see how the approach presented here allows for a good description of the data in a very wide range of Q^2, not only for high values, where the experimental uncertainties are larger, but also in the non-perturbative regions due to our treatment of the running of the coupling. Encouraged by these positive results let us now turn to investigate more differential distributions, that is, the structure functions F_2 and F_L.

4.2.2 Proton structure functions

Let us now compare our theoretical results with the experimental data for the two proton structure functions.

Q^2 (GeV^2)	λ_p^{fit}	x_{min}	x_{max}
0.2	0.116 ± 0.033	0.00000441	0.000251
0.25	0.0960 ± 0.0094	0.00000552	0.00158
0.35	0.0976 ± 0.0072	0.00000662	0.00251
0.4	0.0837 ± 0.0082	0.00000883	0.000631
0.5	0.0998 ± 0.0083	0.0000158	0.0032
0.65	0.1327 ± 0.0099	0.0000158	0.0032
0.85	0.145 ± 0.011	0.00002	0.0032
1.2	0.1583 ± 0.0083	0.00002	0.005
1.5	0.1462 ± 0.0076	0.000032	0.0032
2	0.1625 ± 0.0064	0.00005	0.0032
2.7	0.1603 ± 0.0047	0.00005	0.005
3.5	0.1698 ± 0.0038	0.00008	0.008
4.5	0.1916 ± 0.0053	0.00013	0.0032
6.5	0.2040 ± 0.0043	0.00013	0.005
8.5	0.2134 ± 0.0055	0.0002	0.005
10	0.2243 ± 0.0079	0.0002	0.005
12	0.2232 ± 0.0057	0.0002	0.005
15	0.2400 ± 0.0041	0.00032	0.008
18	0.2439 ± 0.0045	0.0005	0.008
22	0.269 ± 0.012	0.0005	0.008
27	0.2706 ± 0.0048	0.0005	0.008
35	0.2837 ± 0.0058	0.0008	0.008
45	0.2962 ± 0.0065	0.0008	0.008
60	0.3156 ± 0.0083	0.0013	0.008
70	0.330 ± 0.014	0.0013	0.008
90	0.299 ± 0.013	0.002	0.008
120	0.319 ± 0.018	0.002	0.008
150	0.335 ± 0.027	0.0032	0.008
200	0.371 ± 0.040	0.005	0.008
250	0.351 ± 0.053	0.005	0.008
300	0.398 ± 0.082	0.005	0.008

Table 4.1: The results for the fits using the F_2 combined HERA data [28] for $x < 0.01$ in bins of Q^2 to $F_2(x, Q^2) = c \cdot x^{-\lambda_p}$. The errors give the statistical and systematic uncertainties added in quadrature. x_{min} and x_{max} bound the x-range of each bean.

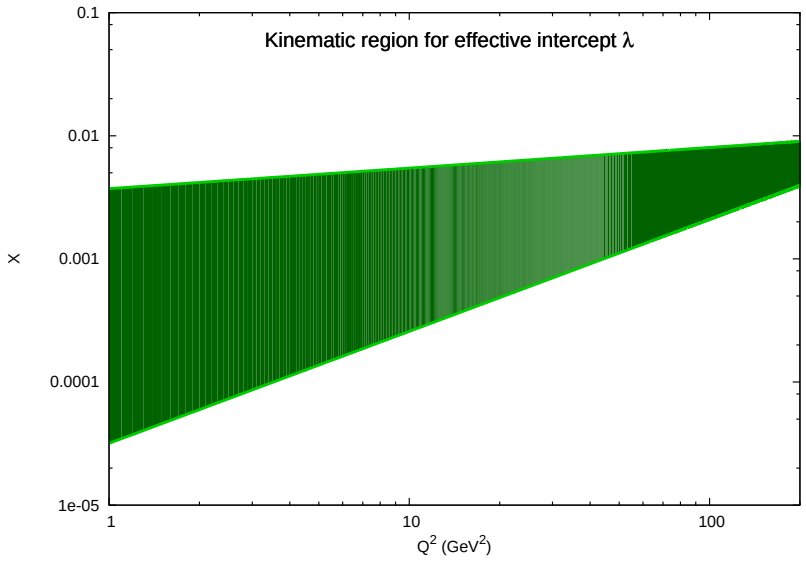

Figure 4.3: Smooth cuts in x used for the effective intercept of F_2.

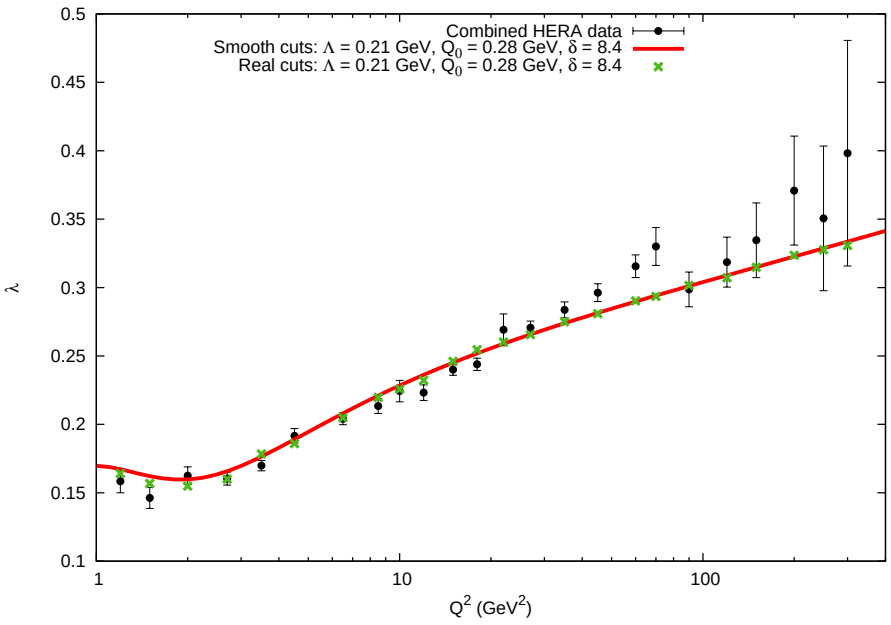

Figure 4.4: Comparison of our prediction with experimental data.

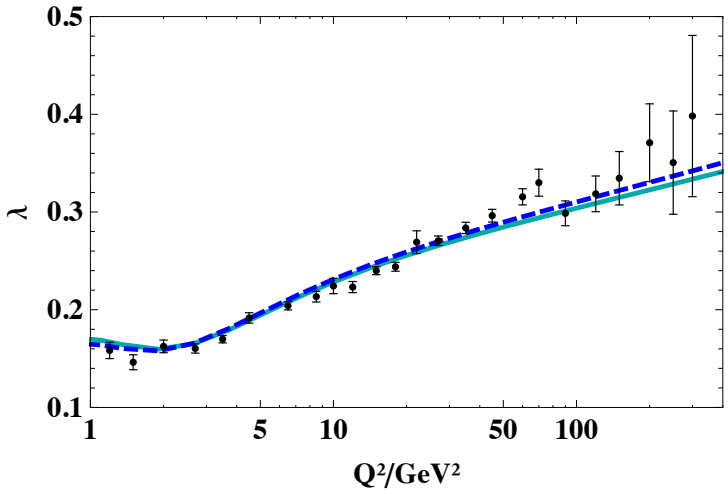

Figure 4.5: Fit to λ for F_2 with the LO photon impact factor (solid line) and the kinematically improved one (dashed line). The data set has been extracted from [28].

Analysis of F_2

In order to present our results we first select data with fixed values of x and compare the Q^2 dependence of our theoretical predictions with them, fixing the normalization for the LO impact factor to $\mathcal{C} = 1.50$ and to 2.39 for the kinematically improved one. The results are presented in fig. 4.6.

The equivalent comparison to data, this time fixing Q^2 and looking into the evolution in the x variable, is shown in fig. 4.7. We observe that our predictions give a very accurate description of the data for both types of impact factors.

We want to remark that the values obtained for the parameters in this fit are in qualitative agreement with what one would expect theoretically for the proton impact factor, since Q_0 is very close to the confinement scale of QCD and the value of δ sets the maximal contribution from the impact factor also in that region. This is reasonable, given the large transverse size of the proton.

Analysis of F_L

The longitudinal structure function is an interesting observable, very sensitive to the gluon content of the proton. We will now present our predictions for F_L using the best values for the parameters previously obtained in the fit of F_2. We will see that the agreement with the data is very good.

In a first set of plots, shown in fig. 4.8, Q^2 is fixed and we study the x

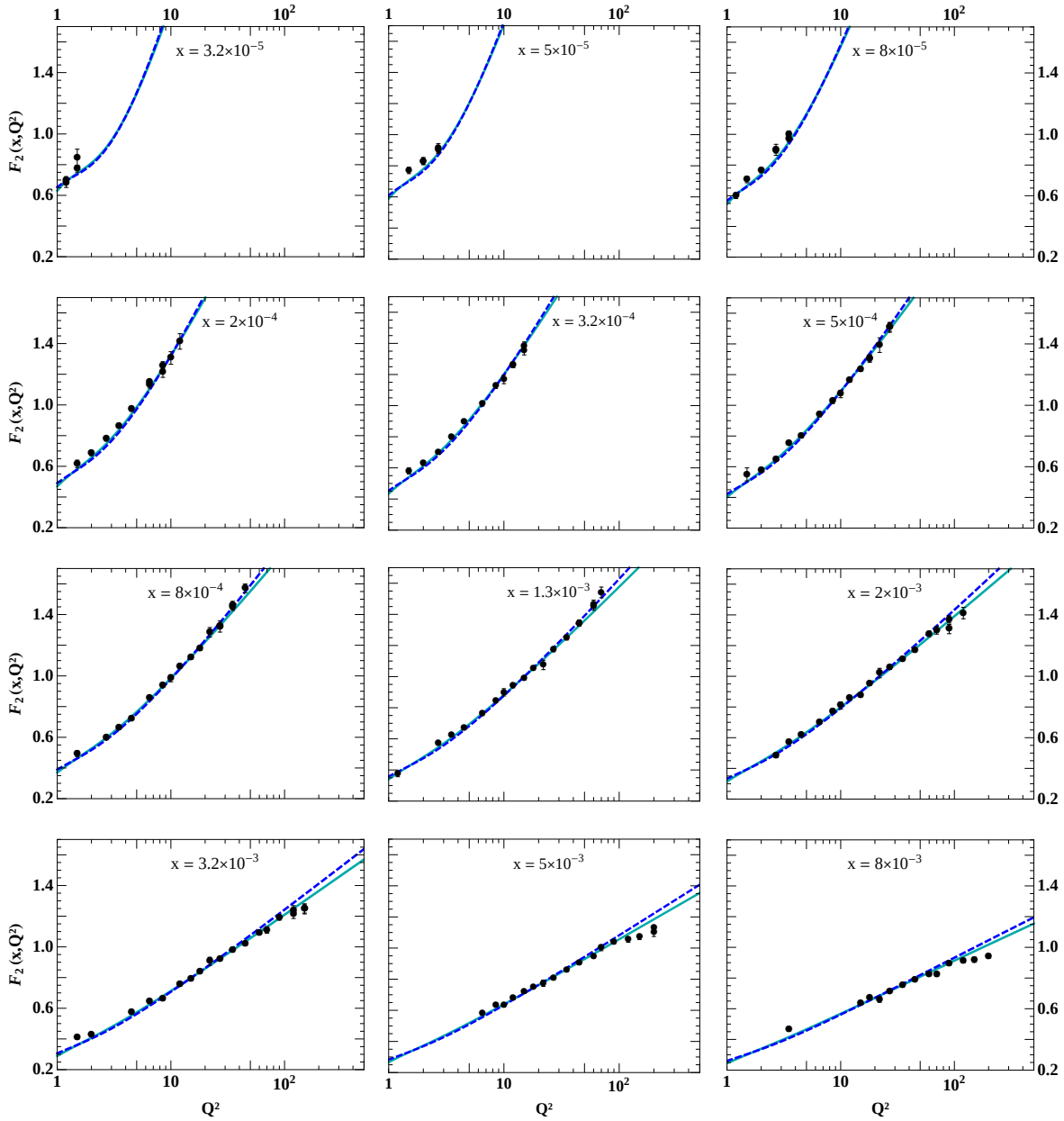

Figure 4.6: Study of the dependence of $F_2(x, Q^2)$ on Q^2 using the LO photon impact factor (solid lines) and the kinematically improved one (dashed lines). Q^2 runs from 1.2 to 200 GeV^2.

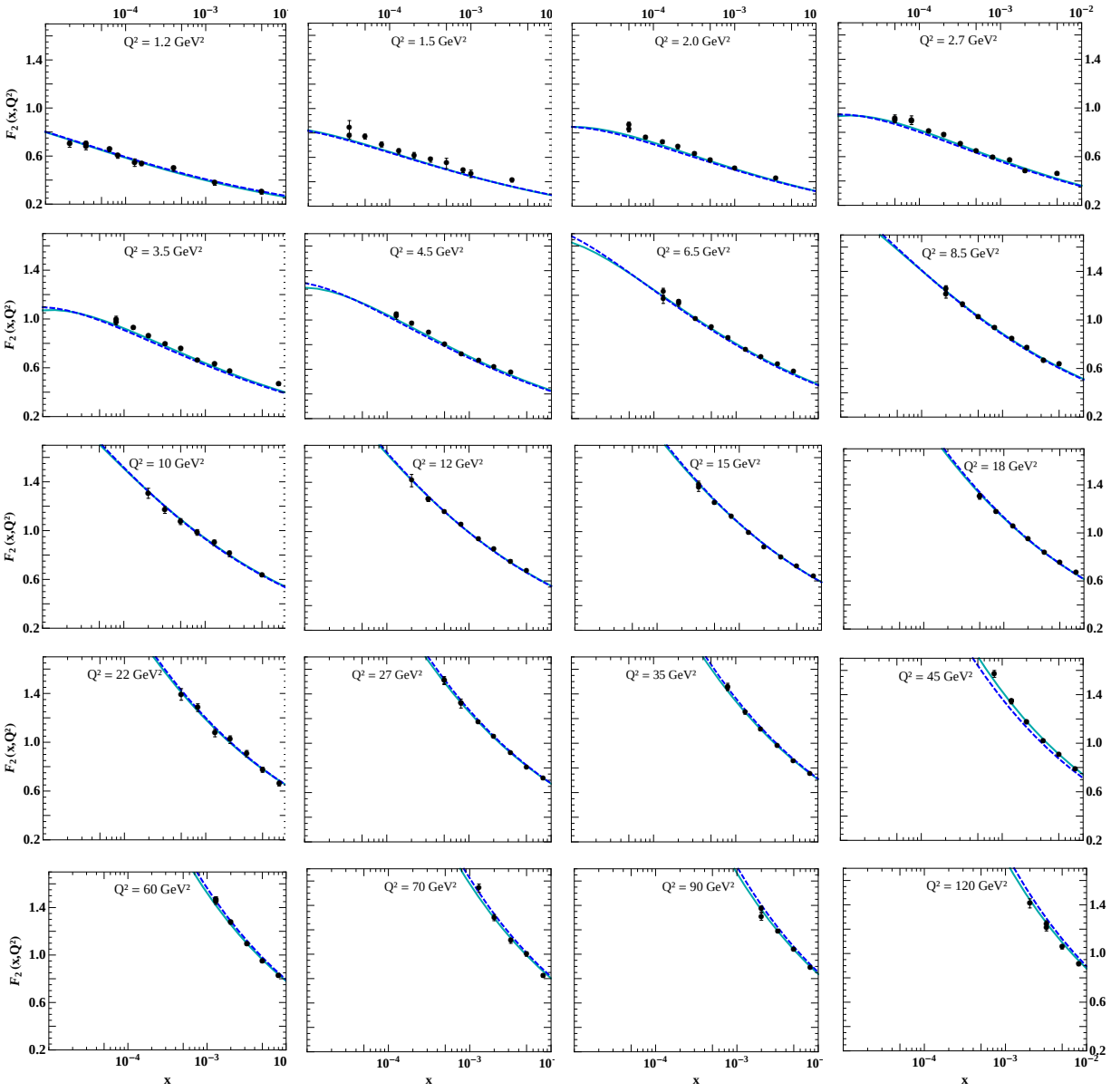

Figure 4.7: Study of the dependence of $F_2(x, Q^2)$ on x using the LO photon impact factor (solid lines) and the kinematically improved one (dashed lines). Q^2 runs from 1.2 to 120 GeV^2.

dependence of F_L. The experimental data have been taken from [25]. To present the Q^2 dependence it is convenient to calculate, for each bin in Q^2, the average value of x, see fig. 4.9. In some sense this is a similar plot to the one previously presented for λ in the F_2 analysis and we can see that the effect of using different types of impact factors is to generate a global shift in the normalization. Again we note that we have an accurate description of the transition from high to low Q^2, which was one of the main targets of our work.

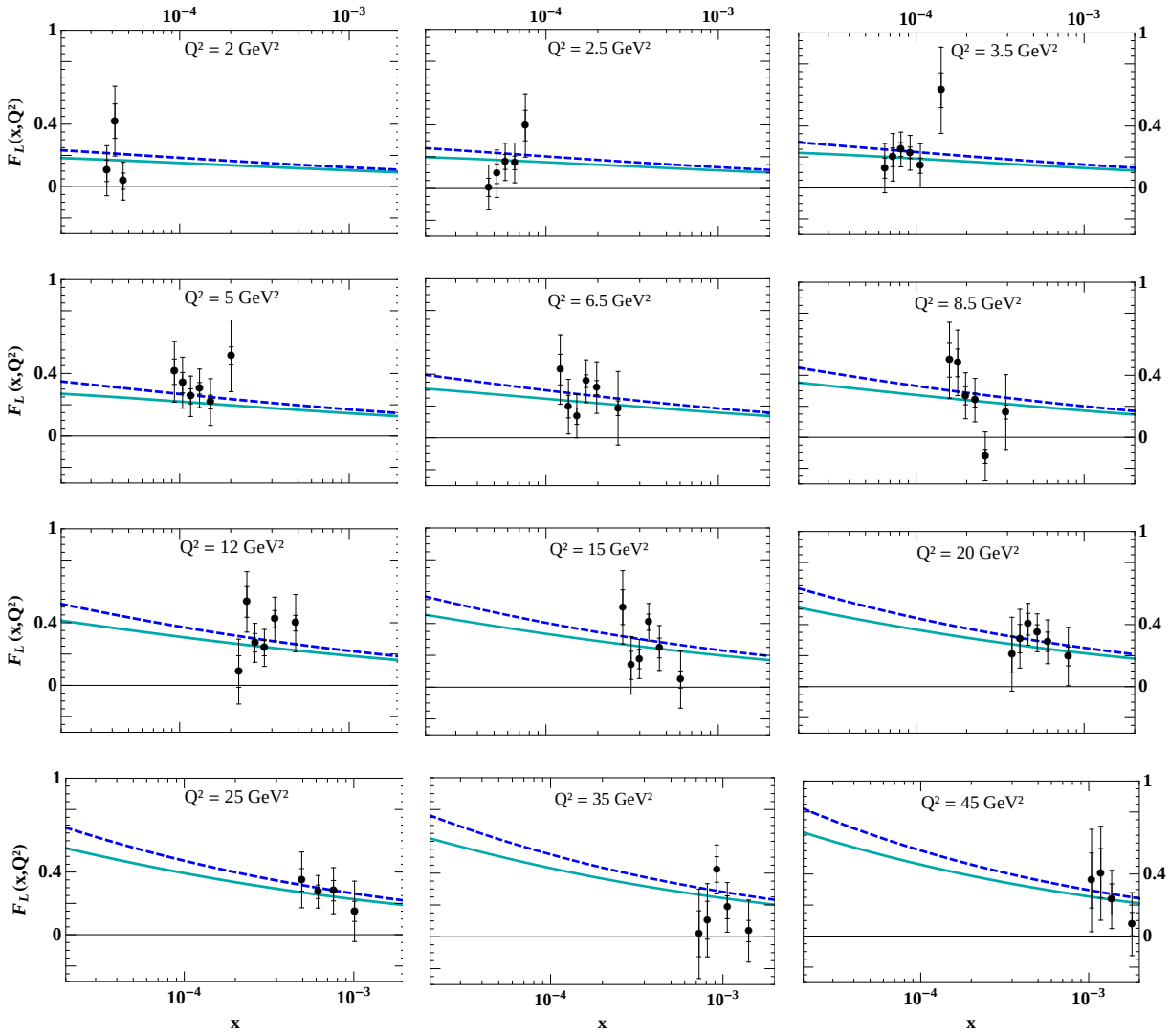

Figure 4.8: Fit to F_L with the LO photon impact factor (solid lines) and the improved one (dashed lines). The experimental data are taken from [25].

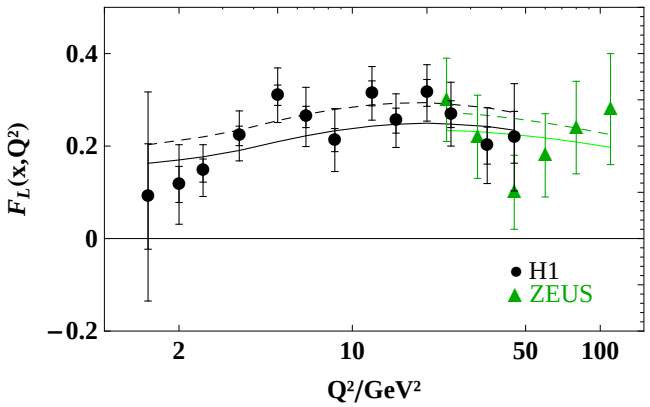

Figure 4.9: The proton structure function F_L as a function of Q^2. The average x values for each Q^2 of the H1 data are given in Figure 13 of [25]. ZEUS data are taken from [22]. The solid lines represent our calculation with the LO photon impact factor and the dashed lines using the kinematically improved one.

4.2.3 Predictions for future colliders

While our predictions for the structure functions are in agreement with the data from the HERA collider experiments H1 and ZEUS, these observables are too inclusive to provide unambiguous evidence for BFKL evolution (for other recent studies in this context see [107]). Even though qualitatively different, predictions from DGLAP evolution and saturation models agree within errors with the currently available data set (see *e.g.* [22,25]). In order to distinguish among different parton evolution sets new collider experiments are needed, such as the proposed Electron-Ion-Collider (EIC) at BNL/JLab (USA) [111,112] or the Large Hadron Electron Collider (LHeC) at CERN (Switzerland) [31, 113]. The latter will be able to measure both F_2 and F_L at unprecedented small values of Bjorken x. In fig. 4.10 we present two studies with our predictions for F_2 and F_L down to values of $x = 10^{-6}$ which can be compared to some predictions presented by the collaboration group of LHeC, shown in fig. 4.11. They take into account linear DGLAP approaches and models with saturation. It can be seen how our predictions are within their presented curves, and how the kinematically improved results would lie very close to the pseudodata for $Q^2 = 10$ GeV^2.

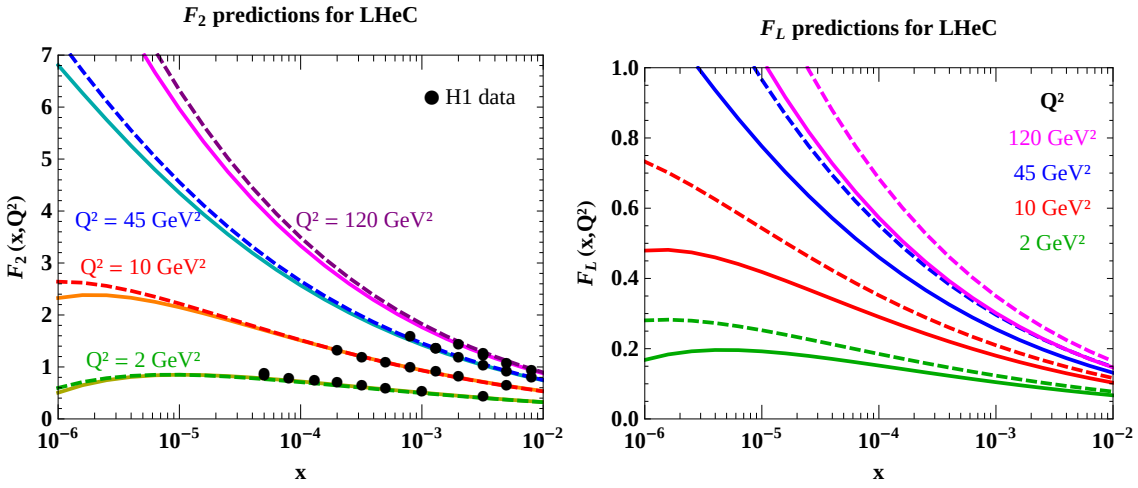

Figure 4.10: Predictions for F_2 (left) and F_L (right) for LHeC. On the left plot, the curve with $Q^2 = 10\text{GeV}^2$ can be compared with fig. 4.13 of [31] (fig. 4.11). Simulated measurements for F_L in the kinematic range plotted here (right) can be found in Figure 3.7 of the same reference.

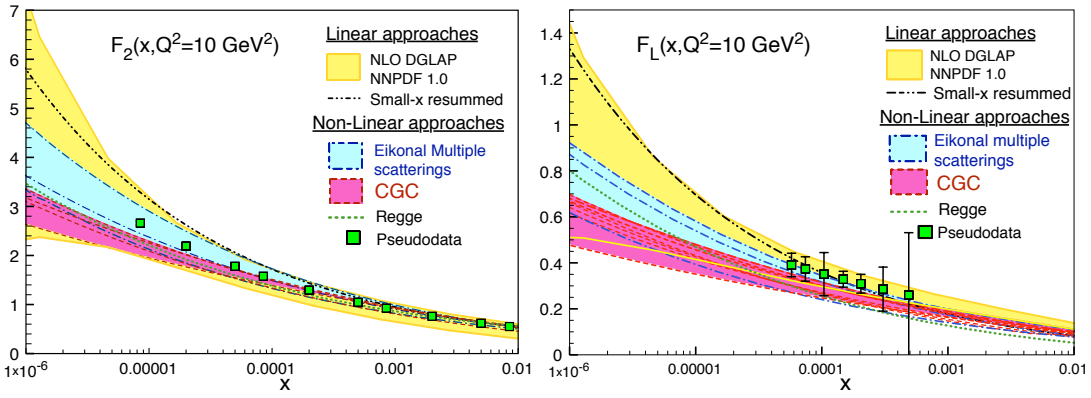

Figure 4.11: Predictions from standard linear DGLAP-based QCD and from models which include saturation effects for $F_2(x, Q^2 = 10\text{GeV}^2)$ (left) and $F_L(x, Q^2 = 10\text{GeV}^2)$ (right) versus x, together with some pseudodata. Detailed explanations can be found in the text of [31], where the figures have been taken from (fig. 4.13).

4.2.4 Conclusions

In this first chapter in phenomenology we have presented a quite challenging application of the BFKL dynamics: the description of the x and Q^2 dependence of the proton structure functions as extracted from Deep Inelastic Scattering HERA data. As a consequence of this we have been able to give some predictions for these observables that could be used at future colliders, specially at the LHeC.

As expected, in order to get a correct dependence on the photon virtuality at high values of the scattering energy, we had to improve the collinear region given by the pure NLL BFKL kernel by getting rid of the collinear poles through an all-order resummation. It was more striking to find the apparent need of optimal renormalization with analytic running coupling in the infrared in order to accurately describe the regions of low Q^2. Good fits were achieved for all regions down to $Q^2 = 4$ GeV^2 in $\overline{\text{MS}}$ scheme. The big achievement of the change of scheme was to be able to fit all data down to $Q^2 = 1$ GeV^2 with great accuracy and up to $Q^2 \simeq 200$ GeV^2, which is more than reasonable, given the fact that we are using a model for the proton impact factor with only two free parameters plus a normalization and a photon impact factor at LO accuracy[2].

It is possible to improve the quality of the fits by introducing subleading contributions such as threshold effects in the running of the coupling (although their effect is very small, we already checked this), heavy quark masses and, of course, higher order corrections to the photon impact factor which are already available [114]. We leave this work, partially on progress, for a future study.

Our next task will be to use these parameterizations to describe more exclusive observables, such as heavy quark production at the Large Hadron Collider at CERN, as it will be presented in the next chapter.

[2]It can be seen in the plots how the results for the kinematically improved one are rather similar.

Chapter 5

Exclusive observables

As we have previously discussed it is very important to study exclusive observables exclusive observables in order to distinguish among different models giving very similar predictions for DIS-like ones [115]. LHC offers high values of s and a very large number of events, allowing for the study of these kind of observables.

In this chapter three different exclusive observables that can be produced at the LHC will be analyzed. Section 5.1 presents a phenomenological study for the production of Mueller-Navelet jets at NLL accuracy in the gluon Green's function and the jet vertices considering collinear corrections and using PMS for the choice of scales, focusing on the ratios of azimuthal angle correlations. This work has been presented in [116]. In sections 5.2 and 5.3 two different processes involving heavy quark hadroproduction are considered. The first one, partially presented in [117] deals with the central production of a pair of heavy quarks that could be produced at the CMS detector [118] while in the second one the quark pair is emitted collinear to one of the parent hadrons leaving enough phase space with respect to the other one so that soft gluon emission can be produced. This creates an asymmetric configuration specially convenient to be measured at the LHCb detector [119]. These two last contributions are work on progress, so the reader might take the results presented as preliminary.

5.1 NLL forward jet production at hadron-hadron colliders with collinearly improved resummation

In this section we will investigate the stability under variation of the renormalization, factorization and energy scales entering the calculation of the cross section for the production of Mueller-Navelet jets at the LHC at next-to-leading order accuracy, taking into account experimental cuts on the tagged jets. To find optimal values for the scales involved in the observable we use the principal of minimal sensitivity (PMS), already introduced in this thesis. We show that the scales found in this way are more similar to the squared transverse momenta of the tagged jets -and therefore they can be considered more natural-, when the BFKL kernel is improved with a resummation of collinear contributions than when the treatment is at a purely next-to-leading order. A key point of our discussion will be the good perturbative convergence of the ratios of azimuthal angle correlations, which will turn out to be quite insensitive to collinear resummations and well described by the original BFKL framework.

This work can be found in [116].

5.1.1 Motivation and theoretical setup

The theoretical framework we are interested in consists on hadron-hadron collision events in which two hard jets of similar squared transverse momentum are tagged with a relative rapidity Y and a relative azimuthal angle ϕ, *i.e.*, Mueller-Navelet jets [120] (see Fig. 5.1). In principle, these Mueller-Navelet jets are interesting because they should manifest some sort of exponential growth with Y when Y is large. However, the hard matrix elements are convoluted via collinear factorization with the PDF's, which reduce this behavior. When the effect of the PDFs is too big it is useful to look for ratios of distributions in order to remove as much as possible their contribution. Some of them are specially appropriate, since they are quite insensitive to the collinear contributions and enjoy an excellent perturbative convergence within the BFKL context (since the NLL corrections are very small). These are the fractions

$$\mathcal{R}_{mn} \equiv \frac{\langle \cos(m\Delta\phi)\rangle}{\langle \cos(n\Delta\phi)\rangle}, \tag{5.1}$$

with the definition of $\langle\cos(m\Delta\phi)\rangle$ given in eq. (5.12). These ratios were proposed as the ideal BFKL observables several years ago in [100, 101] and have been shown to allow for a discrimination between BFKL and other approaches. They prove the conformal structure of QCD at high energies since m and n can be

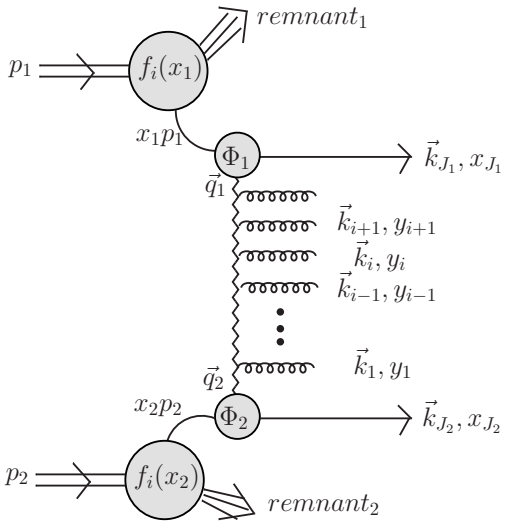

Figure 5.1: Hadroproduction of two Mueller-Navelet jets.

interpreted as conformal spins in elastic scattering, in the so-called pomeron wave function. In this sense it is natural that they exhibit quite a different Y dependence to that generated by more standard methods, such as Monte Carlo event generators based on angular ordering of collinear emissions, since in any other formalism there is not such a two dimensional conformal invariance. The same logic applies to any fixed order calculation. In [121] they were calculated in the $N = 4$ super Yang-Mills theory (other studies of Mueller-Navelet jets can be found in [122, 123]).

Finally, in order to get a good convergence of the BFKL series for conformal spin zero, which corresponds to azimuthal angle averaged quantities directly associated to the exchange of the hard pomeron, we need to use the collinearly improved NLL BFKL kernel already introduced in section 3.4 and used in last chapter. One of the targets of the present work is to show that the collinearly improved result provides a theoretically more judicious prediction than a purely NLL approach. The motivation for this reasoning is that when looking for a region of stability in the three-fold parameter space with renormalization μ_R, factorization μ_F and energy scale s_0, we find that the NLLA "natural" scales are larger than those obtained with a collinearly improved approach. This is a non-trivial statement since this "naturalness" survives the influence of the PDF's, quite sensitive to the choice of factorization scale, similar to what was found in [124–126].

Let us now go to the computation of the observable. The cross section for the process shown in fig. 5.1 differential with respect to the variables parameterizing

the jet phase space ($dJ_i \equiv dx_{J,i} d^{D-2} k_{J,i}$) is given in the high energy limit by means of collinear factorization as a convolution of a partonic cross section with the initial proton PDF's:

$$\frac{d\sigma}{dJ_1 dJ_2} = \sum_{i,j=q,\bar{q},g} \int_0^1 dx_1 \int_0^1 dx_2 \, f_i(x_1,\mu_F) f_j(x_2,\mu_F) \frac{d\hat{\sigma}_{i,j}(x_1 x_2 s,\mu_F)}{dJ_1 dJ_2}, \qquad (5.2)$$

where μ_F is the factorization scale and $x_{1(2)}$ are the longitudinal momentum fractions of the initial state partons. For the hard subprocess it is convenient to write the following representation

$$\frac{d\hat{\sigma}_{i,j}(x_1 x_2 s)}{dJ_1 dJ_2} = \frac{1}{(2\pi)^2} \left(\prod_{i=1,2} \int \frac{d^2\vec{q}_i}{\vec{q}_i^{\,2}} \frac{d\Phi_{J,i}(\vec{q}_i, s_0)}{dJ_i} \right) \int_{\delta - i\infty}^{\delta + i\infty} \frac{d\omega}{2\pi i} \left(\frac{x_1 x_2 s}{s_0} \right)^{\omega} f_\omega(\vec{q}_1, \vec{q}_2) \,,$$

which is valid within NLL accuracy. $d\Phi_{J,1(2)}(\vec{q}_1, s_0)/dJ_{1(2)}$ are the differential jet production vertices, calculated at NLLA in [127, 128] and more recently in [129, 130] (see also the recent derivation using Lipatov's high energy effective action in [131–135]). We can write the kernel in transverse momentum representation as

$$\hat{K} = \bar{\alpha}_s \hat{K}^0 + \bar{\alpha}_s^2 \hat{K}^1 + \hat{K}_{RG}, \qquad (5.3)$$

where $\hat{K}^0$ is the LL kernel, $\hat{K}^1$ the complete NLL correction containing running coupling effects -see eq. (4.24)- and $\hat{K}_{RG}$ contains the collinear corrections to the NLL result. Its eigenvalue after acting on the basis of LL eigenfunctions has been already analyzed in sec. 4.1. It is given in this more general case by eq. (4.25) extended to all conformal spins. The n-dependent $\chi_0(n,\nu)$ and $\chi_1(n,\nu)$ functions are defined in eqs. (3.104,3.105), respectively. It will be convenient at this point to define a function $\bar{\chi}(n,\nu)$ such that

$$\chi_1(n,\nu) = -\frac{\beta_0}{8\,N_c} \left(\chi_0^2(n,\nu) - \frac{10}{3} \chi_0(n,\nu) \right) + \bar{\chi}(n,\nu) \,. \qquad (5.4)$$

The expression for the n-dependent conformal invariant piece of the collinear contribution, $\chi_{RG}(n,\nu)$ [15,100,101], was already introduced in eqs. (3.134,3.135) and eq. (3.136). We can now express the differential cross section for the dijet production in terms of an expansion in Fourier components in the azimuthal angle, *i.e.*

$$\frac{d\sigma}{dy_{J_1} dy_{J_2}\, d|\vec{k}_{J_1}|\, d|\vec{k}_{J_2}| d\phi_{J_1} d\phi_{J_2}} = \frac{1}{(2\pi)^2} \left(\mathcal{C}_0 + \sum_{n=1}^{\infty} 2\cos(n\phi)\, \mathcal{C}_n \right) , \qquad (5.5)$$

where $\phi = \phi_{J_1} - \phi_{J_2} - \pi$, $y_{1(2)}$ are the rapidities of the two produced jets and

$$\mathcal{C}_m = \int_0^{2\pi} d\phi_{J_1} \int_0^{2\pi} d\phi_{J_2} \, \cos[m(\phi_{J_1} - \phi_{J_2} - \pi)] \, \frac{d\sigma}{dy_{J_1} dy_{J_2} \, d|\vec{k}_{J_1}| \, d|\vec{k}_{J_2}| d\phi_{J_1} d\phi_{J_2}} \, . \tag{5.6}$$

The final expression reads

$$\begin{aligned} \mathcal{C}_n = \frac{x_{J_1} x_{J_2}}{|\vec{k}_{J_1}||\vec{k}_{J_2}|} \int_{-\infty}^{+\infty} d\nu \left(\frac{\hat{s}_J}{s_0}\right)^{\bar{\alpha}_s \tilde{\chi}_0} \alpha_s^2 \tilde{c}_1 \tilde{c}_2 \left[1 + \alpha_s \left(\frac{\tilde{c}_1^{(1)}}{\tilde{c}_1} + \frac{\tilde{c}_2^{(1)}}{\tilde{c}_2}\right)\right. \\ \left. + \ln\left(\frac{\hat{s}_J}{s_0}\right) \tilde{\chi}_{RG} + \bar{\alpha}_s^2 \ln\left(\frac{\hat{s}_J}{s_0}\right) \left(\tilde{\chi}_1 + \frac{\beta_0}{8C_A} \tilde{\chi}_0 \ln\left(\frac{\mu_R^4}{\vec{k}_{J_1}^2 \vec{k}_{J_2}^2}\right)\right)\right], \end{aligned} \tag{5.7}$$

where we have introduced the following notation: $\hat{s}_J \equiv x_{J_1} x_{J_2} s$, $\bar{\alpha}_s = \bar{\alpha}_s(\mu_R)$, $\tilde{\chi} \equiv \chi(n,\nu)$ and with the parameters $\tilde{c}_{1(2)} \equiv c_{1(2)}(n, \nu, |\vec{k}_{J1(2)}|, x_{J_{1(2)}}, \mu_F)$ and $\tilde{c}_{1(2)}^{(1)} \equiv c_{1(2)}^{(1)}(n, \nu, |\vec{k}_{J1(2)}|, x_{J_{1(2)}}, \mu_F)$ being, respectively, the LL and NLL contributions to the differential impact factors [130], projected in the ν-space and convoluted with the proton PDF's. We refer the reader to [130, 136] for the explicit expressions. We have taken the approximation of a small cone radius in the jet definition since this makes the numerical study much simpler and the final results are very similar to the equivalent ones using the exact expressions [137, 138].

In order to perform the numerical analysis and investigate the dependence of our results on the energy variable s_0, we use the exponentiated representation

$$\begin{aligned} \mathcal{C}_n^{\exp} &= \frac{x_{J_1} x_{J_2}}{|\vec{k}_{J_1}||\vec{k}_{J_2}|} \int_{-\infty}^{+\infty} d\nu \, \exp\left[(Y - Y_0)\left(\bar{\alpha}_s \tilde{\chi}_0 + \bar{\alpha}_s^2 \left(\tilde{\chi}_1 + \tilde{\chi}_{RG}\right)\right)\right] \\ &\quad \times \alpha_s^2 \tilde{c}_1 \tilde{c}_2 \left[1 + \bar{\alpha}_s^2 \left(Y - Y_0\right) \frac{\beta_0}{8C_A} \tilde{\chi}_0 \ln\left(\frac{\mu_R^4}{\vec{k}_{J_1}^2 \vec{k}_{J_2}^2}\right) + \alpha_s \left(\frac{\tilde{c}_1^{(1)}}{\tilde{c}_1} + \frac{\tilde{c}_2^{(1)}}{\tilde{c}_2}\right)\right] , \end{aligned} \tag{5.8}$$

where we have introduced the rapidity variables

$$Y = \ln\left(\frac{x_{J_1} x_{J_2}}{|\vec{k}_{J_1}||\vec{k}_{J_2}|}\right) \qquad \text{and} \qquad Y_0 = \ln\left(\frac{s_0}{|\vec{k}_{J_1}||\vec{k}_{J_2}|}\right). \tag{5.9}$$

Note that a "natural" value for the free scale s_0 should be such that $Y_0 \simeq 0$.

5.1.2 Discussion of the numerical results

Study of $\mathcal{C}_0$, $\mathcal{C}_1$ and $\mathcal{C}_2$

Let us first show the analysis of the dependence of the coefficients $\mathcal{C}_0$, $\mathcal{C}_1$, $\mathcal{C}_2$ on Y, where $\mathcal{C}_0$ is the differential cross section integrated over azimuthal angle of the tagged jets. Regarding the factorization and renormalization scales,

we will consider two choices of different nature. In the first one we will set $\mu_F = \mu_R$ and let both equally vary when applying the PMS while in the second one we will relax this condition by fixing each of the factorization scales to the squared transverse momentum of their corresponding jet vertex and let only vary μ_R to find the region of stability. We will also use for the analysis the PDF set MSTW2008nnlo [12] and the two-loop running coupling with $\alpha_s(M_Z) = 0.11707$. In order to compare with the scale dependence and values for the different coefficients obtained in previous calculations [136] based on the same approach but without the collinear improvements, the following kinematic settings are selected:

- the LHC design energy: $\sqrt{s}$=14 TeV;
- jet cone size of $R = 0.5$.

Also, two different final state configurations will be considered, depending on the collinearity of the produced jets:

- symmetric configuration: $|\vec{k}_{J_1}| = |\vec{k}_{J_2}| = 35$ GeV and
- asymmetric configuration: $|\vec{k}_{J_1}| = 20$ GeV, $|\vec{k}_{J_2}| = 35$ GeV.

One immediate benefit of the collinearly-improved approach here applied is that, contrary to what happened in the purely NLL calculation given in [136], we will be able in this case to consider also the kinematics with this last asymmetric choice of the jet transverse momenta proposed, finding a stability region for all the quantities under study, as we shall see.

Following the experimental constraints described in [139], we restrict the rapidities of the tagged jets to the region $3 \leq |y_J| \leq 5$. For our choice of forward jet rapidities, Y takes values between 6 and 10. We introduce a rapidity bin size of $\Delta y_J = 0.5$ and then evaluate the sum which runs over all the possible values of $(y_{J_1})_j$ for a given Y. In eq. (5.10) $\tilde{\mathcal{C}}_n(x, y)$ corresponds to the coefficient $\mathcal{C}_n$ where one of the jets has rapidity x and the other y. Fig. 5.2 shows the possible ways of matching the rapidities.

$$C_n(Y) \;=\; \sum_j \tilde{\mathcal{C}}_n\left((y_{J_1})_j, Y - (y_{J_1})_j\right) \Delta y_J \; . \tag{5.10}$$

Formally, our expressions for the coefficients C_n, when expanded at NLL ($\mathcal{O}(\alpha_s^2)$), do not have any dependence on the renormalization, μ_R, and energy, s_0, scales (as we have already indicated, the factorization scale has been already fixed). However, when exponentiating the BFKL kernel following bootstrap terms beyond NLL approximation are introduced and generate a residual dependence on

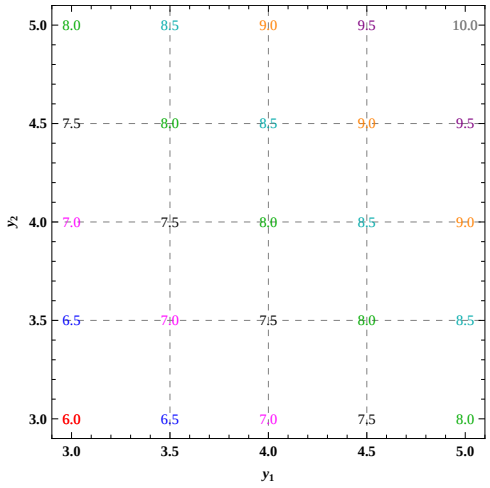

Figure 5.2: Rapidity population. The numbers appearing as markers are the values of the rapidity difference Y.

these scales. This dependence would cancel again order by order in perturbation theory if we had the BFKL kernel and jet vertices calculated at higher orders. In a purely NLL approach (with the conformal invariant pieces of the kernel exponentiated) the dependence on these scales is larger than when introducing the collinear improvements. This is something we explicitly show in our numerical results; we find that the regions of stationary values in the multidimensional scale space are closer to the physical scales in the problem in the latter case than in the former.

Following previous works [124–126,136], we use for our analysis an adaptation of the *principle of minimal sensitivity* (PMS) [20], considering as optimal choices for μ_R and s_0 those values for which the physical quantity under examination exhibits the minimal sensitivity to changes in both of these scales. Without using the RG-improved kernel the optimal choices for these parameters when Y grows were found to be quite far from the external scales of the process [136]. Let us now see how the inclusion of the collinear improvement leads to more "natural" values for the optimal scales (similar results were found in Ref [124–126] in the context of light vector meson production).

In our search for optimal values, we take integer values for Y_0 while for μ_R we look for integer multiples of $\sqrt{|\vec{k}_{J_1}||\vec{k}_{J_2}|}$ in the form

$$\mu_R = n_R \sqrt{|\vec{k}_{J_1}||\vec{k}_{J_2}|}\,. \tag{5.11}$$

In this way, the systematic uncertainty of the optimization procedure stems from the resolution of a grid in the $Y_0 - n_R$ plane and we consider as "natural" values of n_R those close to one.

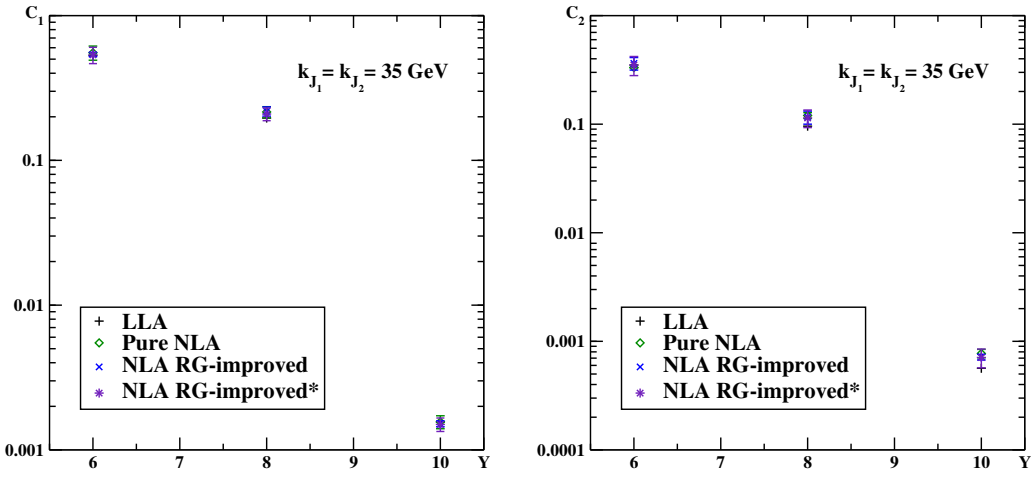

Figure 5.3: Y dependence of C_1 (left) and C_2 (right) for $|\vec{k}_{J_1}| = |\vec{k}_{J_2}| = 35$ GeV at $\sqrt{s} = 14$ TeV.

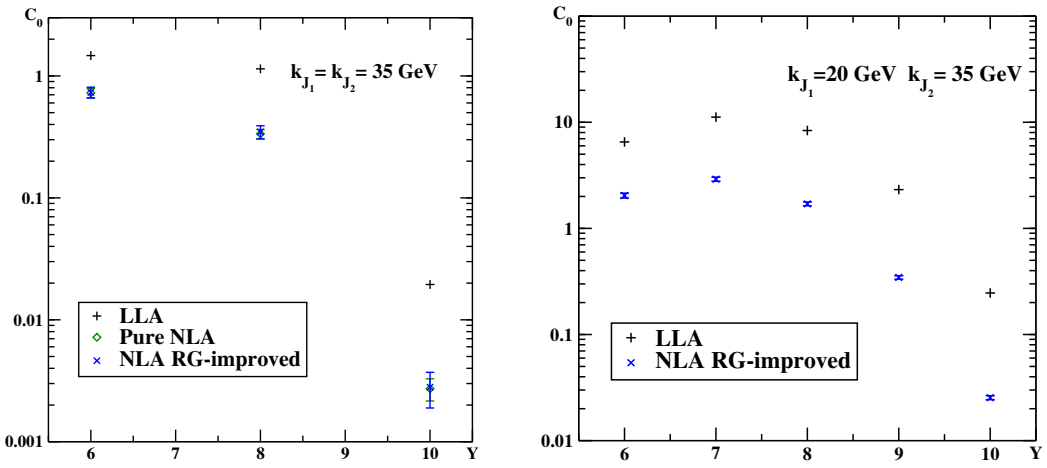

Figure 5.4: Y dependence of C_0 for $|\vec{k}_{J_1}| = |\vec{k}_{J_2}| = 35$ GeV (left) and $|\vec{k}_{J_1}| = 20$ GeV, $|\vec{k}_{J_2}| = 35$ GeV (right) at $\sqrt{s} = 14$ TeV.

Let us first discuss the results for the symmetric kinematics. Filling a grid in the $Y_0 - n_R$ plane we found that a stationary point could always be singled out. Our results, in $\left[\text{nb/GeV}^2\right]$ units, are presented in figs. 5.4 (left) and 5.3 and in tables 5.1. We can see from the tables that there is a small shift towards naturalness regarding the optimal scales when taking into account collinear improvements, in particular for high values of Y. Even if this effect is less evident than in [124–126], it shows that these improvements stabilize the perturbative

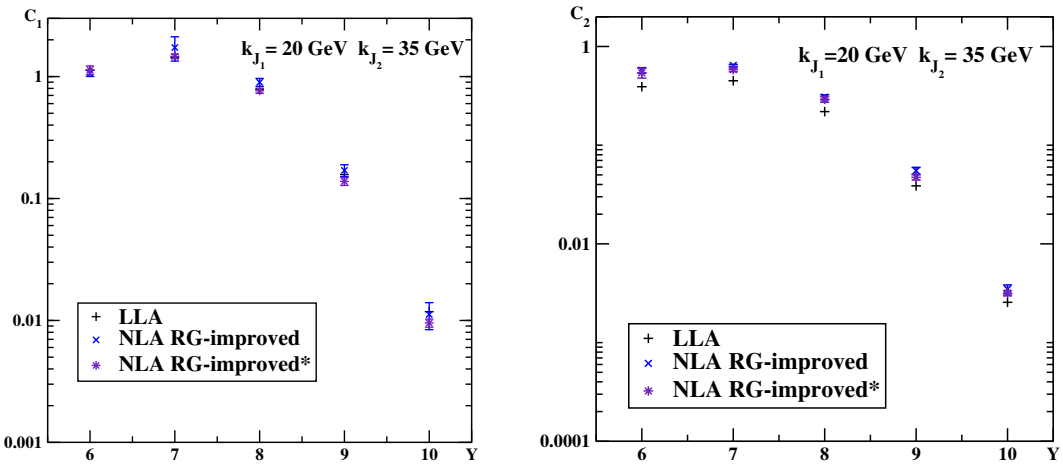

Figure 5.5: Y dependence of C_1 (left) and C_2 (right) for $|\vec{k}_{J_1}| = 20$ GeV, $|\vec{k}_{J_2}| = 35$ GeV at $\sqrt{s} = 14$ TeV.

series. Nevertheless, it is interesting to note that the actual values of the coefficients are in good agreement with the canonical NLL results (they overlap within the error bars), even if the RG-improved results are a bit higher for C_0 and lower for $C_{n>0}$, as it is expected since the RG improvements make the asymptotic pomeron intercept ($n = 0$) to be larger without modifying the $n > 0$ intercepts. This is different to what was found in [124–126], where both approaches generated very different results at the observable level. We believe the main reason for this is that in the case of Mueller-Navelet jets the actual phase space for multijet production is highly constrained by the PDFs, which prevent our cross sections from growing at asymptotic values of Y. It is also noteworthy that the values for C_1 and C_2 obtained with the PMS overlap with the values obtained when being evaluated at the "optimal" scales found for C_0.

For the asymmetric case, with $|\vec{k}_{J_1}| = 20$ GeV and $|\vec{k}_{J_2}| = 35$ GeV, we present our results in figs. 5.4 (right) and 5.5 and in tables 5.2. For C_1 and C_2 we again find the optimal values using the PMS and we also show the values corresponding to the optimal scales obtained for C_0 (last column of tables 5.2, together with the results called "RG-improved*" in fig. 5.5). It is an important fact that in the NLL approach it was not possible to find a stability region in the $n_R - Y_0$ plane and also that the inclusion of the RG-improved kernel proved to be very useful to lower the values of the optimal scales, similar to what happened in [124–126]. In our search for optimal scale values for C_0 and C_1 we always found a stability region, whereas for the coefficient C_2 this was possible only for a few values of Y, finding in other regions local maxima or minima just in one direction of the two-fold parameter space. In such a situation, it was chosen as "optimal" the value for

the parameter exhibiting the least standard deviation in the nearest neighboring points of the chosen grid. It can be seen in the tables how the "optimal" values for the parameters are quite "natural", in particular for C_1 and C_2. On the other hand, the obtained PMS values for C_1 and C_2 and those corresponding to the "optimal" scales for C_0 differ from each other more than in the case of symmetric kinematics, but still overlapping within the error bars.

Study of ratios

Having the complete information about the coefficients C_m we now present the analysis of the Y dependence of the moments of the azimuthal decorrelation, which read

$$\langle \cos(m\phi) \rangle \quad = \quad \frac{\mathcal{C}_m}{\mathcal{C}_0}. \tag{5.12}$$

Let us start by analyzing the results for the symmetric kinematics. Filling a grid in the $n_R - Y_0$ plane we found that a stationary point could always be singled out. Our results are shown in different figures. In fig. 5.6 we present $\langle \cos(\phi) \rangle = C_1/C_0$ and $\langle \cos(2\phi) \rangle = C_2/C_0$ as a function of Y. We observe a strong decorrelation as Y increases. This is generated by the abundance of radiation produced by the iteration of the BFKL kernel. This decorrelation is largely reduced with respect to the LL calculation when the NLL corrections are introduced, showing that the amount of real emissions is much smaller in this approximation. It is interesting to notice how introducing collinear improvements in the NLL result does not have a very big effect. The main reason for this is the symmetric configuration of external momentum scales, which naturally reduces the collinear effects. As we explore more asymmetric configurations the impact of the collinear resummation should be larger, allowing to find stability regions with the collinearly improved NLL result not found in the pure NLL case.

We have presented numerical results for both the ratios

$$C_{m>0}^{(\mathrm{RG-impr-NLA})}/C_0^{(\mathrm{RG-impr-NLA})} \quad \text{and} \quad C_{m>0}^{*(\mathrm{RG-impr-NLA})}/C_0^{(\mathrm{RG-impr-NLA})},$$

giving the results called "RG-improved" and "RG-improved*" in fig. 5.6, respectively, with the latter generating a slightly lower correlation at larger rapidities.

It is important to notice that the origin of the large difference between the LL and NLL results (also with all-order improvements) is due to the influence of C_0 on these observables. The reason for this, as we have already mentioned, is that C_0 does not enjoy a good perturbative convergence due to its direct relation to the conformal spin $n = 0$. However, as the $C_{n>0}$ are nicely convergent within

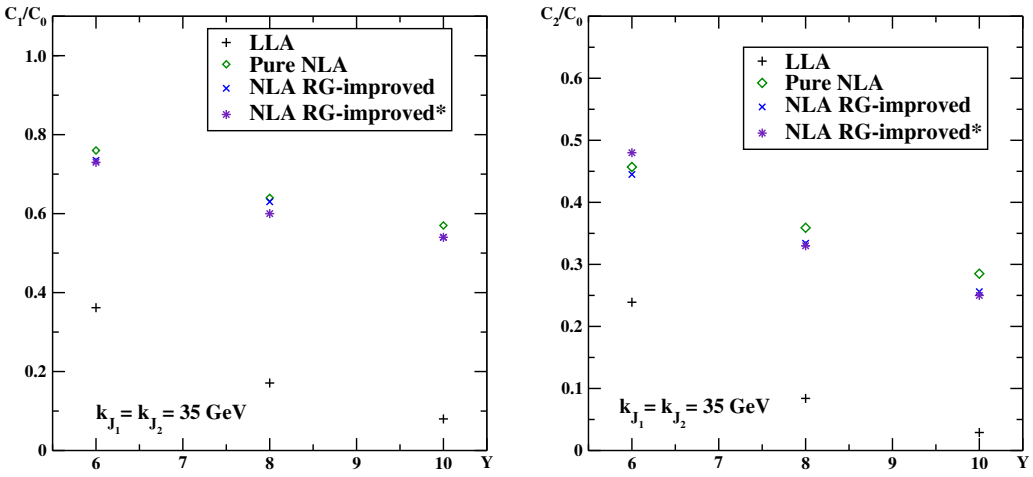

Figure 5.6: Y dependence of C_1/C_0 (left) and C_2/C_0 (right) for $|\vec{k}_{J_1}| = |\vec{k}_{J_2}| = 35$ GeV at $\sqrt{s} = 14$ TeV.

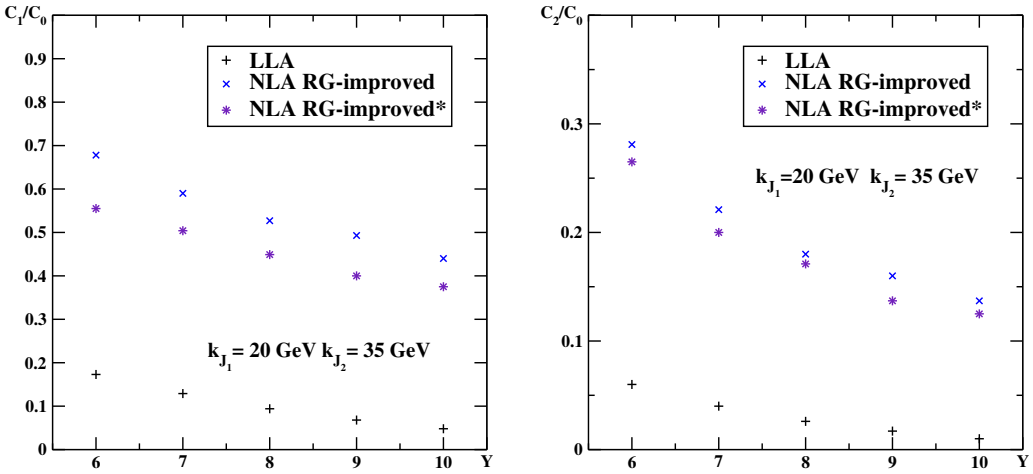

Figure 5.7: Y dependence of C_1/C_0 (left) and C_2/C_0 (right) for $|\vec{k}_{J_1}| = 20$ GeV, $|\vec{k}_{J_2}| = 35$ GeV at $\sqrt{s} = 14$ TeV.

the BFKL formalism, the following ratios are found to be specially convenient BFKL observables [100, 101]:

$$\mathcal{R}_{mn} \equiv \frac{\langle \cos(m\Delta\phi) \rangle}{\langle \cos(n\Delta\phi) \rangle} = \frac{C_m}{C_n}. \tag{5.13}$$

They are free from $n = 0$ contributions if $m, n \neq 0$. We will see how for $\mathcal{R}_{21}$ (the same qualitative behavior would be obtained for any other ratio) that the theoretical predictions are very similar at LL, NLL and with collinear improvements, making of $\mathcal{R}_{mn}$ a robust test of the BFKL formalism. This is shown, for

a symmetric configuration, in fig. 5.8 (left). In order to gauge the theoretical uncertainty of our results we performed four different calculations:

1. $C_2^{(\mathrm{RG-impr-NLA})}/C_1^{(\mathrm{RG-impr-NLA})}$, "RG-improved I" in fig. 5.8 (left).
2. $C_2^{*(\mathrm{RG-impr-NLA})}/C_1^{*(\mathrm{RG-impr-NLA})}$, "RG-improved II" in fig. 5.8 (left).
3. $(C_2/C_1)^{(\mu_{\mathrm{F}}\ \mathrm{fixed})}$, with $\mu_{F_1} = |\vec{k}_{J_1}|$ and $\mu_{F_2} = |\vec{k}_{J_2}|$, using the PMS to find the best values for μ_R and Y_0 -denoted by "RG-improved III" in fig. 5.8 (left), table 5.3 (left)-. Note that the the values obtained for the scales are almost ideal in our understanding of naturalness.
4. $(C_2/C_1)^{(\mu_{\mathrm{F}}=\mu_{\mathrm{R}})}$, "RG-improved IV" in Fig. 5.8 (left), where we restate the condition $\mu_F = \mu_R$ using the same optimal scales as for $(C_2/C_1)^{(\mu_{\mathrm{F}}\ \mathrm{fixed})}$, without finding any deviation in the value of the observable. In this case we could not find any reasonable stability region with optimal scales and this is why we chose the same ones as in the previous point.

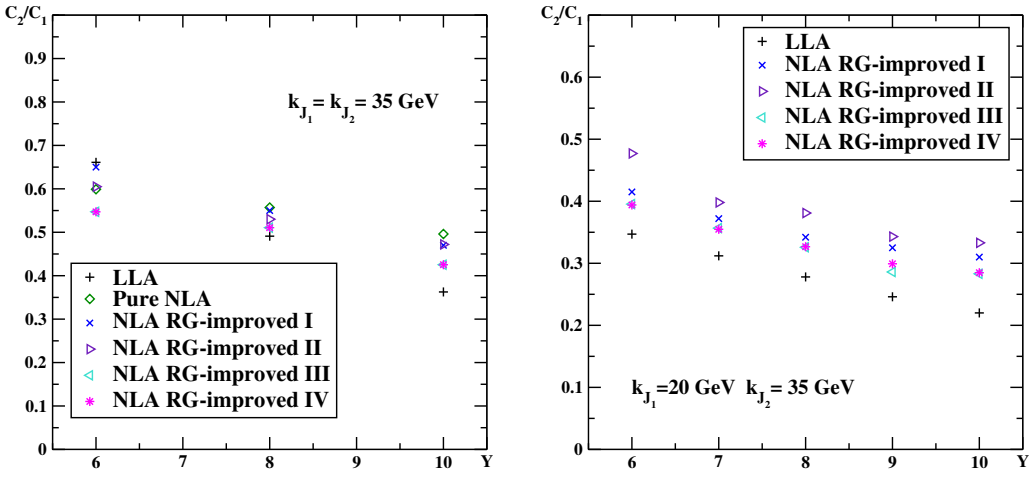

Figure 5.8: Y dependence of C_2/C_1 for $|\vec{k}_{J_1}| = |\vec{k}_{J_2}| = 35$ GeV (left) and for $|\vec{k}_{J_1}| = 20$ GeV, $|\vec{k}_{J_2}| = 35$ GeV (right) at $\sqrt{s} = 14$ TeV.

Let us conclude our analysis with the asymmetric configuration, $|\vec{k}_{J_1}| = 20$ GeV and $|\vec{k}_{J_2}| = 35$ GeV, where the collinear effects are more noticeable. The results are shown in figs. 5.7 and 5.8 (right), corresponding to the values of table 5.3. We found the same lack of stable regions when setting $\mu_F = \mu_R$ than in the pure NLL case, solved by relaxing this condition and taking $\mu_F = |\vec{k}_{J_1}|$ and $\mu_F = |\vec{k}_{J_2}|$ as the factorization scales associated to each of the hadrons. This is a very fortunate choice since it creates a stability region at the "very natural" point $(Y_0, n_R) = (0, 1)$ which is invariant under changes in Y.

5.1.3 Conclusions

We have performed a numerical implementation of a NLL-level calculation for the hadro-production of Mueller-Navelet jets taking into account collinear contributions to all-orders in perturbation theory and using the so-called small-cone approximation for the NLO forward jet vertices. Given the great amount of experimental data produced at the LHC nowadays this is a perfect opportunity to test the perturbative convergence of the BFKL formalism in the theoretical setup here discussed. As we saw in the introduction of this thesis, in a fixed order perturbative calculation there is no dependence in the unphysical degrees of freedom stemming from renormalization or factorization theorems. However, as we already pointed out, due to the bootstrap property of reggeization (to be understood as exponentiation of the kernel) some remaining dependence on the renormalization, factorization and energy scales appears to all orders which we can minimize looking for regions of maximal stability in the variation of these parameters. A good sign of our predictions is the fact that the stability regions found for our scales are quite "natural", not being far from the typical squared transverse momentum of the tagged jets. Moreover, we have found a systematic shift to this naturalness when moving from the pure NLL result to the collinearly improved one. This is not surprising, since, as we have seen, the BFKL expansion needs to be stabilized in the collinear regions beyond quasi-multi-Regge kinematics. Therefore, once this is done, one would expect the optimal values for the free scales to be more natural and stable, something we have actually shown in this work. Comparing with other similar studies [124–126] we have noticed the strong role played by the parton distribution functions in the Mueller-Navelet jets when there is a large rapidity separation. This makes the cross sections, azimuthal angle decorrelations and ratios of them not to vary so much when applying a pure NLL approach or a collinearly improved one, specially if the tagged jets are of similar transverse momentum. The situation changes, however, when an asymmetric configuration is chosen. In this case the collinear improvements are actually needed to obtain stability regions at all (note that in a pure NLL analysis this was not possible).

We would like to extend our work to find stability regions using a Monte Carlo code [18,65,66,68,97] working directly in transverse momentum space. In this way we could treat the running as we did in section 3.2.2 and see how could this could affect the choice of "optimal" scales, as well as how close to the infrared region we could get [16, 17].

5.1.4 Tables

Y	$C_0^{(\mathrm{NLA})}$	Y_0	n_R	$C_0^{(\mathrm{RG-impr-NLA})}$	Y_0	n_R
6	0.726(64)	1	2	0.733(75)	1	2
8	0.335(29)	2	2	0.347(43)	2	2
10	0.00272(56)	4	2	0.00280(91)	3	2

Y	$C_1^{(\mathrm{NLA})}$	Y_0	n_R	$C_1^{(\mathrm{RG-impr-NLA})}$	Y_0	n_R	$C_1^{*(\mathrm{RG-impr-NLA})}$
6	0.554(62)	1	2	0.539(17)	0	1	0.535(69)
8	0.216(19)	2	2	0.218(16)	1	2	0.209(21)
10	0.00156(16)	3	2	0.001516(71)	2	2	0.00150(16)

Y	$C_2^{(\mathrm{NLA})}$	Y_0	n_R	$C_2^{(\mathrm{RG-impr-NLA})}$	Y_0	n_R	$C_2^{*(\mathrm{RG-impr-NLA})}$
6	0.3320(18)	0	1.5	0.326(15)	0	1	0.350(70)
8	0.1203(74)	2	2.5	0.116(16)	2	3	0.114(21)
10	0.000774(69)	4	4	0.000716(43)	2	2	0.00071(14)

Table 5.1: First table: values for C_0 -corresponding to fig. 5.4 (left)- using pure NLL and collinearly improved NLL resummation with symmetric configuration $|\vec{k}_{J_1}| = |\vec{k}_{J_2}| = 35$ GeV at $\sqrt{s} = 14$ TeV. The optimal Y_0 and n_R values are given in the next two columns of the one with the corresponding C_0 choice. Second and third tables: the same but for C_1 -second table, corresponding to fig. 5.3 (left)- and for C_2 -third table, corresponding to fig. 5.3 (right)-. In this case the last column(s) shows the values obtained for C_1 (C_2) using the optimal scales of C_0.

Y	$C_0^{(\mathrm{RG-impr-NLA})}$	Y_0	n_R	$C_1^{(\mathrm{RG-impr-NLA})}$	Y_0	n_R	$C_1^{*(\mathrm{RG-impr-NLA})}$
6	2.04(11)	2	3	1.384(88)	1	1	1.133(89)
7	2.91(13)	1	2.5	1.73(39)	1	1	1.466(63)
8	1.703(70)	2	2.5	0.897(68)	1	1	0.764(35)
9	0.345(13)	1.5	3	0.170(19)	2	1	0.138(10)
10	0.0254(11)	2.5	3	0.0112(28)	3	1	0.00953(72)

Y	$C_2^{(\mathrm{RG-impr-NLA})}$	Y_0	n_R	$C_2^{*(\mathrm{RG-impr-NLA})}$
6	0.574(35)	1	1	0.541(63)
7	0.643(16)	1	0.75	0.583(28)
8	0.307(17)	1	1	0.291(19)
9	0.0552(44)	2	1	0.0473(28)
10	0.00348(36)	2	1	0.00317(19)

Table 5.2: Values for C_0 -corresponding to fig. 5.4 (right)-, C_1 -fig. 5.5 (left)- and C_2 -fig. 5.5 (right)- using collinearly improved NLL resummation with asymmetric configuration $|\vec{k}_{J_1}| = 20$ GeV and $|\vec{k}_{J_2}| = 35$ GeV at $\sqrt{s} = 14$ TeV. The optimal Y_0 and n_R values for C_0 are given in the third and fourth column and for C_1 in the sixth and seventh of the first table while the results for C_2 are shown in the second one. Last column(s) shows the values obtained for C_1 (C_2) using the optimal scales of C_0.

Y	$\mathcal{R}_{21\ \mathrm{sym}}$	Y_0	n_R
6	0.5471	1.5	1
8	0.5105	1.5	1
10	0.4253	0	1

Y	$\mathcal{R}_{21\ \mathrm{asym}}^{(\mu_\mathrm{F}\ \mathrm{fixed})}$	$\mathcal{R}_{21\ \mathrm{asym}}^{(\mu_\mathrm{F}=\mu_\mathrm{R})}$	Y_0	n_R
6	0.3954	0.3940	0	1
7	0.3567	0.3548	0	1
8	0.3258	0.3267	0	1
9	0.2860	0.2992	0	1
10	0.2831	0.2848	0	1

Table 5.3: Right table: values for C_2/C_1 -corresponding to fig. 5.8 (right)- using collinearly improved NLL resummation with asymmetric configuration $|\vec{k}_{J_1}| = 20$ GeV and $|\vec{k}_{J_2}| = 35$ GeV at $\sqrt{s} = 14$ TeV, setting $\mu_{F_1} = |\vec{k}_{J_1}|$ and $\mu_{F_2} = |\vec{k}_{J_2}|$ (second column) and fixing $\mu_{F_1} = \mu_{F_2} = \mu_R$ (third column). The optimal values of Y_0 and n_R, given in the last two columns, are the same for the two cases. Left table: same for symmetric configuration $|\vec{k}_{J_1}| = |\vec{k}_{J_2}| = 35$ GeV, with $\mathcal{R}_{21\ \mathrm{sym}}^{(\mu_\mathrm{F}\ \mathrm{fixed})} = \mathcal{R}_{21\ \mathrm{sym}}^{(\mu_\mathrm{F}=\mu_\mathrm{R})}$.

5.2 Exclusive central production of heavy quarks at LHC

In this section we study the hadro-production of heavy flavors at central rapidities in the high energy limit. We present some (preliminary) numerical results for the fully differential hadronic cross section calculated at NLL accuracy taking into account collinear improvements to the BFKL perturbative series to all-orders in perturbation theory. Our analytical results, presented in [117], are written in a form suitable for a future Monte Carlo implementation.

5.2.1 Introduction

It is our aim to phenomenologically analyze the production of heavy quark-antiquark pairs using the latest CMS data to use it as a direct test of the BFKL formalism and of the universality of unintegrated gluon densities. The large masses of the bottom or top quarks provide a hard scale allowing for a perturbative analysis. However, the masses of the top quark pairs are so large that the typical proved values of Bjorken x are not that small. In this case it is known that cross sections receive significant corrections from threshold logarithms [140–148]. The bottom quarks are lighter, giving rise to smaller values of x for which the BFKL formalism is best suited. Previous investigations of heavy quark production similar to our present calculation were presented in [149]. What we will show in this study is an alternative approach which operates with NLO unintegrated gluon densities in transverse momentum space, does not involve the use of anomalous dimensions, treats the kinematics of the quark-antiquark pair exclusively and is readily suitable for a Monte Carlo analysis. Other analytical analysis which we found of interest in the field of inclusive heavy flavor production are [149–155]. A study devoted to the exclusive central production of jets in hadron-hadron collisions in k_T factorization was presented in [156].

The fully exclusive study that we propose (exclusive to be understood in the sense of not integrating over the momenta of the heavy quarks) allows for the determination of the x values at which the unintegrated gluon densities are probed by applying energy-momentum conservation to the kinematics of the final state. This provides a good control on the accuracy of the approximations that we use in our calculation and makes of this object a very useful observable to be compared with LHC measurements. The dominant production process for both top and bottom pairs is given by gluon-gluon fusion. However, as we already pointed out, only the bottom pair production takes place at small enough x as to justify the resummation of $\ln(x)$ terms in the framework of k_T factorization.

In order to take into account top pair production we would need to match the present calculation with renormalization group evolution, which would be also a way to test our capability of extending our high energy factorization towards the large x region.

5.2.2 Fully-differential cross section with all-order corrections

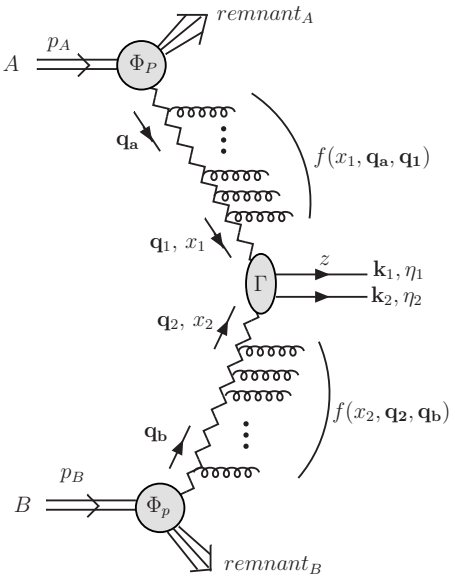

Figure 5.9: Central production of two heavy quarks in k_T factorization

.

To describe the differential cross-section for the exclusive production of a pair of heavy quarks within k_T factorization it is convenient to introduce a Sudakov basis. To this end we define the light-like momenta p_1 and p_2 which coincide in the $s \to \infty$ limit with the momenta of the incoming protons p_A and p_B:

$$p_1 \;=\; p_A - \frac{m_P^2}{s} p_B, \qquad p_2 \;=\; p_B - \frac{m_P^2}{s} p_A, \tag{5.14}$$

with $s = (p_A + p_B)^2$ being the squared center of mass energy of the hadronic process. With these definitions, we can then work with the usual Sudakov decomposition of a general four momentum, *i.e.*

$$k = \alpha\, p_1 + \beta\, p_2 + k_\perp. \tag{5.15}$$

The notation for the relevant momenta in the partonic hard subprocess is given in Fig. 5.9. In the Sudakov basis the momenta of the reggeized gluons in the

high energy limit are given by

$$q_1 \;=\; x_1\, p_1 + q_{1,\perp}, \qquad\qquad q_2 \;=\; x_2\, p_2 + q_{2,\perp}, \tag{5.16}$$

while the ones for the produced heavy quarks read

$$k_i \;=\; \alpha_i\, p_1 + \beta_i\, p_2 + k_{i,\perp}, \qquad\qquad i \;=\; 1,2. \tag{5.17}$$

with

$$\alpha_i \;=\; \sqrt{\frac{M^2+\mathbf{k}_i^2}{s}}\, e^{\eta_i}, \qquad\qquad \beta_i \;=\; \sqrt{\frac{M^2+\mathbf{k}_i^2}{s}}\, e^{-\eta_i}, \qquad\qquad i=1,2, \tag{5.18}$$

where we have used the on-shellness condition. The variable η_1 (η_2) is the rapidity of the produced heavy quark (anti-quark) and $\mathbf{k}_i^2 \equiv -k_{i,\perp}^2$ are the corresponding Euclidean squared transverse momenta. Making use of the definitions

$$s_1 \;=\; (p_1+q_2)^2 = x_2\, s, \qquad\qquad s_2 \;=\; (p_2+q_1)^2 = x_1\, s, \tag{5.19}$$

which correspond to the center of mass energies of the upper and lower subamplitudes in Fig. 5.9, respectively, we can write the following expression for the differential cross-section of heavy quark production:

$$\begin{aligned}\frac{d^6\sigma}{d\eta_1 d\eta_2 d^2\mathbf{k}_1 d^2\mathbf{k}_2} =& \int_0^1 dx_1 \int_0^1 dx_2 \int \frac{d^2\mathbf{q}_1}{2(2\pi)^3} \int \frac{d^2\mathbf{q}_2}{2(2\pi)^3} \left[\int \frac{d^2\mathbf{q}_a}{2\pi} \frac{\Phi_A(\mathbf{q}_a)}{\mathbf{q}_a^2} f\left(\frac{s_1}{s_{0,1}}, \mathbf{q}_a, \mathbf{q}_1\right)\right] \\ &\times \frac{|\Gamma_{\mathrm{RR}\to\mathrm{Q}\bar{\mathrm{Q}}}(\mathbf{q}_1,\mathbf{q}_2;\mathbf{k}_1,\mathbf{k}_2,z)|^2}{\mathbf{q}_1^2\mathbf{q}_2^2} \left[\int \frac{d^2\mathbf{q}_b}{2\pi} \frac{\Phi_B(\mathbf{q}_b)}{\mathbf{q}_b^2} f\left(\frac{s_2}{s_{0,2}}, \mathbf{q}_2, \mathbf{q}_b\right)\right] \\ &\times \delta^{(2)}(\mathbf{q}_1+\mathbf{q}_2-\mathbf{k}_1-\mathbf{k}_2)\, \delta(x_1-\alpha_1-\alpha_2)\, \delta(x_2-\beta_1-\beta_2),\end{aligned} \tag{5.20}$$

where Φ_A and Φ_B are the hadron impact factors, f is the gluon Green's function and $\Gamma_{\mathrm{RR}\to\mathrm{Q}\bar{\mathrm{Q}}}$ is the high energy effective vertex coupling the two reggeized gluons to the heavy quark-antiquark pair, with

$$z = \frac{\alpha_1}{x_1} = \frac{\sqrt{\mathbf{k}_1^2+M^2}}{\sqrt{\mathbf{k}_1^2+M^2}+\sqrt{\mathbf{k}_2^2+M^2}\, e^{\eta_2-\eta_1}} \tag{5.21}$$

being the fraction of the longitudinal momentum of the upper reggeized gluon along p_1 carried by the heavy quark.

As we explained in the last section, when the kernel is exponentiated there is a residual dependence on the scale $s_{0,i}$ which would correspond to NNLL and higher terms. A natural choice for $s_{0,i}$ is then the one which reduces the size of those higher orders corrections to the minimum for a given observable. In the present analysis there exists a hierarchy of scales with a large difference

between the only hard scale provided by the invariant mass of the heavy quark pair system and the large transverse size of the incoming hadrons. Since the scale of the heavy quark anti-quark system $\Sigma \equiv x_1 x_2 s$ is significantly larger than the transverse scales $\mathbf{q}_a^2$ and $\mathbf{q}_b^2$ associated to the scattered protons, a natural choice for the energy scales is $s_{0,i} = \Sigma$, giving rise to the DIS-s (Bjorken x) variables

$$\left(\frac{s_1}{s_{0,1}}\right)^{\omega} = x_1^{-\omega}, \qquad \left(\frac{s_2}{s_{0,2}}\right)^{\omega} = x_2^{-\omega}. \tag{5.22}$$

This naturally leads to the concept of the unintegrated gluon density in a hadron, which represents the probability of resolving an off-shell gluon carrying a longitudinal momentum fraction x off the incoming hadron, together with a transverse momentum k_T:

$$\mathcal{G}(x, \mathbf{k}) = \int \frac{d^2\mathbf{q}}{2\pi} \frac{\Phi_P(\mathbf{q})}{\mathbf{q}^2} f(x, \mathbf{q}, \mathbf{k}). \tag{5.23}$$

At NLL accuracy the BFKL equation is sensitive to changes in the energy scales $s_{0,i}$. As it was pointed out in [156], any shift of scales can be absorbed in the kernel, impact factors, and central production vertex. With the choice of energy scale as in eq. (5.22) the NLL impact factors are modified by an extra logarithmic term of the form

$$\tilde{\Phi}_P^{\mathrm{NLL}}(\mathbf{q}) = \Phi_P^{\mathrm{NLL}}(\mathbf{q}) - \frac{\mathbf{q}^2}{2} \int d^2\mathbf{l} \, \frac{\Phi_P^{\mathrm{LL}}(\mathbf{l})}{\mathbf{l}^2} \, \mathcal{K}_{\mathrm{BFKL}}^{\mathrm{LL}}(\mathbf{l}, \mathbf{q}) \, \ln \frac{\mathbf{l}^2}{\mathbf{q}^2}. \tag{5.24}$$

The NLO kernel receives two additional contributions, corresponding to the incoming and outgoing reggeized gluons:

$$\tilde{\mathcal{K}}_{\mathrm{BFKL}}^{\mathrm{NLL}}(\mathbf{l}_a, \mathbf{l}_b) = \mathcal{K}_{\mathrm{BFKL}}^{\mathrm{NLL}}(\mathbf{l}_a, \mathbf{l}_b) - \frac{1}{2} \int d^2\mathbf{l} \, \mathcal{K}_{\mathrm{BFKL}}^{\mathrm{LL}}(\mathbf{l}_a, \mathbf{l}) \, \mathcal{K}_{\mathrm{BFKL}}^{\mathrm{LL}}(\mathbf{l}, \mathbf{l}_b) \, \ln \frac{\mathbf{l}^2}{\mathbf{l}_b^2}. \tag{5.25}$$

The NLL $Q\bar{Q}$ production vertex also gets two types of corrections, corresponding to the two different evolution chains originating from the hadrons A and B:

$$\begin{aligned} |\tilde{\Gamma}_{\mathrm{RR}\to\mathrm{Q\bar{Q}}}^{\mathrm{NLL}}(\mathbf{q}_1, \mathbf{q}_2; \mathbf{k}_1, \mathbf{k}_2, z)|^2 \;=\; & |\Gamma_{\mathrm{RR}\to\mathrm{Q\bar{Q}}}^{\mathrm{NLL}}(\mathbf{q}_1, \mathbf{q}_2; \mathbf{k}_1, \mathbf{k}_2, z)|^2 \\ & - \frac{\mathbf{q}_1^2}{2} \int \frac{d^2\mathbf{l}}{\mathbf{l}^2} \, \mathcal{K}_{\mathrm{BFKL}}^{\mathrm{LL}}(\mathbf{q}_1, \mathbf{l}) \, |\Gamma_{\mathrm{RR}\to\mathrm{Q\bar{Q}}}^{\mathrm{LL}}(\mathbf{l}, \mathbf{q}_2; \mathbf{k}_1, \mathbf{k}_2, z)|^2 \, \ln \frac{\mathbf{l}^2}{(\mathbf{q}_2 + \mathbf{l})^2} \\ & - \frac{\mathbf{q}_2^2}{2} \int \frac{d^2\mathbf{l}}{\mathbf{l}^2} \, |\Gamma_{\mathrm{RR}\to\mathrm{Q\bar{Q}}}^{\mathrm{LL}}(\mathbf{q}_1, \mathbf{l}; \mathbf{k}_1, \mathbf{k}_2, z)|^2 \, \mathcal{K}_{\mathrm{BFKL}}^{\mathrm{LL}}(\mathbf{l}, \mathbf{q}_2) \, \ln \frac{\mathbf{l}^2}{(\mathbf{q}_1 + \mathbf{l})^2}. \end{aligned} \tag{5.26}$$

Using these definitions, the differential cross section in eq. (5.20) at NLO accuracy

is given by the expression

$$\begin{aligned}\frac{d^6\sigma}{d\eta_1 d\eta_2 d^2\mathbf{k}_1 d^2\mathbf{k}_2} &= \int_0^1 dx_1 \int_0^1 dx_2 \int \frac{d^2\mathbf{q}_1}{2(2\pi)^3} \int \frac{d^2\mathbf{q}_2}{2(2\pi)^3}\, \mathcal{G}^{\rm NLL}(x_1,\mathbf{q}_1)\, \mathcal{G}^{\rm NLL}(x_2,\mathbf{q}_2) \\ &\times \frac{|\Gamma_{\rm RR\to Q\bar{Q}}(\mathbf{q}_1,\mathbf{q}_2;\mathbf{k}_1,\mathbf{k}_2,z)|^2}{\mathbf{q}_1^2\mathbf{q}_2^2}\, \delta^{(4)}(q_1+q_2-k_1-k_2) \\ &= \int d^2\mathbf{q}_1\, \mathcal{G}^{\rm NLL}(\alpha_1+\alpha_2,\mathbf{q}_1)\, \mathcal{G}^{\rm NLL}(\beta_1+\beta_2,\mathbf{k}_1+\mathbf{k}_2-\mathbf{q}_1) \\ &\times \frac{|\Gamma_{\rm RR\to Q\bar{Q}}(\mathbf{q}_1,\mathbf{k}_1+\mathbf{k}_2-\mathbf{q}_1;\mathbf{k}_1,\mathbf{k}_2,z)|^2}{(16\pi^3)^2\mathbf{q}_1^2(\mathbf{k}_1+\mathbf{k}_2-\mathbf{q}_1)^2}. \end{aligned} \tag{5.27}$$

This means that the polarizations of the transversely polarized reggeized gluons are chosen to satisfy

$$\sum_\lambda \epsilon^\mu_{(\lambda)}(q_i)\epsilon^\nu_{(\lambda)}(q_i) \;=\; \frac{\mathbf{q}_i^\mu \mathbf{q}_i^\nu}{\mathbf{q}_i^2}, \qquad \text{with } i=1,2, \tag{5.28}$$

and can be related up to an overall factor $\Sigma^2/\mathbf{q}_1^2\mathbf{q}_2^2$ to the usual longitudinally polarized reggeized gluons by means of a Ward-identity for the t-channel gluons.

At present the complete NLO expression for the heavy quark production vertex $\Gamma_{\rm RR\to Q\bar{Q}}$ is not available, existing only rough approximations for some of the NLO corrections [157–159], still with big uncertainties. For the present study we consider the LO expression [149] which can be written in the following form:

$$|\Gamma^{\rm LO}_{\rm RR\to Q\bar{Q}}(\mathbf{q}_1,\mathbf{q}_2;\mathbf{k}_1,\mathbf{k}_2,z)|^2 = g^4\left(\frac{N_c}{2}A_1(\mathbf{q}_1,\mathbf{q}_2;\mathbf{k}_1,\mathbf{k}_2,z)+\frac{1}{2N_c}A_2(\mathbf{q}_1,\mathbf{q}_2;\mathbf{k}_1,\mathbf{k}_2,z)\right). \tag{5.29}$$

The expressions for the functions A_1 and A_2 used for the numerical analysis here presented can be found in [117]. The explicit form of the vertex in eq. (5.29), keeping all the information on the outgoing $Q\bar{Q}$ system, will permit a comprehensive study of differential distributions (see section 5.2.3 for a first numerical approach) in exclusive observables. For this we will also need to keep track of the multiple soft emission stemming from the gluon evolution. How to achieve this task was carefully discussed already in sections 3.2.2 3.3.1. We saw there how the kernel could be split into a part accounting for the real emissions, affected by the choice of energy scales $s_{0,i}$, and the gluon Regge trajectory, $\epsilon_\lambda(-\mathbf{q}^2)$, introduced in eq. (3.99), accounting for the virtual corrections only and unaltered by changes of the energy scales. In this way we could always write the gluon

Green's function in the following iterative form:

$$f(x,\mathbf{q},\mathbf{k}) = x^{-\omega_\lambda(\mathbf{q})}\Big\{\delta^{(2)}(\mathbf{q}-\mathbf{k}) + \sum_{n=1}^{\infty}\prod_{i=1}^{n}\int d^2\mathbf{l}_i\Big[\tilde{\mathcal{K}}_\lambda^{\rm real}(\mathbf{q}+\sum_{j}^{i-1}\mathbf{l}_j,\mathbf{q}+\sum_{j}^{i}\mathbf{l}_j) \times \int_{x_{i-1}}^{1}\frac{dx_i}{x_i}x_i^{-\omega_\lambda(\mathbf{q}+\sum_{j=1}^{i}\mathbf{l}_j)+\omega_\lambda(\mathbf{q}+\sum_{j=1}^{i-1}\mathbf{l}_j)}\Big]\delta^{(2)}(\mathbf{q}+\sum_{j=1}^{n}\mathbf{l}_j-\mathbf{k})\Big\}, \qquad (5.30)$$

(with $x_0 \equiv x$), allowing for a Monte Carlo implementation which has full control over the emitted particle phase space. At NLL accuracy each iteration of the kernel, or each of the terms in the sum of eq. (5.30), corresponds to one or two emissions well separated in rapidity from previous and subsequent clusters of particles. Therefore, inserting this function in the formula for the differential distributions will generate our exclusive observables.

5.2.3 (Preliminary) numerical results & scope

In order to numerically analyze eq. (5.27) we express the unintegrated gluon density in γ space:

$$\mathcal{G}(x,\mathbf{q}) = \frac{1}{\pi}\int\frac{d\omega}{2\pi i}\int_{1/2-i\infty}^{1/2+i\infty}\frac{d\gamma}{2\pi i}x^{-\omega}\frac{1}{\omega-\mathcal{K}(\gamma)}(\mathbf{q}^2)^{\gamma-1}\Phi(\gamma)\,, \qquad (5.31)$$

using as a model for the proton impact factor the one given in eq. (4.11) with the values for the parameters taken from [16,17] and being $\delta = 8.4$, $Q_0 = 0.28$ GeV, $\Lambda = 0.21$ GeV and $\mathcal{C} = 1.50$. For the numerical analysis here presented we will consider only the conformal invariant piece of the NLL BFKL kernel plus collinear improvements and leave the corrections due to the running of the coupling for a future study. The eigenvalue of the kernel can be written as,

$$\mathcal{K}(\gamma) = \bar{\alpha}_s\chi_0(\gamma) + \bar{\alpha}_s^2\chi_1(\gamma) + \bar{\alpha}_s^2\chi^{RG}(\gamma).$$

with the exact expressions given in section 4.1.

Let us analyze and compare the first numerical results obtained at LL, pure NLL and collinear improved NLL accuracies for the fully-differential cross section as given in eq. (5.27). We warn the reader that the results here presented are work in progress and therefore are susceptible to changes, planning on having a final version available very soon.

In figures 5.10 and 5.11 we consider two differential cross sections given at

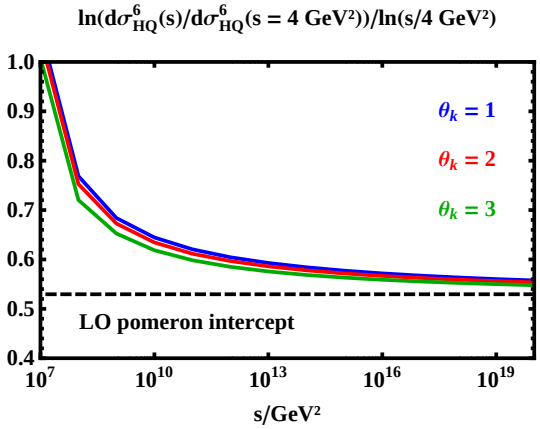

Figure 5.10: Ratio of two differential LL hadronic cross sections versus the energy for different values of the azimuthal angle formed by the heavy quark pair and $k_1^2 = 100\ \mathrm{GeV}^2$, $k_2^2 = 9\ \mathrm{GeV}^2$, $\eta_1 = \eta_2 = 0$.

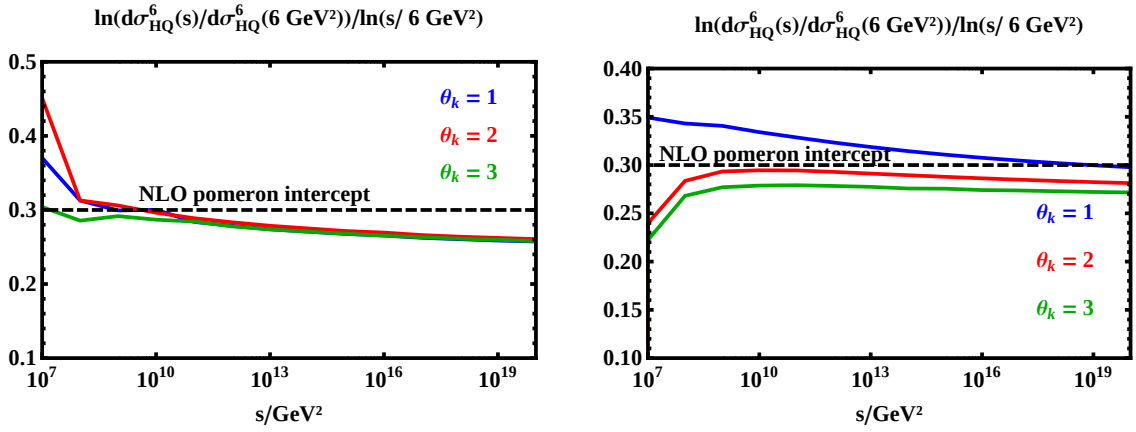

Figure 5.11: Ratio of two differential NLL (left) and NLL plus collinear resummation (right) hadronic cross sections versus the energy for different values of the azimuthal angle formed between the heavy quark pair and $k_1^2 = 100\ \mathrm{GeV}^2$, $k_2^2 = 9\ \mathrm{GeV}^2$, $\eta_1 = \eta_2 = 0$.

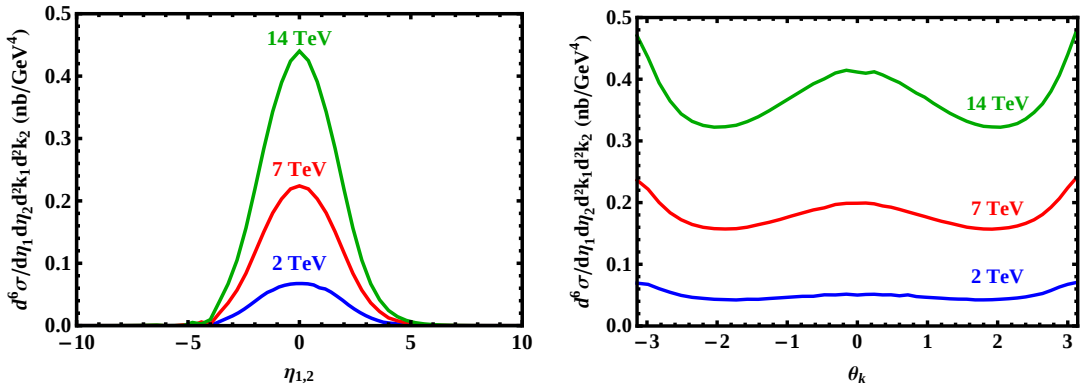

Figure 5.12: Dependence of the fully-differential LL hadronic cross section on the pseudorapidity of the produced heavy quarks with $k_1^2 = k_2^2 = 9\ \mathrm{GeV}^2$, $\theta_k = 3$ (left) and on the azimuthal angle formed between the heavy quarks with $k_1^2 = k_2^2 = 9\ \mathrm{GeV}^2$, $\eta_1 = \eta_2 = 0$ (right) for different values of the center of mass energy $\sqrt{s}$, as labeled in the plots.

squared center of mass energies s_1 and s_2 and study the following quantity:

$$\Lambda(s_1, s_2) \;=\; \frac{\left[\mathrm{d}\sigma^6(s_1)/\mathrm{d}^6R\right] / \left[\mathrm{d}\sigma^6(s_2)/\mathrm{d}^6R\right]}{\ln(s_1/s_2)}\,, \tag{5.32}$$

where $\mathrm{d}^6R \equiv \mathrm{d}\eta_1\mathrm{d}\eta_2\mathrm{d}^2\mathbf{k}_1\mathrm{d}^2\mathbf{k}_2$, fixing the value of s_2 and the rest of the external parameters and studying the dependence of the function on the variable s_1. The results are compared for different values of the azimuthal angle θ_k between the heavy quarks for conformal component of spin $n = 0$. At asymptotically high energies the trajectory given by $\Lambda(s_1 \to \infty,\, s_2 \text{ fixed})$ should reach the value of the pomeron intercept, since the cross section behaves asymptotically as $\sigma \sim s^{\lambda_p}$. We do observe this behavior in the figures. In the LL case (fig 5.10) the lines approach the LL 0.5 pomeron while in the other two NLL cases (figs. 5.11) the stability value lowers towards the NLL solution, around 0.3, as expected. It is noteworthy to mention that the results obtained with collinear improvements were, for all cases, more stable than for the pure NLL case, specially for plots such as fig. 5.11 where the squared transverse momentum scales of the heavy quarks are so asymmetric: $k_1^2 = 100\mathrm{GeV}^2$, $k_2^2 = 9\mathrm{GeV}^2$. We also see that the effect of the azimuthal angle is not important at these asymptotically large energies for the object analyzed.

Finally, we present in fig. 5.12 the LL dependence of the differential cross section on the difference in pseudorapidity (left) of the heavy quarks for a symmetric configuration of their transverse momentum and fix azimuthal angle and on the azimuthal angle (right) for pseudorapidity zero. We compare the results for different values of the squared center of mass energy, chosen at Tevatron and LHC characteristic values. Similar plots would be obtained for the NLL and collinear improved NLL cases, and will be presented elsewhere soon.

A very interesting recent result about the charm production at LHC in the context of k_T factorization is given in [160]. Other stimulating analysis in the literature in this line can be found in [161–164]. In the future analysis under preparation it is our intention to compute physical observables that we can compare with the experimental data provided by the ALICE detector of LHC [165] or CMS [166] and also by Tevatron older measurements [167]. We are also working on the Monte Carlo implementation of the fully-differential expression for the cross section to have a complete control over the final state configuration. In this way we will be able to differentiate between different theoretical approaches and we can treat the running coupling effects directly in transverse momentum space, following the procedure explained in section 3.2.2 of this thesis.

5.3 Forward production of heavy quarks at LHCb

In this last study we investigate the production of a heavy quark pair at the LHC very collinear to one of the scattered protons allowing for enough phase-space to produce multiple soft gluon radiation between the quark pair and the other parent proton. In this kinematic regime large logarithms of energy appear and need to be resummed using low Bjorken x evolution equations. We calculate the expression for the hadronic cross section using both the collinear and high energy factorization theorems and present a numerical analysis of the total hadronic cross section. This work is under construction. It is our intention to show a comparative numerical analysis of our results with the work presented in [19] in the near future.

5.3.1 Kinematics and general structure of the cross section

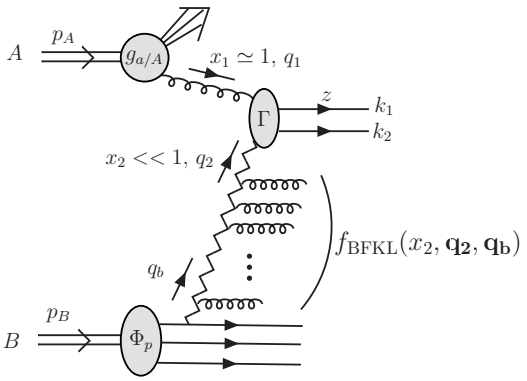

Figure 5.13: Kinematics of the process

The process under consideration is depicted in fig. 5.13. In order to analyze the hadronic cross section using high energy factorization we use the Sudakov parametrization introduced in section 5.2 in which any general four momentum k can be decomposed as in eq. (5.15).

The on-shell gluon carries a large momentum fraction $x_1 \simeq 1$ of its parent proton p_1, so it presents almost no momentum in the transverse plane. Therefore, it can be approximated in the high energy limit by $q_1 = x_1 p_1$. On the other hand, we impose the off-shell (reggeized) t-channel gluon to carry a very small fraction of longitudinal momentum of p_2, $x_2 << 1$, leading to a large transverse momentum. We can express it as $q_2 = x_2 p_2 + q_{2\perp}$, $q_{i\perp}^{\mu} = (0, \mathbf{q}_i, 0)$.

The momenta of the produced heavy quarks are given by eq. 5.17. It is convenient to define a new variable z, the fraction of the longitudinal momentum of the on-shell gluon along p_1 carried by the heavy quark with momentum k_1,

such that $\alpha_1 = x_1 z$. If we also drop indexes so that $\beta_2 = \beta$ and $q_{2,\perp} = q_\perp$, the four 4-momenta, after applying momentum conservation, can be expressed as

$$\begin{aligned} q_1 &= x_1 p_1 \,, \\ q_2 &= x_2 p_2 + q_\perp \,, \\ k_1 &= x_1 z p_1 + (x_2 - \beta) p_2 + k_{1,\perp} \,, \\ k_2 &= (1-z) x_1 p_1 + \beta p_2 + (q_\perp - k_{1,\perp}) \,. \end{aligned} \tag{5.33}$$

In principle there are four angles to be defined. However, we can use the constraint coming from momentum conservation, $q_1^\mu + q_2^\mu = k_1^\mu + k_2^\mu$, also the on-shellness condition $\mathbf{q}_1^2 = \mathbf{0}$ and perform a rotation of the basis so that one of the angles is fixed and there is only another one left to be set. More specifically, let us change the basis so that the outgoing heavy quark with transverse momentum $\mathbf{k}_1$ lays on the new OX' axis and define the remaining angle as $\alpha_k \equiv \hat{(\mathbf{k}_1, \mathbf{k}_2)}$.

The Sudakov parameters α_i and β_i are given by eq (5.18). The Mandelstam invariants involved in the construction of the partonic cross section are:

$$\begin{aligned} \hat{s} &= (k_1 + k_2)^2 = x_1 x_2 s - \mathbf{q}^2 = \Sigma - \mathbf{q}^2 \,, \\ \hat{t} &= (q_1 - k_1)^2 = -\frac{1-z}{z}(\mathbf{k}_1^2 + M^2) - \mathbf{k}_1^2 \,, \\ \hat{u} &= (q_1 - k_2)^2 = -\frac{z}{1-z}(\mathbf{k}_2^2 + M^2) - \mathbf{k}_2^2 \,. \end{aligned} \tag{5.34}$$

We have introduced a new variable $\Sigma = x_1 x_2 s$, which can be taken to be the hard scale of the heavy quark system.

With a symmetric configuration such as the one analyzed in section 5.2 [117], high energy factorization could be used to calculate the hadronic cross section, finding

$$\sigma_{Q\bar{Q}}^{tot}(s) = \int \frac{\mathrm{d}^2\mathbf{q}_1}{\pi} \int \frac{\mathrm{d}x_1}{x_1} \int \frac{\mathrm{d}^2\mathbf{q}_2}{\pi} \int \frac{\mathrm{d}x_2}{x_2} \, \mathcal{G}(x_1, \mathbf{q}_1) \, \hat{\sigma}(\mathbf{q}_1, \mathbf{q}_2, x_1 x_2 s) \, \mathcal{G}(x_2, \mathbf{q}_2). \tag{5.35}$$

However, in the case under consideration the collinear (on-shell) gluon carries a large longitudinal fraction of the momentum of the parent hadron, becoming collinear factorization, instead of k_T factorization, mandatory. In this case a parton distribution function (PDF) has to be introduced instead of an unintegrated gluon density. Nonetheless, these two objects can be matched by taking the limit of zero transverse momentum to make one of the gluons to be on-shell, $\mathbf{q}_1^2 \to 0$. In order to do so, let us define an angular averaged partonic cross section

$$\tilde{\sigma}(\,|\mathbf{q}_1|, \mathbf{q}_2, \Sigma) = \int_0^{2\pi} \frac{\mathrm{d}\phi_1}{2\pi} \, \hat{\sigma}(\,|\mathbf{q}_1|, \phi_1, \mathbf{q}_2, \Sigma) \,. \tag{5.36}$$

Catani, Ciafaloni and Hauttman showed in [151] that the new cross section is finite in the limit $\mathbf{q}_1^2/M^2 \to 0$ and agrees with the partonic cross section for the process under consideration[1], $gR \to Q\bar{Q}$. Regarding the matching between the gluon density $\mathcal{G}(x_1, \mathbf{q}_1)$ and the gluon PDF, in the limit $\mathbf{q}_1^2/M^2 \to 0$ we have

$$\int_0^{\mu_F^2} \frac{\mathrm{d}^2\mathbf{q}_1}{\pi}\, \mathcal{G}(x_1, \mathbf{q}_1) = g\left(x_1, \mu_F^2\right) , \tag{5.37}$$

$g(x_1, \mu_F^2)$ being the conventional gluon PDF with factorization scale μ_F^2. Under all these considerations the total hadronic cross section can be expressed as

$$\sigma_{Q\bar{Q}}^{\mathrm{tot}} = \sum_{colors} \int \frac{\mathrm{d}x_1}{x_1} \int \frac{\mathrm{d}x_2}{x_2} \int \frac{\mathrm{d}^2\mathbf{q}_2}{\pi} g(x_1, \mu_F^2)\tilde{\sigma}(\mathbf{q}_2, x_1 x_2 s)\mathcal{G}(x_2, \mathbf{q}_2) . \tag{5.38}$$

Note that we have not specified the integration limits for the Bjorken variables x_1 and x_2. Fig. 5.14 shows the region of phase-space covered by the detector. It can be seen how x_1 cannot be smaller than 10^{-2} but can go up to 1 while x_2 can go down to 10^{-5} but cannot be bigger than 0.1. Two of these constrains arise from the experimental cuts in rapidity needed at the LHCb:

$$1.9 < y_1,\ y_2 < 4.9 . \tag{5.39}$$

The third one comes from the fact that Σ, the squared mass of the heavy quark system, can never be bigger than the square of the sum of the masses of each heavy quark, that is

$$x_1\, x_2\, s = \Sigma \geq (m_b + m_{\bar{b}})^2 = 4M^2 . \tag{5.40}$$

This condition is given by the purple line in the figure, for which we have taken the values $\sqrt{s} = 7$ TeV and $M = 4.19$ GeV, according to the $\overline{MS}$ prescription. M is the mass of the bottom quark. Regarding the two constraints given by eq. (5.39), in order to be rigorous we would need to use eq. (5.18) to relate x_1 and x_2 to the rapidities y_1 and y_2 and this would imply introducing an extra dependence on the transverse momenta of the heavy quarks. However, we can work within the approximation

$$1.9 < y_{Q\bar{Q}} < 4.9 \tag{5.41}$$

[1]The use of polarization tensor $q_1^\mu q_1^\nu/\mathbf{q}_1^2$ ensures that the limit $\mathbf{q}_1^2 \to 0$ agrees after angular averaging over the angle of $\mathbf{q}_1$ with the corresponding factored expression: $\langle \frac{q_1^\mu q_1^\nu}{\mathbf{q}_1^2} \rangle_{\phi_1, |\mathbf{q}_1|} = g^{\mu\nu}$.

where $y_{Q\bar{Q}}$ stands for the rapidity of the heavy quark pair and obeys the relation

$$y_{Q\bar{Q}} = \frac{1}{2}\log\left(\frac{x_1}{x_2}\right) . \tag{5.42}$$

From these last two equations the magenta and green lines of fig. 5.14 are obtained. In the following sections we analyze the constituent blocks of eq. (5.38).

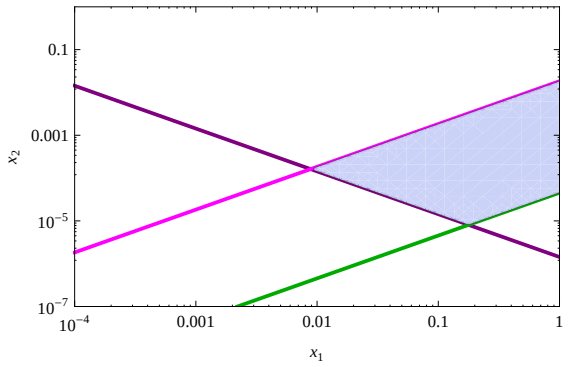

Figure 5.14: Experimental cuts for x_1 and x_2. The colored region is the permitted one.

Following section 5.2.3 we use eq. (5.31) to write the unintegrated gluon density in γ-space and solve the equation for different choices of the BFKL kernel $\mathcal{K}(\gamma)$, taking 4.11) as the model for the proton impact factor. Choosing $s_0 = \Sigma$ and $A = 0.073$, $Q_0^2 = 0.368$ GeV^2 and $\delta = 1.246$ for the parameters of the proton impact factor (with $A = C/\Gamma(\delta)$), we have plotted in figure 5.15 the dependence of the LL unintegrated gluon density on the squared transverse momentum for different values of x. The figure shows how the effect of decreasing x is to enlarge

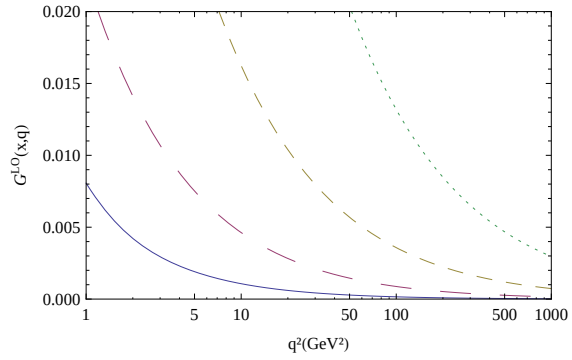

Figure 5.15: Dependence of the LL unintegrated gluon density on $\mathbf{q}^2$ for $s_0 = \Sigma$ and different values of x: from bottom to top, $x = 10^{-1}$, 10^{-2}, 10^{-3}, 10^{-4}.

the unintegrated gluon density, since more soft gluon radiation can be produced

in the ladder –therefore increasing the transverse momentum exchanged in the t-channel– due to the broadening of internal phase space.

5.3.2 Partonic cross section

The partonic differential cross section can be expressed as

$$\mathrm{d}^6\hat{\sigma} = \frac{1}{2\Sigma}|\mathcal{A}(q_1,q_2;k_1,k_2;s)|^2\mathrm{d}P_2 \tag{5.43}$$

with the phase space given by

$$\mathrm{d}P_2 = \frac{\mathrm{d}y_1\,\mathrm{d}^2\mathbf{k}_1}{2(2\pi)^3}\,\frac{\mathrm{d}y_2\,\mathrm{d}^2\mathbf{k}_2}{2(2\pi)^3}\,(2\pi)^4\,\delta^{(4)}(q_1+q_2-k_1-k_2)\,, \tag{5.44}$$

the flux factor being 2Σ and $\mathcal{A}$ standing for the leading order (LO) amplitude. Due to energy-momentum conservation the heavy quark 4-momenta are under the constraint $k_1^2 = k_2^2 = M^2$. The amplitude can be defined through a heavy quark vertex $I^{Q\bar{Q}}$ so that

$$|\mathcal{A}(q_1,q_2;k_1,k_2;M,s)|^2 \propto \frac{4\Sigma^2}{\mathbf{q}_2^4} I^{Q\bar{Q}}(q_1,q_2;k_1,k_2;M,s)\,. \tag{5.45}$$

In order to calculate this vertex one has to take into account the different polarizations coming from the on-shell and off-shell gluons. The former will follow the usual prescription,

$$\sum_\lambda \epsilon^\mu_{(\lambda)}(q_1)\epsilon^\nu_{(\lambda)}(q_1) = g^{\mu\nu}\,, \tag{5.46}$$

while the latter will have the modified relation given in eq. (5.28). The final expression for the vertex is given in eq. (B4) of [19].

Partonic cross section in γ-space

Following [149] we can express the heavy quark vertex in γ-space by taking the double Mellin transform of the amplitude for the process $RR \to Q\bar{Q}$ and then considering the limit $\gamma_1 \to 0$, where γ_1 stands for the on-shell gluon. To be more specific, we can introduce a dimensionless quantity

$$\mathcal{H}\left(\gamma_1,\gamma_2,\frac{4M^2}{\Sigma}\right) = M^2\int_0^\infty \frac{\mathrm{d}\mathbf{q}_1^2}{\pi\mathbf{q}_1^2}\left(\frac{\mathbf{q}_1^2}{M^2}\right)^{\gamma_1}\int_0^\infty \frac{\mathrm{d}\mathbf{q}_2^2}{\pi\mathbf{q}_2^2}\left(\frac{\mathbf{q}_2^2}{M^2}\right)^{\gamma_2}\hat{\sigma}\left(\mathbf{q}_1,\mathbf{q}_2,\Sigma\right)\,, \tag{5.47}$$

and then define the following transformations:

$$\mathcal{H}_\omega(\gamma_1,\gamma_2) = \int_0^\infty \frac{\mathrm{d}\Sigma}{\Sigma}\left(\frac{4M^2}{\Sigma}\right)^\omega \mathcal{H}\left(\gamma_1,\gamma_2,\frac{4M^2}{\Sigma}\right) \tag{5.48}$$

and

$$\mathcal{H}\left(\gamma_1,\gamma_2,\frac{4M^2}{\Sigma}\right)=\oint\frac{\mathrm{d}\omega}{2\pi i}\left(\frac{4M^2}{\Sigma}\right)^{\omega}\mathcal{H}_\omega(\gamma_1,\gamma_2)\;. \tag{5.49}$$

At LLA in the high energy limit any contribution with $\omega\geq 1$ is power suppressed. Therefore, we are only interested in the zero component $\mathcal{H}_0(\gamma_1,\gamma_2)$, with general expression

$$\begin{aligned}\mathcal{H}_0(\gamma_1,\gamma_2) &= \frac{\pi\alpha_s^2}{N_c^2-1}\mathcal{B}(\gamma_1,1-\gamma_1)\mathcal{B}(\gamma_2,1-\gamma_2)\\ &\times\left\{4N_c\left[\frac{\mathcal{B}(3-\gamma_1-\gamma_2,3-\gamma_1-\gamma_2)}{(1-\gamma_1-\gamma_2)}-\frac{\mathcal{B}(3-\gamma_1-\gamma_2,3-\gamma_1-\gamma_2)}{(1-\gamma_1-\gamma_2)^3\mathcal{B}^2(1-\gamma_1,1-\gamma_2)}\right]\right.\\ &\left.-\frac{2}{N_c}\frac{\Gamma(2-\gamma_1)\Gamma(2-\gamma_2)\Gamma(2-\gamma_1-\gamma_2)}{\Gamma(4-2\gamma_1)\Gamma(4-2\gamma_2)}\frac{7-5(\gamma_1+\gamma_2)+3\gamma_1\gamma_2}{1-\gamma_1-\gamma_2}\right\}\;,\end{aligned} \tag{5.50}$$

where $\mathcal{B}(a,b)$ is the beta function, defined in eq. (4.10). The limit when one of the off-shell gluons becomes an on-shell one is directly related to the residues of the single poles in γ_1 and γ_2. Let us, then, introduce a function $h(\gamma_1,\gamma_2)$ such that

$$\mathcal{H}_0(\gamma_1,\gamma_2)=\frac{1}{\gamma_1}\frac{1}{\gamma_2}h(\gamma_1,\gamma_2) \tag{5.51}$$

and define the residue of $\mathcal{H}_0$ for the pole in γ_1 as

$$\int_{\delta-i\infty}^{\delta+i\infty}\frac{\mathrm{d}\gamma_1}{2\pi i}\mathcal{H}_0(\gamma_1,\gamma_2)=\int\frac{\mathrm{d}^2\mathbf{q}_2}{\pi\mathbf{q}_2^2}\left(\frac{\mathbf{q}_2^2}{M^2}\right)^{\gamma_2}\hat{\sigma}(\mathbf{q}_2,\Sigma)=\frac{h(0,\gamma_2)}{\gamma_2}\;, \tag{5.52}$$

with [168]

$$h(0,\gamma_2)=\frac{\pi\alpha_s^2}{V_c}\mathcal{B}(1+\gamma_2,1-\gamma_2)\mathcal{B}(1-\gamma_2,1-\gamma_2)\left[\frac{N_c\,2(2-\gamma_2)}{(3-2\gamma_2)(5-2\gamma_2)}-\frac{1}{2N_c}\frac{(7-5\gamma_2)}{(3-2\gamma_2)}\right] \tag{5.53}$$

There is an important consequence of the approximation $\omega\to 0$ considered. In that limit eq. (5.49) introduces a delta function in Σ:

$$\mathcal{H}\left(\gamma_1,\gamma_2,\frac{4M^2}{\Sigma}\right)\simeq\lim_{\omega\to 0}\oint\frac{\mathrm{d}\omega}{2\pi i}\left(\frac{4M^2}{\Sigma}\right)^{\omega}\mathcal{H}_\omega(\gamma_1,\gamma_2)=\mathcal{H}_0(\gamma_1,\gamma_2)\;\delta(\Sigma-4M^2)\;, \tag{5.54}$$

which constrains the system to be in the energy threshold.

5.3.3 Hadronic cross section

The final expression for the hadronic cross section is given by

$$\sigma_{\mathrm{had}}^{\mathrm{tot}} = \int\frac{\mathrm{d}x_1}{x_1}\int\frac{\mathrm{d}x_2}{x_2}g(x_1,\mu_F^2)\mathcal{R}(x_2,\Sigma)\;, \tag{5.55}$$

with

$$\mathcal{R}(x_2,\Sigma) \;=\; \frac{1}{\pi}\int\frac{\mathrm{d}^2\mathbf{q}_2}{\pi\mathbf{q}_2^2}\int\frac{\mathrm{d}\gamma_2}{2\pi i}x_2^{-\mathcal{K}(\gamma_2)}(\mathbf{q}_2^2)^{\gamma_2}\,\Phi_P\left(\gamma_2\right)\hat{\sigma}(\mathbf{q}_2,\Sigma)\,. \tag{5.56}$$

We can now use eq. (5.52) and the expression

$$\int\frac{\mathrm{d}^2\mathbf{q}_2}{\pi\mathbf{q}_2^2}\left(\frac{\mathbf{q}_2^2}{M^2}\right)^{\gamma_2}\hat{\sigma}(\mathbf{q}_2,\Sigma)\simeq\frac{1}{M^2}\mathcal{H}_0(0,\gamma_2)\delta(\Sigma-4M^2) \tag{5.57}$$

to rewrite eq. 5.56 as

$$\mathcal{R}(x_2,\Sigma)=\frac{1}{\pi M^2}\int\frac{\mathrm{d}\gamma_2}{2\pi i}\Phi_{Q\bar{Q}}\left(\gamma_2\right)x_2^{-\mathcal{K}(\gamma_2)}\,\Phi_P\left(\gamma_2\right)\delta(\Sigma-4M^2)\,, \tag{5.58}$$

with

$$\Phi_{Q\bar{Q}}(\gamma)\equiv(M^2)^{\gamma}\frac{h(0,\gamma)}{\gamma} \tag{5.59}$$

and $h(0,\gamma)$ given in eq. (5.53).

For both the LL and NLL scale invariant pieces of the BFKL kernel, eq. (5.55) with $\mathcal{R}$ given in eq.(5.58) can be used as it stands. Fig. 5.16 shows the dependence of $\mathcal{R}$ on x_2 at leading LLA. The dashed curve is an approximation to the exact solution using the analytical expression given in eq. (5.68). Given the accuracy of the fit the analytic approximation will be used for the numerical analysis here presented.

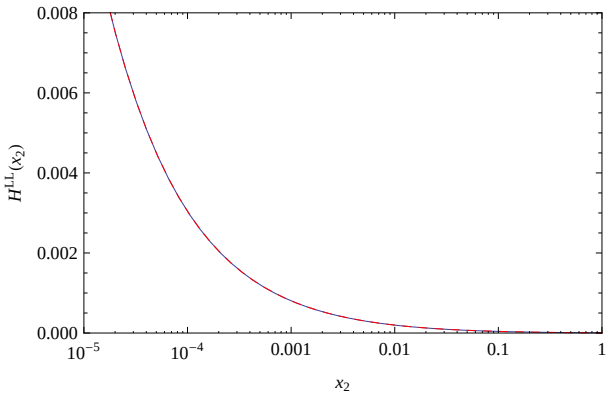

Figure 5.16: Dependence of $\mathcal{R}(x_2,M^2,\Sigma)$ on x_2 at leading logarithmic accuracy.

When we include running coupling effects, however, the kernel cannot be exponentiated as done in eq. (5.58), since it is an operator. In the present study the asymmetric choice for the differential operator should be considered, leading to the action of the kernel on the impact factor given by eq. (3.120), with the proton impact factor to be replaced by the heavy quark vertex. In this case $\mathcal{R}$

has the following expression: [2]

$$\begin{aligned}\mathcal{R} &= \frac{1}{\pi M^2}\int\frac{\mathrm{d}\omega}{2\pi i}\int\frac{\mathrm{d}\gamma_2}{2\pi i}x_2^{-\omega}\Phi_{Q\bar{Q}}\left(\gamma_2\right)\Phi_P\left(\gamma_2\right)\left[\frac{1}{\omega-\bar{\alpha}_s\tilde{\chi}_0-\tilde{\mathcal{K}}(\gamma_2)}+\bar{\alpha}_s^3\left(\frac{1}{\omega-\bar{\alpha}_s\tilde{\chi}_0}\right)^3 B\tilde{\chi}_0'\right]\\ &= \frac{1}{\pi M^2}\int\frac{\mathrm{d}\gamma_2}{2\pi i}\Phi_{Q\bar{Q}}\left(\gamma_2\right)\Phi_P\left(\gamma_2\right)\left[x_2^{-\bar{\mathcal{K}}(\gamma_2)}+x_2^{-\mathcal{K}^{\mathrm{LL}}(\gamma_2)}\bar{\alpha}_s^3(M)\,B\,\tilde{\chi}_0'\frac{1}{2}\log^2\left(x_2\right)\right]\,, \qquad (5.60)\end{aligned}$$

where $\tilde{\chi}\equiv\chi(\gamma_2)$, A and B are defined in eq. (3.118) and we have introduced the definition

$$\bar{\mathcal{K}}(\gamma) \equiv \mathcal{K}^{\mathrm{LL}}(\gamma)+\bar{\alpha}_s^2\left(A+B\partial_\gamma\log\Phi_{Q\bar{Q}}(\gamma)\right). \qquad (5.61)$$

The new exponent is given by

$$\begin{aligned}\bar{\mathcal{K}}(\gamma) &= \bar{\alpha}_s\tilde{\chi}_0+\bar{\alpha}_s^2\left[\tilde{\chi}_1+\frac{\beta_0}{8N_c}\left(2\chi_0\log(\mu^2)+\tilde{\chi}_0'-2\tilde{\chi}_0\partial_\gamma\log\left(\Phi_P(\gamma)\right)\right)\right]\\ &= \tilde{\chi}_0\left[\bar{\alpha}_s-\bar{\alpha}_s^2\frac{\beta_0}{4N_c}\log\left(\frac{M^2}{\mu^2}\right)\right]+\bar{\alpha}_s^2\tilde{\chi}_1+\bar{\alpha}_s^2\frac{\beta_0}{4N_c}\tilde{\chi}_0\left[\frac{1}{2}\frac{\tilde{\chi}_0'}{\tilde{\chi}_0}-\partial_\gamma\log\left(\frac{h(0,\gamma)}{\gamma}\right)\right]\\ &\simeq \bar{\alpha}_s(M)\tilde{\chi}_0+\bar{\alpha}_s^2(M)\left\{\tilde{\chi}_1+\frac{\beta_0}{4N_c}\tilde{\chi}_0\left[\frac{1}{2}\frac{\tilde{\chi}_0'}{\tilde{\chi}_0}-\partial_\gamma\log\left(\frac{h(0,\gamma)}{\gamma}\right)\right]\right\}\,. \qquad (5.62)\end{aligned}$$

In order to write the last line we have used RG analysis. We can introduce this running of the coupling in all terms in eq.(5.60) without modifying the expression at $\mathcal{O}(\alpha_s^2)$. The last term of the expression above reads

$$\begin{aligned}\partial_\gamma\log\left(\frac{h(0,\gamma)}{\gamma}\right) &= \frac{2}{3-2\gamma}+\frac{2}{5-2\gamma}-\frac{1}{\gamma}+\frac{20\gamma+4N_c^2-39}{4N_c^2(\gamma-2)(2\gamma-5)(5\gamma-7)}\\ &\quad+2\psi(2-2\gamma)-3\psi(1-\gamma)+\psi(1+\gamma)\,. \qquad (5.63)\end{aligned}$$

One can also be concerned about exponentiating the non scale invariant piece of the kernel given in eq. (5.61). We could also leave it down as it is done in [126].

The final ingredient to be added into the kernel is the term $\mathcal{K}^{\mathrm{RG}}$, accounting for the collinear improvements. Since the running coupling effects break the scale invariance, the pole structure in γ and $1-\gamma$ will now be different. The new piece

[2] Do not confuse the Mellin transform variable ω appearing here with the one used for the transformations given by eqs. (5.48) and (5.49).

in this case will be given by

$$\begin{aligned}\mathcal{K}^{\rm RG}(\gamma) &= \left\{\sum_{m=0}^{\infty}\left[\left(\sum_{n=0}^{\infty}\frac{(-1)^n(2n)!}{2^n n!(n+1)!}\frac{\left(\bar{\alpha}_s(M)+\mathrm{a}\,\bar{\alpha}_s^2(M)\right)^{n+1}}{\left(\gamma+m-\mathrm{b}\,\bar{\alpha}_s(M)\right)^{2n+1}}\right)-\frac{\bar{\alpha}_s(M)}{\gamma+m}\right.\right.\\ &\left.\left.-\bar{\alpha}_s^2(M)\left(\frac{\mathrm{a}}{\gamma+m}+\frac{\mathrm{b}}{(\gamma+m)^2}-\frac{1}{2(\gamma+m)^3}\right)\right]\right\}\\ &+\left\{\sum_{m=0}^{\infty}\left[\left(\sum_{n=0}^{\infty}\frac{(-1)^n(2n)!}{2^n n!(n+1)!}\frac{\left(\bar{\alpha}_s(M)+\tilde{\mathrm{a}}\,\bar{\alpha}_s^2(M)\right)^{n+1}}{\left(1-\gamma+m-\tilde{\mathrm{b}}\,\bar{\alpha}_s(M)\right)^{2n+1}}\right)-\frac{\bar{\alpha}_s(M)}{1-\gamma+m}\right.\right.\\ &\left.\left.-\bar{\alpha}_s^2(M)\left(\frac{\tilde{\mathrm{a}}}{1-\gamma+m}+\frac{\tilde{\mathrm{b}}}{(1-\gamma+m)^2}-\frac{1}{2(1-\gamma+m)^3}\right)\right]\right\}\,, \qquad (5.64)\end{aligned}$$

with the coefficients being

$$\begin{aligned}a &= -\frac{55}{36}-\frac{13n_f}{36Nc^3}-\frac{b_0}{10N_c}\left(\frac{25-18N_c^2}{35-8N_c^2}\right)\,,\\ b &= -\frac{11}{12}-\frac{n_f}{6Nc^3}-\frac{b_0}{8N_c}\,,\\ \tilde{a} &= -\frac{55}{36}-\frac{13n_f}{36Nc^3}-\frac{13b_0}{8N_c(-3+2N_c^2)}\,,\\ \tilde{b} &= -\frac{11}{12}-\frac{n_f}{6Nc^3}-\frac{b_0}{2N_c}\,, \qquad (5.65)\end{aligned}$$

defined such that the pole structure of the kernel is

$$\bar{\mathcal{K}}(\gamma)\to\frac{a}{\gamma}+\frac{b}{\gamma^2}+\frac{\tilde{a}}{(1-\gamma)}+\frac{\tilde{b}}{(1-\gamma)^2}-\frac{2}{\gamma^3}-\frac{2}{(1-\gamma)^3}\,. \qquad (5.66)$$

Putting everything together the total hadronic cross section is be given by

$$\begin{aligned}\sigma_{\rm had}^{\rm tot}(s,M^2) &= \int\frac{\mathrm{d}x_1}{x_1}\int\frac{\mathrm{d}x_2}{x_2}\delta(x_1x_2s-4M^2)g(x_1,\mu_F^2)\int\frac{\mathrm{d}\gamma}{2\pi i}\frac{1}{\pi M^2}\Phi_{Q\bar{Q}}(\gamma)\Phi_P(\gamma)x_2^{-\mathcal{K}(\gamma)}\\ &= \int\frac{\mathrm{d}x_1}{x_1}\int\frac{\mathrm{d}\Sigma}{\Sigma}g(x_1,\mu_F^2)\,\mathcal{R}\left(\frac{\Sigma}{x_1s},M^2\right)\delta(\Sigma-4M^2)\\ &= \frac{1}{4M^2}\int_{x_{min}}^{x_{max}}\frac{\mathrm{d}x_1}{x_1}g(x,\mu_F^2)\,\mathcal{R}\left(\frac{\tau}{x},M^2\right)\,, \qquad (5.67)\end{aligned}$$

where we have introduced the definition $\tau\equiv 4M^2/s$. The momentum scale μ_F^2 should be taken to be $\mu_F^2=4M^2$. The integration limits x_{min} and x_{max} are given below. Fig. 5.17 shows the dependence of $\mathcal{R}(x_2,M^2)$ on x_2 at LLA, scale invariant NLL kernel with collinear improvements and complete kernel, considering running coupling effects and eq. (5.64) for the collinear resummation. These curves can be parametrized with the following analytic approximations:

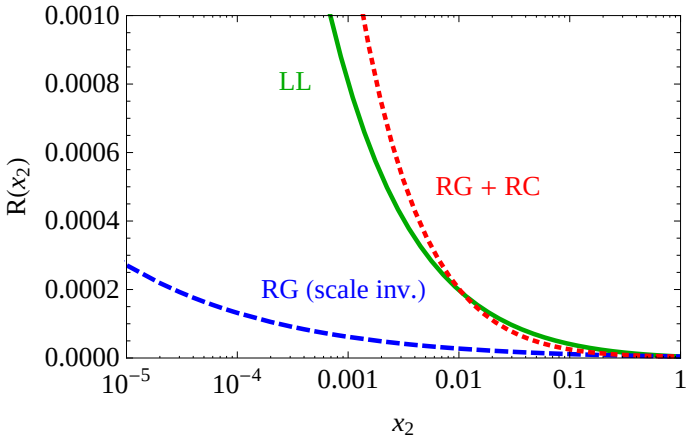

Figure 5.17: $\mathcal{R}(x_2, M^2)$ versus x_2 for LL (green, solid line), collinear improved for the scale invariant part of the NLL kernel (blue, dashed line) and collinear improved including running coupling corrections (red, dotted line).

$$\mathcal{R}_{\rm fit}^{\rm LL}(x) = \sum_{n=0}^{9} c_n^{\rm LL} x^{-1/n},$$
$$\mathcal{R}_{\rm fit}^{\rm BR}(x) = \sum_{n=0}^{9} c_n^{\rm BR} x^{-1/n},$$
$$\mathcal{R}_{\rm fit}^{\rm BRAsy}(x) = \sum_{n=0}^{11} c_n^{\rm BRAsy} x^{-1/n}. \tag{5.68}$$

finding in the three cases results as accurate as the LL one, shown in fig. 5.16.

In order to compute the complete hadronic cross section as given in eq. (5.67) one needs to introduce the distribution function of the on-shell gluon. We have used the MSTW PDF's [12] at NNLO approximation. The Mathematica code generated by G. Watt has been used for the numerical implementation. Figure 5.18 shows the dependence of the total hadronic cross section on μ_F^2 and on the upper integration limit x_{max} for the three cases analyzed, with $s = 4.9\times10^7$ GeV^2, $M^2 = 17.556$ GeV^2 and $\bar{\alpha}_s = 0.2$. The integration limits $x_{\rm min}$ and $x_{\rm max}$ are fully determined by the constraints given in eqs. (5.40) and (5.41) plus the threshold condition. They are given by

$$x_{\rm min} = \sqrt{\frac{4M^2}{s}} e^{1.9} \simeq 0.008 \qquad \text{and} \qquad x_{\rm max} = \sqrt{\frac{4M^2}{s}} e^{4.9} \simeq 0.16\,. \tag{5.69}$$

We see how the dependence on both the factorization scale and on x_{max} is very small for the three cases. Figure 5.19 shows the same dependence for the LL case in more detail, revealing its weakness but still existence.

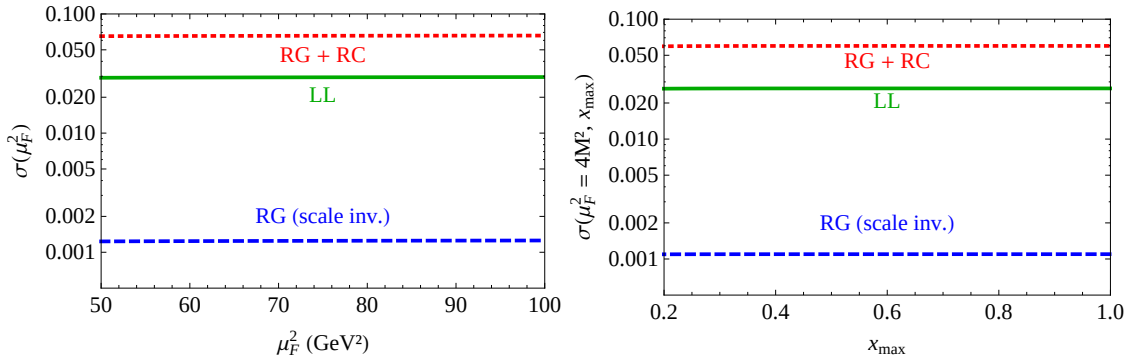

Figure 5.18: Dependence of the hadronic cross section on the renormalization scale μ_F^2 (left) and on the upper integration limit x_{max} appearing in eq. (5.67).

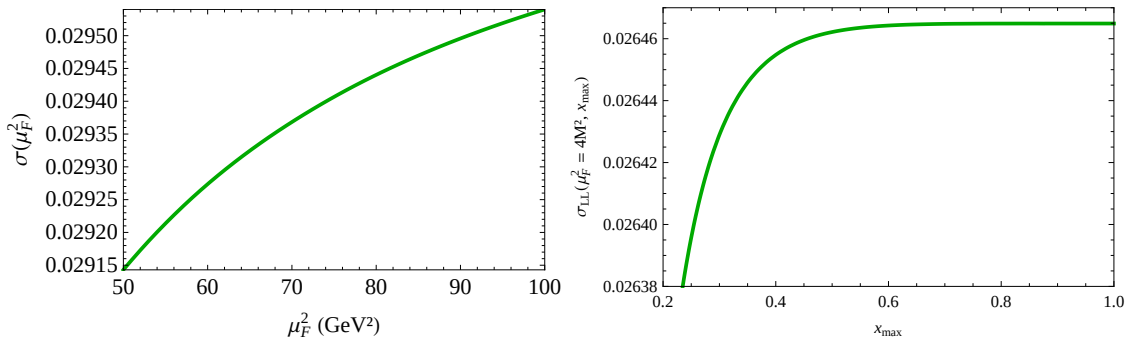

Figure 5.19: Dependence of the hadronic cross section on the renormalization scale μ_F^2 (left) and on the upper integration limit x_{max} appearing in eq. (5.67) at LLA.

We would like to stress that this results are very preliminary and are susceptible to changes. In order to measure the impact of producing the heavy quark pair collinear to one of the protons it is our aim to compare our numerical results, together with the (also preliminary) ones of the previous section, with [19], where the production of heavy quark pairs is studied exactly at LO and NLO. This would give us a good taste of the relevance of the different resummation effects.

Chapter 6

Conclusions & Outlook

In this thesis we have analyzed the formalism of the BFKL resummation up to next-to-leading logarithmic accuracy mainly from a phenomenological point of view. At NLL accuracy, the BFKL equation is governed by quasi-multi-regge kinematics and resums terms of the form $\bar{\alpha}_s(\bar{\alpha}_s \ln(s/s_0))^n$. At LL accuracy the energy scale s_0 is a free parameter but this is not the case for the next order. As we have seen throughout this work, the NLL corrections to the BFKL gluon Green's function are large and negative compared to the LL ones and need to be stabilized in order to get accurate descriptions of the experimental data and make reliable predictions. This odd behavior arises from the freedom in the choice of energy scale s_0 at the first order of accuracy, which introduces double logarithms in transverse momentum space (or collinear poles in its Mellin transform) which are incompatible with renormalization group evolution and that become numerically large in collinear regions of phase space. When the series is truncated at NLL accuracy there is a remaining dependence on these logarithms due to the exponentiation of the BFKL kernel that would be canceled exactly if higher order terms of the perturbative expansion were included. A way to improve such a situation is by including collinear corrections to all-orders in perturbation theory following [14, 15]. In the second half of this work we have considered different phenomenological scenarios which highlight the importance of adding collinear improvements to obtain an adequate description of physical observables.

Our first example was worked out in chapter 4, with the analysis of DIS data in the low x region using the BFKL resummation. The pure NLL approach was not sufficient to reproduce the experimental data and collinear contributions had to be added. Moreover, in order to get a good description of the combined HERA data in the low Q^2 or infrared region we needed to introduce a physical scheme with optimal renormalization scale and use a model for the coupling with an analytic behavior in the infrared. In this way we were able to get a smooth

transition from a hard to a soft pomeron in good agreement with the experimental data [16, 17]. Subleading corrections which may help to improve the accuracy of our results in future works would be the inclusion of quark masses or taking into account threshold effects. We are at present working on including these refinements, together with the implementation of the full NLO photon impact factor, in a Monte Carlo event generator analysis.

Another non-trivial point to be worth investigating when introducing NLL corrections is the treatment of the running of the coupling. From an analytical point of view, as we saw in section 3.3.2, this is a source of theoretical uncertainties entering as higher order corrections in the coupling, $\mathcal{O}(\bar{\alpha}_s^3)$, but still leading to sizeable effects when calculating physical observables. A better way to deal with the running in this case is numerically. In section 3.2.2 we presented an iterative solution to the non-forward LL BFKL equation including running coupling effects compatible with bootstrap and provided numerical results for the gluon Green's function using Monte Carlo integration techniques [18]. The next step in this direction will be to convolute these results with some physical, relevant impact factors to be able to give predictions for exclusive observables such as azimuthal angle decorrelations of jets (see section 5.1) or multi-jet production, needed to be able to distinguish between the predictions given by different resummation programs. A good observable to be analyzed would be the one proposed in [169], which is based on the transverse momentum transfer in the gluon ladder. To study it, one needs to tag each soft gluon emission and leave it unintegrated so that final state p_T distributions can be analyzed. In this direction one could try to extend the Mueller-Navelet original setup to have more tagged jets in central regions of the detector. For this the use of Monte Carlo event generators is mandatory since it allows for a full control of the p_T and multiplicity distributions in the final state. An important target for future work is to extend out study of the large t elastic amplitudes to NLL and integrate them with the corresponding NLO impact factors for the production of Mueller-Tang diffractive events at the LHC. Results in this direction at the level of the gluon Green's function can be found for $N = 4$ SYM in [66].

In section 5.1 we studied the production of Mueller-Navelet jets with NLO jet vertices, using the so-called small cone approximation and with the gluon Green's function taken at NLL accuracy. In order to fix the factorization, renormalization and energy scales we used the principle of minimum sensitivity, considering as optimal choices those values for which the physical quantity under examination exhibits minimal variations. Note that this way of choosing the "free" scales makes our theory predictive, in the sense that we do not need any external input

to fix them. An important result shown in this work is that adding collinear improvements to the NLL solution naturally reduces the values of the scales making them to be more similar to the typical squared transverse momentum of the tagged jets. We also could find stability zones for the parameters using collinear resummation in the region further away from the original quasi-multi-Regge kinematics –where the jets have very different transverse momentum– whereas this was not possible in the pure NLL case. Finally, we also show how the best suited observables are the azimuthal angle decorrelations, which are quite insensitive to collinear contributions and are very convergent within the QCD context. Our next target in this direction will be to implement this work with the Monte Carlo code mentioned above to be able to work directly in transverse momentum space and see how different ways of the treatment of the running of the coupling would affect the stability regions of the parameters of the theory.

Finally, from the fit of DIS data performed in section 4 we extracted a model for the proton impact factor that were then able to use in the construction of cross sections for the hadro-production of heavy quarks. Two phenomenological preliminary studies were presented in sections 5.2 and 5.3. In the first one a heavy quark pair is produced in the central region of rapidity, leaving enough phase space between the two parent hadrons and the hard vertex to emit soft gluon radiation and incorporate BFKL resummation. In the second case, however, the heavy quark pair is produced collinear to one of the hadrons and both, collinear and k_T factorization have to be applied. It is our intention to make a comparative analysis of these results with the one obtained in [19].

With this overview of the past, present and future work we conclude this doctoral thesis, whose results have been obtained at a very interesting time: the starting of the running of the LHC which offers a unique opportunity to investigate the high energy limit of QCD and low x physics. The data being analyzed by the LHCb and CMS experiments will keep us busy for the next few years, while awaiting for the (hopefully) arrival of new colliders specially designed for the measure of small x physics such as the EIC [111,112] (BLN/JLab) or the LHeC [31] (CERN).

Bibliography

[1] Y. L. Dokshitzer. Phil.Trans.Roy.Soc.Lond. **A359** (2001) 309–324, arXiv:hep-ph/0106348 [hep-ph].

[2] M. Praszalowicz. Acta Phys.Polon. **B12** (1981) 773–791.

[3] P. Collins. Cambridge **445p** (1977) .

[4] A. Donnachie and P. Landshoff. Phys.Lett. **B296** (1992) 227–232, arXiv:hep-ph/9209205 [hep-ph].

[5] L. Lipatov. Sov.J.Nucl.Phys. **23** (1976) 338–345.

[6] V. S. Fadin, E. Kuraev, and L. Lipatov. Phys.Lett. **B60** (1975) 50–52.

[7] E. Kuraev, L. Lipatov, and V. S. Fadin. Sov.Phys.JETP **44** (1976) 443–450.

[8] E. Kuraev, L. Lipatov, and V. S. Fadin. Sov.Phys.JETP **45** (1977) 199–204.

[9] I. Balitsky and L. Lipatov. Sov.J.Nucl.Phys. **28** (1978) 822–829.

[10] T. Muta. World Sci.Lect.Notes Phys. **5** (1987) 1–409.

[11] H. D. Politzer. Physics Reports **14** no. 4, (1974) 129 – 180. http://www.sciencedirect.com/science/article/pii/0370157374900143.

[12] A. Martin, W. Stirling, R. Thorne, and G. Watt. Eur.Phys.J. **C63** (2009) 189–285, arXiv:0901.0002 [hep-ph].

[13] J. R. Forshaw and D. Ross. Cambridge Lect.Notes Phys. **9** (1997) 1–248.

[14] G. Salam. JHEP **9807** (1998) 019, arXiv:hep-ph/9806482 [hep-ph].

[15] A. Sabio Vera. Nucl.Phys. **B722** (2005) 65–80, arXiv:hep-ph/0505128 [hep-ph].

[16] M. Hentschinski, A. S. Vera, and C. Salas. arXiv:1209.1353 [hep-ph].

[17] M. Hentschinski, A. S. Vera, and C. Salas. arXiv:1301.5283 [hep-ph].

[18] G. Chachamis, A. S. Vera, and C. Salas. arXiv:1211.6332 [hep-ph].

[19] J. R. Andersen, V. Del Duca, S. Frixione, F. Maltoni, and W. J. Stirling. JHEP **0411** (2004) 061, arXiv:hep-ph/0408239 [hep-ph].

[20] P. M. Stevenson. Phys.Lett. **B100** (1981) 61.

[21] F. Close.

[22] S. Chekanov *et al.* Phys.Lett. **B682** (2009) 8–22, arXiv:0904.1092 [hep-ex].

[23] M. Derrick *et al.* Z.Phys. **C69** (1996) 607–620, arXiv:hep-ex/9510009 [hep-ex].

[24] F. Aaron *et al.* Phys.Lett. **B665** (2008) 139–146, arXiv:0805.2809 [hep-ex].

[25] F. Aaron *et al.* Eur.Phys.J. **C71** (2011) 1579, arXiv:1012.4355 [hep-ex].

[26] T. Ahmed *et al.* Nucl.Phys. **B439** (1995) 471–502, arXiv:hep-ex/9503001 [hep-ex].

[27] S. Habib. PoS **DIS2010** (2010) 035.

[28] F. Aaron *et al.* JHEP **1001** (2010) 109, arXiv:0911.0884 [hep-ex].

[29] N. Raicevic. Nucl.Phys.Proc.Suppl. **198** (2010) 75–83.

[30] J. Schwartz. arXiv:1010.1023 [hep-ex].

[31] J. Abelleira Fernandez *et al.* J.Phys. **G39** (2012) 075001, arXiv:1206.2913 [physics.acc-ph].

[32] V. Barone and E. Predazzi.

[33] R. K. Ellis, W. J. Stirling, and B. Webber. Camb.Monogr.Part.Phys.Nucl.Phys.Cosmol. **8** (1996) 1–435.

[34] G. Altarelli and G. Parisi. Nucl.Phys. **B126** (1977) 298.

[35] V. Gribov and L. Lipatov. Sov.J.Nucl.Phys. **15** (1972) 438–450.

[36] Y. L. Dokshitzer. Sov.Phys.JETP **46** (1977) 641–653.

[37] N. Ellis and R. Fleischer.

[38] N. Ellis and J. March-Russell.

[39] S. Catani, F. Fiorani, and G. Marchesini. Phys.Lett. **B234** (1990) 339.

[40] G. Marchesini. Nucl.Phys. **B445** (1995) 49–80, arXiv:hep-ph/9412327 [hep-ph].

[41] M. Ciafaloni. Nucl.Phys. **B296** (1988) 49.

[42] S. Catani, M. Ciafaloni, and F. Hautmann. Phys.Lett. **B242** (1990) 97.

[43] T. Regge. Nuovo Cim. **14** (1959) 951.

[44] J. Mathews and R. Walker. Addison Wesley (1971) 501.

[45] T. Regge. Nuovo Cim. **18** (1960) 947–956.

[46] G. Chew and S. C. Frautschi. Phys.Rev.Lett. **7** (1961) 394–397.

[47] G. Chew and S. C. Frautschi. Phys.Rev.Lett. **8** (1962) 41–44.

[48] I. Y. Pomeranchuk, V. Sudakov, and K. Ter-Martirosyan. Phys.Rev. **103** (1956) 784–802.

[49] L. L. Foldy and R. F. Peierls. Phys.Rev. **130** (1963) 1585–1589.

[50] L. Gribov, E. Levin, and M. Ryskin. Phys.Rept. **100** (1983) 1–150.

[51] T. Jaroszewicz. Acta Phys.Polon. **B11** (1980) 965.

[52] A. Watanabe and K. Suzuki. Phys.Rev. **D86** (2012) 035011, arXiv:1206.0910 [hep-ph].

[53] J. Bartels, L. Lipatov, and A. Sabio Vera. Phys.Rev. **D80** (2009) 045002, arXiv:0802.2065 [hep-th].

[54] B. Andersson, G. Gustafson, and H. Kharraziha. Phys.Rev. **D57** (1998) 5543–5554, arXiv:hep-ph/9711403 [hep-ph].

[55] Y. V. Kovchegov and A. H. Mueller. Phys.Lett. **B439** (1998) 428–436, arXiv:hep-ph/9805208 [hep-ph].

[56] R. S. Thorne. Phys.Rev. **D60** (1999) 054031, arXiv:hep-ph/9901331 [hep-ph].

[57] J. R. Forshaw, D. Ross, and A. Sabio Vera. Phys.Lett. **B498** (2001) 149–155, arXiv:hep-ph/0011047 [hep-ph].

[58] Y. V. Kovchegov and H. Weigert. Nucl.Phys. **A789** (2007) 260–284, arXiv:hep-ph/0612071 [hep-ph].

[59] H. Kowalski, L. Lipatov, and D. Ross. arXiv:1205.6713 [hep-ph].

[60] M. Braun. Phys.Lett. **B348** (1995) 190–195, arXiv:hep-ph/9408261 [hep-ph].

[61] E. Levin. Nucl.Phys. **B453** (1995) 303–333, arXiv:hep-ph/9412345 [hep-ph].

[62] Y. V. Kovchegov and H. Weigert. Nucl.Phys. **A784** (2007) 188–226, arXiv:hep-ph/0609090 [hep-ph].

[63] V. S. Fadin and R. Fiore. Phys.Lett. **B440** (1998) 359–366, arXiv:hep-ph/9807472 [hep-ph].

[64] M. Braun, G. P. Vacca, and G. Venturi. Phys.Lett. **B388** (1996) 823–831, arXiv:hep-ph/9605304 [hep-ph].

[65] G. Chachamis and A. Sabio Vera. Phys.Lett. **B709** (2012) 301–308, arXiv:1112.4162 [hep-th].

[66] G. Chachamis and A. S. Vera. Phys.Lett. **B717** (2012) 458–461, arXiv:1206.3140 [hep-th].

[67] J. R. Andersen and A. Sabio Vera. JHEP **0501** (2005) 045, arXiv:hep-ph/0411231 [hep-ph].

[68] G. Chachamis, M. Deak, A. S. Vera, and P. Stephens. Nucl.Phys. **B849** (2011) 28–44, arXiv:1102.1890 [hep-ph].

[69] J. Bartels, H. Lotter, and M. Vogt. Phys.Lett. **B373** (1996) 215–222, arXiv:hep-ph/9511399 [hep-ph].

[70] J. Bartels and H. Lotter. Phys.Lett. **B309** (1993) 400–408.

[71] V. S. Fadin and L. Lipatov. Phys.Lett. **B429** (1998) 127–134, arXiv:hep-ph/9802290 [hep-ph].

[72] V. S. Fadin, R. Fiore, and M. Kotsky. Phys.Lett. **B387** (1996) 593–602, arXiv:hep-ph/9605357 [hep-ph].

[73] V. S. Fadin, M. Kotsky, and R. Fiore. Phys.Lett. **B359** (1995) 181–188.

[74] V. S. Fadin and L. Lipatov. Nucl.Phys. **B406** (1993) 259–292.

[75] V. Fadin, M. Kotsky, and L. Lipatov. Phys.Lett. **B415** (1997) 97–103.

[76] M. Kotsky, V. S. Fadin, and L. Lipatov. Phys.Atom.Nucl. **61** (1998) 641–656.

[77] V. S. Fadin, R. Fiore, A. Flachi, and M. Kotsky. Phys.Lett. **B422** (1998) 287–293, arXiv:hep-ph/9711427 [hep-ph].

[78] V. S. Fadin, M. Kotsky, R. Fiore, and A. Flachi. Phys.Atom.Nucl. **62** (1999) 999–1007.

[79] L. Lipatov. Sov.Phys.JETP **63** (1986) 904–912.

[80] D. Ross. Phys.Lett. **B431** (1998) 161–165, arXiv:hep-ph/9804332 [hep-ph].

[81] M. Ciafaloni, D. Colferai, and G. Salam. Phys.Rev. **D60** (1999) 114036, arXiv:hep-ph/9905566 [hep-ph].

[82] M. Ciafaloni, D. Colferai, G. Salam, and A. Stasto. Phys.Rev. **D68** (2003) 114003, arXiv:hep-ph/0307188 [hep-ph].

[83] G. Altarelli, R. D. Ball, and S. Forte. Nucl.Phys. **B742** (2006) 1–40, arXiv:hep-ph/0512237 [hep-ph].

[84] J. Blumlein, V. Ravindran, W. van Neerven, and A. Vogt. arXiv:hep-ph/9806368 [hep-ph].

[85] E. Levin. arXiv:hep-ph/9806228 [hep-ph].

[86] N. Armesto, J. Bartels, and M. Braun. Phys.Lett. **B442** (1998) 459–469, arXiv:hep-ph/9808340 [hep-ph].

[87] S. J. Brodsky, V. S. Fadin, V. T. Kim, L. N. Lipatov, and G. B. Pivovarov. JETP Lett. **70** (1999) 155–160, arXiv:hep-ph/9901229 [hep-ph].

[88] C. R. Schmidt. Phys.Rev. **D60** (1999) 074003, arXiv:hep-ph/9901397 [hep-ph].

[89] J. R. Forshaw, D. Ross, and A. Sabio Vera. Phys.Lett. **B455** (1999) 273–282, arXiv:hep-ph/9903390 [hep-ph].

[90] G. Altarelli, R. D. Ball, and S. Forte. Nucl.Phys. **B674** (2003) 459–483, arXiv:hep-ph/0306156 [hep-ph].

[91] J. R. Andersen and A. Sabio Vera. Phys.Lett. **B567** (2003) 116–124, arXiv:hep-ph/0305236 [hep-ph].

[92] J. R. Andersen and A. Sabio Vera. Nucl.Phys. **B679** (2004) 345–362, arXiv:hep-ph/0309331 [hep-ph].

[93] M. Ciafaloni and G. Camici. Phys.Lett. **B430** (1998) 349–354, arXiv:hep-ph/9803389 [hep-ph].

[94] A. Kotikov and L. Lipatov. Nucl.Phys. **B582** (2000) 19–43, arXiv:hep-ph/0004008 [hep-ph].

[95] V. Fadin and R. Fiore. Phys.Lett. **B610** (2005) 61–66, arXiv:hep-ph/0412386 [hep-ph].

[96] V. Fadin and R. Fiore. Phys.Rev. **D72** (2005) 014018, arXiv:hep-ph/0502045 [hep-ph].

[97] F. Caporale, G. Chachamis, J. Madrigal, B. Murdaca, and A. S. Vera. arXiv:1305.1474 [hep-th].

[98] F. Schwennsen. arXiv:hep-ph/0703198 [HEP-PH].

[99] B. R. Webber. JHEP **9810** (1998) 012, arXiv:hep-ph/9805484 [hep-ph].

[100] A. Sabio Vera. Nucl.Phys. **B746** (2006) 1–14, arXiv:hep-ph/0602250 [hep-ph].

[101] A. Sabio Vera and F. Schwennsen. Nucl.Phys. **B776** (2007) 170–186, arXiv:hep-ph/0702158 [HEP-PH].

[102] A. Vogt, S. Moch, and J. Vermaseren. Nucl.Phys. **B691** (2004) 129–181, arXiv:hep-ph/0404111 [hep-ph].

[103] A. Kotikov, L. Lipatov, A. Onishchenko, and V. Velizhanin. Phys.Lett. **B595** (2004) 521–529, arXiv:hep-th/0404092 [hep-th].

[104] J. Kwiecinski, A. D. Martin, and A. Stasto. Phys.Rev. **D56** (1997) 3991–4006, arXiv:hep-ph/9703445 [hep-ph].

[105] A. Bialas, H. Navelet, and R. B. Peschanski. Nucl.Phys. **B603** (2001) 218–230, arXiv:hep-ph/0101179 [hep-ph].

[106] A. Sabio Vera and F. Schwennsen. Phys.Rev. **D77** (2008) 014001, arXiv:0708.0549 [hep-ph].

[107] H. Kowalski, L. Lipatov, D. Ross, and G. Watt. Eur.Phys.J. **C70** (2010) 983–998, arXiv:1005.0355 [hep-ph].

[108] S. J. Brodsky, G. P. Lepage, and P. B. Mackenzie. Phys.Rev. **D28** (1983) 228.

[109] W. Celmaster and R. J. Gonsalves. Phys.Rev. **D20** (1979) 1420.

[110] S. J. Brodsky and L. Di Giustino. Phys.Rev. **D86** (2012) 085026, arXiv:1107.0338 [hep-ph].

[111] A. Accardi, J. Albacete, M. Anselmino, N. Armesto, E. Aschenauer, *et al.* arXiv:1212.1701 [nucl-ex].

[112] D. Boer, M. Diehl, R. Milner, R. Venugopalan, W. Vogelsang, *et al.* arXiv:1108.1713 [nucl-th].

[113] O. Bruening and M. Klein. arXiv:1305.2090 [physics.acc-ph].

[114] I. Balitsky and G. A. Chirilli. arXiv:1207.3844 [hep-ph].

[115] Z. Ajaltouni, S. Albino, G. Altarelli, F. Ambroglini, J. Anderson, *et al.* arXiv:0903.3861 [hep-ph].

[116] F. Caporale, B. Murdaca, A. S. Vera, and C. Salas. arXiv:1305.4620 [hep-ph].

[117] G. Chachamis, M. Hentschinski, A. Sabio Vera, and C. Salas. arXiv:0911.2662 [hep-ph].

[118] V. Khachatryan *et al.* Phys.Rev. **D83** (2011) 112004, arXiv:1012.5545 [hep-ex].

[119] R. Aaij *et al.* Eur.Phys.J. **C72** (2012) 2025, arXiv:1202.6579 [hep-ex].

[120] A. H. Mueller and H. Navelet. Nucl.Phys. **B282** (1987) 727.

[121] M. Angioni, G. Chachamis, J. Madrigal, and A. Sabio Vera. Phys.Rev.Lett. **107** (2011) 191601, arXiv:1106.6172 [hep-th].

[122] C. Marquet and C. Royon. Nucl.Phys. **B739** (2006) 131–155, arXiv:hep-ph/0510266 [hep-ph].

[123] C. Marquet and C. Royon. Phys.Rev. **D79** (2009) 034028, arXiv:0704.3409 [hep-ph].

[124] D. Y. Ivanov and A. Papa. PoS **DIFF2006** (2006) 027, arXiv:hep-ph/0612322 [hep-ph].

[125] F. Caporale, D. Y. Ivanov, and A. Papa. Eur.Phys.J. **C58** (2008) 1–7, arXiv:0807.3231 [hep-ph].

[126] F. Caporale, A. Papa, and A. Sabio Vera. Eur.Phys.J. **C53** (2008) 525–532, arXiv:0707.4100 [hep-ph].

[127] J. Bartels, D. Colferai, and G. Vacca. Eur.Phys.J. **C24** (2002) 83–99, arXiv:hep-ph/0112283 [hep-ph].

[128] J. Bartels, D. Colferai, and G. Vacca. Eur.Phys.J. **C29** (2003) 235–249, arXiv:hep-ph/0206290 [hep-ph].

[129] F. Caporale, D. Y. Ivanov, B. Murdaca, A. Papa, and A. Perri. JHEP **1202** (2012) 101, arXiv:1112.3752 [hep-ph].

[130] D. Y. Ivanov and A. Papa. JHEP **1205** (2012) 086, arXiv:1202.1082 [hep-ph].

[131] M. Hentschinski and A. S. Vera. Phys.Rev. **D85** (2012) 056006, arXiv:1110.6741 [hep-ph].

[132] G. Chachamis, M. Hentschinski, J. Madrigal Martinez, and A. Sabio Vera. Nucl.Phys. **B861** (2012) 133–144, arXiv:1202.0649 [hep-ph].

[133] M. Hentschinski, B. Murdaca, and A. S. Vera. arXiv:1206.1622 [hep-ph].

[134] G. Chachamis, M. Hentschinski, J. M. Martinez, and A. S. Vera. arXiv:1211.2050 [hep-ph].

[135] G. Chachamis, M. Hentschinski, J. D. Madrigal, and A. S. Vera. arXiv:1212.4992 [hep-ph].

[136] F. Caporale, D. Y. Ivanov, B. Murdaca, and A. Papa. arXiv:1211.7225 [hep-ph].

[137] B. Ducloué, L. Szymanowski, and S. Wallon. arXiv:1302.7012 [hep-ph].

[138] D. Colferai, F. Schwennsen, L. Szymanowski, and S. Wallon. JHEP **1012** (2010) 026, arXiv:1002.1365 [hep-ph].

[139] S. Cerci and D. d'Enterria. AIP Conf.Proc. **1105** (2009) 28–32, arXiv:0812.2665 [hep-ex].

[140] R. Bonciani, S. Catani, M. L. Mangano, and P. Nason. Nucl.Phys. **B529** (1998) 424–450, arXiv:hep-ph/9801375 [hep-ph].

[141] S. Moch and P. Uwer. Phys.Rev. **D78** (2008) 034003, arXiv:0804.1476 [hep-ph].

[142] M. Cacciari, S. Frixione, M. L. Mangano, P. Nason, and G. Ridolfi. JHEP **0809** (2008) 127, arXiv:0804.2800 [hep-ph].

[143] N. Kidonakis and R. Vogt. Phys.Rev. **D78** (2008) 074005, arXiv:0805.3844 [hep-ph].

[144] N. Kidonakis. arXiv:0909.0037 [hep-ph].

[145] M. Czakon and A. Mitov. Phys.Lett. **B680** (2009) 154–158, arXiv:0812.0353 [hep-ph].

[146] M. Czakon, A. Mitov, and G. F. Sterman. Phys.Rev. **D80** (2009) 074017, arXiv:0907.1790 [hep-ph].

[147] P. Nason, S. Dawson, and R. K. Ellis. Nucl.Phys. **B303** (1988) 607.

[148] W. Beenakker, W. van Neerven, R. Meng, G. Schuler, and J. Smith. Nucl.Phys. **B351** (1991) 507–560.

[149] R. Ball and R. K. Ellis. JHEP **0105** (2001) 053, arXiv:hep-ph/0101199 [hep-ph].

[150] J. C. Collins and R. K. Ellis. Nucl.Phys. **B360** (1991) 3–30.

[151] S. Catani, M. Ciafaloni, and F. Hautmann. Nucl.Phys. **B366** (1991) 135–188.

[152] E. Levin, M. Ryskin, Y. Shabelski, and A. Shuvaev. Sov.J.Nucl.Phys. **53** (1991) 657.

[153] S. Baranov and M. Smizanska. Phys.Rev. **D62** (2000) 014012.

[154] S. Baranov, A. Lipatov, and N. Zotov. Yad.Fiz. **67** (2004) 856, arXiv:hep-ph/0302171 [hep-ph].

[155] H. Jung. Phys.Rev. **D65** (2002) 034015, arXiv:hep-ph/0110034 [hep-ph].

[156] J. Bartels, A. Sabio Vera, and F. Schwennsen. JHEP **0611** (2006) 051, arXiv:hep-ph/0608154 [hep-ph].

[157] S. Moch, P. Uwer, and A. Vogt. Phys.Lett. **B714** (2012) 48–54, arXiv:1203.6282 [hep-ph].

[158] M. Czakon and A. Mitov. JHEP **1212** (2012) 054, arXiv:1207.0236 [hep-ph].

[159] M. Czakon and A. Mitov. JHEP **1301** (2013) 080, arXiv:1210.6832 [hep-ph].

[160] R. Maciula and A. Szczurek. arXiv:1301.3033 [hep-ph].

[161] B. Kniehl, V. Saleev, and D. Vasin. Phys.Rev. **D74** (2006) 014024, arXiv:hep-ph/0607254 [hep-ph].

[162] B. Kniehl, A. Shipilova, and V. Saleev. Phys.Rev. **D79** (2009) 034007, arXiv:0812.3376 [hep-ph].

[163] B. Kniehl, V. Saleev, and A. Shipilova. Phys.Rev. **D81** (2010) 094010, arXiv:1003.0346 [hep-ph].

[164] M. Baumgart and B. Tweedie. JHEP **1303** (2013) 117, arXiv:1212.4888 [hep-ph].

[165] B. Abelev *et al.* JHEP **1201** (2012) 128, arXiv:1111.1553 [hep-ex].

[166] S. Chatrchyan *et al.* JHEP **1204** (2012) 084, arXiv:1202.4617 [hep-ex].

[167] D. Acosta *et al.* Phys.Rev.Lett. **91** (2003) 241804, arXiv:hep-ex/0307080 [hep-ex].

[168] R. K. Ellis and D. Ross. Nucl.Phys. **B345** (1990) 79–103.

[169] E. De Wolf and P. Van Mechelen. arXiv:hep-ph/9907309 [hep-ph].